Automated Phase Plate Application In Transmission Electron Microscopy

Marco Oster

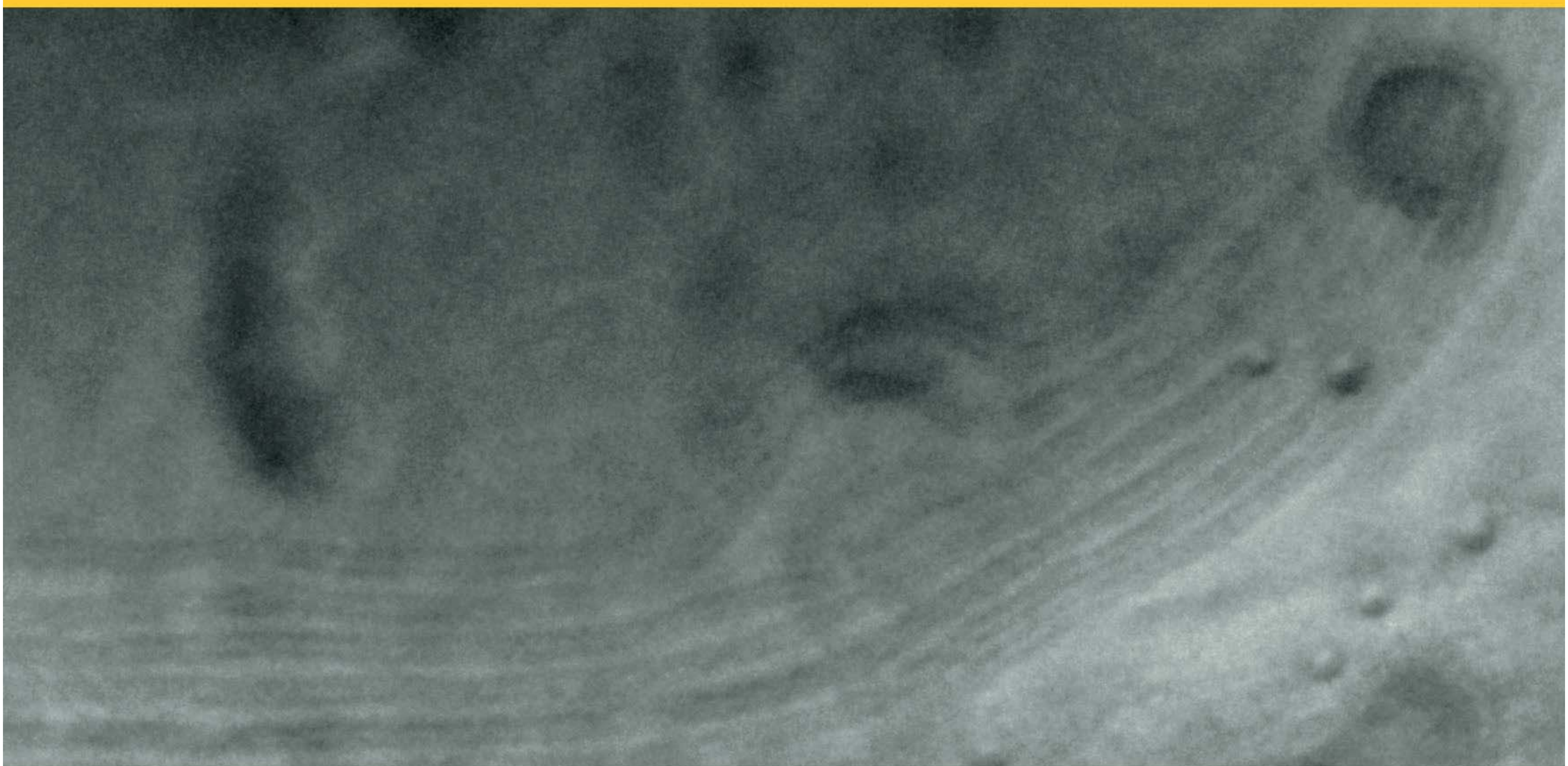

Cuvillier Verlag Göttingen
Internationaler wissenschaftlicher Fachverlag

AUTOMATED PHASE PLATE APPLICATION IN TRANSMISSION ELECTRON MICROSCOPY

Von der Fakultät für Elektrotechnik, Informationstechnik, Physik
der Technischen Universität Carolo-Wilhelmina zu Braunschweig

zur Erlangung des Grades eines Doktors
der Ingenieurwissenschaften (Dr.-Ing.)

genehmigte Dissertation

von Marco Emanuel Oster
aus Ludwigshafen am Rhein

Eingereicht am 28. März 2016
Mündliche Prüfung am 10. August 2016

1. Referent: Prof. Dr.-Ing. Wolfgang Kowalsky
2. Referent: Prof. Dr. rer. nat. Rasmus R. Schröder

Druckjahr: 2017

AUTOMATED PHASE PLATE APPLICATION IN TRANSMISSION ELECTRON MICROSCOPY

MARCO EMANUEL OSTER

Bibliografische Information der Deutschen Nationalbibliothek
Die Deutsche Nationalbibliothek verzeichnet diese Publikation in der Deutschen Nationalbibliografie; detaillierte bibliografische Daten sind im Internet unter `http://dnb.d-nb.de` abrufbar.
1. Aufl. - Göttingen: Cuvillier, 2017
Zugl.: (TU) Braunschweig, Univ., Diss., 2017

Dissertation an der Technischen Universität Braunschweig,
Fakultät für Elektrotechnik, Informationstechnik, Physik

Marco Oster: *Automated Phase Plate Application in Transmission Electron Microscopy,* © March 2016

Nonnenstieg 8, 37075 Göttingen
Telefon: 0551-54724-0
Telefax: 0551-54724-21
`www.cuvillier.de`

1. Auflage, 2017
Gedruckt auf umweltfreundlichem, säurefreiem Papier aus nachhaltiger Forstwirtschaft.

ISBN 978-3-7369-9562-8
eISBN 978-3-7369-8562-9

ZUSAMMENFASSUNG

Die Transmissionselektronenmikroskopie dient als essentielles Werkzeug der Strukturaufklärung biologischer und materialwissenschaftlicher Systeme. Ein Großteil der dort untersuchten Proben sind Phasenobjekte, d. h. ihre Interaktion mit der durchlaufenden Elektronenwelle bewirkt eine Phasenänderung selbiger. Zur Sichtbarmachung dieses Signals werden in der konventionellen Transmissionselektronenmikroskopie Linsenaberrationen benutzt, wobei das entstehende Bild von entsprechenden Abbildungsfehlern behaftet ist.

Phasenplattenmikroskopie bietet eine alternative Möglichkeit der Kontrasterzeugung ohne dabei Linsenaberrationen zu benötigen. Jedoch verhindern sowohl die zur Anwendung notwendigen diffizilen Bedientechniken, als auch die große Empfindlichkeit heutzutage verfügbarer Phasenplattensysteme bisher einen routinemäßigen Einsatz.

In dieser Arbeit werden Möglichkeiten einer automatisierten Anwendung von Phasenplatten erarbeitet, und deren Einsatzfähigkeit evaluiert. Der Fokus liegt hierbei auf der Begrenzung des sogenannten *cut-on* Effekts, welcher die Phasenkontrastübertragung für kleine Ortsfrequenzen limitiert. Dazu werden zum einen die Eigenschaften eines eigens zur Behebung dieses Problems konstruierten Prototypengeräts evaluiert, und zum anderen die Merkmale eines neuen, bisher nicht detailliert beschriebenen Abbildungsmodus theoretisch erarbeitet und seine praktische Anwendung auf strahlungsempfindlichen Proben unter Zuhilfenahme der entwickelten Automatisierungstechniken demonstriert.

ABSTRACT

Transmission electron microscopy is an essential tool to determine the structure of biological and material-science samples. A majority of the studied specimen are phase objects, i. e. they impose a small distortion on the phase on the traversing electron-wave. To visualize this signal, conventional transmission electron microscopy needs to apply intended lens aberrations, which results in distorted images.

Phase plate microscopy offers an alternative possibility to generate phase contrast without relying on the lens-aberrations. However, the delicate

alignment of the phase plates and their quick degeneration prevent their routine application.

In this work, approaches for automating the phase plate alignment are developed. To further improve the applicability, different means to reduce the so-called *cut-on* effect are evaluated. For that, the characteristics of a prototype instrument especially constructed to solve the cut-on problem are assessed and the properties of a new dynamic imaging mode examined in a theoretical study and by simulation. The applicability of the approach is demonstrated on beam-sensitive samples using the developed automation routines.

CONTENTS

Abbreviations

2D	Two Dimensional
3D	Three Dimensional
aCTF	Amplitude Contrast Transfer Function
API	Application Programming Interface, software interface designed for interaction with another software
CTF	Contrast Transfer Function
DMU	Diffraction Magnification Unit, provides magnified diffraction plane for phase plates
DNA	Deoxyribonucleic acid
DQE	Detection Quantum Efficiency
eV	Electron Volt
FEG	Field Emission Gun
FIB	Focused Ion Beam
HM	High Magnification Mode
LM	Low Magnification Mode
MTF	Modulation Transfer Function
pCTF	Phase Contrast Transfer Function
RF	Radio Frequency
SEM	Scanning Electron Microscopy
SI	Système international d'unités
TEM	Transmission Electron Microscopy

Symbols

a	Attenuation factor of the illuminating wave due to absorption in the specimen, usually close to unity
a_0	Attenuation of a structure factor by a phase plate
A_1	Twofold astigmatism parameter of the pCTF, directional defocus
Å	Ångstrom, 1×10^{-10} m
α_i	Illumination aperture, angular distribution present in Ψ_0
β	Induced beam tilt
c	Speed of light in vacuum
C_c	Chromatic aberration coefficient of the optical system, usually in the range of f
C_s	Spherical aberration coefficient of the optical system, usually in the range of f
δ	Dirac delta distribution, representation of the reference wave in reciprocal space
Δz	Defocus, deviation from Gaussian focus
ΔE	Energy spread of the electron-source
ε	Specimen amplitude factor, $1 - a$
E	Damping envelopes in reciprocal space
e	Elementary charge
E_0	Electron rest energy
$\mathcal{F}$	Fourier transform
$\mathcal{F}^{-1}$	Inverse Fourier transform
f	(effective) Focal length of the objective lens
h	Planck's constant
i	Imaginary unit

K_c	Temporal coherence envelope function in reciprocal space
K_s	Spatial coherence envelope function in reciprocal space
λ	Wave length in vacuum
M	Magnification factor
m_o	Electron rest mass
φ_{pp}	Phase shift induced by a phase plate
Φ	Fourier transform of the image wave, $\mathcal{F}\left[\Psi_i(\mathbf{r})\right]$
φ	Phase shift
Ψ	Wave function
Ψ_o	Illuminating plane wave, also known as unscattered electron-beam or zero-order beam
Ψ_i	Image wave, the object wave modulated by the CTF
Ψ_s	Specimen exit wave, also known as object wave
$\mathbf{q}$	Reciprocal space coordinate
q	Reciprocal space spatial frequency
q_c	Cut-on frequency
$q_{\max}$	Instrument resolution limit
r	Direct space distance
$\mathbf{r}$	Direct space coordinate in specimen or object plane
r'	Physical distance in the diffraction plane
r, θ, ϕ	Polar unit vectors
$\mathbf{s}$	Image shift on the camera
θ	Scattering angle
t	Specimen thickness
U	Acceleration Voltage or High Tension

V_i	Mean inner potential
V_t	Projected specimen potential
γ	Wave aberration function in reciprocal space
z	Unit vector normal to the specimen plane

Affiliations and Companys

CEOS	Corrected Electron Optical Systems GmbH, Heidelberg, Germany
CryoEM	CryoEM AG Schröder, Bioquant CellNetworks, Universitätsklinikum Heidelberg, Heidelberg, Germany
FEI	FEI Co., Hillsboro, Oregon, USA
ibss	ibss Group Inc., Burlingame, California, USA
iL	InnovationLab GmbH, Heidelberg, Germany
Kleindiek	Kleindiek Nanotechnik GmbH, Reutlingen, Germany
KonTEM	KonTEM GmbH, Bonn, Germany
LEM	Labor für Elektronenmikroskopie, Karlsruher Institut für Technologie, Karlsruhe, Germany
Zeiss	Carl Zeiss NTS GmbH, Oberkochen, Germany

1

INTRODUCTION

The present work deals with the properties and development of automated phase plate application in Transmission Electron Microscopy (TEM). In this chapter, the problem is motivated at the example of the imaging requirements for specimen of current research interest. The relevance of TEM is illustrated and the difficulties to generate contrast for transparent, beam-sensitive specimen are pointed out. A possible solution to the problems is the application of physical phase plates for contrast generation, which is however impeded by other negative effects.

With the context provided in this overview, the essential questions are formulated and the chapter organisation of the thesis is presented.

STRUCTURE-FUNCTION RELATIONSHIP

The efficiency and function of organic electronics is not only dependent on the properties of the materials used, but also on their structural composition. For instance, in the active layer of organic photovoltaic cells, excited states of electron-hole-pairs, so-called excitons, are generated by absorption of incident photons. The excitons need to be separated into electrons and holes and subsequently transported to the respective electrodes in order to contribute to a usable electrical current [71].

During its short lifetime, the exciton is able to travel a certain characteristic distance before it is annihilated by recombination. This distance is called diffusion length. In typical materials used for organic photovoltaic cells, this distance is in the order of 2–10 nm [84, 71].

Distinct constituents of organic electronics may differ in their electron-affinity as an intrinsic material property. In the context of organic electronics, materials with lower and higher electron affinity are called donor and acceptor materials. Both form the active layer of an organic photovoltaic cell, since brought into contact, electrostatic forces are generated in the interfacial area, which help separate the excitons. For an efficient charge separation, such an interface has to be present within the diffusion length of an exciton.

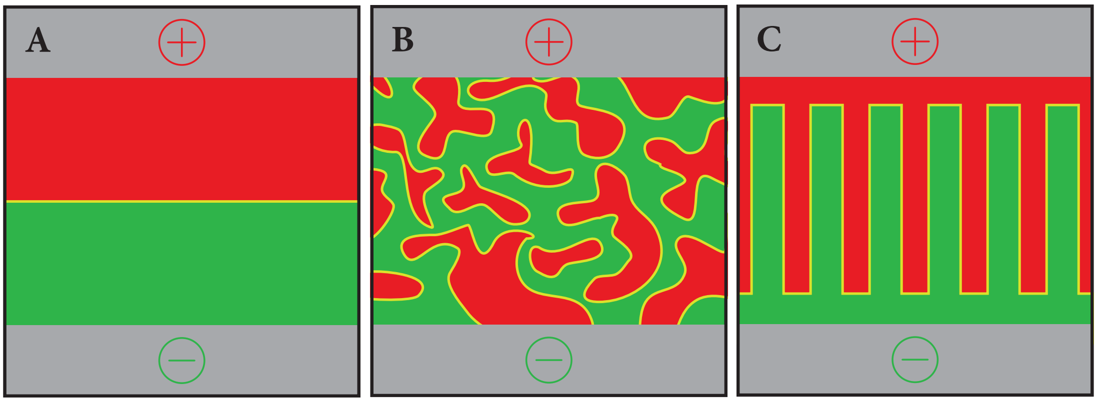

Figure 1.1: Schematic morphologies of active layers of organic photovoltaic cells. The size of the interfacial area (yellow) between electrode-connected regions of donor and acceptor materials increases from planar configuration (**A**), bulk heterojunction (**B**) to the theoretical optimum, a fine interdigitation (**C**) in a comb structure with the width of the fingers twice the exciton diffusion length [71]. Donor- and acceptor-rich regions are marked in green and red, electrodes in grey.

After charge separation, holes and electrons subsequently need to be transported to cathode and anode contacts, which requires an uninterrupted percolation path of low series resistance to the respective electrodes. The existence of such a pathway can be guaranteed for planar configurations of the active layer, as can be seen in figure 1.1 (**A**). However, as efficient absorption of photons requires a larger bulk thickness, many of the generated excitons cannot reach the interfacial area and recombine before separation. This results in a small likelihood of a successful charge separation and therefore a poor power conversion efficiency.

By replacing the 2D planar donor-acceptor interface with a 3D bulk heterojunction, shown in figure 1.1 (**B**), the size and distribution of the interfacial area can be optimized, but this only results in better power conversion efficiency, if uninterrupted electrical connections to the electrodes with low series resistance can be maintained [85]. An ideal configuration, a finely interdigitated comb structure, is shown in figure 1.1 (**C**) [71].

Variation of the process parameters during manufacture of the organic solar cells influence various morphological properties, such as domain sizes, level of donor-acceptor intermixture, degree of crystallinity or preferential location of the domains, which all have an influence on the device performance. In order to better approximate the ideal comb structure, the influence of process parameters on the resulting morphology need to be understood for a target-driven optimisation of a manufacturable structure. Therefore, the possibility of direct visualisation of the resulting morphology can provide key insights to understanding the structural reasons for a certain device performance and provide hints for improvement.

For characterisation of the domain sizes, the relevant dimensions are in the order of the exciton diffusion length, i. e. about 2–10 nm. Distinct crystalline features, such as characteristic π–π-stacking distances can be useful for material identification within the active layer, which usually requires a better point resolution of about 1–20 Å, depending on the properties of the materials. Ideal conditions would be able to image both the fine and the coarse resolution scale equally efficient.

Comparable to organic electronics, biological systems are mainly composed of a selection of light elements with low atomic numbers. Constructed after the blueprints encoded in the DNA, miniature machines, so-called macromolecular complexes serve as building blocks of life. The individual shape of the nanometer-sized macromolecular complexes is adapted to the specific function. Similar to organic electronics, structure determination helps understanding the key mechanisms of certain diseases or how living organisms work in general. The required point resolution for such deductions is also in a range of a few Å.

RESOLUTION

In 1878 Ernst Abbe formulated his famous equation, which relates the attainable resolution of an optical system to its numerical aperture and the wavelength λ of the illuminating wave [1]. Restricted to visible light with a wavelength of a few hundred nm, the maximal attainable point resolution of a general object is limited to about 200 nm, even for a perfect, i. e. aberration free optical system with maximal numerical aperture. To attain higher resolution, shorter wavelengths are needed. Non-visible light of higher energy, such as X-rays, offers smaller wavelengths in the range of 10 nm–10 pm, but due to the resulting decreased interaction with matter, construction of usable lenses becomes more and more difficult.

The wavelength of sufficiently accelerated electrons can be several orders of magnitude smaller than that of photons for which acceptable optics can be manufactured. Using a suitable optical system, which allows to form images using electrons, a much higher resolution is therefore feasible. The first steps towards implementation of such an optical system were the experiments of Ernst Ruska, who managed to create a magnetic field of suitable shape to focus electrons into a spot, originally with the aim to improve the performance of cathode ray tubes used in oscilloscopes [68]. Shortly after, with optimisations of the shape of the magnetic field, the aberrations could be controlled well enough to demonstrate its use as a lens suitable for imaging. Combining two of such lenses, an optical system was demonstrated, which allowed to surpass the resolution attainable by visible-light microscopy.

PHASE OBJECTS AND PHASE CONTRAST

A theoretical investigation by Hans Boersch [8] analysed the attainable contrast in TEM and noted that atoms imaged with electrons at medium acceleration voltages essentially appear as transparent *phase objects*, where the individual atoms in the sample offer a locally varying refraction index to the electron wave. After passing through the sample, the object's information is almost exclusively encoded in a small modulation of the phase of the beam, which unfortunately results in negligible contrast on a detector, if an aberration-free optical system is used for imaging.

From light optics, such specimen were already known as phase objects. A solution to imaging such objects with nonvanishing contrast was offered by Frits Zernike [88]. For contrast generation, an additional phase shift of $\pi/2$ needs to be introduced in between the part of the wave having interacted with the sample and the unscattered reference wave. This can be realized using an additional optical element with two areas of different optical thickness, where the optical pathway trough one region is an odd multiple of $\lambda/4$ longer than the other.

This so-called *phase plate* needs to be inserted in a diffraction plane, where there is a spatial separation between scattered and unscattered beams. For parallel illumination, the unscattered or *zero-order beam* is focused into a spot, while beams having interacted with the specimen are scattered to higher angles. Using this spatial separation, the phase-shifting effect can be applied to either scattered or unscattered beams, if phase plate structures of suitable size and shape can be manufactured.

Boersch suggested to adapt Zernike's phase contrast method for TEM [8]. Unlike structured glass phase plates for photons, the $\lambda/4$ plate equivalents for electron microscopy make use of an electrostatic potential to provide a phase shift. The inner potential of a thin film material of suitable thickness can be source of an approximately homogeneous potential generating a phase shift of $\pi/2$. By cutting out a hole in such a film, a discontinuity in the

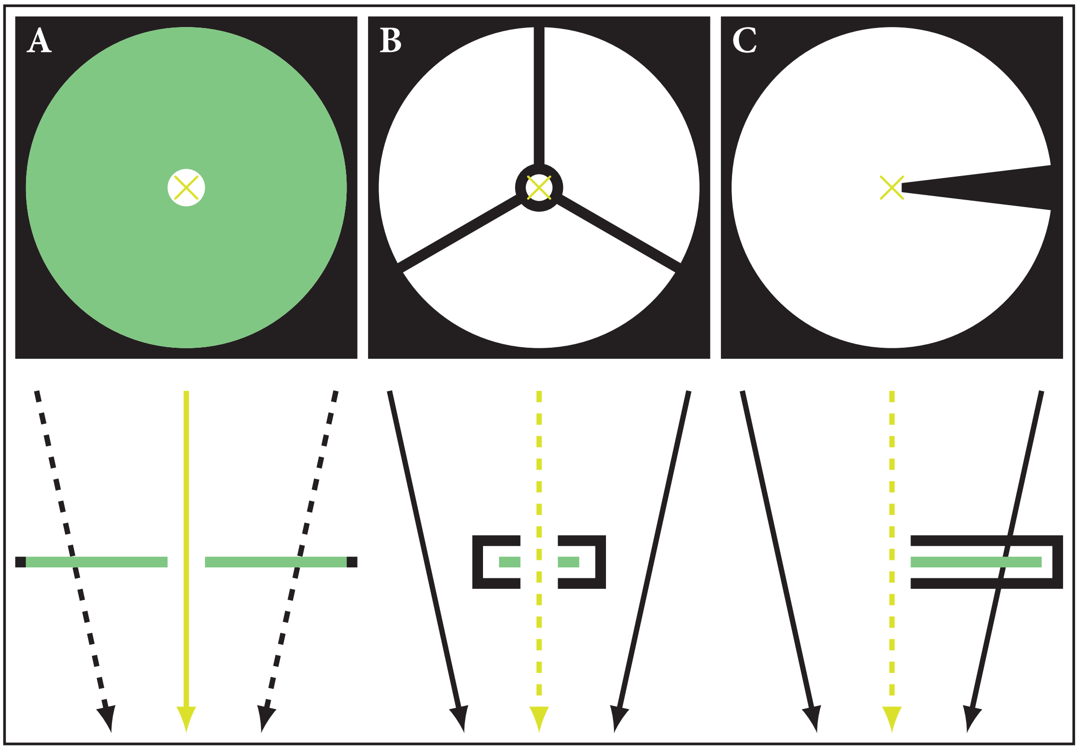

Figure 1.2: Phase plates suitable for TEM in plan (upper row) and orthogonal (lower) views through the aperture center in the diffraction plane. Zernike film phase plate in (**A**) consisting of a thin matter foil of suitable thickness with cut-out hole for the zero-order beam (×). Electrostatic phase plate design proposed by Boersch in (**B**) and its optimized successor, the Zach phase plate with smaller electron-obstructing area in (**C**). Therein, the phase-shifting potential is generated by an applied voltage. The elements responsible for the phase shift are highlighted in green. The supporting structure is kept at ground potential (solid black). For an additional phase shift (- ►) of $\pi/2$ between scattered and unscattered beams, either the unscattered beam (**B–C**) or all scattered beams (**A**) have to be phase shifted relative to the respective unshifted beams (→).

potential distribution is realized and the necessary relative phase shift is generated, if the reference wave is allowed to pass through this cut-out hole and all scattered electrons pass through the matter foil. This is depicted in figure 1.2 (**A**).

Alternatively, miniature electrode assemblies generating a localized electrostatic field can be used to adjust the phase of the reference wave. Compared to the film phase plates, this has the advantage that the scattered electrons, which carry all the specimen information, are not subjected to another scattering process in the phase plate, avoiding a negative influence on the attainable point resolution. Furthermore, the amount of phase shift is tunable with variation of the applied potential.

Boersch also noted that lens aberrations, most importantly defocus and spherical aberration, influence the phase of the electrons and can be used to enable phase contrast transfer. This is especially true for small real space object distances or high spatial frequencies in reciprocal space, corresponding to large scattering angles [8, 73]. While this is the most important source of phase contrast transfer in standard TEM images, it is impeded by the resulting oscillating transfer function. This complicates quantitative and often even qualitative image interpretation, due to unavoidable contrast inversions and transfer gaps. Therefore, the transferred contrast always suffers from dislocation, i. e. the relative position of an object feature is not faithfully reproduced in the image. This is especially true for low spatial frequencies, as their transfer demands relatively large intended aberrations and therefore large contrast dislocations, which obscure the true shape of an object.

To obtain an unaberrated phase contrast image using conventional methods, a so-called exit-wave reconstruction has to be performed, wherein the information from many differently aberrated images is combined [58, 64]. However, to reproduce the true object properties in such a reconstruction, a precise knowledge of the actual aberration parameters for each of the individual images is necessary, which can be difficult to measure accurately. For beam-sensitive specimen, the amount of exposures at the same sample position is limited and therefore only a small set of differently aberrated images can be acquired. Depending on the required range of accurately reconstructed spatial frequencies, a certain amount of measuring points are required, and the dose budget has to be split accordingly. Eventually, this results in poor signal-to-noise ratios in the individual images, which ultimately prohibits a faithful reconstruction.

Using ideal physical phase plates and suitable imaging conditions, unaberrated phase contrast images can be acquired in a single exposure. If an electrostatic phase plate with adjustable phase shift is used, a full exit-wave reconstruction can be realized in only three images [33].

3D IMAGING AND DOSE PROBLEM

Even though the samples in TEM have to be relatively thin to allow passage of the beam through the sample, many applications still require 3D object information. Unlike techniques restricted to accessing surface information, in TEM the electron-beam is influenced by the whole bulk of the sample. In a single image, a projected view of the specimen potential is generated. Using electron-tomography, the 3D object information can be reconstructed, if a sufficient amount of views at different projection angles is available. For general specimen, such views can be generated by acquisition of a tomographic tilt series. Depending on the required resolution, this requires acquisition of about 30 to more than 100 individual images at the same specimen position, which exposes relatively small sample areas to a high electron dose.

Unfortunately, typical samples of organic specimen such as biological macromolecules and organic electronics degrade if exposed to the intense electron beam, i. e. their spatial conformation changes. For imaging, this means only a certain dose budget is available, which ultimately limits the attainable signal-to-noise ratio.

A standard approach to reduce the structure-changing effects of the electron exposure is maintaining the specimen at cryogenic temperatures. While this can increase the sustainable dose of a delicate specimen by an order of magnitude [35], it usually does not enable recording of high spatial resolution with sufficient signal-to-noise ratio on its own.

To increase the signal-to-noise ratio with biological macromolecules, the so-called single-particle approach is widely used. Therein, the ability of biological systems to produce large amounts of virtually identical particles is exploited. The attained signal-to-noise ratio in a 2D projection image then only has to allow a reasonable determination of the particle's relative rotation and translation parameters [38, 29]. By taking the combined information of several thousand single particles gathered from hundreds of images and leveraging the signal from the different angular views present in the dataset, low-noise 3D maps with resolutions better than 3 Å can be generated [3, 12].

While usual fabrication steps of organic electronics involving vapour deposition or solution processing may result in locally ordered structures due to self-assembling properties of the individual materials, the general bulk morphology is non-repetitive, i. e. no identical copies of regions can be expected to occur. Therefore, no single-particle approach is feasible to increase the signal-to-noise ratio while maintaining low-dose conditions and only the acquisition of tomographic tilt series allows reconstruction of the 3D object information. To limit the sample degradation and maximize the signal-to-noise ratio, the dose budget has to be transferred into image contrast most efficiently. As phase plates optimize the contrast transfer, they can be an enabling technology to extend the applicability of such advanced acquisition schemes also on dose-sensitive samples.

Similarly, also the single-particle approach can benefit from phase plate application. Typically, biological macromolecules are imaged close to their native state, i. e. embedded in a vitrified aqueous solution. Due to the low difference of atomic numbers between sample and background, the available signal is rather small, and conventionally requires use of an excessive amount of intended defocus to produce recognizable contrast. For small macromolecules with dimensions of e. g. 10–20 nm, this often means the apparent contrast dislocation is larger than the dimensions of the actual particle, which limits the practical use of this approach. Phase plate application is a potential key technology to enable imaging of such delicate objects.

1.1 CHALLENGES OF PHASE PLATE USE

Theoretically, the superior imaging properties of phase plate microscopy demand its application to all kind of TEM problems. So far, the practical application of phase plates has been impeded by a couple of detrimental effects. For instance, the requirement to impose different phase shifts to zero-order and scattered beams can often only be approximated, due to the small extent of the zero-order beam focus in the diffraction plane. Especially if an electrostatic phase plate is used for generating the phase shift, current micromanufacturing techniques fail to produce sufficiently small electrodes that the obstructions of the opaque electrode support material are negligible.

For certain phase plate geometries involving a cut-out hole, such as Zernike film and electrostatic Boersch phase plates, only spatial frequencies exceeding a certain, so-called *cut-on frequency* are subject to the necessary phase shift of $\pi/2$. The main effect is a sudden, step-like onset of contrast transfer for the film phase plate and the obstruction of a certain range of spatial frequencies corresponding to the radius of the cut-out hole for the electrostatic phase plate (cf. figure 1.2 (**A**) and (**B**)), which both introduce image distortions. The detrimental effects can be alleviated if smaller physical phase plate structures are used.

Since the manufacturing technology does not allow a further significant minimisation of the electrostatic phase plate structure, they can be inserted into an optically magnified diffraction plane for a relative size reduction compared to the unmagnified conditions. In the KRONOS instrument, this has been realized in an additional column element, the Diffraction Magnification Unit (DMU).

Intense electron-beams can channel adsorption of residual molecules stemming from imperfect vacuum conditions to a surface [27, 26]. The deposited contaminations create poorly conducting patches on the surface of a phase plate, which subsequently accumulate a charge and influence the electrostatic potential distribution.

In the electrode assembly of an electrostatic phase plate, insulating materials need to be used for construction. Irradiated with highly accelerated electrons, the electron-obstructing structure is partially penetrated and inelastic interactions occur within the material, which can generate positive and negative charges [82]. Due to the low charge carrier mobility present in insulators, the generated charges are trapped and permanently influence the phase-shifting behaviour of the phase plate. Most detrimental effects of contamination and charge deposition can therefore be avoided, if the phase plate is handled with the utmost care, and the physical structure never exposed to the intense zero-order beam.

Finally, to generate the desired phase-shifting effect, the physical phase plates need to be aligned very precisely relative to the zero-order beam. Manual alignment can be very tedious and time consuming, especially if suboptimal electron-optical alignment does not allow side-effect free variation of individual parameters of the optical system. Time consuming, tedious and delicate handling tasks are often better left to machines, rather than human operators. Fully automated phase plate application could therefore provide a key contribution to establish phase contrast microscopy as a standard tool in TEM.

1.2 GOALS AND OUTLINE

Phase plate microscopy potentially enables superior imaging of phase objects. Towards establishing this technology as a standard technique in TEM, this thesis contributes insights to the following questions:

- Can an automatic application of a phase plate be realized?
- How can the necessary functionality be integrated in standard automated image acquisition software?

As phase plate microscopy requires tight control of the beam conditions in the diffraction plane, where the phase plates are installed, further points of interest for a successful realisation are:

- What requirements have to be met by the electron-optical alignment to allow automated phase plate microscopy?
- What are the consequences of introducing a DMU to the optical setup? Does it provide a better environment for phase plate application?
- Are there alternative means to reach a similar goal with standard electron-optics?

Unlike human operators, who need a continuous visual feedback for manual phase plate alignment, automation algorithms can precisely determine the current positioning error and compute a matching correction from a static exposure. Such a discrete alignment scheme potentially imposes a lower dose on the phase plate structure. An additional aspect is therefore:

- Can automated phase plate alignment routines help prevent phase plate degradation and increase their effective lifetime?

To answer the questions, this thesis is laid out as follows: In chapter 2, the theoretical mechanisms of contrast formation in TEM are described. In the following chapter 3, an introduction of the concepts of automated image acquisition is given. The source of electron-optical alignment problems are identified and appropriate means for controlling the beam in the diffraction plane are presented. Afterwards, several methods to determine the current phase plate position are shown. All aspects are combined in an automatic alignment routine, whose performance is evaluated.

The experimental results acquired using electrostatic phase plates and evaluation of the DMU properties are given in chapter 4. With the development of a new imaging mode for film phase plates, which is described in chapter 5, the implementation of automated alignment strategies are demonstrated on beam-sensitive samples. The results are presented in chapter 6.

Finally, the implications of the different phase plate technologies, microscope properties and benefits from automation are discussed in chapter 7.

2 CONTRAST FORMATION IN TEM

This chapter begins with a description of the main structural components of a transmission electron microscope and introduces the names and location of the most important lenses and principal planes. Then, the interaction of an electron wave with matter, such as a specimen or a thin film phase plate is discussed. Afterwards, the image contrast transfer of the optical system is discussed using the idealized properties of a pure phase object. Some more attention is given to the properties of phase contrast transfer using various phase plate designs. Finally, the known limitations of physical phase plates and possible remedies are discussed.

2.1 STRUCTURAL COMPONENTS OF A TRANSMISSION ELECTRON MICROSCOPE

In most transmission electron microscopes the same principal building blocks can be found in a similar sequential configuration. The individual components are stacked in a column, with an evacuated beam pipe in the centre. Electron-source and camera are located at top and bottom of the column, respectively. In between, round electron-lenses, deflectors and other beam-shaping electron-optical elements are arranged in specialized groups, such as condenser, objective and projective, which are responsible for a certain, often specialized task. An annotated image of a modern transmission electron microscope used in this work is shown in figure 2.1.

In the electron gun, free electrons are extracted from a pointed tip using thermal or tunnelling effects. Important properties of the electron-source are the attainable radiant intensity, the effective source size and the width of the energy distribution of the emitted electrons, which determine spatial and temporal coherence parameters of the illumination. Modern field emission gun (FEG) electron-sources offer both high spatial and temporal coherence, with the energy spread ΔE of a thermally assisted FEG in the range of 0.2–0.7 eV, which can be further reduced by an integrated monochromator [45].

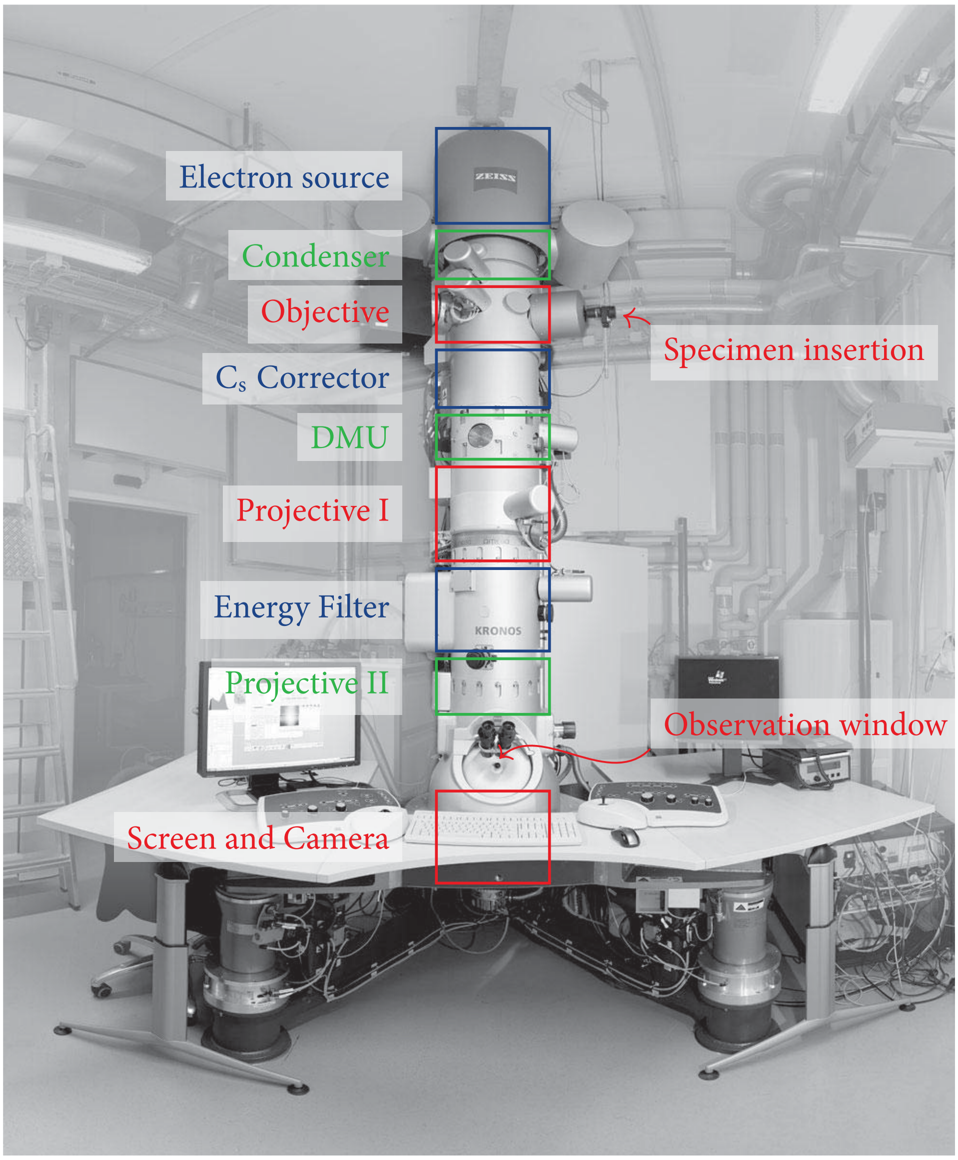

Figure 2.1: Annotated view of a specialised transmission electron microscope used in this work. From top to bottom, the electrons are emitted from the electron-source, conditioned to provide a sample illumination of the desired parameters, interact with the sample and are projected to a screen or other detector. Many high-performance instruments feature additional electron-optical elements to enhance certain optical properties, such as correcting for the spherical aberration C_s or provide devices allowing analytical studies, such as imaging energy filters and spectrometers. Additional to the provisions of standard instruments, this microscope features an accessible magnified diffraction plane in a dedicated unit (DMU) for phase plate application. The height of this instrument is about 4.5 m and the column diameter about 35 cm. Image courtesy of Levin Dieterle/iL.

Subsequently, the electrons are accelerated to the desired high-voltage and fed into the condenser. The resulting electron wavelength is given by

$$\lambda = \frac{h}{\sqrt{2m_0 eU \left(1 + \frac{eU}{2m_0 c^2}\right)}}$$

with electron wavelength λ, Planck's constant h, m_0 the electron rest mass, e the elementary charge, U the acceleration voltage and c the speed of light in vacuum.

In the condenser system, the parameters of the illuminating plane wave, such as the size and intensity of the illuminated area at specimen level can be varied by choosing different excitations of lenses arranged in a single or double zoom system. The condenser is also responsible for projecting a beam cross-over, i. e. a demagnified image of the electron-source in the front focal plane of the objective prefield lens. This ensures parallel (plane-wave) specimen illumination. Details of the resulting ray paths can be seen in the schematic overview shown in figure 2.2.

The specimen is immersed in the magnetic field of a Riecke-Ruska-type single-field condenser-objective lens. In the ray diagrams shown in this work, it is represented by two separate lenses, the objective prefield and the objective lens. The objective prefield lens in front of the specimen is responsible for forming the illuminating beam. The objective lens located thereafter receives the electrons scattered by the specimen and provides the first, most critical refraction. Since in the entire microscope, only the objective lens needs to deal with large scattering angles, its performance is decisive for the fidelity of the optical system.

During its passage through the thin specimen, the electron-wave interacts with the specimen potential and undergoes elastic and inelastic scattering events. After passing through the bulk of the specimen, the so-called *exit* or *object wave* is formed.

The objective is responsible for focusing rays diffracted into a certain angle to a certain position in the back focal plane. It can be shown that this property forms a reciprocal space representation of the object wave in the back focal plane, which corresponds to the Fourier transform of the specimen's potential [45, 28]. Of further note is the correspondence of shifts in the diffraction plane to tilts in the object plane and vice-versa.

In the back focal plane, electrons scattered to higher angles are focused at larger distances with respect to the optical axis. By introduction of an aperture in this plane, the angular distribution of scattered electrons can

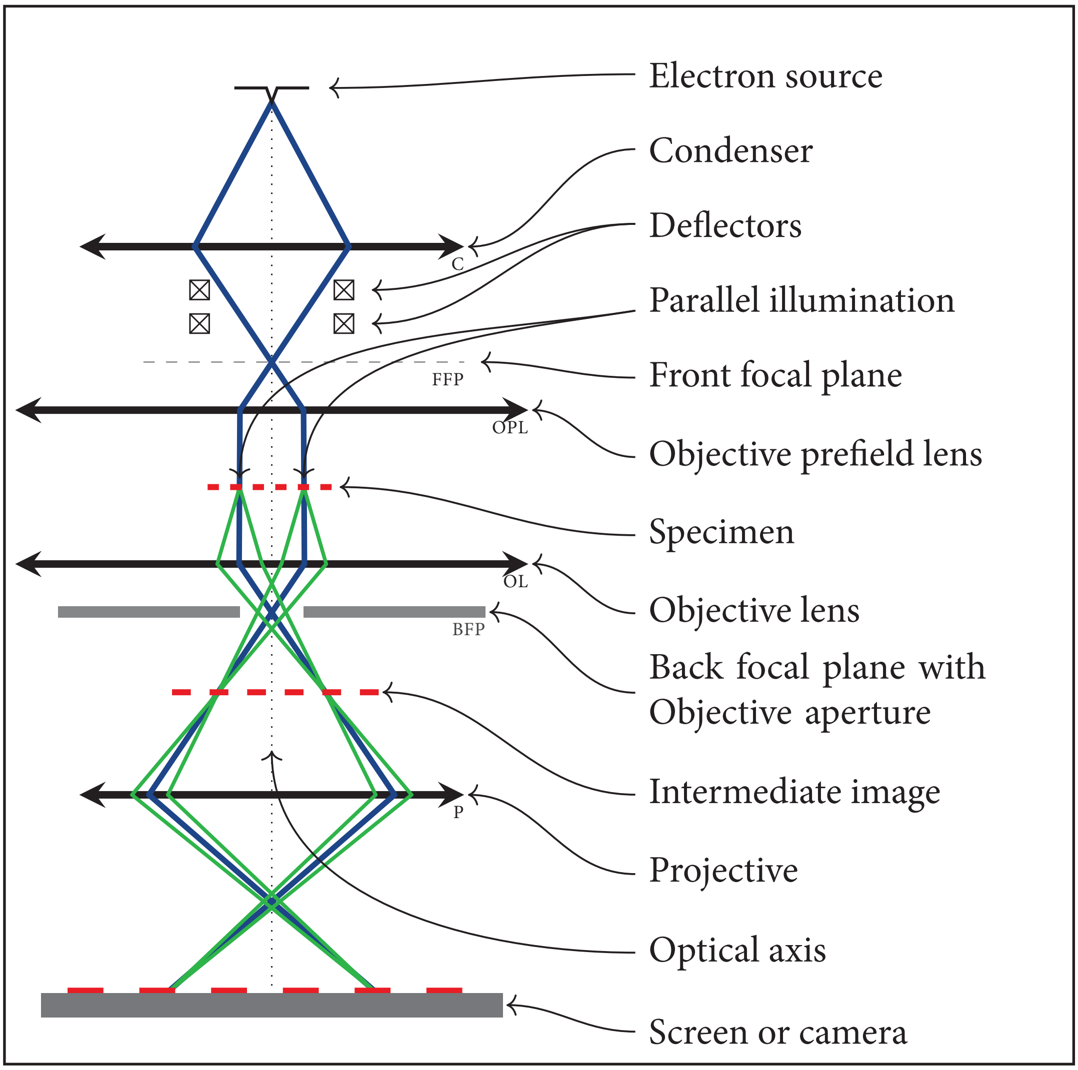

Figure 2.2: Schematic view of the components of a transmission electron microscope. In actual microscopes, condenser and projective systems drawn here as single lenses (⟷) are usually implemented using a group of several round lenses and other electron-optical elements.
The condenser system focuses an image of the electron-source in the front focal plane of the objective prefield lens, to provide parallel specimen illumination. After having interacted with the specimen, electrons scattered into equal angles are focused at same positions in the first diffraction or back focal plane behind the objective lens, which produces a spatial separation of diffracted (green) and undiffracted (blue) rays. This separation is used for application of apertures and phase plates.
For aberration-free in-focus imaging conditions, every sample point is projected into a single image point on the screen.

be limited to a maximum value. Phase plates require a spatial separation of diffracted and undiffracted beams, so they are physically installed in the back focal plane or a conjugated diffraction plane, often instead of an objective aperture.

For thin lenses, the distance of the back focal to object plane is characterized by the focal length f of the lens. Smaller values for f are found in stronger lenses. Typical values for the effective focal length of objective lenses used in TEM are in the range of 0.5–5 mm.

Further propagated, the electrons form an image of the object-wave in the first image plane, wherein scattered electrons originating from a single point in the sample are unified into an image point. To provide further magnification, the projective system uses additional lenses to image such a conjugated plane on the fluorescent screen or camera.

In the projective system, additional electron-optical devices can be present, which offer the possibility to perform advanced tasks. For instance, a C_s corrector corrects for the always-positive and never vanishing spherical aberration of round magnetic lenses [72, 37]. Likewise, C_c correctors compensate for the different beam paths seen by electrons of different energy [36]. Imaging energy-filters use an electron-prism to form an energy-dispersive plane, which can be projected to the screen or camera to measure an electron energy-loss spectrum. By introduction of a slit aperture of certain spatial extent in the energy-selective plane, corresponding limits on the energy distribution of the electrons contributing to the imaging process can be imposed, which provides higher contrast and valuable analytical insight into the specimen's properties.

The inclination of the optical axis in a transmission electron microscope is often defined by the orientation of the objective lens. To provide a straight path from electron-source over the centre of the objective lens to the centre of the screen or camera, a precise mechanical alignment of the individual components is necessary. To account for residual mechanical misalignment, the column features deflecting electromagnetic elements located at strategic positions throughout the beam path.

Most misalignments can be compensated by applying a certain shift to the beam to account for a lateral misalignment and a certain tilt to compensate for an orientation mismatch. Practically, every single lens in the beam path is slightly misaligned and would need a correcting element, but due to limited amount of space in the microscope column, not every lens features such a correcting element. In the context of an electron-optical alignment, a compromise needs to be found to establish an as straight as possible optical axis throughout the entire optical system.

2.2 ELECTRON-MATTER INTERACTION

The interaction of a specimen with the electron-beam can be divided into two main categories, *elastic* and *inelastic* interaction. During inelastic interaction, electrons transfer a fraction of their primary energy to the sample. The resulting effects can be manifold, such as exciting higher energy states, generation of secondary electrons, electron-hole pair generation or stimulation of collective oscillations, e. g. plasmons [83]. In this work, inelastic effects are usually not considered and largely removed from the imaging process by means of zero-loss filtering using an energy filter.

An electron is considered as elastically scattered, if momentum changes with only negligible energy loss in a scattering event. In this case, the source of the most relevant force exerted on the probing electron is the attractive screened Coulomb potential $V(\mathbf{r},z)$ of the specimen nuclei [45].

In high-resolution TEM, specimen are usually thin and illuminated by a plane wave $\Psi_0(\mathbf{r}) = 1$ of constant intensity, with $\mathbf{r}$ designating a 2D coordinate in the specimen plane. For thin specimen, nearly no illuminating electrons are lost, i. e. absorbed by the specimen or scattered to such high angles, that they are subsequently obstructed by an aperture.

The electrostatic potential of the specimen influences the phase of the electron wave, which can be expressed as a modulation with $\exp(-i\varphi(\mathbf{r}))$. It can be shown [28], that the local phase modulation $\varphi(\mathbf{r})$ by the object is proportional to the projected electrostatic specimen potential $V_t(\mathbf{r})$, as in

$$\varphi(\mathbf{r}) = \frac{\pi}{\lambda U} \int_0^t V(\mathbf{r}, z)\, dz = \frac{\pi}{\lambda U} V_t(\mathbf{r})\,. \tag{2.1}$$

The unit vector parallel to the illuminating beam and normal to the specimen plane is designated by z.

If the specimen is an amorphous film of a pure material, the phase shift gained during transversal can be estimated with the help of a material constant, the averaged mean inner potential $V_i = \frac{1}{t}\int_0^t V(\mathbf{r}, z)\, dz$ and the film thickness t to

$$\varphi(t) = \frac{\pi}{\lambda U} \cdot V_i \cdot t.$$

Mean Inner Potential

For such films, the phase shift imposed by the inner electrostatic potential is proportional to the film thickness. For 200 keV electrons and a calculated mean inner potential of 7.8 V for amorphous carbon, the needed film thickness for imposing a phase shift of $\pi/2$ is approximately 28 nm [45].

However, the measured effective mean inner potentials of fabricated amorphous carbon films can vary from 8–16 V, depending on the specific specimen preparation [17]. If the film is to be used as a phase plate film material, the correct thickness has to be adapted and the actual phase shift needs to be verified for a deterministic application.

2.3 WEAK-PHASE APPROXIMATION

A specimen can be characterized by its projected local phase modulation $\varphi(\mathbf{r})$ and its projected local specimen absorption coefficient $a(\mathbf{r}) \in [0, 1]$. As the specimen modulates the illuminating plane wave Ψ_0, the resulting object wave Ψ_s can be expressed by [45]

$$\Psi_s(\mathbf{r}) = \Psi_0 a(\mathbf{r}) \exp(-i\varphi(\mathbf{r})).$$

The expression can be simplified by writing a as $1 + \varepsilon$, since a differs only little from unity for thin specimen, as absorption can be neglected. With $|\varphi|, |\varepsilon| \ll 1$, the exponential function can be approximated by its truncated Taylor series, with vanishing cross terms:

$$\Psi_s(\mathbf{r}) = \Psi_0 (1 + \varepsilon(\mathbf{r})) \exp(-i\varphi(\mathbf{r})) \approx \Psi_0 (1 + \varepsilon(\mathbf{r}) - i\varphi(\mathbf{r}))$$

The specimen modelled by this approximation is known as a *weak-phase weak-amplitude object*. If the specimen is thinner than about 10 nm and only consisting of light atoms, also ε can be omitted for intermediate and high electron-energies [45]. The object wave for such a *weak-phase object* becomes

$$\Psi_s(\mathbf{r}) \approx \Psi_0 (1 - i\varphi(\mathbf{r})) = 1 - i\varphi(\mathbf{r})$$

with the plane wave amplitude set to unity, to mark its character as a reference wave. Thus for thin specimen, the object wave depends linearly on the local phase modulation of the illuminating wave. The imaginary unit i indicates that the specimen-signal is phase shifted by $\pi/2$ with respect to the reference wave $\Psi_0 = 1$.

Figure 2.3 shows the conditions during the vector addition in the complex plane. The reference wave Ψ_0 contributes the background intensity. The image intensity is given by the absolute value of the vector addition. In aberration-free imaging conditions, the small phase modulation therefore yields vanishing phase contrast transfer. The only possible way of

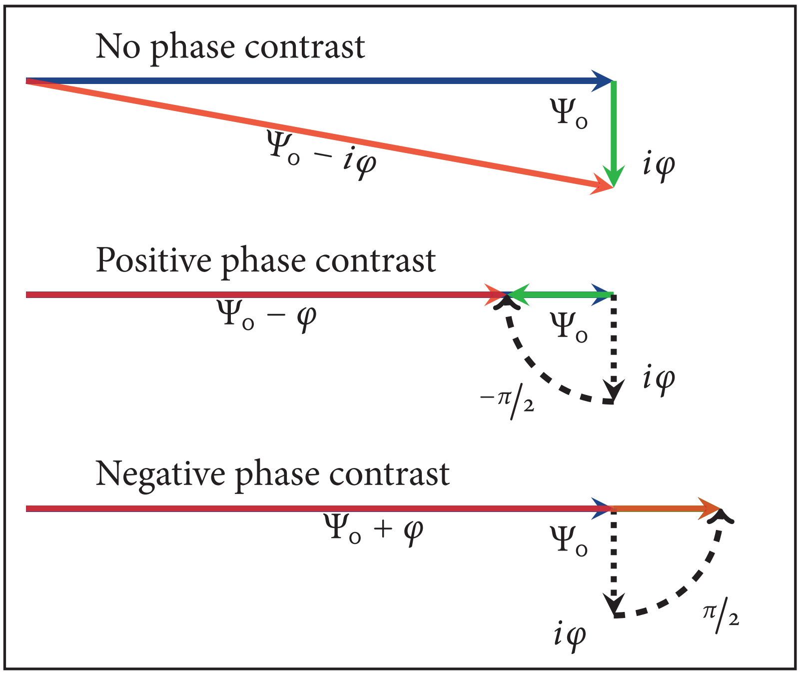

Figure 2.3: Vector addition in the complex plane. For weak phase objects, the observed intensity (red) does not differ from the background (blue). If the phase-modulated signal (green) is shifted for another $\pi/2$, observable contrast is generated. Figure after [45].

generating contrast from phase objects is by finding a means to add an additional phase shift to $i\varphi$ relative to the reference wave Ψ_o. The lower two diagrams in figure 2.3 show positive and negative phase contrast for an additional phase shift of $\mp\pi/2$ of the scattered electrons, which means the resulting image intensity is lower (positive phase contrast) or higher (negative phase contrast) than the background intensity. This definition has been introduced in [89].

The image contrast is generated by interference of object and reference wave. Upon measuring, i. e. the electron hits the screen or camera sensor, the wave function collapses and the electron deposits its energy at a specific detector position according to the probability density function of the interference pattern. To form an image of sufficient signal-to-noise ratio, the signal from many electrons is incoherently summed on the screen or detector.

2.4 MODULATION OF THE OBJECT WAVE

Owing to the physical properties of the imaging system, a few additional properties influence the image contrast transfer. For example, any instrument will be diffraction limited due to the finite size of the lenses or an explicit aperture in a diffraction plane. The inevitable effect is that object points, are imaged as Airy discs.

Also the aberrations of the optical system and the properties of the illuminating wave, namely its spatial and temporal coherence, influence the image formation process. Finally, the physical stability of the microscope column and the properties of the detector affect the contrast transfer as well. For modelling, those effects can be expressed as a convolution of the object wave with appropriate transfer functions, forming the so-called *image wave* [58].

Convolution operations are most conveniently applied in reciprocal or Fourier-domain representation, where they can be expressed in a simple multiplication of the Fourier-transformed operands. Direct-space distances r are related to spatial frequencies q in reciprocal space and scattering angles θ by

$$r \mathrel{\hat{=}} \frac{1}{q} = \frac{\lambda}{\theta}. \tag{2.2}$$

2.4.1 *Effects from Partial Coherence*

The ability of an optical system to focus two electrons originating from the same source location and only differing in their energy onto the same image point is characterized by the chromatic aberration coefficient C_c with dimension of a length. The effect on the image formation process is an incoherent summation of many images transferred with an energy-dependent defocus variation. This has only a small effect on low spatial frequencies, as large object features are less likely to be imaged at a different pixel position on a camera. For sample information stemming from fine structures encoded in high spatial frequencies, this is not the case and a blurring occurs. Expressed as a function of spatial frequencies, the effect can be modelled by a chromatic envelope function K_c [45]

$$K_c(\mathbf{q}) = \exp\left(-\left(\frac{\pi\lambda\mathbf{q}^2}{4\sqrt{\ln 2}}\frac{\Delta E}{eU}\cdot C_c\frac{1+eU/E_0}{1+eU/2E_0}\right)^2\right)$$

with electron rest energy E_0. The chromatic envelope is determined by the physical properties of the instrument, and largely independent from small variations of the parameters of the optical system.

For the spatial coherence envelope K_s this is not the case, as it depends on the defocus Δz and the spherical aberration coefficient C_s [45]. It can be modelled by

$$K_s(\mathbf{q}) = \exp\left(-\frac{\left(\pi C_s \lambda^2 \mathbf{q}^3 - \pi \Delta z \mathbf{q}\right)^2 \alpha_i^2}{\ln 2}\right),$$

with α_i the selected illumination aperture corresponding to the effective size of the electron-source.

Together, K_c and K_s form a dampening envelope E, which imposes a frequency-dependent modulation of the object wave. Other sources of dampening are the physical stability of the microscope column, as well as instabilities of acceleration voltage and lens current supplies, which can be modelled by additional envelopes. The properties of the detector can be reflected by a corresponding modulation transfer function (MTF) and detection quantum efficiency (DQE)[69].

2.4.2 *Phase Shifts from Lens Aberrations*

Non-perfect imaging conditions, i. e. no phase-correct transfer of all optical paths originating from a specimen point to a single image point, are reflected in additional phase modulations of the object wave. A deliberate introduction of aberrated imaging conditions can be used to generate an additional phase shift of $\pi/2$ for certain spatial frequencies, which enables phase contrast transfer.

In TEM, this dependency is described by the contrast transfer function (CTF). In a well-aligned optical system, the two most important parameters, the *defocus* Δz and the *spherical aberration* C_s, are sufficient for a discussion. In this case, the CTF modulates the object wave by the wave aberration function γ

$$\gamma(\mathbf{q}) = \tfrac{2\pi}{\lambda}\left(\frac{1}{2}\Delta z \lambda^2 \mathbf{q}^2 + \frac{1}{4} C_s \lambda^4 \mathbf{q}^4\right).$$

Advanced applications, e. g. exit-wave reconstructions, might require inclusion of higher-order terms. Also, azimuthally varying aberrations, such as the twofold astigmatism A_1 or coma might need to be taken into account, if the corresponding aberrations are present in the optical system.

The image wave $\Psi_i(\mathbf{r})$ and its Fourier transform $\Phi(\mathbf{q})$ describe the object wave modulated by the envelopes and the CTF :

$$\begin{aligned} \Phi(\mathbf{q}) &= \mathcal{F}[\Psi_i(\mathbf{r})] = \mathcal{F}[1+\varepsilon(\mathbf{r}) - i\varphi(\mathbf{r})] \cdot \exp(-i\gamma(\mathbf{q})) \cdot E(\mathbf{q}) \\ &= \{\delta(\mathbf{q}) + \hat{\varepsilon}(\mathbf{q}) - i\hat{\varphi}(\mathbf{q})\} \cdot (\cos\gamma(\mathbf{q}) - i\sin\gamma(\mathbf{q})) \cdot E(\mathbf{q}) \end{aligned}$$

Split into real and imaginary parts, transformed into direct space and with omitted envelopes, the image wave becomes

$$\begin{aligned} \Re\{\Psi(\mathbf{r})\} &= 1+\varepsilon(\mathbf{r}) * \mathcal{F}^{-1}[\cos\gamma(\mathbf{q})] + \varphi(\mathbf{r}) * \mathcal{F}^{-1}[\sin\gamma(\mathbf{q})] \\ \Im\{\Psi(\mathbf{r})\} &= \varepsilon(\mathbf{r}) * \mathcal{F}^{-1}[\sin\gamma(\mathbf{q})] + \varphi(\mathbf{r}) * \mathcal{F}^{-1}[\cos\gamma(\mathbf{q})] \end{aligned}$$

The first-order image intensity is then with both $|\varepsilon|, |\varphi| \ll 1$ and therefore vanishing cross terms

$$\begin{aligned} I(\mathbf{r}) &= \Psi(\mathbf{r})\,\Psi^*(\mathbf{r}) = \Re\{\Psi(\mathbf{r})\}^2 + \Im\{\Psi(\mathbf{r})\}^2 \\ &\approx 1 + 2\varepsilon(\mathbf{r}) * \mathcal{F}^{-1}[\cos\gamma(\mathbf{q})] \\ &\quad + 2\varphi(\mathbf{r}) * \mathcal{F}^{-1}[\sin\gamma(\mathbf{q})]\,. \end{aligned} \tag{2.3}$$

For phase contrast, the image intensity is modulated by the sine of the wave aberration function. This results in a vanishing contrast transfer of low spatial frequencies, as the sine function starts with 0 and rises only slowly.

Suitable values of the lens aberrations C_s and Δz impose a phase shift $\pm\pi/2$ for certain spatial frequencies and the corresponding phase information can contribute to the image contrast.

Conveniently, the CTF function is split into its contributions to amplitude and phase information. The parts are called aCTF and pCTF :

$$\begin{aligned} \mathrm{aCTF}(\mathbf{q}) &= \cos\gamma(\mathbf{q}) \\ \mathrm{pCTF}(\mathbf{q}) &= \sin\gamma(\mathbf{q}) \end{aligned}$$

Examples for phase contrast transfer functions for low and high defocus values are visualized in figure 2.4.

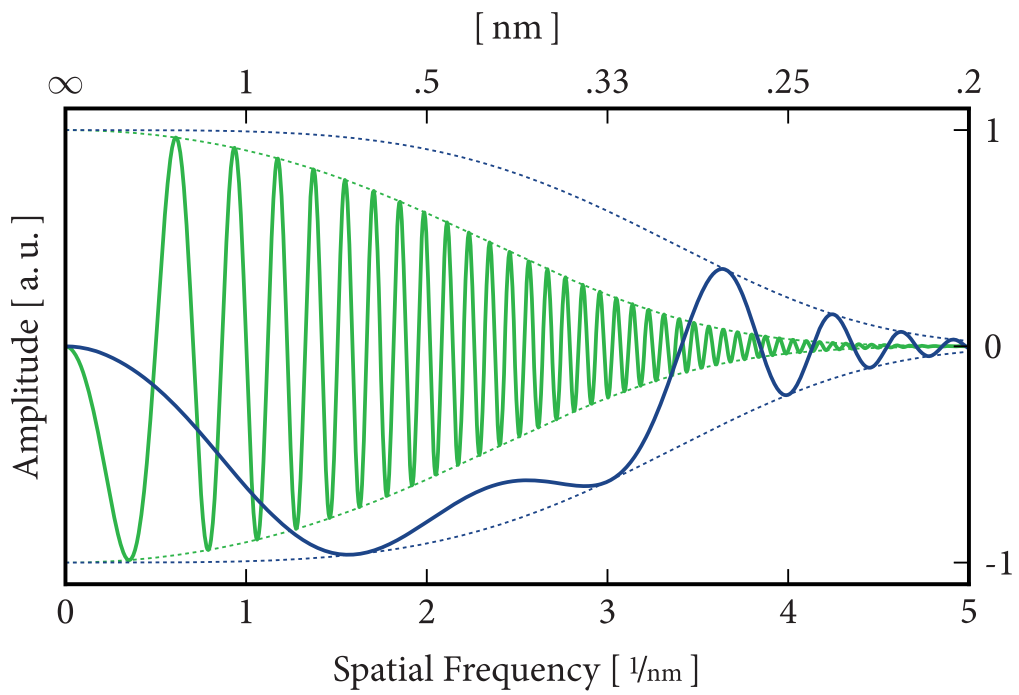

Figure 2.4: Comparison of the pCTF for Scherzer focus of −85.7 nm (blue) and a defocus of −1.6 µm (green). The used illumination aperture is 50 µrad, the source energy-width 2 eV and $C_s = C_c = 2.7$ mm. Note the influence of the defocus variation on the envelopes (dotted).

Phase Plates from Lens Aberrations

With nonvanishing spherical aberration, the defocus can be chosen in such a way that a wide band of spatial frequencies is strongly transferred [73, 49]:

$$\Delta z = -\sqrt{\frac{4}{3} C_s \lambda}.$$

This is known as Scherzer defocus, shown in figure 2.4. Although being very useful for high-resolution TEM, as large spatial frequencies are strongly transferred, it usually fails for imaging biological specimen, since important structure factors are present in the low spatial frequency range. Conventionally, low spatial frequencies can only be transferred using much higher defocus values. Such imaging conditions suffer from strongly oscillating contrast transfer with zero-crossings, which result in partially vanishing or inverted image contrast. Exemplary images exhibiting the effects can be seen in figure 2.5.

Amorphous sample regions, such as the widely used amorphous carbon film support material, contain continuous structure factors over the whole

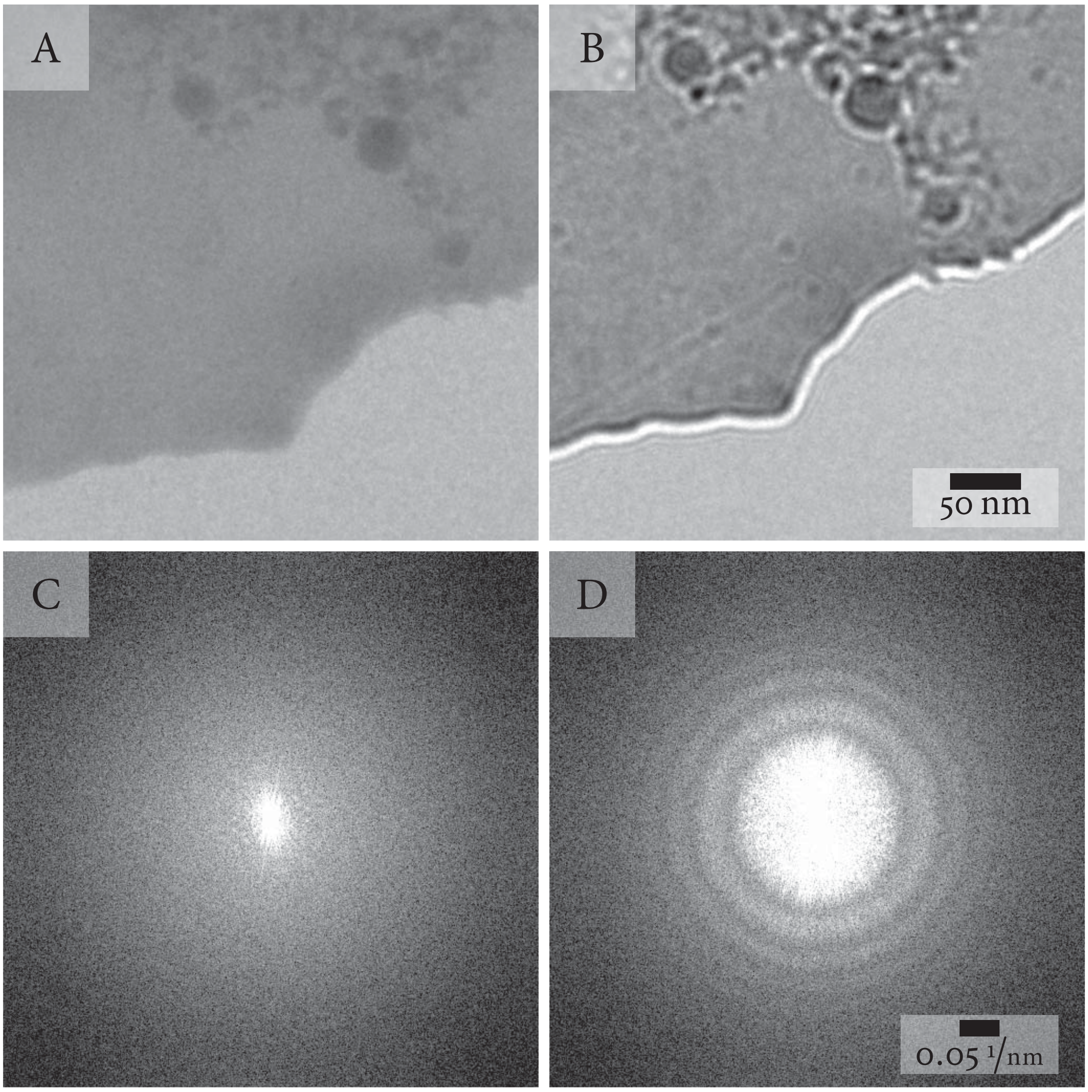

Figure 2.5: Poor transfer of low spatial frequencies close-to-focus, but potentially presence of high-resolution information in (**A**). Better low spatial frequency transfer in (**B**), but visible image artefacts, such as contrast dislocation and sign inversion using a large defocus of about −50 µm. The corresponding diffractograms are shown in (**C**) and (**D**), the latter with visible Thon rings.

range of spatial frequencies. Therefore, the modulation of the pCTF can be seen in the diffractograms, i. e. the logarithm of the Fourier-transformed images. The spatial frequencies corresponding to pCTF zero-crossings show significantly less intensity compared to the extrema. This results in a characteristic ring system in diffractograms of sufficient resolution (cf. Figure 2.5 (**D**)), which are known as Thon rings. The aberration-specific shape of the ring system is exploited for determination of the imaging conditions present in recorded images. The necessary image processing algorithms are implemented in software packages, e. g. *ctffind4* [67], *ATLAS* [4] or the unnamed algorithm reported in [81]. For low signal-to-noise ratios, small defocus values and an amorphous specimen material with small structure factor amplitudes, such as vitreous water ice, reliable detection of the Thon rings can be challenging [81, 57].

To reflect the true properties of the object, unaberrated distortion-free contrast is highly desirable. As low spatial frequencies are conventionally only transferred using high defocus values, the modulation present in the image has to be determined and corrected for. The missing spatial information located in the pCTF zero-crossings of one image can be compensated if a series of differently defocused images are combined into an exit-wave reconstruction [58, 64].

However, the attainable reconstruction fidelity is directly related to the quality of the aberration measurement, which often depends on a sufficient signal-to-noise ratio present in every image of the focal series. Beam-sensitive samples only have a limited dose budget, which can impede successful acquisition of a meaningful image series. Physical phase plates potentially offer an alternative way to an exit wave reconstruction using only three to five images [33, 23].

C_s-Correction

The availability of C_s-correctors renders the spherical aberration of the optical system a tunable parameter [37]. In practice, C_s can be chosen as low as a few µm, which is several orders of magnitude better than the usual uncorrected values in the order of mm. Figure 2.6 shows a typical pCTF for a C_s of 10 µm and in-focus conditions ($\Delta z = 0$). The additional degree of freedom of an adjustable C_s can be exploited: Depending on the

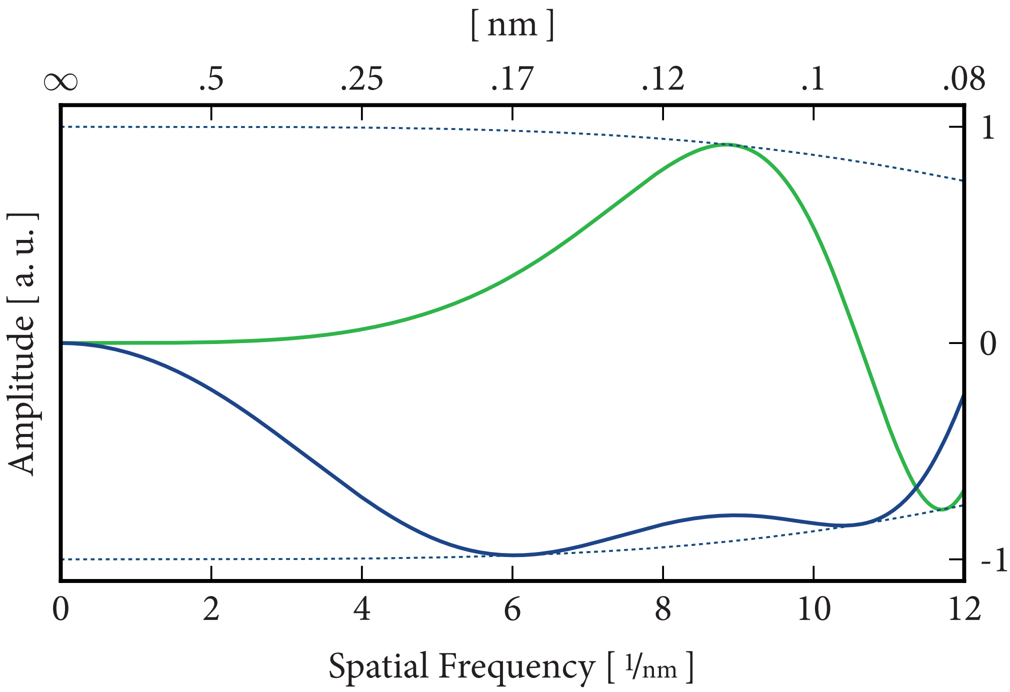

Figure 2.6: Phase contrast transfer function for C_s = 10 µm and Δz = 0 (green) and for the Lentzen defocus (blue), which optimizes the transfer band for resolutions up to 1 Å. Compared to figure 2.4, the spatial frequency range has been extended and the chromatic envelope adjusted by limiting the energy spread to 0.1 eV, e. g. with the help of a monochromator.

instrument resolution $q_{\max}$, optimized values known as Lentzen defocus for C_s and Δz can be found to

$$\begin{aligned}\Delta z_{\text{opt}} &= -\frac{16}{9\lambda q_{\max}^2}\\ C_{s,\text{opt}} &= \frac{64}{27\lambda^3 q_{\max}^4},\end{aligned}$$

which enhance the contrast transfer over an even wider frequency band than the Scherzer focus [49]. Still, mostly high spatial frequencies are strongly transferred, as can be seen in figure 2.6.

2.5 PHYSICAL PHASE PLATES

In the last section, phase contrast transfer was realized by an additional phase shift of $\pi/2$ using lens aberrations, which is only effective for high spatial frequencies. Now, the applied physical phase plate introduces an additional degree of freedom which allows to add an arbitrary phase shift φ_{pp} to the wave-aberration function. The modified phase contrast transfer function then becomes

$$pCTF(\mathbf{q}) = \sin\left(\gamma(\mathbf{q}) + \varphi_{\text{pp}}(\mathbf{q})\right). \tag{2.4}$$

For a perfect phase plate with a constant $\varphi_{\text{pp}} = \pi/2$ over the whole range of spatial frequencies (omitting the zero-order beam), the sine is transformed into a cosine function, which provides full phase contrast transfer starting with the lowest spatial frequencies. But as manufacturable phase plates can only approximate this ideal property, the actual contrast transfer is more complicated.

Physical phase plates are applied in a diffraction plane, i. e. a plane conjugated to the back focal plane (cf. figure 2.2). The spatial separation of electrons scattered by the specimen is used to apply a phase shift to either the scattered or unscattered part of the image wave.

Optimal defocus with applied phase plate

Similarly to finding the conditions for Scherzer and Lentzen defocus, an optimal focus for applied phase plates with a $\pi/2$ phase shift can be found.

The position of the first zero-crossing of the pCTF can be optimized [18] by setting the defocus to

$$\Delta z_{\mathrm{opt}} = -0.73\sqrt{C_s \lambda}. \tag{2.5}$$

For C_s-corrected instruments, the optimal defocus is therefore $\Delta z = 0$, which results in a full and uniform contrast transfer over the whole spatial frequency range, and the image wave is only modulated by the envelopes. In an actual microscope, some residual aberrations will not vanish and eventually limit the phase contrast transfer.

Optimal phase shift

For weak phase objects with a phase shifting potential corresponding to up to about $\pi/10$, the additional phase shift resulting in highest contrast transfer is $\pi/2$ [53]. This can be attained exclusively by the phase plate or by combining it with phase shifts from lens aberrations.

If the amount of phase shift is regarded a tunable parameter, certain aspects of the resulting contrast transfer can be optimized. For instance, a $\pi/4$ phase plate can be combined with controlled lens aberrations to optimize the transfer band similar to the conditions above, as described in [44].

General phase objects with a larger phase shifting potential require also a larger additional phase shift by the phase plate for optimal contrast transfer [5, 53]. E. g., with a phase shifting potential corresponding to $\pi/4$, an additional phase shift of $0.56\,\pi$ rad is needed.

Contrary to film phase plates, the phase shift of electrostatic phase plates is tunable, which offers more flexibility to attain optimal imaging conditions.

2.5.1 *Electrostatic Phase Plates*

With the advent of microfabrication techniques such as focused ion beam (FIB), Boersch's idea of implementing a phase plate using an electrostatic field became viable [8]. With the feasibility verified in a theoretical study [56], a working implementation could be demonstrated about 60 years after publication of the original idea [76].

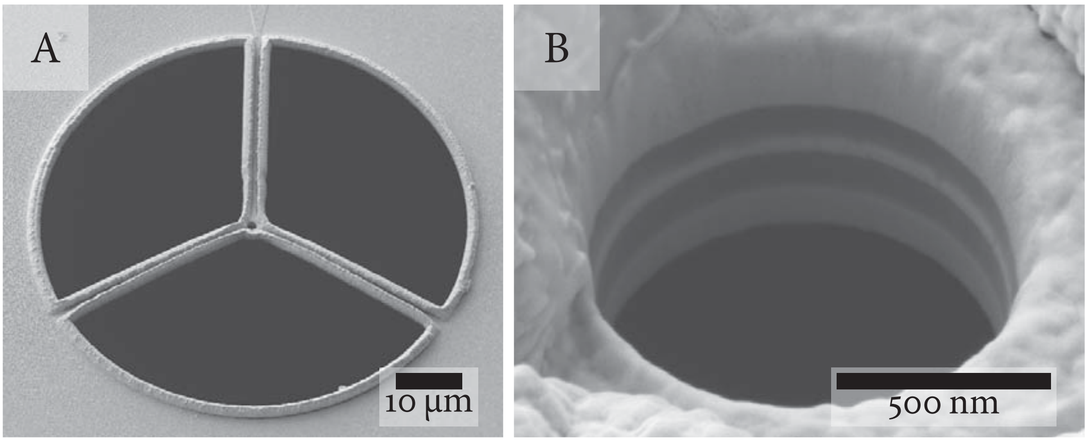

Figure 2.7: SEM micrograph of a Boersch phase plate (**A**). Detail of the electrode (**B**) shows a five-layered structure with two outer shielding electrodes (bright), insulators (dark) and the central electrode, where the phase-shifting potential is applied. The electron-obstructing structure around this central einzel lens obstructs certain low spatial frequencies. Images courtesy of Katrin Schultheiß/LEM [75].

Boersch Phase Plate

In the implemented design, an externally applied, variable potential with magnitudes in the range of ± a few Volts is used to generate an electrostatic field. It needs to be confined exclusively to the zero-order beam which is ensured by constructing an annular electrode made in a 5-layered structure with alternating conductive and insulating elements. The phase-shifting potential is applied to the central electrode, while the surrounding shielding electrodes are kept at ground potential. A scanning electron microscopy (SEM) image of the implemented device is shown in figure 2.7.

The support-structure of the annular ring electrode needs to be relatively thick in order to provide the necessary mechanical strength, making it opaque to the corresponding structure factors of the specimen.

OBSTRUCTION-EFFECTS AND FRIEDEL-SYMMETRY Because the specimen potential is a real-valued quantity, its optical Fourier transform in the diffraction plane possesses certain symmetry properties, the so-called Friedel-symmetry. Therein, each structure factor is the complex conjugate of its point-symmetric Friedel pair, relative to the diffraction plane origin at the zero-order beam, as expressed by

$$\Phi(\mathbf{q}) = \Phi^*(-\mathbf{q}).$$

For total elimination of a certain structure factor from the object wave, *both* Friedel pairs need to be obstructed. If only one of the Friedel pairs is suppressed, so-called single-sideband contrast conditions occur. Using image processing, the amplitude of the partially obstructed structure factors can be restored with half the attainable signal-to-noise ratio [89, 52, 11]. Therefore, large electron-obstructing areas are not detrimental if they feature an odd symmetry, as it is the case with the threefold support rods (cf. figure 2.7 (**A**)).

In contrast, the annular electrode features a circular symmetry which means that all spatial frequencies of a certain magnitude are obstructed. Specifically, the low spatial frequencies up to the frequency corresponding to the outer radius of the electrode support structure, the so-called cut-on frequency q_c, are excluded from image contrast transfer. All higher spatial frequencies are transferred with a sudden onset.

CUT-ON This property imposes a lower limit on the structure factors, which can be present in an object suitable for phase-contrast imaging. Only objects with dimensions smaller than the corresponding cut-on frequency can expect faithful contrast transfer. The actual relation of a spatial frequency q to a physical distance r' in the diffraction plane is proportional to the effective focal length of the objective lens (cf. Figure 2.2):

$$r' = f\lambda q. \tag{2.6}$$

Effective focal lengths are usually in the range of 0.5–5 mm and the currently most advanced implementation of Boersch phase plates feature an outer electrode radius of about 1 µm [82]. For $f = 5\,\mathrm{mm}$ and $U = 200\,\mathrm{k}V$, this corresponds to image features of about 12 nm in size, which is often too small for not imposing severe limitations on the imaging process, as interesting specimen structures easily exceed such a dimension.

With the manufacturing process at its limits, the only possibility for further reduction of the cut-on frequency is either increasing the effective focal length of the objective lens or using longer wavelengths (cf. equation 2.6). Longer focal lengths correspond to weaker lenses, which usually suffer from a larger spherical aberration. This limits the benefit of a direct increase of the objective lens' focal length. But since an optical system can feature several conjugated planes, another magnified diffraction plane can be established by electron-optical means to provide a larger effective focal length.

A pair of prototype instruments named PACEM and KRONOS implement such a magnified diffraction plane in the DMU (cf. figure 2.1) [7, 51]. Most of the competing major manufacturers of transmission electron microscopes also investigated into this idea [11, 54].

The DMU provides a diffraction plane magnification of about 3.2×, which results in an effective focal length of about 15 mm. Compared to an application in the first diffraction plane, the effective cut-on frequency of the same phase plate corresponds to 3.2× smaller spatial frequencies in the magnified diffraction plane, which potentially enables productive use with phase plates manufacturable with today's microstructuring techniques. The resulting phase contrast transfer functions for magnified and unmagnified application are visualized in figure 2.8.

Zach Phase Plate

The Zach phase plate design evolved from the Boersch phase plate implementation by omission of the annular electrode and two of the supporting rods [86]. A SEM micrograph of the resulting structure can be seen in figure 2.9 (**A**). While maintaining an odd global symmetry, this results in a reduction of the electron-obstructing material.

The applied potential is no longer strictly confined to a physical structure, but leaks out of the open end of the electrode. The resulting phase-shifting potential for a certain voltage is visualized in figure 2.9 (**B**). At a nominal voltage of about −1 V, the field imposes a phase shift of $\pi/2$ on the spatial frequency focused 1 µm in front of the electrode tip.

Since there is no electron-obstructing structure in the direct vicinity of the zero-order beam, there is no fundamental limitation on the effective range of spatial frequencies the phase plate is able to affect. However, the spatial frequencies in the area in between the point, where a phase shift of $\pi/2$ is attained, and the edge of the electrode receive a steeply increasing phase shift, which results in a non-linear phase contrast modulation. Best results for low spatial frequencies are obtained by choosing a small distance between electrode-tip and zero-order beam and applying a weaker potential, which results in a steeper potential gradient in the vicinity of the $\pi/2$ phase shift.

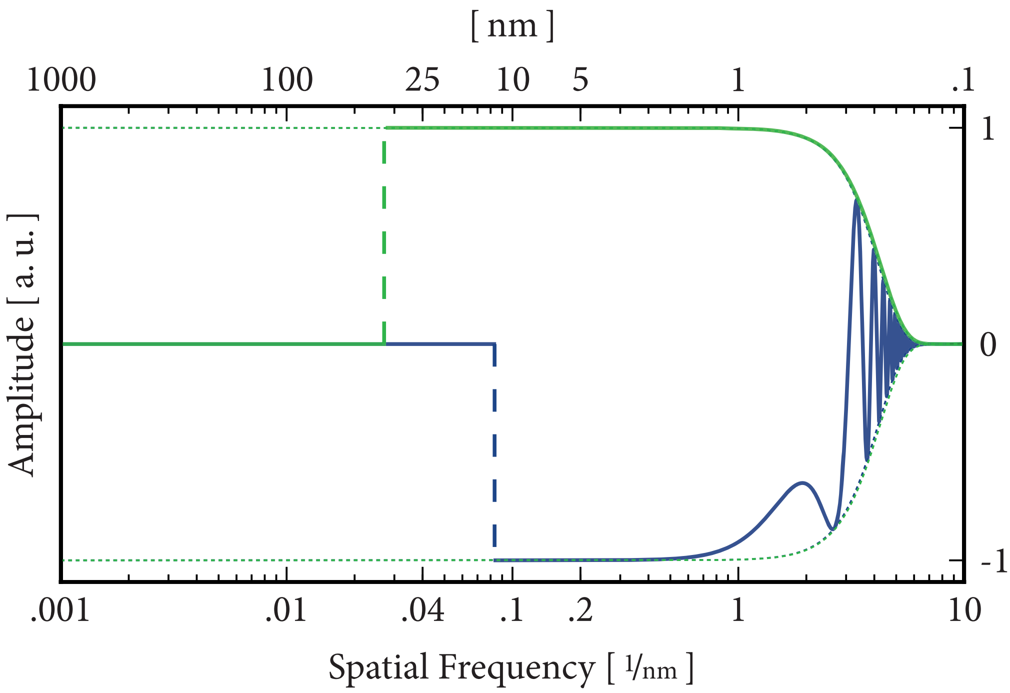

Figure 2.8: Phase contrast transfer of Boersch phase plate suffering from cut-on. Optimal defocus conditions (cf. equation 2.5) for $f = 5\,\mathrm{mm}$, $C_s = C_c = 2.7\,\mathrm{mm}$, $U = 200\,\mathrm{kV}$ and $\pi/2$ phase shift in (blue). Same phase plate in the $3.2\times$ magnified diffraction plane yields much lower cut-on frequency, for $C_s = \Delta z = 0$ (green). For better visibility in the diagram, the phase-shifting potential of the latter has been inverted, such that it provides negative phase contrast. Note the sudden onset of contrast transfer at the respective effective cut-on frequencies (dashed).

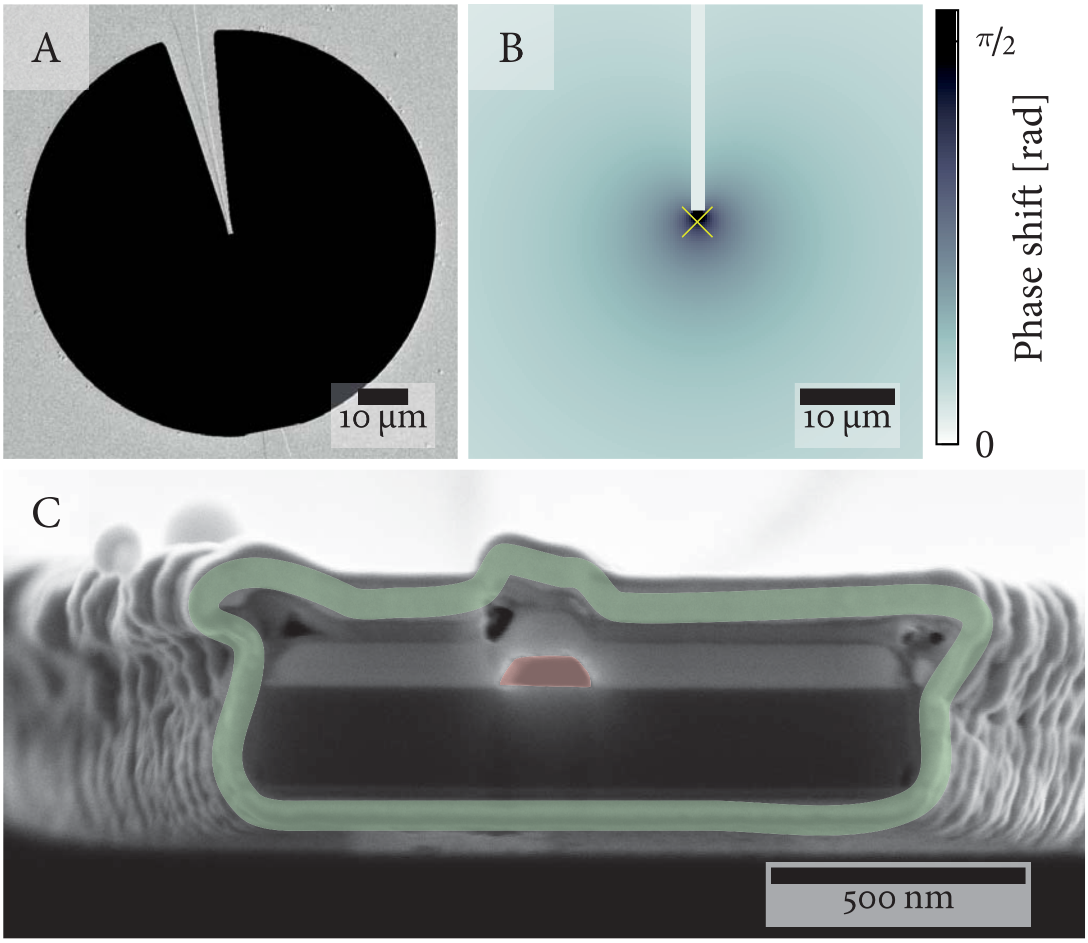

Figure 2.9: SEM micrographs of a Zach phase plate (**A**), manufactured and imaged by Simon Hettler/LEM. Corresponding simulated phase-shifting potential distribution at nominal voltage in (**B**), also courtesy of Simon Hettler. Note the placement of the zero-order beam on the slope of the phase-shifting electrostatic field (×), about 1 µm from the electrode. Detail of the phase plate tip with central electrode (red), surrounding insulator and shielding electrode (green) on ground potential in (**C**), image courtesy of Johan Zeelen/CryoEM.

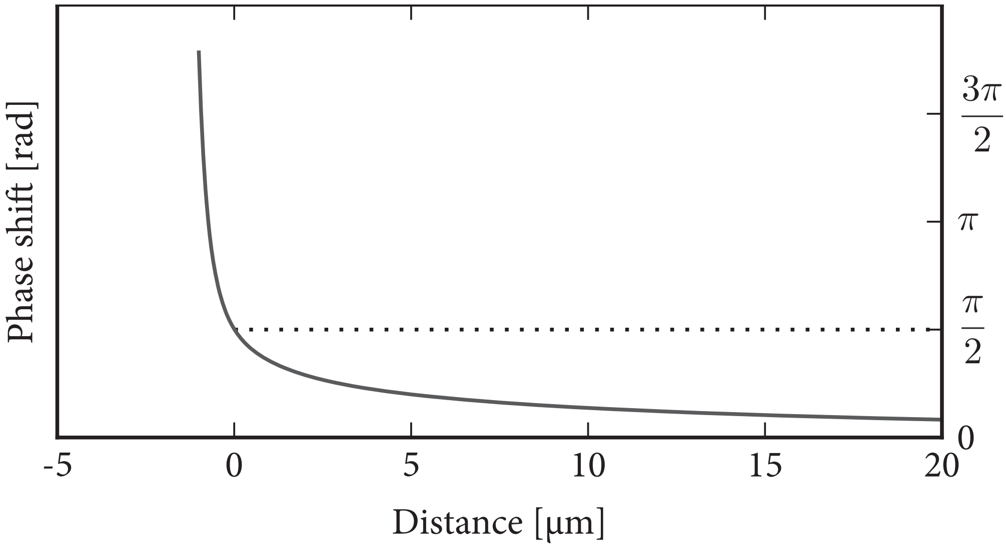

Figure 2.10: Profile of the projected phase-shifting potential of a Zach phase plate with an applied potential of 1 V. The tip of the supporting rod is located at a distance of 1 μm from the zero-order beam (placed at 0 on the abscissa), which gains a phase shift of $\pi/2$ relative to the electrons passing at infinite distance from the zero-order beam. Finite element simulation data courtesy of Simon Hettler/LEM.

The closer the electrode is positioned to the zero-order beam, the more of the low spatial frequency structure factors are partially obstructed. In principle, due to the odd symmetry of the electrode, the correct magnitude of the obstructed spatial frequencies can be reconstructed in an image, but only if the exact position of the phase plate can be determined.

Low signal-to-noise ratios in the Fourier-transformed image complicates a precise position detection. Therefore, the quality of the attainable images directly profits from reduced obstructed area. Since further physical minimisation of the structure is not feasible, also the Zach design can benefit from an application in a magnified diffraction plane.

Due to the steep gradient of the phase-shifting potential, the actual attained phase shift is a function of the applied voltage and the position of the electrode relative to the zero-order beam. A line scan of the applied phase shift directly emanating from the electrode centre for an applied potential of 1 V is plotted in figure 2.10. If the zero-order beam is located at the position, where it receives a phase shift of $\pi/2$, the effective phase shifts received by the individual structure factors is the phase difference of zero-order beam and the structure factors. This results in a soft, gradual contrast transfer onset.

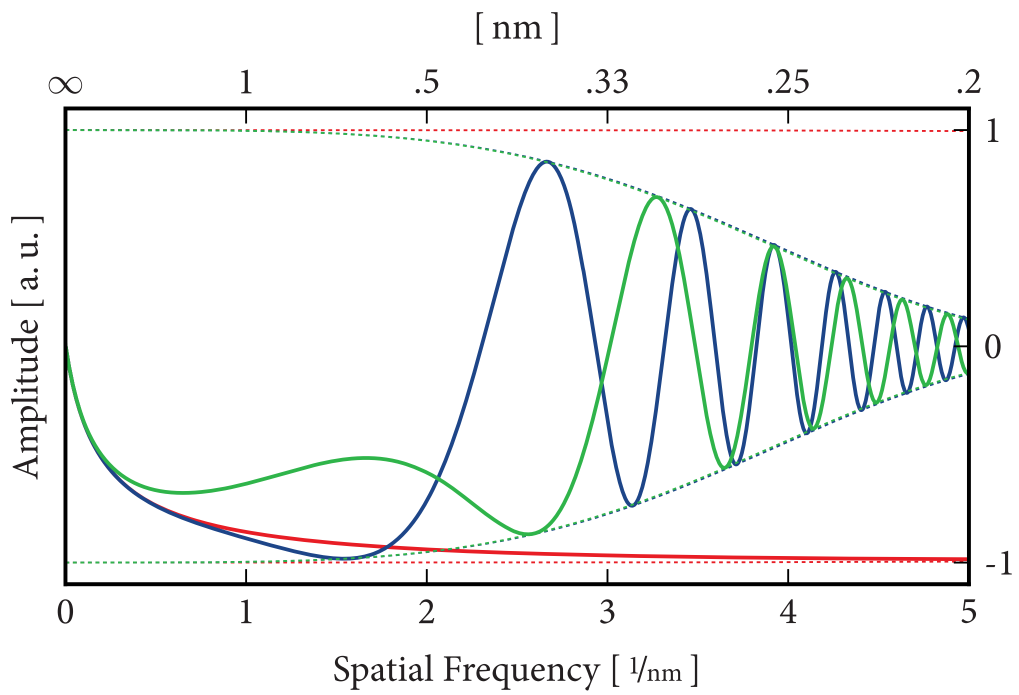

Figure 2.11: Phase contrast transfer function with applied Zach phase plate. In-focus (blue) and optimized (green) focus conditions for $C_s = f = 2.7\,\mathrm{mm}$ and a high tension of 200 kV. For finite C_s, the assumed energy spread is 2 eV, which is reduced to 0.1 eV for vanishing C_s and Δz (red). Note the gradual onset of contrast transfer for low spatial frequencies.

A possible pCTF derived from the potential distribution at design voltage, a focal length of 2.7 mm and a high voltage of 200 kV is plotted in figure 2.11. For a C_s-corrected instrument, this results in almost optimal phase contrast transfer conditions.

2.5.2 *Film Phase Plates*

Film phase plates utilize the mean inner potential of a film material of appropriate thickness (cf. section 2.2). Several designs have been proposed, which differ in the microstructured shape, the required film thickness and the way the inhomogeneous potential is generated.

The surface texture of the films has a certain influence on the phase shifting properties. For instance, if the surface is rough or the density in the bulk is inhomogeneous, the projected potential and therefore also the amount of phase shift vary.

Also the crystallinity of the phase plate films has an influence on the imaging process. Metal foils usually consist of crystalline grains of varying sizes. The effect of this property has been discussed in [22]: Upon elastic interaction of the electron-wave with the grains in the phase plate foil, the Bragg conditions are fulfilled for certain distinct scattering angles. Tilts applied in diffraction planes correspond to shifts in image planes. The discrete scattering in the phase plate film therefore results in the introduction of ghost images.

The resulting image shift s can be calculated to

$$\mathbf{s} = \lambda f \mathbf{g}$$

with a material-dependent reciprocal lattice vector **g** of the crystallites. A simple remedy is given by the proposition to limit the size of the illuminated sample area for exclusion of the ghosts from the imaged field of view.

Practically, this imposes no relevant restriction, as for a high tension of 200 kV and a focal length of 3.8 mm the radius of the illuminated area must not exceed about 20 μm for a gold phase plate film. Even on a large detector, such a field of view can only be imaged using low magnifications. For medium magnifications and an illuminated area roughly corresponding to the field of view, no practical limitations arise.

Zernike Phase Plate

Also proposed by Boersch, the Zernike phase plates exploit the mean inner potential of a thin-film material, which usually has a certain thickness to result in a phase shift of $\pi/2$. Contrary to the previously discussed electrostatic phase plate designs, the phase-shifting effect is not imparted on the zero-order beam, but on the scattered electrons. The latter have already interacted with the specimen and carry the corresponding information. Since they need to undergo another scattering process in the phase plate, the attainable resolution and signal-to-noise ratio using Zernike phase plates is limited [2].

For generating the required phase-shifting potential difference, a hole is cut into a film material. For application in a microscope, the centre of the cut-out hole needs to be aligned to the zero-order beam in a diffraction plane. This generates phase contrast transfer beginning with the spatial frequency corresponding to the hole radius. Similar to the restrictions of the Boersch electrostatic phase plate, this spatial frequency is also called cut-on frequency. A lens diagram in figure 2.12 illustrates the geometry.

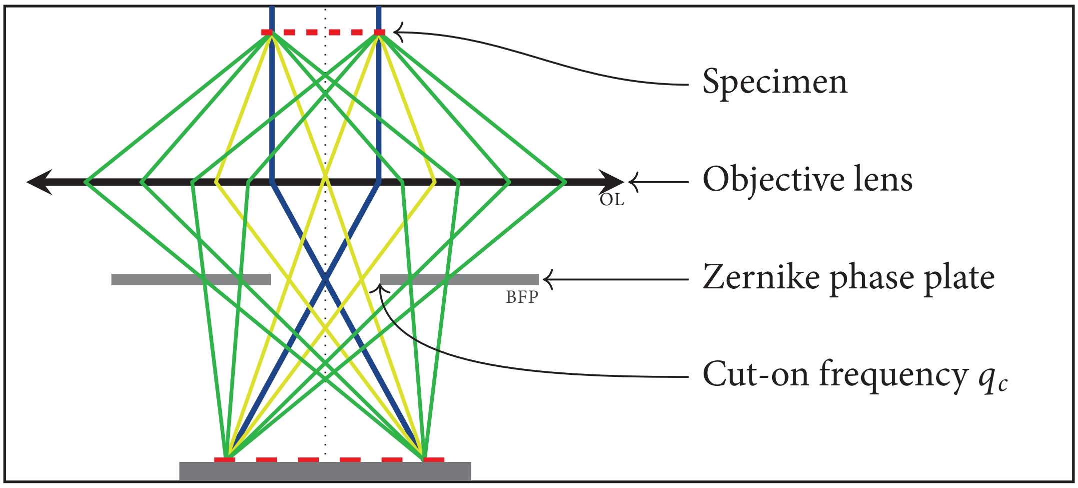

Figure 2.12: Origin of cut-on for a Zernike phase plate. The illumination (blue) interacts with the specimen and scattered electrons (green, yellow) are generated, which are refracted to specific positions according to their scattering angle in the back focal plane (cf. equations 2.2 and 2.6). The phase plate imparts a phase shift on all electrons scattered to a higher angle than the angle corresponding to the cut-on frequency (green).

Compared to the electrostatic phase plates, the manufacturing process of Zernike film phase plates is trivial, as it only requires cutting a hole in a film of suitable thickness. Using FIB, holes with diameters as small as a few 10 nm can be cut into thin films. This potentially enables lower cut-on frequencies of Zernike phase plates compared to the Boersch design.

The step-like onset of contrast transfer at the cut-on frequency gives rise to particular fringing image artefacts. An example of the effect can be seen in figure 2.13.

The required film thickness for attaining a phase shift of $\pi/2$ is depending on the high tension the microscope is operated at and the mean inner potential of the film material (cf. equation 2.1). The latter depends on the chosen material.

First implementations used amorphous-carbon films [18]. They show several shortcomings, most importantly an ageing effect, which alters the phase-shifting properties of the material over time and requires a frequent exchange of the phase plates [17]. Also, amorphous-carbon is prone to charging, i. e. the accumulation of an unwanted additional electrostatic potential [10, 20, 34]. To overcome the limitations, the performance of metal foils were evaluated as their higher conductivity may result in more favourable charging behaviour [55, 22].

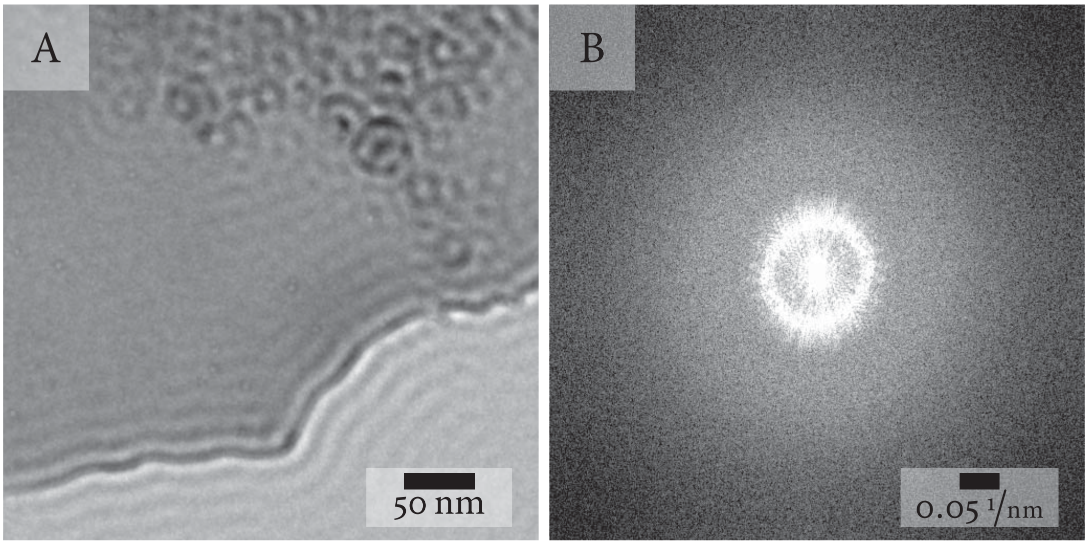

Figure 2.13: Cut-on effect of a Zernike film phase plate. Sudden transfer onset of spatial frequencies results in fringe artefacts in the image (**A**). The cut-on frequency of the Zernike phase plate can be seen in the corresponding diffractogram (**B**) as a bright ring around the central zero-order beam.

The phase-shifting films can also be made of two or more layers of same or different materials, as long as the projected electrostatic potential is sufficient to provide a phase shift of $\pi/2$. There are even ideas of hybrid film-electrostatic phase plates, where an externally applied voltage assists the insufficient mean inner potential of a thin Zernike film phase plate. This has the advantage of requiring a smaller film thickness and therefore reduces additional scattering (personal communication Patrick Kurth/KonTEM).

Hilbert Phase Plate

Hilbert phase plates work by applying an asymmetric phase shift of π to half of the diffraction plane, such that only one of the Friedel pairs is affected. For this purpose, films of twice the thickness compared to those used for Zernike phase plates are needed.

To apply the phase-shifting effect to half of the diffraction plane, a straight edge is microstructured into the film material, and a part of the film material removed. For application, the edge is brought close to the zero-order beam, with the remaining distance between phase plate edge

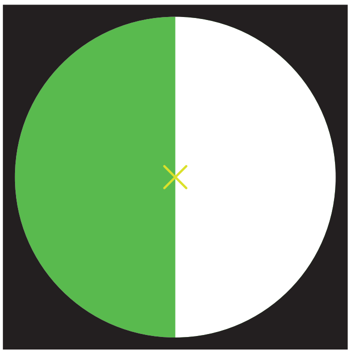

Figure 2.14: Schematic view of a Hilbert phase plate. The film material (green) imparts a phase shift of π on half of the structure factors. The position of the zero-order beam is indicated by (×)

and zero-order beam corresponding to a certain cut-on frequency. A schematic view is shown in figure 2.14.

The resulting phase contrast transfer shows a characteristic contrast modulation, as detailed in [19]:

$$I(\mathbf{r}) = 1 + 2\varphi\mathcal{F}^{-1}\Big[\frac{1+a_0}{2} i\,\mathrm{sign}(q_x \cdot \mathbf{q}) \cos\gamma(\mathbf{q}) - \frac{1-a_0}{2}\sin\gamma(\mathbf{q})\Big], \tag{2.7}$$

with q_x the unit vector in reciprocal space perpendicular to the phase plate edge and a_0 a factor to account for the attenuation caused by electron-absorption or inelastic interaction of electrons with the phase plate film. The described phase contrast transfer is also valid for single-sideband contrast conditions if a_0 is set to 0.

Using a simple image-processing operation, the recorded intensity can be transformed into equivalent regular Zernike contrast [19].

Volta Phase Plate

The Volta phase plate uses a continuous amorphous-carbon film heated to a certain temperature. Unlike for the films used for Zernike or Hilbert phase plates, the exact film thickness is not a critical parameter. The pristine film material provides a homogeneous phase shift to the electrons. The required potential difference to provide a phase-shifting effect is introduced by resting the intense zero-order beam on the film surface for some time, which generates a charge-dependent phase plate confined to the extent of the zero-order beam [16].

Volta phase plates currently seem to offer the best performance, due to several beneficial properties. Specifically, perfect alignment can be achieved without complicated user interaction just by using flood beam illumination and waiting for the required charge to be put into a fresh location on the film material. To avoid a broadening of the zero-order beam during charge deposition, no sample should be present, e. g. by choosing an opening in the sample.

Secondly, the phase-shifting effect seems to be strictly confined to the extent of the zero-order beam, which results in no noticeable distortions from a nonvanishing cut-on frequency. Lastly, since no microstructuring of the film material is necessary, there is a virtually unlimited supply of phase plates on a 2D film surface, which enables using a fresh phase plate for each exposure.

There should be a small penalty in the attainable signal-to-noise ratio, as the electrons scattered by the specimen may undergo an additional scattering event in the phase plate film material. However, the film thickness can be chosen smaller compared to the foils used for Zernike film phase plates, which results in smaller dampening.

2.5.3 *Other Phase Plate Designs*

Several other phase plate designs have been realized or proposed in theoretical investigations. Due to the obstruction of spatial frequencies and the inherent charging problems of physical phase plates, investigation in matter-free designs seems to be consequent. One design suggests to accomplish the localized phase-shifting effect making use of an intense flux of photons in the focus of an optical cavity [61].

Another slightly more conventional design requires a sequence of two diffraction planes, which have been elongated in orthogonal directions using suitable electron-optics [74]. Two partial phase shifts of $\pi/4$ at a time are applied in the diffraction planes by means of two electrostatic phase plate slit apertures, which combine to the necessary phase shift of $\pi/2$ in the position of the zero-order beam. For both of the matter-free designs, actual implementations have not been reported yet.

Other design-proposals have already been realized, such as a dedicated single-sideband aperture, which generates phase contrast without exertion of a phase shift [11]. Also, the use of magnetic ring structures as phase plates have been investigated [25]. No widespread use of the ideas has been reported yet, possibly since the required support structures are prone to charging and the additional complication using the devices does not pay off in terms of an enhanced contrast transfer.

Most recently, an optimisation of film phase plates has been reported, which restricts the thick film material required for the appropriate phase shift to an area in the vicinity of the zero-order beam [66]. This can be realized by mounting a small circular patch of the phase-shifting foil on a low-dimensional support, such as graphene. The low spatial frequencies can then be transferred using the phase shift generated by the inner potential of the film material, while high spatial frequencies are phase shifted using lens aberrations. This optimizes the signal-to-noise ratio in the recorded images, as the additional dampening for high spatial frequencies is practically avoided.

3 AUTOMATED TEM

In this chapter, the basic operation and general concepts of automation software is discussed, and the most important terminology introduced. Then, the additional requirements to enable automated phase plate application are described, categorized in the necessary modifications to the microscope and extensions to the software. Finally, an exemplary automated alignment procedure is presented and evaluated.

3.1 BASIC OPERATION

The single-particle method used in structure biology demands collection of several thousand individual views of a biological macromolecule to yield a sufficient signal-to-noise ratio in a high-resolution reconstruction, which often requires collection of hundreds of individual images with constant quality. This quickly sparked research interest in an automation of this task, as it offers an opportunity to save precious time of microscopists and enables a better utilisation of expensive instrumentation.

Also other fields benefit from the developed automation routines due to the rich automatic documentation of the imaging process, which may save microscope and specimen preparation time if specific questions arising after the actual imaging process can be answered in retrospective using the already acquired data. The necessary standardisation of image acquisition routines can increase the repeatability of experiments not only temporally, but also spatially across laboratories.

Manual performance of low-dose imaging techniques can be tedious to the user, as it requires additional precautions during image acquisition. Since automation software has been designed with application to beam-sensitive specimen in mind, the image acquisition process can be tuned to make most efficient use of a specimen's dose budget, while maintaining a constant image quality.

Phase plate application may drastically benefit from automated operation, as some sources of untimely phase plate degradation can be attributed to incautious use. The unmatched precision of the phase plate movements attainable within an automation framework potentially results in an improved lifetime and a better usability of the phase plate, as delicate and time-consuming handling tasks are offloaded from the user. This may help establishing phase plate technology as a standard tool in TEM.

While a couple of commercial and closed-source implementations of automation software exist, the source-code of the Leginon framework [78] is freely available and in regular productive use across many laboratories. It supports several different modes, including automated image acquisition with autonomous target identification, acquisition of tilt-series and other advanced techniques. It was therefore chosen as the foundation to implement the automated application of physical phase plates.

3.1.1 *Requirements on the Instruments*

To be usable for automated TEM, a microscope has to meet certain requirements. For instance, it has to offer some kind of remote control capabilities, i. e. a documented software application programming interface (API). In the API, a critical set of the microscope parameters need to be exported, with both read and write access.

Secondly, an image sensor such as one or more cameras has to be present. Every used camera needs a means to trigger the acquisition of a new image and set parameters such as the desired exposure time. At least one of the cameras needs to have the capability of digitally exporting the newly acquired image data using an API.

The modifications to the internal data structure representing the abstracted instrument state are translated into the API-calls of the actual microscopes using a hardware-dependent driver module. In the beginning, the only available microscopes suitable for phase plate application were manufactured by Zeiss. As Zeiss instruments were not supported by the Leginon framework, adaptations became necessary.

3.1.2 *Calibrations*

The microscope uses an internal data representation of its current state, which corresponds to individual currents and voltages of electron-optical elements or specific positions of mechanical components. Sometimes, the API offers meaningful values compatible with SI units for an individual element, such as the stage position in meters. Other values, e. g. the present manipulation of the optical axis using deflectors may be reflected by the corresponding digitized values in arbitrary units.

The automation software needs to manipulate the microscope state in a deterministic way. For computation of the necessary change of microscope parameters to make a transition from one state to another, the individual values have to be linearised and translated into a common reference frame. Most conveniently, this reference frame corresponds to the projected specimen dimensions on the camera, if applicable.

Pixel Size

The most basic calibration of a microscope is the pixel size calibration. For that, a specimen with structures of known dimensions is inserted and imaged at the various magnifications the instrument offers. With the physical pixel size of the detector, the magnification can be calibrated.

In the field of a magnetic lens, the electrons are forced on circular trajectories proportional to the strength of the magnetic field [45]. Therefore, for a changed magnification, i. e. changed excitations of the projective lenses, a rotation of the reference frame about the optical axis may occur. If the fixed orientation of the camera is used as the reference frame, this magnification-dependent rotation has to be accounted for, to compare orientations across different magnifications.

Deflectors and Specimen Stage

The information from the pixel size calibration can be used to relate the values presented on the microscope API to absolute values. Most prominently, this is the stage position, which influences the position of the sample relative to the optical axis. An identical manipulation can be achieved, if the optical axis is deflected above and below a stationary specimen, as depicted in figure 3.1.

The deflectors in the beam path directly above the specimen are referred to as *beam shift* or *illumination shift* deflectors, the deflector below as the *image shift* deflectors. As each of the deflectors operates in two dimensions, careful calibration of the magnitude and direction of the individual effects on the optical axis have to be performed prior to a synchronized operation. By using a common reference frame such as the camera, the individual matching excitations can be calculated.

For calibration of the image shift deflector, a specimen is inserted into the microscope and imaged. Afterwards, the excitation of the individual deflector axes is changed separately, and the resulting shift of the image on the detector measured. Using cross-correlation or related algorithms,

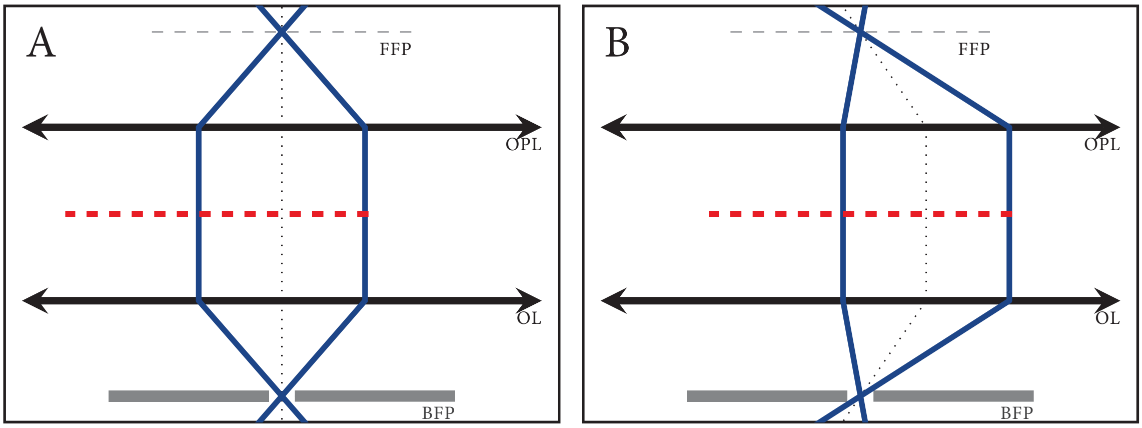

Figure 3.1: Moving the area of interest on the sample. In (**A**), the physical position of the sample is adjusted using the microscope stage, while in (**B**), the sample is kept stationary, and matching deflections above and below the objective lens adjust the optical axis.

such as the normalized mutual- or phase correlation functions [58], the relative change on the detector can be identified. An example of such a resulting *correlation map* can be seen in figure 3.2 (**C**).

Using the pixel vector information, a system of two linear equations can be established, which relates the change of the excitation of a deflecting element to the resulting change on the camera. Since the relation is linear, the result can also be inverted for calculation of the necessary changes of microscope parameters to yield a specific change of the image projected on the camera.

The unified reference frame of all manipulating elements in the microscope offers more freedom how to centre certain specimen features on the camera. Manipulating the specimen position using the microscope stage should not have any side-effects to the quality of the attainable image. But since the movement is executed using mechanical means, it is subject to the shortcomings of mechanical systems, which can result in a non-linear relationship of intended and actual movements. Usually, the electron-optical means to manipulate the reference frame are more reliable and enable a higher repeatability compared to the mechanical methods. However, the resulting shift of the optical axis may give rise to additional image aberrations and suffer from limited range. Therefore, it should be used for small movements only.

To enable a precise relocation of the specimen using the mechanical stage, it can be operated in closed-loop control: Starting with a reference

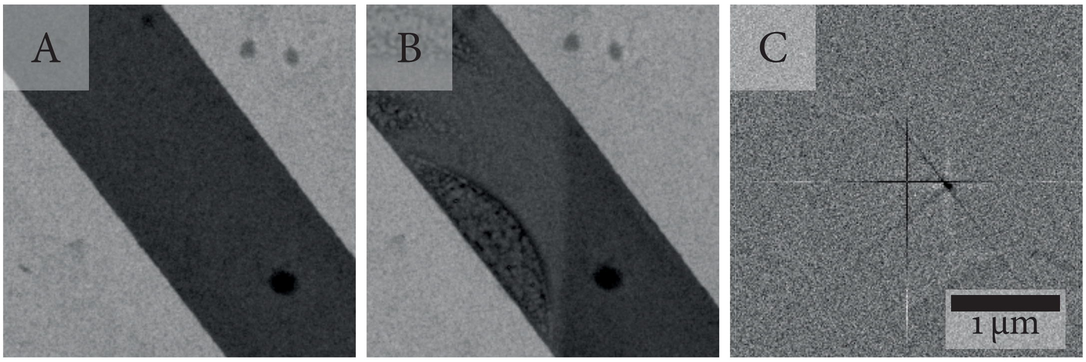

Figure 3.2: Measurement of the spatial relationship of two separate images. A reference view of the specimen is shown in (**A**). Change of microscope parameters or sample drift give rise to a change of the reference frame, as shown in (**B**). The corresponding pixel distance can be measured by correlating reference and changed position, and finding the position of the maximum in the resulting correlation map (**C**).

image and a certain *target* pixel position of the intended change, the stage is asked to move by the intended distance. After the move has been performed, the result is checked using a correlation of current state and the reference. The measured positioning error is then used for the refined stage target coordinates. If the error is below a certain threshold, the target position has been reached. A possible variation is performing a coarse relocation with the mechanical stage followed by a fine adjustment using the electron-optical means.

Focusing

Besides the capability of changing the microscope state to centre a certain specimen feature, i. e. manipulating the specimen perpendicular to the optical axis, the second most important feature is probably a reliable autofocus routine, which is correcting for a mismatch of specimen and object plane in the direction parallel to the optical axis. In principle, the current focus mismatch can be measured by fitting the positions of the zero-crossings in a diffractogram (cf. figure 2.5). But this relies on the presence of amorphous specimen features and can suffer from uncertainties depending on the attained signal-to-noise ratio in the image. Furthermore, over- and underfocus conditions may result in similar ring systems, especially when the spherical aberration is corrected.

A more robust focusing technique has been described in [47], where a focus-dependent image shift upon a tilt variation of the illuminating beam is exploited. In first order, this relation is linear. Therefore, the current focus can be measured by determining the shift of two images acquired with varied illumination tilt.

Similarly to the manipulation of the lateral specimen position in the plane perpendicular to the optical axis, also two possibilities for manipulating the focus exist: Firstly, the focus can be corrected using mechanical means of the stage in z-direction, parallel to the optical axis. Often, changing the mechanical specimen position is not completely side-effect free, and some unwanted change in the xy-plane usually occurs. This can be avoided if the focus is corrected by adjusting the objective lens' current, given the illuminating beam is coincident with the orientation of the objective lens.

Too strong deviations from the design excitation of the lens can result in additional aberrations. Furthermore, as the microscope alignment is optimized to a certain specific normal objective lens excitation, the resulting change of the beam path may cause other alignment problems. For coarse focus, usually the stage is used in z-direction. Fine variation or application of an intended defocus to enable phase contrast transfer is performed by varying the strength of the objective lens.

3.1.3 *Multi-Scale Imaging*

Samples in TEM are usually mounted on circular copper grids with a typical diameter of about 3 mm, often with a support film made of amorphous carbon featuring regularly spaced openings. An image of a part of such a grid can be seen in figure 3.3, which has been combined from about 60 individual exposures using a low magnification of 125 ×. Given the attainable resolution in TEM and the restricted areas of the detectors, the sample area presents overwhelming detail, making it impossible to image every part of the specimen at high-resolution. For efficient sample investigation, the identification of interesting regions across multiple scales is one method to approach the problem.

In figure 3.3, interesting regions may be present is the darker area on the mesh, as the sample is only present in this area. For biological samples, which are often prepared using thin films of a vitrified aqueous solution, a similarly reasonable choice may exist on this coarse scale: Often, the attained ice thickness is too thick to enable high-resolution imaging, or

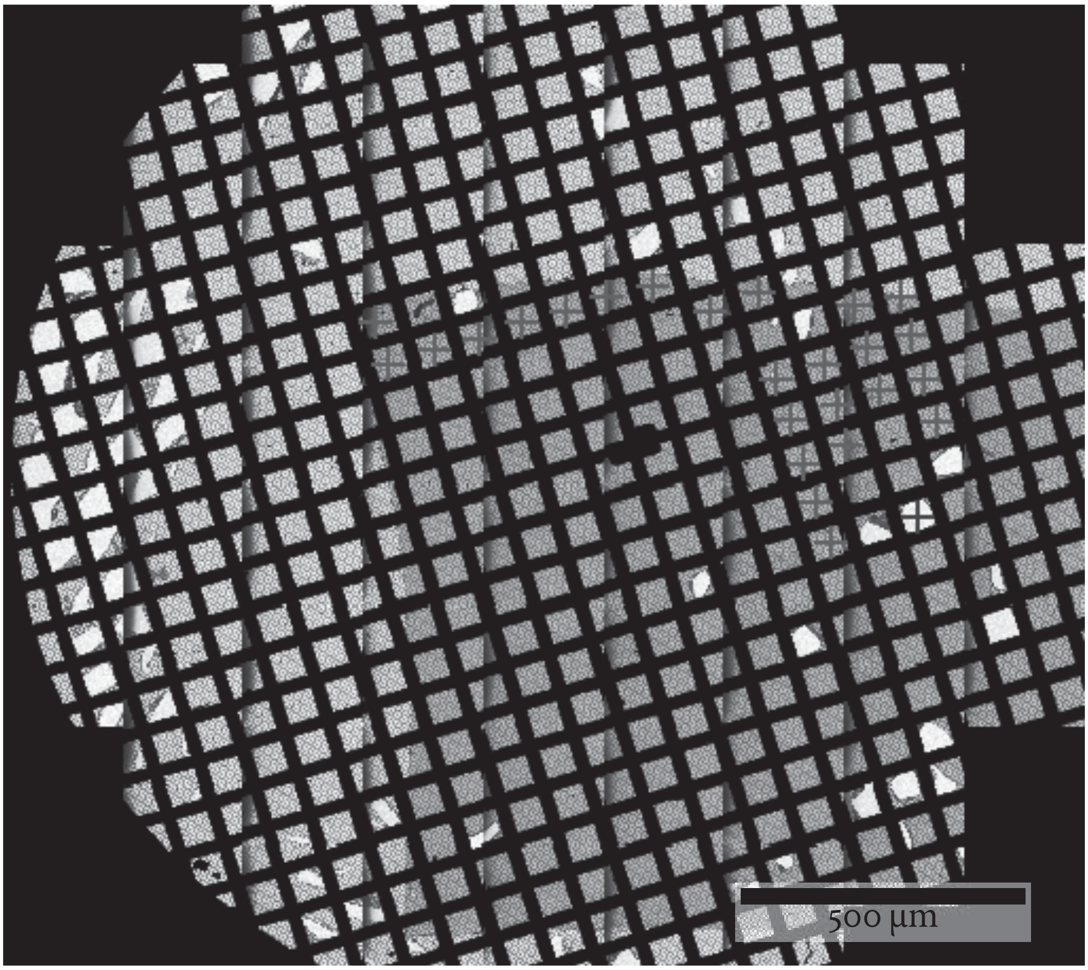

Figure 3.3: Combined image of several low-magnification images. Usually, thin specimen foils are mounted on round copper meshes with a diameter of about 3 mm. The metal mesh is formed by so-called *grid bars* and the sample area in between are called *squares*. Promising squares are selected as targets (+).

too thin to offer sufficient stability. Sometimes, a thickness gradient is present across the grid, and ideal conditions can only be found in a couple of squares, i. e. the sample area in between the grid bars.

After identification of the interesting squares, they can be imaged using a slightly higher resolution suitable for refinement of the region of interest. If a regularly structured amorphous-carbon support is used, another obvious choice are the openings in the support film, which are subsequently imaged at an even higher resolution and eventually at the desired final magnification. Exemplary images of such an acquisition scheme can be seen in figure 3.4.

The different magnifications required for the multi-scale approach usually demand adapted illumination conditions. For low magnifications, the coherence of the illuminating beam is only of minor importance, rather than a large size of the illuminated area and sufficient intensity. For target magnification, the requirements are inverted. Therefore, it makes sense to combine several microscope parameters to so-called *presets*.

Due to alignment problems in the projective, changing the magnification is not necessarily side-effect free, i. e. it results in a shift of the reference frame. A key requirement of the multi-scale approach is a known relationship of the relative shift of the presets used throughout the imaging process. Most conveniently, the center of all presets should be coincident that switching presets results in the same sample region imaged at varied magnification. For the required preset alignment, the image shift and beam shift deflectors are used. Since only the aberrations at the final magnification are of major importance, the corresponding preset is used as the alignment reference, and all presets with lower magnifications are aligned to it.

The quality of the intermediate preset alignment is not too critical, as long as it manages to bring a certain feature selected at a lower-magnification preset in the field of view of the detector at the higher-magnification preset. Depending on the quality of the electron-optical alignment of the microscope, manipulation of certain parameters may suffer from side-effects, which can result in a dynamic mismatch of the individual preset alignment. To increase the robustness of the imaging process, the electron-optical alignment should be good and the most critical coincidence of the presets involved in the final imaging steps should be checked regularly. For further improvement, a camera with a large field of view should be used.

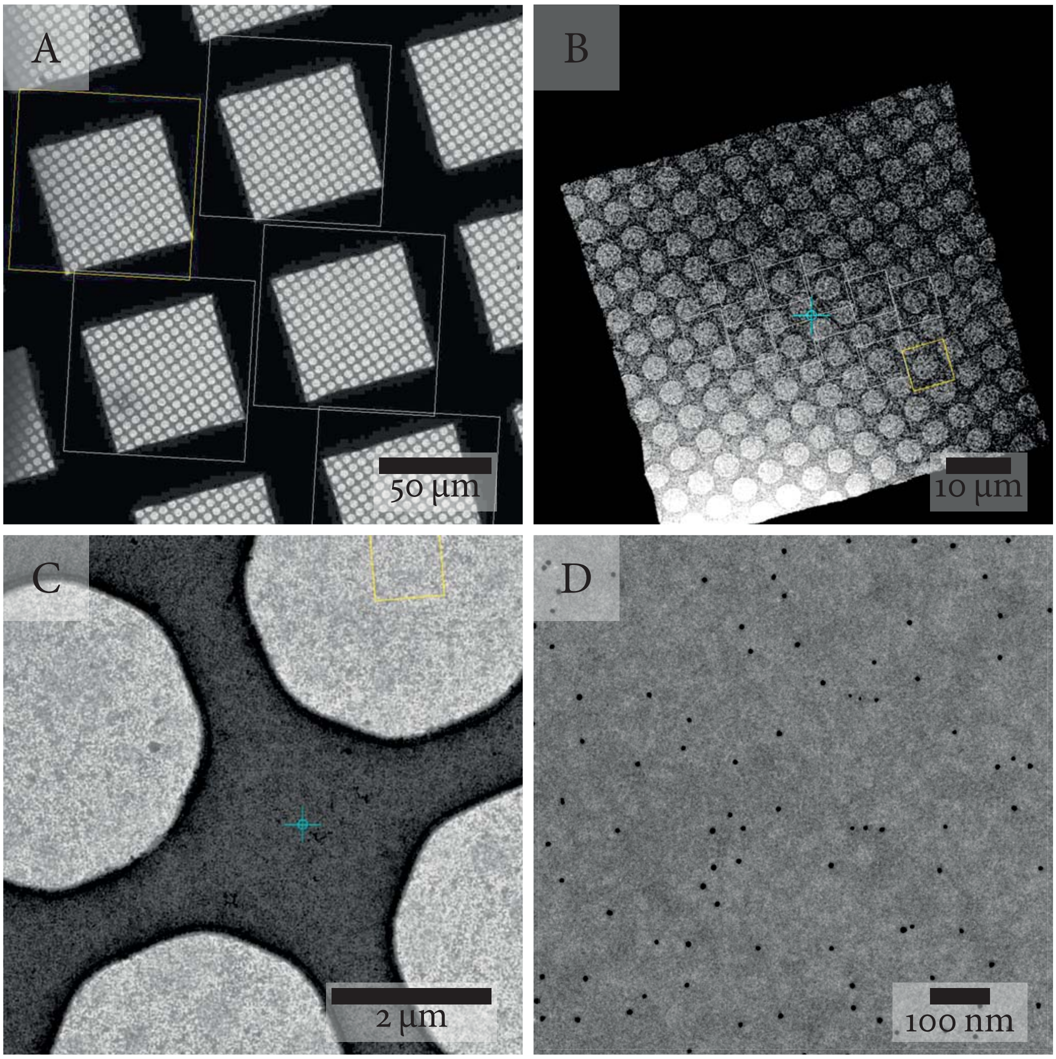

Figure 3.4: Multi-scale imaging. The targets are identified at different scales (**A–C**) to be investigated at the chosen high-resolution (**D**). Yellow squares indicate the position of the camera frame at the next preset. The blue crosses indicate targets for focusing purpose. Note the misalignment of desired and actual position in between (**B**) and (**C**), due to mechanical imperfections of the microscope stage.

Low-Dose Imaging

Beam-sensitive specimen alter their physical appearance upon exposure to an intense electron-beam. As a rule of thumb, the typical dose budget of beam-sensitive biological samples is in the order of $10\,e^{-}\,\text{Å}^{-2}$. The presented multi-scale approach is well suited to low-dose imaging, as the target-identification is done using a lower magnification, requiring only a small electron-dose per sample-area for a sufficient signal-to-noise ratio adapted to the low resolution.

High signal-to-noise ratios and high-resolution images may be required to attain correct focus, but the focusing process can be done on a part of the sample in the vicinity of the region of interest, such that the dose budget for the actual area of interest is not reduced.

3.1.4 *Automated Imaging*

Single-Particle Approach

For automated collection of images useful for the single-particle approach, the functionality described above is almost sufficient. For unattended operation, the target finding, i. e. identification of regions of interest, has to be automated.

A fully automated approach needs a certain image processing capability for assessing the sample in the individual steps of the multi-scale imaging process. If the specimen is prepared on a support film featuring a regular pattern of openings (cf. figure 3.4 (**A–C**)), the interesting sample areas are located in the same regular pattern, which can be identified by an algorithm. With the position of the openings found, certain features such as the mean intensity and shape of the feature can be extracted to decide whether interesting sample of usable thickness or vacuum is present at an individual location. Using that information, the subsequent targets can be set up, including selection of appropriate nearby regions for focusing.

Alternatively, a semi-automated approach can be implemented, in which the attention of the operator is used with a better time-efficiency: Beginning with a coarse overview image of the whole grid, the user manually selects several squares that are intact and feature promising sample conditions. Then, the automation software prepares the higher-resolution views and again requires the user to select subsequent areas of interest. It takes only seconds for an experienced user to decide which part of the sample looks most promising. This minimises the time the user is required to spent in front of the instrument. Furthermore, it enables advanced scenarios, where only a telepresence is required.

This operation mode is implemented by storing the intermediate images of the multi-scale imaging process along with the selected targets and the microscope state the intermediate images were taken with. For executing the subsequent steps, e. g. focusing and taking a high-resolution exposure, the microscope is requested to assume the identical microscope state. In the meantime, a shift of the reference frame due to sample drift, limited repositioning capability of the stage or other external changes might have occurred and the effective position differs from the reference image, even though every microscope parameter appears to be the same. To account for the resulting shift, a new image is taken and correlated with the old reference, similar to the conditions shown in figure 3.2. The targets are then adjusted by the corresponding shift vector, and the automated image acquisition process continues.

Using this technique, a large amount of targets can be prepared in short time, which the microscope can subsequently work off unattended. This enables continuous use of the instrument for a better sample throughput.

Tomography

Manual acquisition of tomographic tilt-series is a tedious task, as the movements of the sample upon changing the stage tilt angle have to be accounted for. The first automated implementations [46] only combined automated focusing and tracking routines to adjust the view at the current tilt angle to the view from the last recorded tilt angle before taking a high-dose image.

Later investigations [93] identified the reason for the specimen movement: If the mechanical tilt axis does not contain the point of intersection of the microscope's optical axis and the specimen plane, any change in tilt results in a shift of the specimen view on the detector, as well as a change in focus. Tracking a specimen during a tilt-series acquisition is therefore a 3D problem. A sketch of the underlying geometry can be seen in figure 3.5.

The proposed acquisition scheme populates a model based on this geometry with the relevant distances. In a calibration tilt series using low magnification and large tilt increments, the distances of mechanical tilt axis, optical axis and specimen plane are determined. The resulting model of the actual geometry is then used for a high-magnification tilt-series acquisition with fine increments, and the movements of the sample are

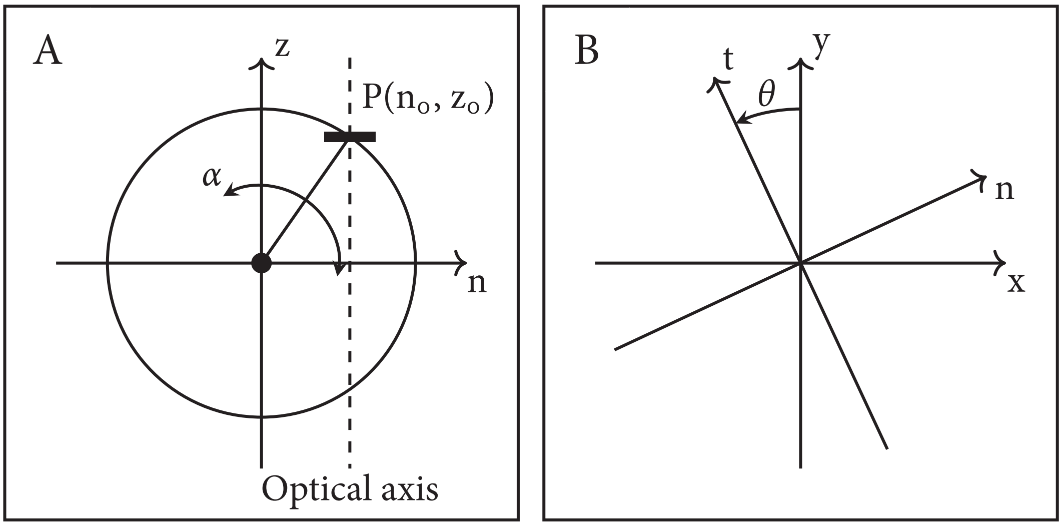

Figure 3.5: (**A**) The specimen translation is a function of the applied stage tilt angle α and can be expressed in a model with two parameters, such as initial horizontal and vertical distance (n_o, z_o) from the mechanical tilt axis (●). (**B**) Stage coordinate system (n, t) might be rotated by θ to camera coordinate system (x, y). Figure reproduced from [91].

accounted for using appropriate electron-optical means, i. e. image shift deflectors for specimen shift in x, y and defocus change for shifts in z.

The currently most advanced algorithm reported is an improvement of this scheme [91]: In a preparatory step, optical axis, mechanical tilt axis and specimen plane are brought into coincidence as good as possible. The remaining mismatch is calculated and a matching model of the geometry is determined using a low-magnification calibration tilt-series.

With this approximate model, acquisition of the tilt-series at higher magnifications is started. By comparison of expected and actual specimen movements, the initial parameters of the model are refined to be compatible with the observed specimen movement.

Since the model calculates the 3D translation of the sample, it can correct for specimen translation and defocus change, i. e. it does not need to perform an intermediate focus step before each acquisition. This algorithm has been implemented in a standalone program [92] and also in a Leginon module [79].

Due to shortcomings of the model geometry or mechanical imperfections of the specimen stage, predicted and actual positions may not perfectly coincide. This eventually limits the feasibility of performing an automated tilt-series acquisition, as the sample tracking is lost as soon as the mismatch between predicted and actual specimen position exceeds the field of view on the camera. Therefore, automated tilt-series acquisition becomes more challenging for higher magnifications and smaller detectors.

Automated Phase Contrast Imaging

The methods described so-far have already been implemented in the open-source software framework Leginon. The necessary steps to implement the automated phase-contrast imaging can be divided into three main parts:

- The key capability is an automated alignment of a physical phase plate. For high-precision position manipulation, the standard aperture drives have to be replaced by software-controllable high-precision manipulators. For the electrostatic phase plates, access to a suitable voltage supply needs to be integrated as well.
- Standard electron-optical alignment routines often focus on optimizing the image planes, i. e. make sure the illumination is parallel and the beam is not lost upon changing the microscope parameters. Automated phase-contrast imaging has higher requirements on the quality of the electron-optical alignment, as it needs tight control not only of the planes conjugate to the specimen plane, but also the corresponding diffraction planes. Here, protocols have to be established to improve the overall alignment quality to enable variation of certain parameters of the optical system without side-effects.
- For automatic phase plate alignment, image processing routines to accurately determine the current phase plate position and their deviation from the optical axis have to be developed. As phase plates are applied in a diffraction plane, which is not safely[1] visible using standard imaging techniques, methods for imaging objects in the diffraction plane have to be established and the corresponding functionality integrated into Leginon.

1 The diffraction plane can be projected on the camera using the diffraction mode, but the focused zero-order beam has the potential to destroy the scintillator (cf. section 3.4.3).

3.2 PHASE PLATE TRANSLATION

For translation of the phase plates, custom motors have to be fitted to the microscopes, as the aperture drives from the manufacturers lack the necessary precision.

The company KonTEM tried to commercialize their phase plate technology and offered a manipulator design specifically developed for the requirements of phase plate microscopy. It allows for closed-loop positioning thanks to the integrated position encoders. The encoders have a resolution of 61 nm, and the motors itself are specified to an even finer resolution of about 1 nm [65]. The attainable absolute positioning-accuracy is only slightly better than about 1 μm, due to mechanical imperfections of the motion-transducing mechanics. That means, while the desired position may be perfectly attained for the positioning encoders, the actual position of the phase plate varies and needs a subsequent adjustment.

The electrostatic Zach phase plates have traditionally been used with a very compact Kleindiek MM3A fitted into a vacuum flange, which allows integration of the whole motor into the microscope column. In *coarse* mode, the motors of the Kleindiek system work by stick-slip-motion of its piezo actuators [42] and none of the axes feature position encoders. Translation is requested in the form of a number of *ticks* at different *speed levels*. Each individual combination yields a different and slightly random amount of actual translation. Therefore, a closed-loop control has to be externally realized using the imaging capabilities of the microscope. The *fine* position resolution of the motors is actually very good, as the controller allows to strain the piezo actuators with a static voltage[2] in the order of ±10 V, which results in a very small and well-controlled translation better than 0.5 nm [43].

Both mechanical translation systems only allow for non-Cartesian motion. Figure 3.6 shows images of the motors, with the motion directions of the actuators indicated by arrows.

3.2.1 *Coordinate Systems*

KonTEM

In KonTEM's design, shown in figure 3.6 (**A**), the motion is generated by linear motors, which is transduced to the phase plate by a long rod. In

2 Surprisingly, application of this rather high static voltage does not have any perceivable effect on the image.

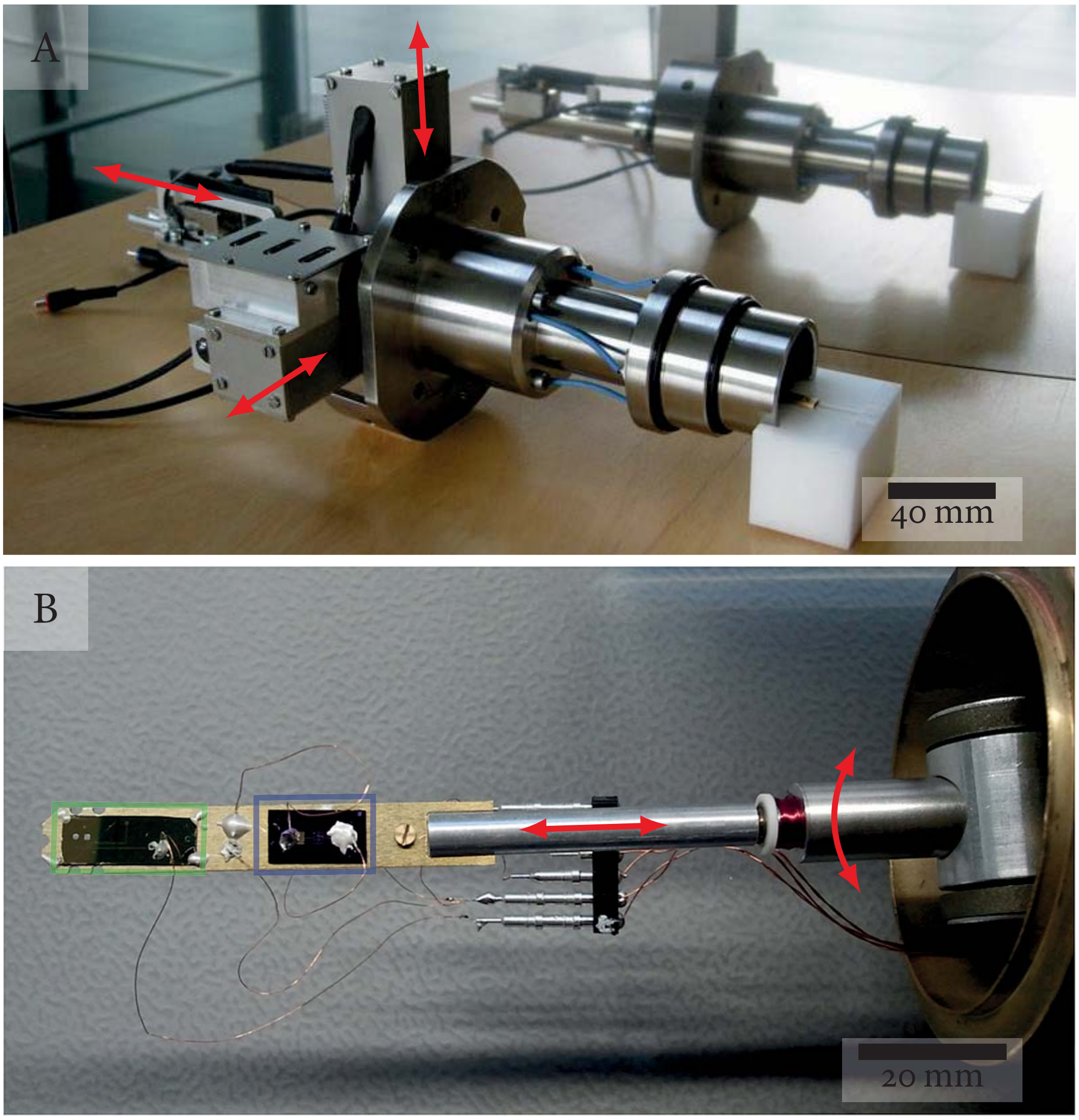

Figure 3.6: Phase plate translation devices. KonTEM's design in (**A**) with three linear translators and encoders. The forces exerted are transduced via a rod and a sliding contact bearing (not visible). The assembly the phase plates are mounted on along with their heating element is missing. Image courtesy of Jörg Wamser/KonTEM .
Kleindiek's design in (**B**) features one linear and two rotary actuators (only one visible). The silicon chip with two electrostatic Zach phase plates is marked by a green rectangle, the separate heating by a blue one.

between motors and phase plate, the rod is supported by a sliding contact bearing.

The axis responsible for moving in and out requires a sliding motion at the support, while the orthogonal axes pivot the rod around it. This implements a polar coordinate system, with vectors r, θ, φ and origin at the sliding contact bearing. Motion in θ and φ is amplified by the resulting lever arm.

Linearisation to a Cartesian coordinate system is straightforward. As the origin and optical axis remain in fixed positions to each other, relative motion always has the same leverage between axes r and θ or φ, given by the geometry. For one of the microscopes used, the motors for θ and φ are located about 40 mm from the sliding contact bearing, and the optical axis is about another 125 mm further. This implies a leverage of about 3.1.

Kleindiek

The Kleindiek design, shown in figure 3.6 (**B**) features one linear motor responsible for in and out direction, and two separate rotary motors for pivoting, which would require a more complicated model to linearise the motions in a Cartesian coordinate system. Fortunately, the rotary axis responsible for motion in z-direction does not need to be adjusted during normal operation. Therefore, the same polar model as for the KonTEM drive can be used.

Beam Tilt

A relative motion of the phase plate to the zero-order beam can also be established by means of the beam tilt deflectors (or any other tilt deflector in between electron-source and phase plate), as shifts in the diffraction plane correspond to tilts in the object plane. The attainable precision and repeatability is outstanding, as no mechanical motion is involved. Due to the small angles involved, the beam tilt angle forms a quasi-Cartesian coordinate system of the diffraction plane.

In order to minimize complexity, the diffraction plane coordinates can be described by a beam tilt angle for both, the mechanical motors and the electron-optical tilt deflectors. To further reduce complexity, the most precise linear axis of the motors r is used as the reference for defining the x direction of a common coordinate system. The excitation of the beam tilt deflector system is rotated accordingly, such that both illumination tilt and motor x axes point in the same direction. This results in unified coordinates, which can be directly applied to physically move the phase plate with the translation devices or to induce a relative motion by tilting the zero-order beam to attain the same relative position.

3.3 CONTROLLING THE DIFFRACTION PLANE

Phase plate application requires tight control of the zero-order beam position in the diffraction plane. Lateral control of the zero-order beam position is equivalent to controlling the inclination of the optical axis.

For non-parallel illumination conditions, the zero-order beam is not focused in a diffraction plane and no clear spatial separation of diffracted and undiffracted beams is present. Such conditions have to be avoided for phase plate imaging, i. e. the specimen illumination has to be parallel by focusing an image of the electron-source in the front focal plane of the objective prefield lens.

Besides the specimen and the phase plate, all electron-optical elements located in-between the electron-source and the diffraction plane have an influence on the inclination of the optical axis. Most importantly, these are lenses and other electron-optical elements, the specimen and the phase plate itself. In the following paragraphs, the effects of each element are discussed.

Specimen and Phase Plate

Non-ideal specimen and phase plates may exhibit patches of electrically insulated regions. Exposed to the electron-beam, a charge is deposited, which is only slowly compensated. The conduction anomaly gives rise to an additional localized potential, which varies according to the present exposure to electrons. This varying local potential can have a strong influence on the position and inclination of the optical axis.

A charged Zernike phase plate film can also show effects similar to a lens, and change the effective focus. This can be compensated to a certain extent by a matching change of the objective lens' excitation, but eventually demands using another, uncharged phase plate, as the electrons scattered in one point of the sample are not necessarily focused to identical points in the image, which results in a blurred contrast.

There are some methods to avoid specimen charging, like evaporation of a conductive amorphous-carbon coating or working at an elevated partial pressure [9]. Also, extending the size of the illuminated area to include part of the amorphous-carbon support film [10] or using highly stable and conductive gold support films [70] can be helpful. The feasibility of such treatments depends on the specimen. Generally, changing the specimen preparation method to yield sufficiently conductive samples is to be preferred.

Deflectors

The inclination of the optical axis can be influenced by specialised electron-optical elements, the deflectors. They are found at strategic positions of the microscope column, often at the boundaries of lens assemblies. To be useful, most deflectors are effective in a 2D plane perpendicular to the optical axis. In the electron-optical alignment, the deflectors are used to thread the optical axis through the individual lens' centres, with the inclination defined by the lens normal, i. e. the direction perpendicular to the plane of the lens.

For that, not only deviations in tilt but also shifts have to be compensated for. A single deflector is only able to influence the local inclination of the beam. The lateral position of the beam can be adjusted using a consecutive double deflection, with some distance in between the two planes where the individual tilts are applied.

Application of a pure shift without changing the inclination requires both deflectors to apply a certain combination of tilts, such that the beam effectively rocks about the lens' front focal plane. Likewise, for a pure tilt without shift, another combination is necessary. Within an alignment procedure, the ratio of the excitation strength of both deflector pairs is adjusted, such that shift and tilt can be varied independently. Examples for such different combinations can be seen in figure 3.7.

For small quick and precise movements on the specimen, automation software preferably uses the image shift deflectors. As they are physically applied below the first diffraction plane, a phase plate located in-there is not affected. However, with low-dose imaging approaches, the illuminated sample area is only slightly larger than the field of view, and the illumination has to follow this shift of the optical axis. As the illumination deflectors are located above the phase plate plane, the applied shift must not introduce any change to the inclination of the optical axis to not change the position of the zero-order beam cross-over in the diffraction plane.

The standard alignment procedures are not precise enough to ensure this property for the illumination conditions used with applied phase plate. A protocol potentially resulting in a sufficiently good alignment is described in appendix B.

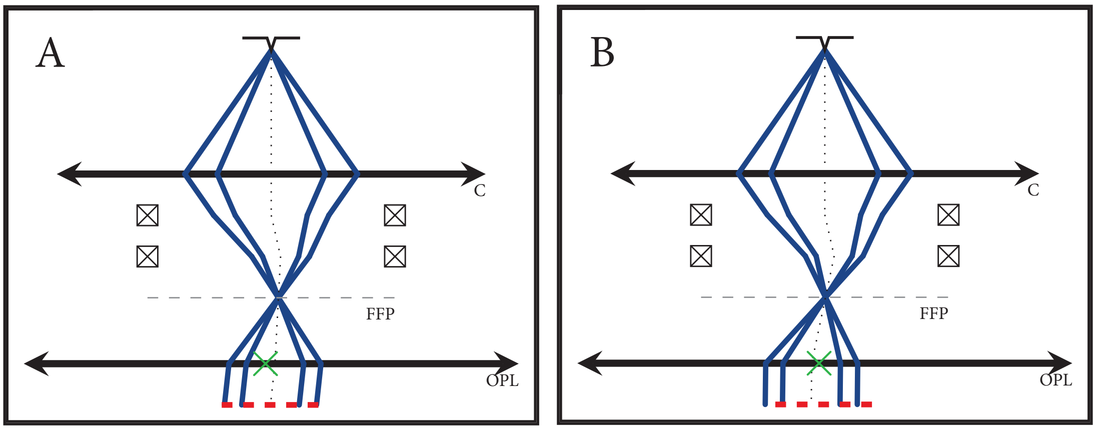

Figure 3.7: Double deflection system to apply tilt (**A**) and shift (**B**) to the beam. With careful calibration of the ratio of the necessary deflector excitations, side-effect free variation of shift and tilt can be achieved. Lens center is marked by (×).

Lenses

As the most-important lens of the microscope, the orientation of the objective can be used to define the inclination of the optical axis[3], which defines both the absolute orientation of the parallel illumination and the physical position of the zero-order beam focus in the diffraction plane. This is a good choice, since for contrast generation, the strength of the objective lens is constantly varied to enable phase contrast transfer using the defocus aberration. As mentioned in section 3.1.2, application of a defocus results in an image shift on the detector if the illumination is tilted, which is inconvenient for deterministic use.

Besides influencing the phase-contrast transfer properties of the optical system, an applied defocus also has an influence on the vertical position of the diffraction plane, i. e. parallel to the optical axis. In practice, application of a defocus in the order of a few μm does not result in a noticeable position-change of the zero-order beam focus. This is due to the symmetry of the combined condenser-objective lens and the condenser system focusing a spot in a plane conjugate to the phase plate plane. The resulting specimen illumination slightly deviates from parallel conditions, though.

The condenser system is usually made of several lenses. In modern transmission electron microscopes, there are often three magnetic lenses

3 Another meaningful choice of inclination is one that minimizes coma, in the so-called coma-free alignment [87].

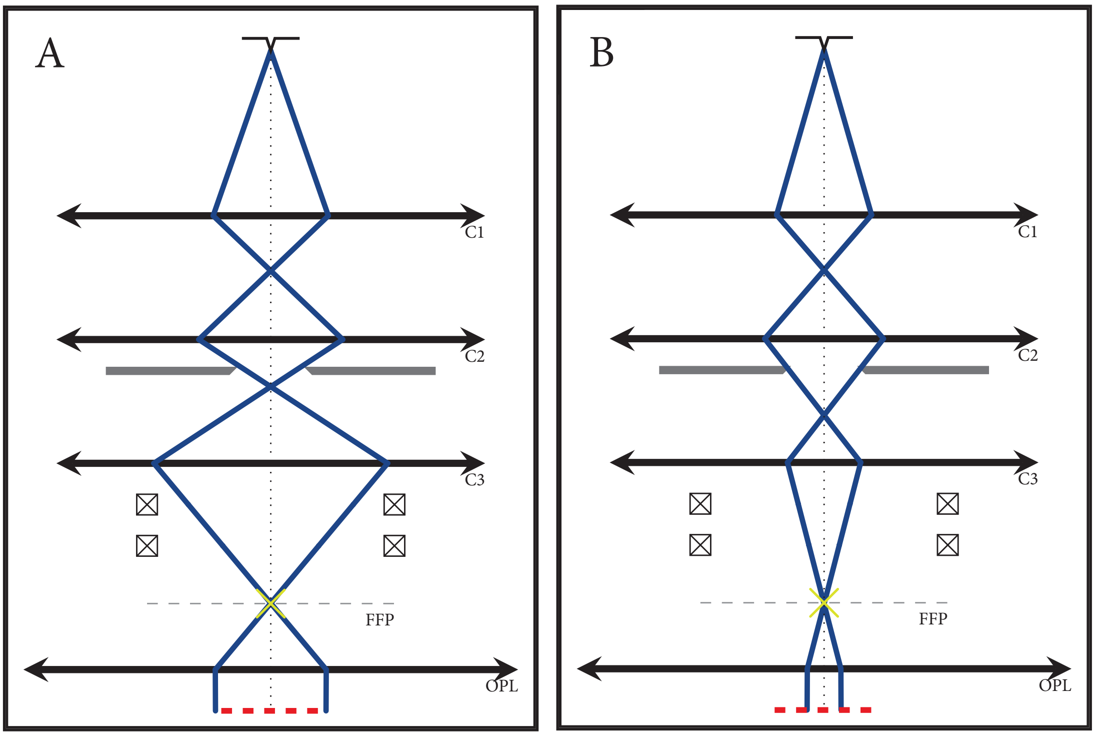

Figure 3.8: Changing the size of the illuminated area. From (**A**) to (**B**), the strength of the second condenser lens is reduced and the change of the cross-over position compensated with the third condenser lens. The marginal rays (blue) are defined by the aperture below the second condenser lens.

in the condenser to provide three degrees of freedom on the parameters of the illumination. Those are

- variable demagnification of the electron-source, which controls the coherence and beam intensity,
- size of the illuminated area at specimen level, and the
- angular distribution of the illumination at specimen level.

The latter is controlled by the relative position of the image of the source and the front focal plane. In on-plane conditions, parallel illumination is established. For any deviation, the illumination becomes spreading or condensing (cf. Figure 3.13), which in turn influences the position of the zero-order beam focus relative to the diffraction plane.

To change the size of the illuminated sample area, the strength of a lens in the condenser is varied, as shown in figure 3.8. An aperture limits the angular distribution of rays from electron-source to specimen. The projected size on specimen-level can be influenced by changing the aperture size or adjusting the focus of the lenses in front of the aperture. For the conditions shown in figure 3.8, variation of the strength of the second condenser lens and a matching focus compensation of the third condenser lens changes the projected size of the aperture on the specimen while maintaining parallel illumination conditions.

Likewise, the illumination intensity can be adjusted using the first and second condenser lenses in a similar zoom-system. In practice, this zoom system is often used in a few discrete parameter combinations and not in a continuous fashion. This is due to the changing lens-characteristics upon variation of the excitation, as this may influence the effective lens orientation. Restriction to a few discrete parameter sets allows for compensation of the effects using deflectors.

For the lower zoom system consisting of the second and third condenser lenses, it makes sense to provide a continuous operation, as this enables a variable size of the illuminated area on the specimen. As a consequence, not only all combinations of second and third condenser lens excitations need to result in a focused beam in the front focal plane of the objective prefield lens, also the lateral position has to be unchanged for constant inclination of the illumination. Consequently, the optical axis in between the condenser lenses has to be aligned to the respective centres and local lens orientations.

A similar situation can be seen in figure 3.9, only with a misaligned electron-source in shift and tilt which is compensated by the deflection system below the last condenser lens to provide a specimen illumination normal to the objective lens orientation. With the misalignment corrected at the wrong position in the beam path, the changed excitation of one of the zoom systems results in a shifted and tilted illumination, as can be seen in (**B**). Therefore, continuous operation of a zoom system with a constant excitation of the deflectors requires the corresponding lenses in the electron-optical system to be well-aligned.

During automated image acquisition using the multi-scale approach, the magnification is constantly changed. The large field of view imaged using low magnifications requires use of broad illumination, while high-resolution imaging demands high coherence and small illuminated areas to restrict the beam damage to a certain region. This can be implemented using a small set of presets, with individual offsets to the illumination tilt to result in common optical axis. Therefore, automated phase contrast microscopy puts no special requirements on the quality of the alignment. However, the set-up time required to establish the presets can be non-

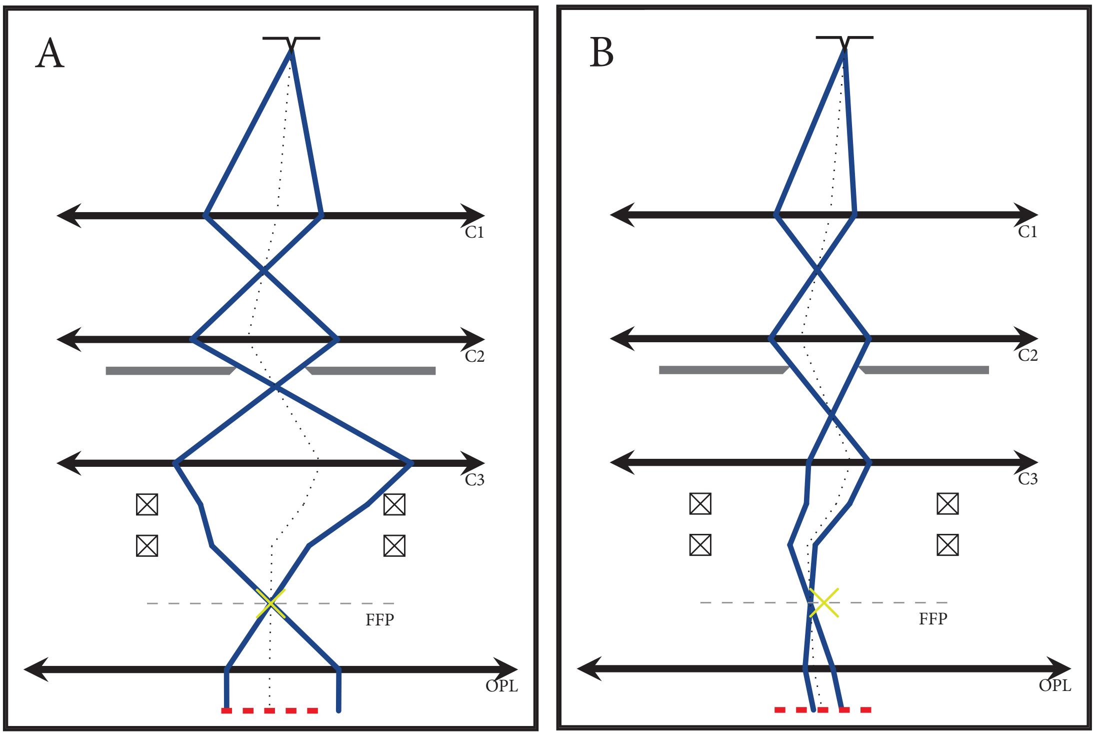

Figure 3.9: Misaligned condenser system. Tilt and shift misalignments present on the electron-source are compensated by a set of deflectors below the third condenser lens for one condenser setting (**A**). With the same deflections in (**B**), the excitation of the lower zoom system is changed identically to figure 3.8, which now results in a still parallel, but tilted and shifted specimen illumination.

negligible, if the quality of the electron-optical alignment is particularly off.

The general robustness on the automated image acquisition is increased by a good electron-optical alignment, as the effects from lens hysteresis and other dynamic perturbations have a smaller influence on the direction of the optical axis. An iterative strategy for attaining an optimized alignment over a broad range of illumination conditions is presented in appendix B.

Projective Alignment

In standard electron-optics found in TEM, the phase plate is applied in the first diffraction plane, directly below the objective lens. The alignment of the projective system is not critical for phase plate application, as it only influences the beam path below the phase plate.

However, if the phase plate is applied in a magnified diffraction plane, some more electron-optical elements are found in between electron-source and phase plate, and the considerations for the additional lenses, deflectors and quality of alignment are as valid as for the condenser system.

In the Kronos instrument, the microscope column is extended by the DMU housing a single lens and a pair of deflectors to implement the magnified diffraction plane. Physically, the DMU is located after another electron-optical device, a CEOS C_s-corrector. The corrector itself roughly doubles the amount of round lenses in between electron-source and magnified diffraction plane, compared to a standard electron-optical set-up with the phase plate applied in the back focal plane. This elevates the demands on the quality of the electron-optical alignment.

The alignment is further complicated, as the magnified diffraction plane amplifies the effects of minute misalignments in the condenser system, which results in an extraordinarily small error margin for the condenser alignment. A schematic view of the conditions below the object plane can be seen in figure 3.10.

In the corrector, the positive spherical aberration of the objective lens (and the rest of the optical system) is compensated by the negative C_s of two hexapoles, i. e. non-round electron-optical elements. Other additional elements provide the necessary degrees of freedom to correct other aberrations as well. During the iterative tuning procedure of the C_s-corrector, the present aberrations are measured and a matching set of parameters for compensation is generated. After application of the new parameters, the changed and hopefully smaller residual aberrations are again determined and the process is repeated.

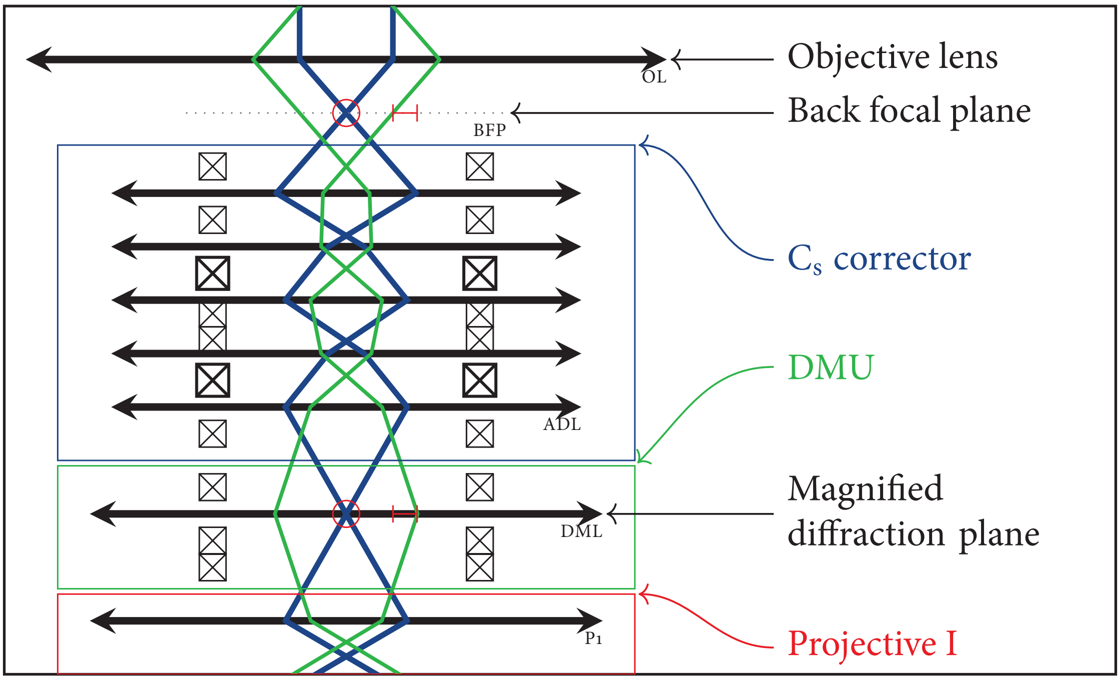

Figure 3.10: Beginning of the projective system of the KRONOS. Below the objective, the beam traverses C_s-corrector, diffraction magnification unit and the first projective. The zero-order beam foci in the conjugated diffraction planes are marked by (○). Diffracted rays are shown in green, undiffracted rays in blue. The magnification of the conjugate diffraction planes is marked by (⊢⊣). In the actual device, the attained magnification is 3.2 ×.

This iterative procedure does not necessarily result in an aligned state for every single round lens within the corrector (personal communication Thomas Riedel/CEOS). Therefore, perfect electron-optical alignment for all elements in between magnified diffraction plane and electron-source while maintaining full correction of the spherical aberration might be impossible.

3.4 POSITION DETERMINATION

To enable an automated alignment of the physical position of the phase plate to the optical axis, the automation software needs to determine the present mismatch of the phase plate alignment and provision for a matching compensation. Phase plates are applied in a diffraction plane of the microscope, which is not directly visible in a regular image. Therefore, the different possibilities of how an object in a diffraction plane can be imaged need to be evaluated for usability in an automation process.

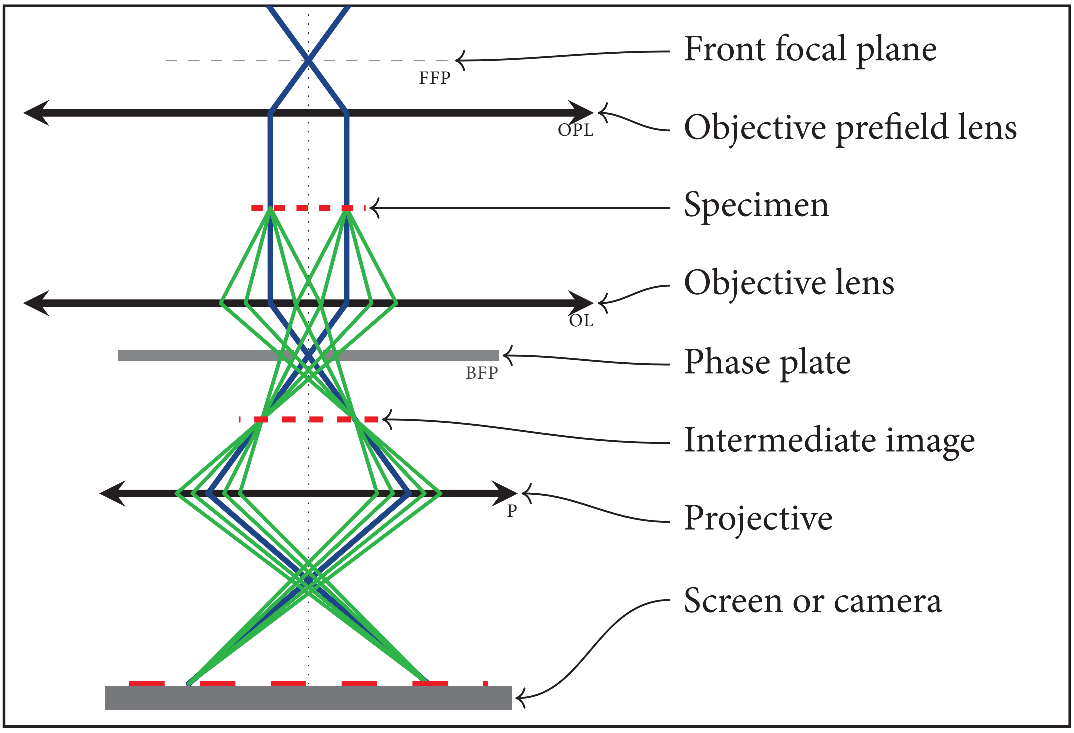

Figure 3.11: Ray paths for HM mode. The rays from the parallel illumination (blue) are focused in the diffraction plane, where the phase plate is installed. Rays intersecting with the phase plate (green) are generated by a scattering specimen.

3.4.1 *Parallel Illumination*

With the objective lens excited at its standard current in high magnification (HM) mode using a short focal length, the parallel illumination results in a focused spot in the diffraction plane. To generate a signal, probing particles need to interact with the object to be imaged. In this case, this is not the specimen, but the phase plate structure in the diffraction plane. Since a focused spot is unsuitable to image an extended structure in one single exposure, a specimen with some scattering power into all angles like an amorphous carbon film is required, to provide the probing particles for the diffraction plane. The scattered electrons interact with the phase plate structure, allowing its position to be detected.

Figure 3.11 shows a lens diagram with condenser, objective pre- and postfield lenses and a projector lens. The electron-source is imaged into the front focal plane of the objective prefield, which results in a parallel zero-order beam through the specimen plane. The scattered electrons that have interacted with the phase plate carry some information about it, which

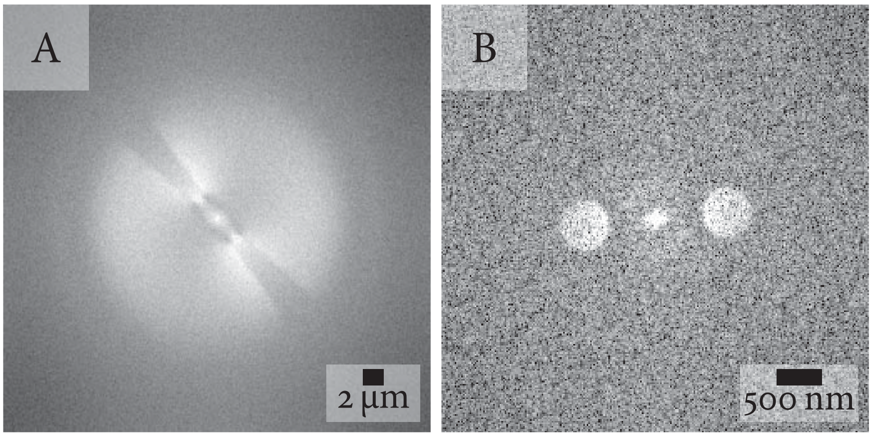

Figure 3.12: Power spectra show Friedel-symmetric images of different types of phase plates. Zach phase plate in (**A**), Zernike phase plate in (**B**), both imaged close-to-focus.

contributes to the image contrast on the detector. The interaction can be a change of phase or attenuation of the signal due to electron-absorption or scattering into high angles.

Image and diffraction planes are connected by a Fourier transform, thus a Fourier-transformed image of an amorphous sample shows modulation by the phase plate structure. Typical power spectra are shown in figure 3.12 for Zach (**A**) and Zernike-type (**B**) phase plates.

Both power spectra feature a point symmetry about the origin, which is a property of Fourier transforms of real objects (cf. Friedel symmetry in section 2.5.1). The scale bars in figure 3.12 have been adjusted to reflect the direct space distances in the back focal plane, according to equation 2.6.

Due to the weak interaction with the thin specimen, most of the image intensity is concentrated in the zero-order beam. The amount of scattered electrons per solid angle is dependent on the specimen's differential cross section. For non-crystalline specimen, scattering into smaller angles is more probable, which results in a higher amount of electrons available for interacting with a phase plate in the vicinity of the zero-order beam. Furthermore, the modulation from the envelopes (cf. section 2.4.1) further dampens the transfer of high spatial frequencies. Therefore, the position information of the phase plate represented in the Fourier-transformed image is modulated, and higher signal-to-noise ratios can be expected for small misalignments of the phase plate position with respect to the zero-order beam.

Usability for Automation

If the phase plate position is already close to the zero-order beam and the signal from the phase plate can be separated from the background, it is feasible to use a diffractogram of an amorphous part of the specimen for determination of the phase plate misalignment. Its main advantage over other imaging possibilities is that an identical configuration of condenser and objective lenses can be used for phase plate alignment and subsequent imaging of the specimen area of interest.

Unfortunately, the attainable signal-to-noise ratio is low and depending on the misalignment (cf. section 3.5.2). In case of a point-symmetric phase plate structure, the introduction of a Friedel-symmetric second image of the phase plate makes it difficult to decide which of the two candidate images corresponds to the real phase plate. The problem can be mitigated if some symmetry-breaking prior knowledge is available.

For a successful detection of the phase plate position, there should be as few as possible additional sources of modulation present in the diffractogram, i. e. no modulation by a contrast transfer function or dampening envelope, a uniform diffractogram background and a phase plate free from unwanted charge. For the final high-precision alignment step close to the zero-order beam, nanoparticles of 2–10 nm diameter can be very helpful to boost the amount of electrons scattered into small angles, which increases the attainable signal-to-noise ratio for imaging the phase plate.

3.4.2 *Defocused Condenser*

Deviating from parallel illumination conditions changes the vertical position of the zero-order beam cross-over behind the objective lens. As can be seen in figure 3.13, the specimen illumination can be made convergent or divergent by not projecting an image of the electron-source in the objective prefield lens' front focal plane. If the deviation from parallel illumination is big enough, the conical zero-order beam intersects the phase plate plane in a disk, which generates a spatially extended beam that can interact with the phase plate structure. Changes to the angular distribution of the zero-order beam are referred to as a change of the *beam convergence* angle.

Figure 3.14 shows a Zernike phase plate at various condenser settings. This imaging-method does not rely on scattered electrons by a specimen, as the primary electrons from the defocused illumination are used for probing the position of the phase plate. Figure 3.14 (**A**) shows the phase

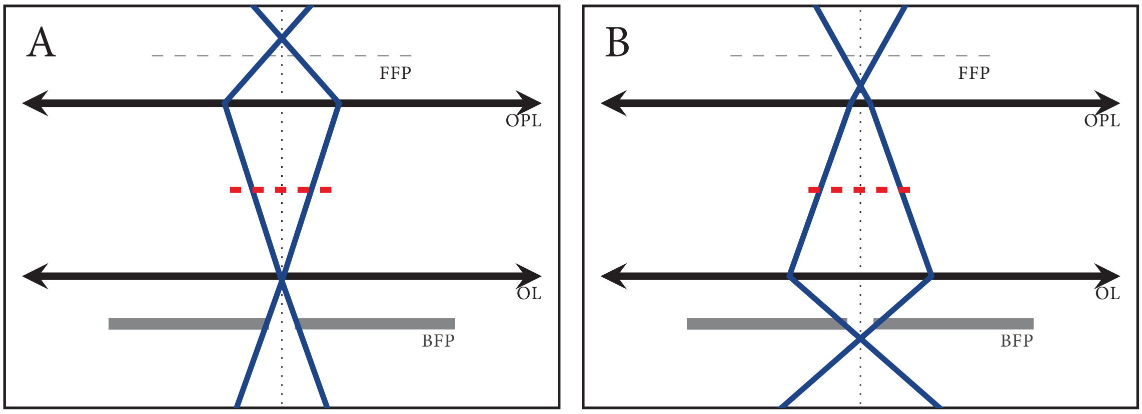

Figure 3.13: Lens diagrams for non-parallel illumination. Depending on where the image of the source is projected relative to the front focal plane, the illumination is parallel, condensing (**A**) or spreading (**B**).

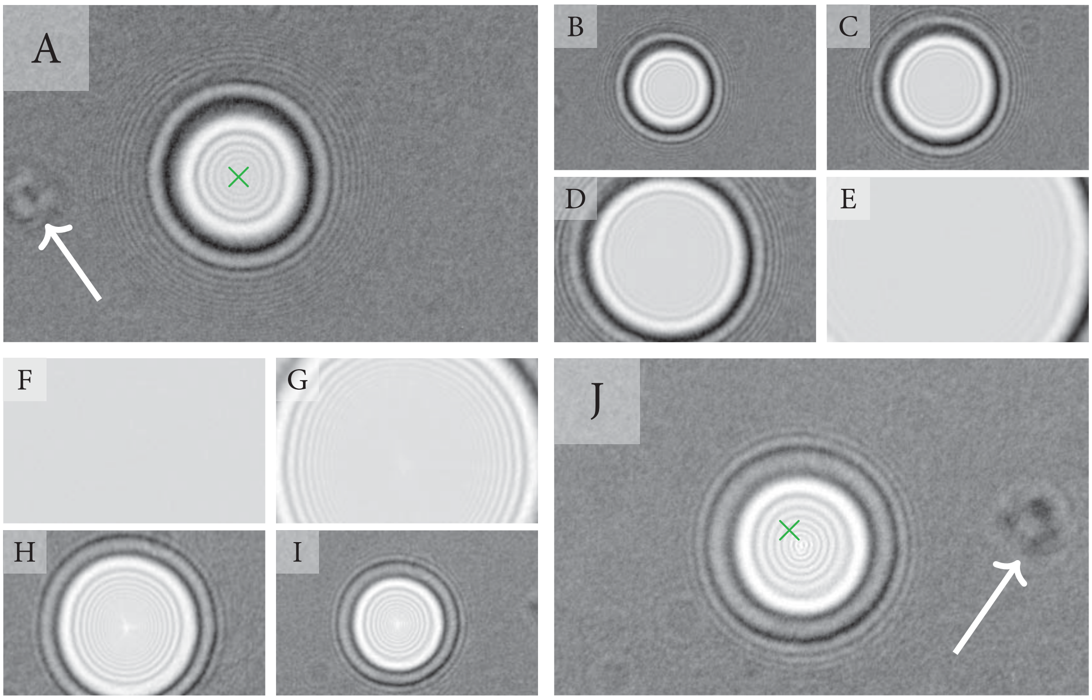

Figure 3.14: Condenser defocus series without a specimen. Overfocus with condensing illumination (**A–E**), focus (**F**) and underfocus (**G–J**). The phase plate diameter was 650 nm. Note the apparent change of phase plate position (×) and the contrast inversion of a contamination particle on the phase plate film (white →). Also note the small change in ellipticity from (**A**) to (**J**), which can be corrected by the illumination stigmator.

plate with condensing illumination, which is gradually (**B–E**) changed to parallel illumination by changing the excitation of the second condenser lens.

In (**F**), parallel illumination with a sharp cross-over in the diffraction plane images the edge of the phase plate structure at infinite distance, which is the condition used for imaging the specimen. Since there is no specimen inserted, which generates diffracted electrons, the Fourier transform of this specific image does not show a modulation by the phase plate.

Underfocus conditions are shown in (**G–J**), with a spreading illumination setting, which results in similar images compared to overfocus conditions. Since the amount of beam cross-overs after the phase plate plane is changed from over- to underfocus conditions, the orientation of the image is rotated about the zero-order beam.

The apparent change of the phase plate centre position from (**A**) to (**J**) stem from non-perfect alignment of the condenser system. Also, a small difference in ellipticity can be seen, due to a changed stigmation of the zero-order beam, again introduced by the change of the lens excitation.

Such a condenser focal-series can be used for manual centring of a Zernike phase plate: As the beam convergence is changed, the ring-system should concentrically open and close. If in both under- and overfocus conditions the phase plate appears centred around the same position, its physical position is close to the optical axis and the electron-optical alignment of the condenser system is usable.

Usability for Automation

Direct imaging of the phase plate structure using non-parallel illumination does not suffer from the ambiguity found in the Friedel-symmetric diffractogram representations. Furthermore, it does not rely on the scattering properties of a sample and is usable with or without a specimen.

The apparent magnification of the phase plate structure can be controlled by the beam convergence angle, besides the magnification of the projective. The more the convergence angle of the zero-order beam approaches parallel conditions in the diffraction plane, the smaller is the apparent magnification of the phase plate structure, which makes the method applicable to small and large misalignments.

However, the required changes to the condenser system usually result in small changes of the position and inclination of the optical axis. Small electron-optical alignment shortcomings of the condenser system can be tolerated, as long as the image of the phase plate is still projected on the detector. This offers the possibility to measure and adjust the phase plate position using multiple scales, if the relative difference of the respective zero-order beam positions are known. Such differences can be compensated by an additional tilt parameter for each preset.

3.4.3 *Diffraction mode*

If the projective of the microscope is focused on the back focal plane rather than a conjugate image plane, an image of the intensity distribution in the diffraction plane is projected on the camera, which also allows a direct imaging of a phase plate, if the structure is illuminated by electrons. As above, the source of such electrons can be either diffracted electrons from a scattering specimen or a defocused zero-order beam.

Using parallel illumination conditions, the intensity normally present in the image background and distributed across the whole illuminated area is concentrated in a spot in the diffraction plane, so that the electrons scattered by the specimen are the only source of probing electrons in the diffraction plane. Depending on the scattering power of the specimen, the signal from their interaction with a phase plate structure can be weak. To compensate, relatively long exposure times are necessary for recording a sufficient signal. For long exposure times, the intense flux of the zero-order beam can damage the detector. Usually, this is averted by introduction of a beam stop, i. e. a physical obstruction of the zero-order beam. The beam stop needs to be aligned using an insensitive detector, e. g. the fluorescent screen. For an automation software, access to such an insensitive detector is often limited, which reduces the practicability of this approach.

The intense zero-order beam can be avoided, if it is focused in a plane below or above the phase plate, i. e. by adjusting the convergence angle of the illumination. Effectively, this results in a variation of the defocused-condenser method with a different magnification of the projective.

3.4.4 *Low Magnification Mode*

Most transmission electron microscopes feature a separate low-magnification (LM) mode lens program. Its main characteristics are a bigger field of view and the lower attainable magnifications, which are typically in the range of 80–2500 × [13]. The lower magnifications are mainly realized by using a smaller excitation of the objective lens compared to HM, yielding a much

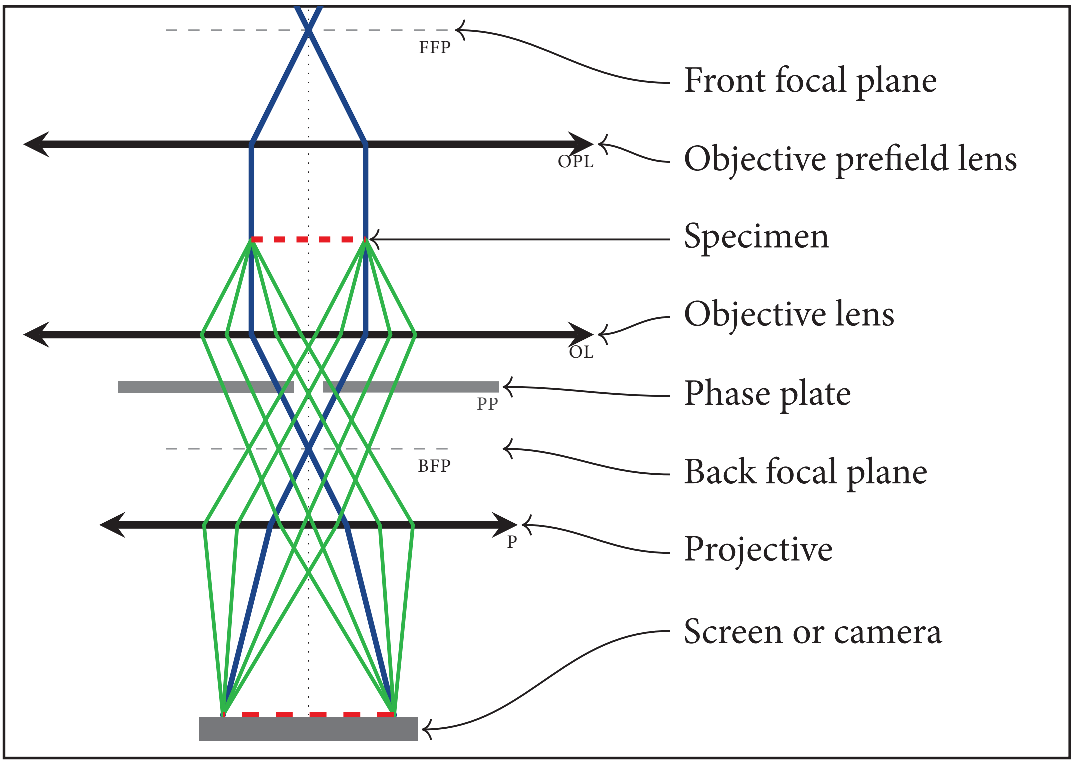

Figure 3.15: Diffracted (green) and undiffracted (blue) beams for a low magnification mode configuration. The phase plate aperture stays in a diffraction plane for HM mode, which does not coincide with any special plane for LM.

larger effective focal length. A schematic overview of the resulting beam paths is shown in figure 3.15.

Since the physical position of the phase plate remains in a HM mode diffraction plane, it is now situated in a different electron-optical plane in LM. Due to the longer focal length, the illumination now directly interacts with the phase plate structure, and no specimen with a scattering power is needed. The presence of a specimen does not severely impede the practicability of this mode, as it only results in a superimposed image from object and phase plate.

For an electron-obstructing Zach phase plate, a hard shadow-image is cast on the detector. Semi-transparent films attenuate the local intensity of the illuminating wave and the areas with and without film can be distinguished.

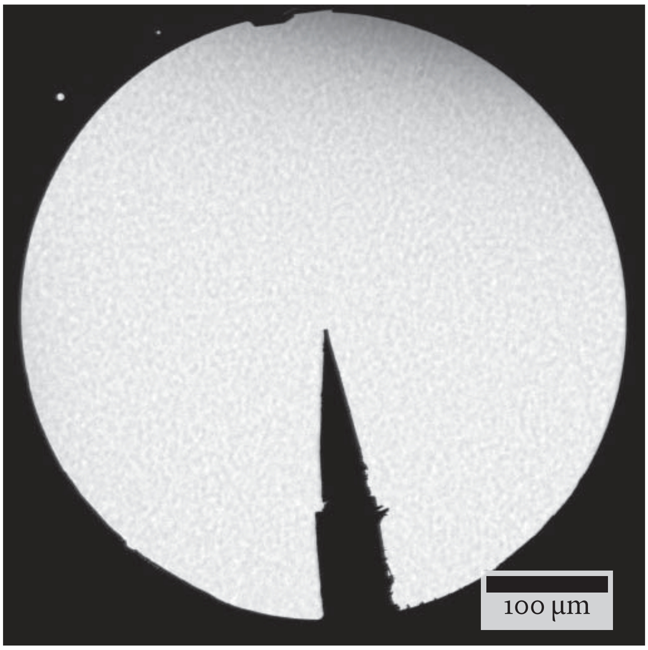

Figure 3.16: Zach phase plate imaged in LM mode.

Usability for Automation

LM mode is usable for a very coarse alignment of Zach-type phase plates, because of the much larger structure compared to a Zernike-type phase plate hole and the higher contrast from the hard shadow-image, as shown in figure 3.16. The Zernike-type film phase plates do not produce such a distinct signal, but given a suitable magnification, their location can also be determined.

The electrostatic phase plates have been used with a Kleindiek micromanipulator (cf. section 3.2). For that device, external coarse control is necessary, as it does not feature position encoders and therefore no internal closed-loop operation, which results in a poor absolute positioning-accuracy. For the Kleindiek drive, use of the LM mode is therefore required. Zernike film phase plates have been used with the KonTEM drive, which offers a much higher position-repeatability thanks to its integrated encoders and closed-loop operation, which make a very coarse alignment step in LM mode unnecessary.

Switching from HM to LM and back introduces a large current change in the objective lens, which in turn can cause hysteresis problems. To avoid frequent mode switches, the large Zach phase plate structure can be coarsely aligned to a certain distance of the zero-order beam, which permits use of other imaging techniques for determining the phase plate

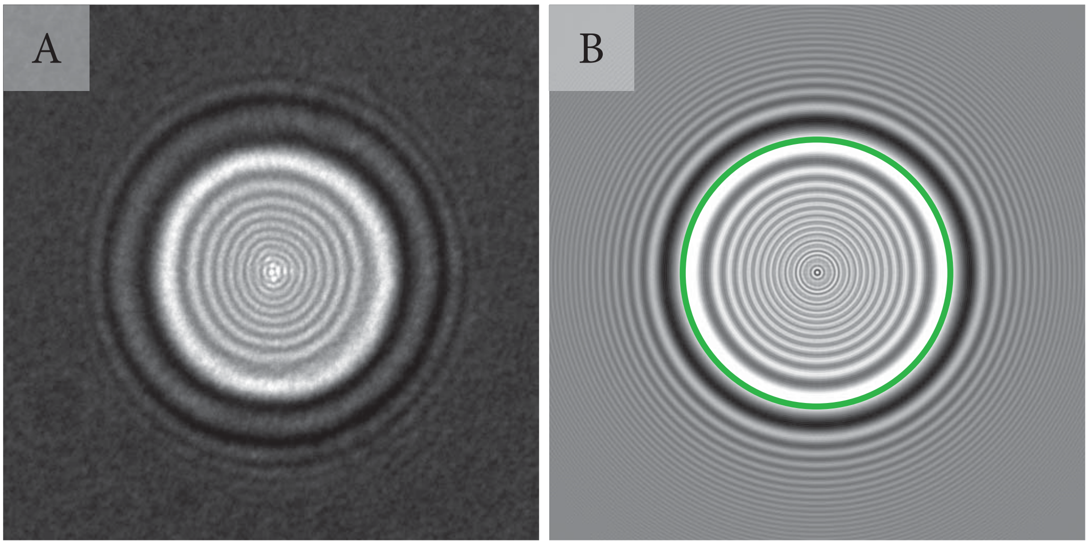

Figure 3.17: Comparison of a Zernike phase plate, imaged with the defocused condenser method (**A**) and simulation (**B**). The edge of the simulated phase plate hole is marked by a circle.

position, as described above. For imaging without applied phase plate, no potential is applied and the structure is used as a slightly misaligned objective aperture.

3.5 PHASE PLATE RECOGNITION

For the images acquired using the methods described above, image processing algorithms capable of extracting the position of the phase plate need to be developed. The attainable images can be divided into two categories: Direct visualisation techniques, such as the defocused-condenser and LM mode method and Fourier-domain techniques with parallel illumination. In the following, suitable algorithms for position-determination are presented.

3.5.1 *Defocused Zernike Phase Plate*

If non-parallel illumination conditions are used, the phase plate can appear in different sizes, depending on the chosen condenser setting (cf. Figure 3.14). By modelling the Zernike phase plate as a semi-transparent aperture with phase-shifting properties, the characteristic ring system of a defocused phase plate can be generated, as shown in figure 3.17.

Figure 3.18: Template of a defocused Zernike plate, generated from twenty views with varying background.

It proves to be difficult to match the shape of an experimental image of a defocused phase plate with a simulation result, since the actual appearance is not only depending on the phase-shifting and electron-absorbing properties of the phase plate, but also on the convergence angle of the zero-order beam used for illuminating the phase plate. The potentially imperfect properties of the phase plate further complicate the analysis. While a simulated image can in principle be used as a template in a template-matching algorithm, better results could be obtained using a template generated from actual phase plate views.

Template Matching

Template matching algorithms offer an efficient approach to finding arbitrary structures in images, provided a template similar enough to the structure to be found is available. For generating such a template, twenty images of the very same phase plate with identical illumination conditions, but varying background contribution from different specimen positions have been aligned and combined into a low-noise representation. The relevant part has been centred, cropped and rotationally averaged. An example of a resulting template is shown in figure 3.18.

To account for different phase plate sizes (cf. section 3.4.2), the template image can be linearly scaled. The scaled template and the phase plate image are then correlated and a peak-finding algorithm is applied to the correlation map. The peak corresponds to the phase plate position, as can be seen in figure 3.19.

If the apparent size of the phase plate is unknown, e. g. by a mismatch of requested and resulting electron-optical settings due to lens hysteresis, a range of different radii can be assumed, a corresponding set of scaled

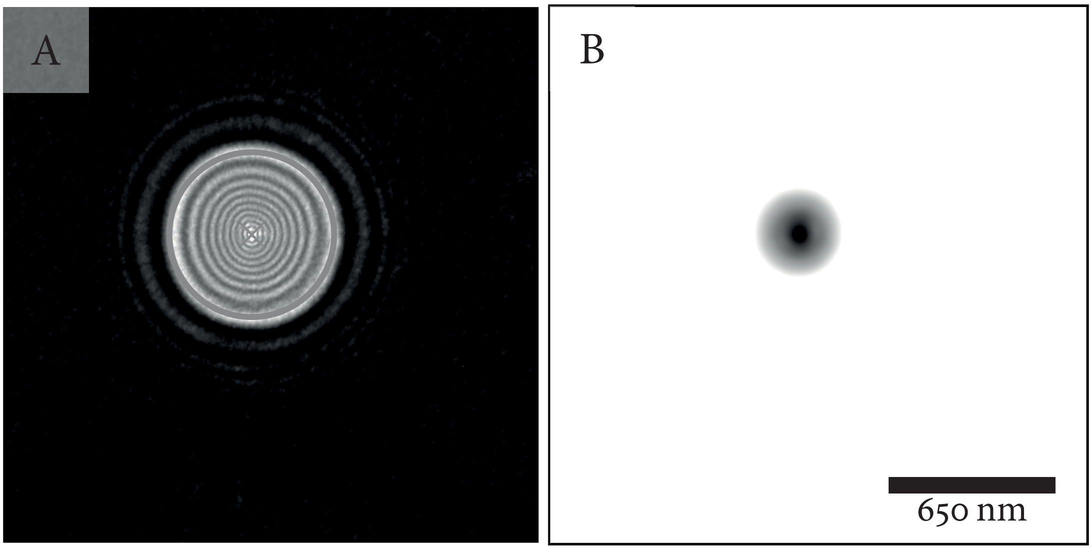

Figure 3.19: Template from figure 3.18 scaled to match the green circle is applied to (**A**). Resulting correlation map in (**B**). The found phase plate position and size is highlighted by a circle with marked centre (×).

templates generated and correlated with the image. After normalisation, the best matching template yields the highest peak of all correlation maps, which determines both the phase plate position and its apparent size. The latter is useful, if the effective beam convergence angle needs to be determined.

Algorithm Evaluation

To measure the performance of the phase plate detection algorithm, all intermediate images during an automated phase-contrast imaging session have been recorded. During routine application of the automated phase-contrast imaging, those images are only used for alignment and are usually not kept.

In the acquired dataset, a total of 484 images have been evaluated of which 432 show a phase plate. Illumination conditions, magnification and camera acquisition time were kept constant. The electron dose was $14\,e^{-}\,nm^{-2}$, which is about a hundred times smaller than typical doses used for imaging beam sensitive specimen.

Depending on the specimen position, the local specimen thickness varies, which is reflected in the mean intensity of the acquired images. Thicker specimen locations result in a lower image intensity, and a smaller signal-to-noise ratio in such images can be assumed. For comparison, the

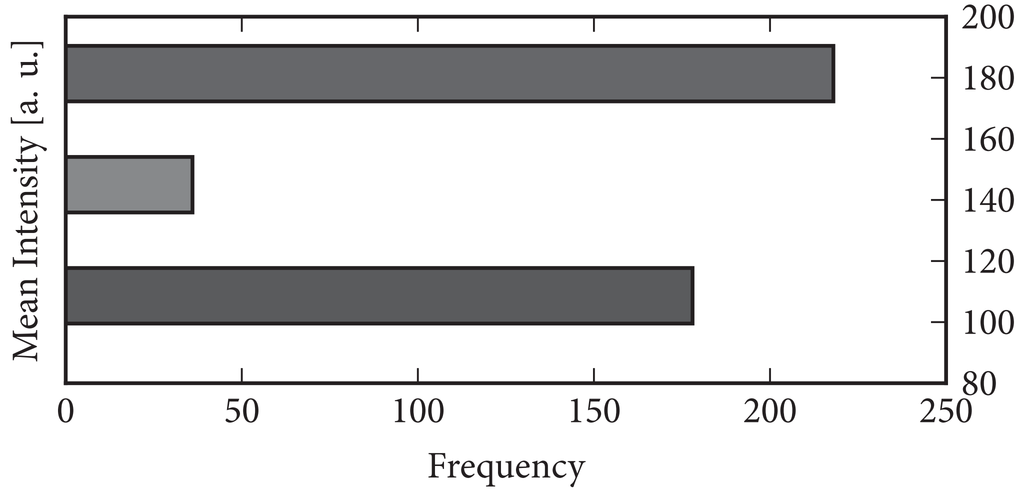

Figure 3.20: Image mean intensity distribution in intermediate alignment steps during an automated phase-contrast microscopy session. Depending on the local specimen thickness, different mean values are attained, which correspond to the signal-to-noise ratio present in the images. Higher values correspond to thinner parts of the specimen.

images in the dataset have been partitioned by their mean intensity into three classes, as shown in figure 3.20.

This partition is used to differentiate the imaging conditions for the evaluation of the algorithm's performance. Ground-truth reference positions of the phase plate center are marked manually and compared to the positions found by the algorithm. A graphic representation of the results is shown in figure 3.21.

For low signal-to-noise ratios, a significant amount of outliers is present, which suggests a poor reliability. For intermediate and high signal-to-noise ratios, the positioning error is reduced.

Another source of error may be hidden in the way the reference positions are generated, since they were acquired manually by visual inspection, which also suffers from a low signal-to-noise ratio. Therefore, the assumed reference positions might exhibit a small error.

An automated phase plate centring algorithm should therefore use a well-matching template and monitor the mean image intensity. To account for varying specimen-thickness, the camera acquisition time can be adjusted accordingly to ensure a sufficient signal-to-noise ratio for reliable phase plate position determination.

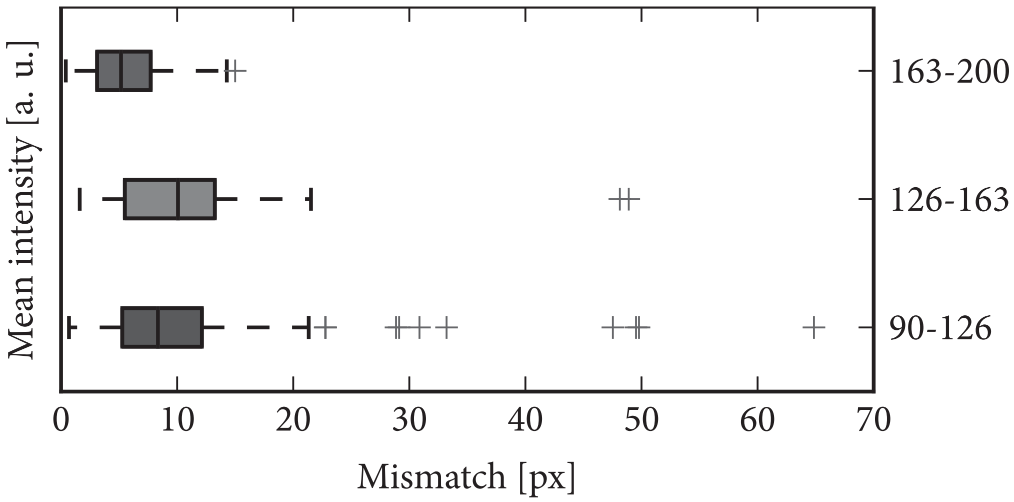

Figure 3.21: Box plot of the mismatch between reference position and positions found by the template-matching algorithm, differentiated in classes of different signal-to-noise ratio, corresponding to figure 3.20. With higher mean image intensity, an increased amount of outliers (+) is present, suggesting a failure to detect the correct phase plate position.

3.5.2 *Zernike Phase Plate in Fourier-Domain*

The method described in the previous section has the disadvantage of relying on non-parallel illumination, but is useful to bring the phase plate close to the optical axis, such that a Fourier-domain based algorithm does not need to be able to deal with large mismatches.

To take the image of the specimen with applied phase plate, the illumination conditions have to be changed to parallel illumination. The necessary change of condenser lens excitations might result in an altered optical axis, which can be accounted for in a static calibration of the used presets, where the effective illumination tilts are harmonised.

A harder problem is posed by phase plates exhibiting less conductive regions, which show a varying amount of charging depending to the current exposure to electrons. The charging results in an additional parasitic electrostatic potential, which has a strong influence on the zero-order beam, and is able to alter both its position and focus. This complicates the alignment, since the alignment goal is a relative positioning of the phase plate to the zero-order beam, which should most conveniently not be a moving target.

Since the additional parasitic potential appears to be constant as long as the illumination conditions are unchanged, phase plates prone to charging effects need to be aligned using the condenser settings of the final exposure.

As this requires parallel illumination, charging phase plates need to be aligned in a Fourier-domain representation.

Ideal conditions, such as imaging with minimal lens aberrations, pristine phase plate, thin, homogeneous amorphous-carbon film background and a moderate electron dose of about 66 $e^{-}\,nm^{-2}$ result in a clear and sharp signal in the diffractogram. To test phase plate finding algorithms with a standardized data set, a series of images with deliberate phase plate misalignment using the described imaging conditions was acquired. Two members of this data set are shown in figure 3.22 (**A–B**).

The contrast resulting from the slightly misaligned phase plate in figure 3.22 (**A**) is interesting. The part of the diffractogram covered by the phase plate hole is transferred with high intensity, iff exactly one of the Friedel mates passes through the phase plate film material and the other through the hole. A more precise discussion of the contrast formation in this configuration can be found in appendix A.

In a naive implementation of a phase plate position determining algorithm, the noise reduced diffractograms are transformed into an edge representation, e. g. by application of the Sobel operator, as shown in figure 3.22 (**C–D**). From the edge representation, the position of circles corresponding to the size of the Zernike phase plate can be found by application of the circular Hough transform [24].

The Hough transform uses an accumulator array of a size equivalent to the image dimensions. For each non-zero pixel in the source image, the corresponding pixels in the accumulator array in distance r are incremented. In the resulting accumulator array, the pixel position being r distant from the center of a circle of radius r therefore receives the majority of votes, and can be found by a peak-finding algorithm.

The resulting accumulator array for the image shown in 3.22 (**C**) can be seen in figure 3.23 (**A**), with two clearly recognizable peaks corresponding to the Friedel-symmetrized phase plate centres.

With the described method applied to all members of the test data set, the correct phase plate centres can be found for all the 55 test images with linearly spaced mismatches up to 0.35 mrad. This can be seen in a maximum projection of all the resulting accumulator arrays shown in figure 3.23 (**B**).

Besides the optimal reference data set, image-series with controlled non-ideal imaging conditions were acquired, which can be used to test the robustness of a phase plate finding algorithm. Several of such data sets exist, which vary in their signal-to-noise ratio, defocus, sample background and parasitic charge of the used phase plate.

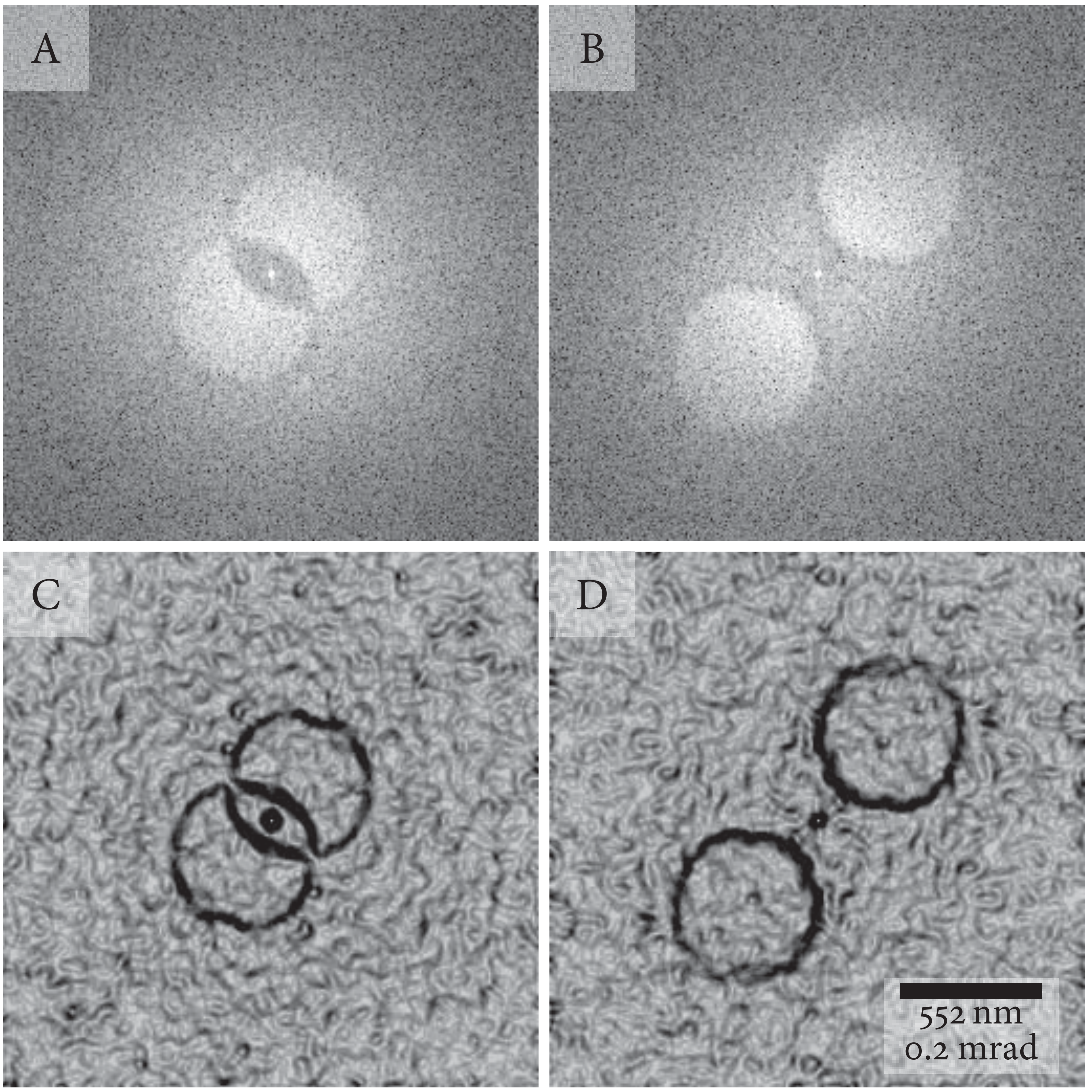

Figure 3.22: (**A–B**) Diffractograms of images acquired under ideal conditions with different phase plate misalignment. In (**A**), the zero-order beam is still within the phase plate hole, in (**B**) not. An edge representation of (**A–B**) is shown in (**C–D**).

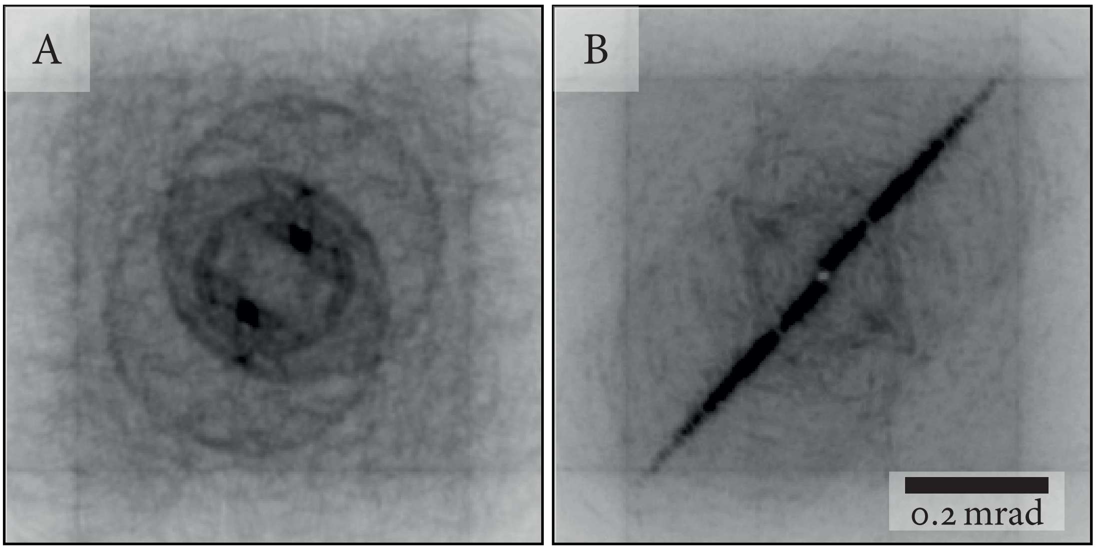

Figure 3.23: Hough transform of figure 3.22 (**C**) in (**A**) shows two clear peaks corresponding to the mismatch. Maximum projection of 55 accumulator arrays from a test bench with deliberate misalignments in (**B**) confirms successful application to all members of a test data set.

Figure 3.24 shows two members of a non-ideal test data set with similar position mismatches as in figure 3.22. The naive method fails as soon as the used edge-finding algorithm fails to highlight the outline of the phase plate hole, which easily happens if the contrast is modulated by a nonvanishing CTF. Because of the lacking robustness, the naive approach is not suitable for automation.

Application to Non-Ideal Circumstances

The modulated background in the diffractograms proves to be challenging for image processing algorithms, as it occludes the small signal of the phase plate. For a similar problem, the determination of CTF parameters from diffractograms, the literature describes several approaches to extract and subsequently subtract the background signal [59, 4, 81]. Unfortunately, the reported methods are unable to reliably deal with the azimuthally varying contrast present in diffractograms with an applied Zernike phase plate.

The automation software does not need to rely on the data present in a single image, as it controls the image acquisition process. Better background models can be attained by measuring the individual image background contribution in an additional reference exposure prior to phase plate insertion. The diffractogram background of the reference

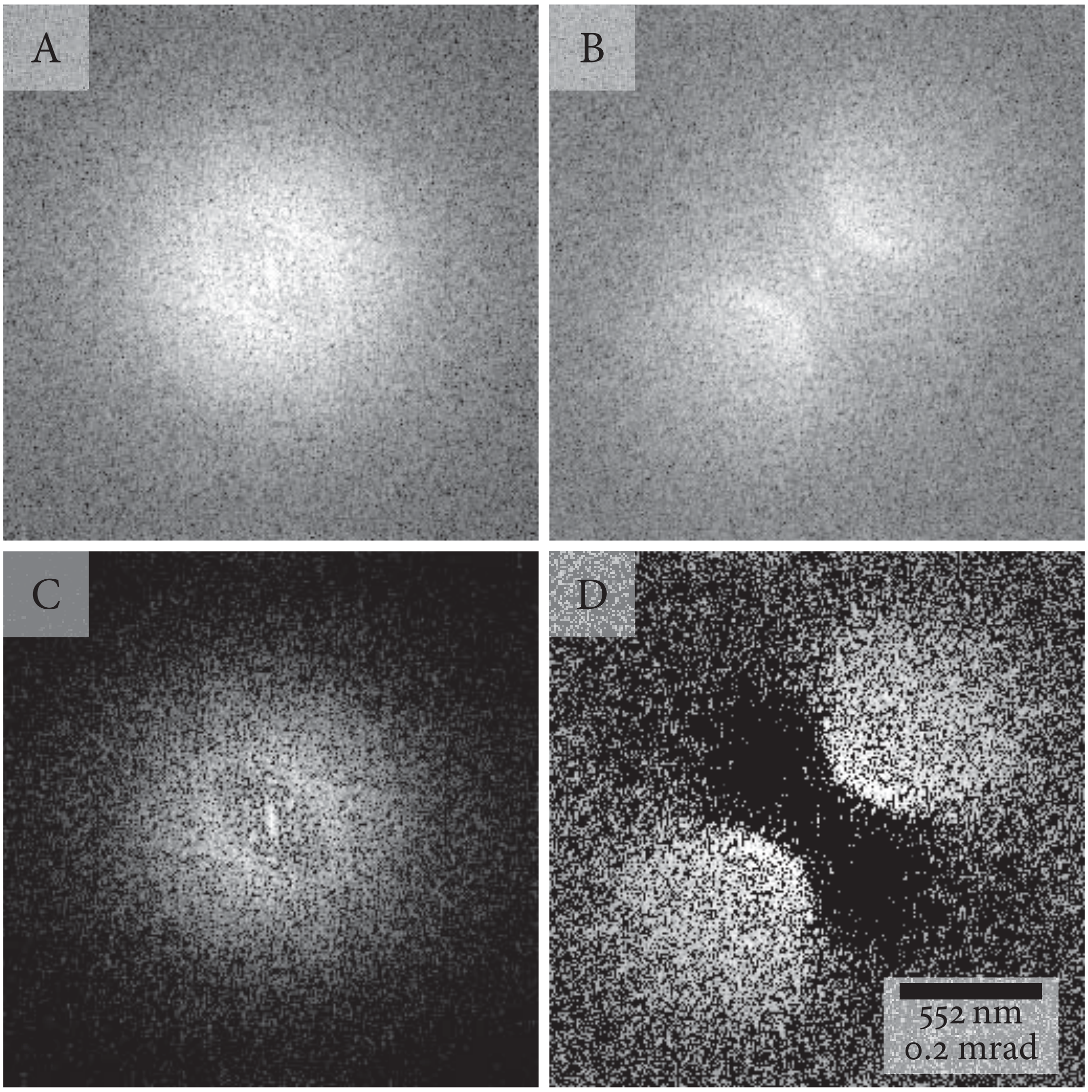

Figure 3.24: (**A–B**) Diffractograms of non-ideal images with different phase plate misalignment and angularly varying background signal. Background-subtracted versions of (**A–B**) are shown in (**C–D**).

image can then be subtracted from the more or less identical image with applied phase plate.

However, even this potentially perfect approach can fail, if insertion of the phase plate results in a change of the effective wave-aberrations, e. g. by introducing an additional defocus.

As shown in figure 3.24 (**C–D**), also the background-subtracted data is modulated. The part of the phase plate with smallest distance to the zero-order beam appears to be transferred with stronger intensity compared to the rest.

For such modulated data, no universally applicable thresholding method could be established, which allows a reliable separation of remaining background and phase plate signal. Therefore, methods that do not require thresholding have been investigated:

The most successful approach is again based on template correlation, for which efficient algorithms exist for Cartesian coordinate systems. Due to the imposed Friedel-symmetry in the diffractograms, the mismatch positions are better represented by a polar coordinate system, with identical values found for azimuthal angles modulo π. For efficient template correlation, the Fourier-domain diffractogram is transformed into a corresponding polar representation. The result of such a transformation can be seen in figure 3.25.

Subsequently, a correlation of the polar representations with calculated templates, each corresponding to the resulting contrast for a certain radial mismatch (cf. last column in figure 3.25) is performed. The resulting correlation maps, one for each tested radial mismatch, can be combined into a unifying map, where each of the correlation results contributes one column corresponding to the radial mismatch tested by the individual template. Using a peak-finding algorithm, both the azimuthal and radial phase plate mismatch can then be extracted.

In figure 3.26, such resulting unified maps are shown for ideal and less-ideal imaging conditions. While for ideal imaging conditions this algorithm is able to extract coordinates compatible with the deliberate misalignment in the test data set, its performance is not robust for the less-ideal diffractogram data.

The efforts to increase the robustness can be summarized in the following insights:

- Presence of a modulated background is a major obstacle. If the phase plate itself changes the parameters of the CTF, even potentially perfect background subtraction using an image from an identical

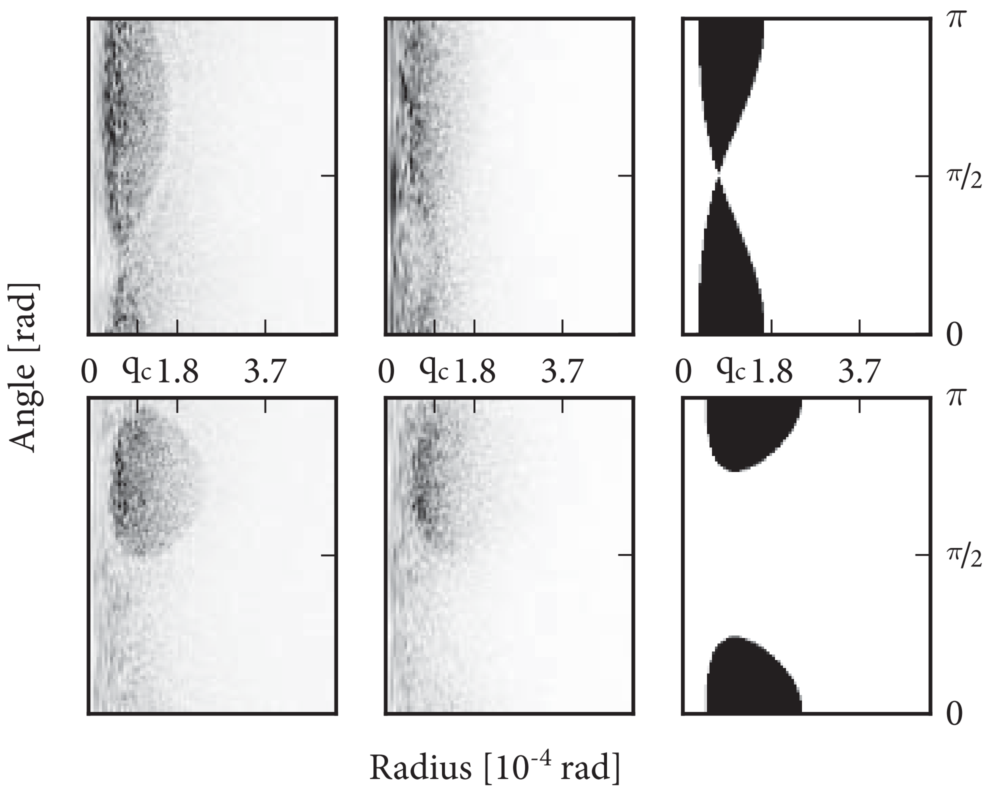

Figure 3.25: Polar representation of the background subtracted Fourier transform of misaligned Zernike phase plates. Upper row corresponds to the smaller misalignment of figures 3.22 and 3.24 (**A**), the lower row to the larger misalignment found in (**B**). The last column shows a corresponding template, centred at the angular origin. Phase plate hole radius is designated by q_c.

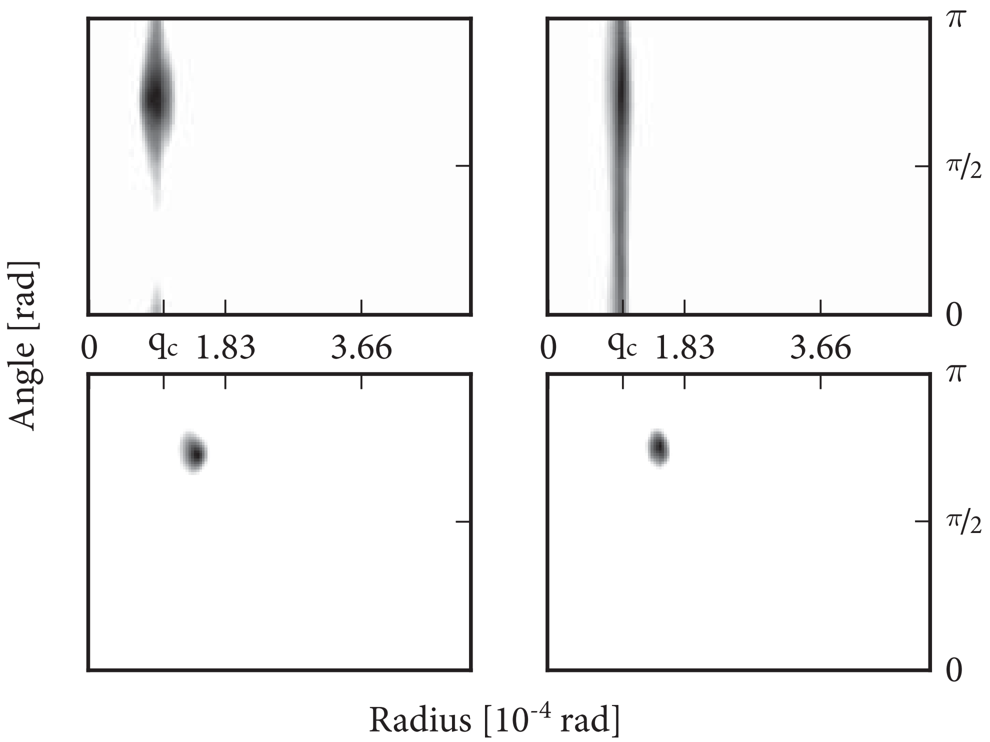

Figure 3.26: Maps resulting from correlating all possible templates with the polar transformed and background-subtracted representation of a Fourier-transformed phase plate image. Each template (e. g. last column in figure 3.25) contributes one pixel column according to the respective radial mismatch. With ideal conditions (left column), the phase plate position can be extracted for both mismatches. With less ideal conditions (right column), the detection fails for mismatches smaller than the phase plate radius (upper row).

specimen position often fails to separate phase plate and background signal.

- The phase plate signal is influenced by the current amount of contamination or charge present on the perimeter of the phase plate hole. It varies with local specimen and illumination conditions.

Therefore, presence of a charge on the phase plate is detrimental for robust phase plate detection algorithms working on a Fourier-domain signal, mostly due to problems of separating signal and background.

Possibly, the situation can be improved, if images of better quality can be reliably acquired, which mainly means that the additional aberrations introduced by the phase plate itself need to be accounted for. As the magnitude of additional defocus introduced by the phase plate does not appear to be constant and no static compensation can be found, attempts to extend the auto-focusing routine to work with an applied Zernike film phase plate were attempted.

As the auto-focusing routine works by comparing the resulting image shift upon application of a varied illumination tilt, the physical position of the phase plate has to be adjusted accordingly and at least roughly aligned to the resulting zero-order beam positions in the diffraction plane. With manual supervision, this technique can result in a slightly better image quality, but the robustness of the approach is poor, as the phase plate needs to be aligned twice. A non-robust means to cure the shortcomings of another non-robust process is a poor choice, though. For automated phase plate image acquisition, this approach does not appear to be feasible.

To summarize, non-ideal phase plates should be avoided for automated image acquisition, as their effects on the image contrast appear to be uncontrollable for an algorithm.

Positioning in Friedel-Symmetric Representation

Since the Friedel-symmetry only allows to determine the azimuthal mismatch angle modulo π, the correct angle has to be determined by choosing one of the two possible azimuthal angles and checking the correctness of the assumption in a subsequent acquisition. Failure in guessing the correct angle often results in a configuration, where the zero-order beam is focused on the phase plate hole perimeter, which quickly introduces a parasitic charge and renders the phase plate unusable. To avoid this undesired situation, the previous coarse alignment steps using the defocused condenser lens method should actually position the phase plate at a

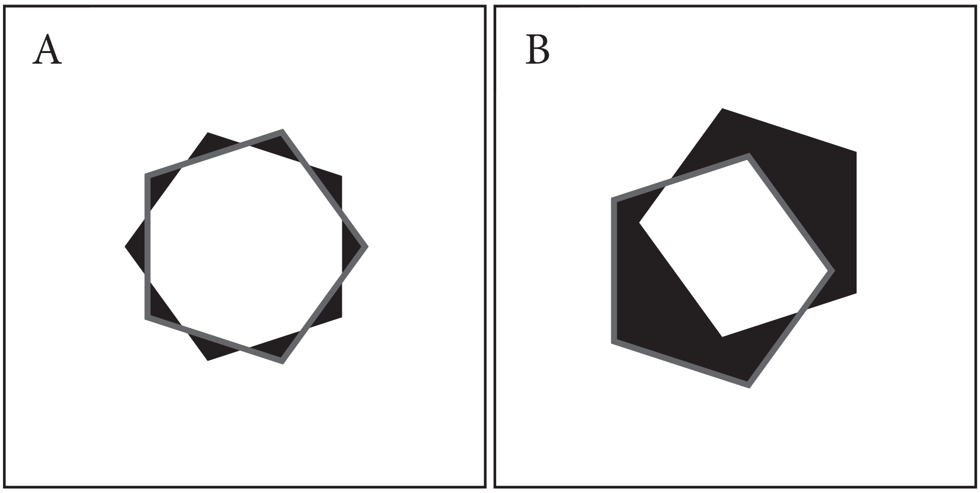

Figure 3.27: Proposed modification of a Zernike phase plate shape featuring an odd symmetry. At perfectly aligned position (**A**), a small single-sideband signal is present in the Fourier-transformed image, which may help a human operator or an algorithm to decide whether the aligned state has been successfully reached. Since the true orientation of the misaligned shape is known (**B**), the ambiguity of even symmetric objects is resolved.

certain offset to the optical axis. With this prior knowledge, the correct angle can be chosen on first try.

For phase plates with large holes, it is feasible to target a position in between hole center and edge so that the intense zero-order beam does not interact with the phase plate. For phase plates with hole radii smaller than the mechanical repeatability of the positioning device this can result in a targeted position, where the zero-order beam has to pass through the phase plate film material.

If a small azimuthal variation of the effective cut-on frequency is tolerable, the round phase plate hole can be approximated by a polygon with a small *odd* amount of sides, e. g. a pentagon, as shown in figure 3.27. Because of the odd symmetry, the actual position can be distinguished from its mirror image, if the true orientation of the polygon is known (**B**). A further advantage is the presence of a recognizable signal even for perfect alignment (**A**) due to single-sideband contrast, which may help an algorithm or a human operator to decide whether the alignment goal has been reached.

Necessity of Fourier-Domain Alignment

Phase plates prone to charging effects demand performing the final alignment step with the illumination conditions used for imaging, as any change of the illumination condition results in a differently charged phase plate which alters the relative position of phase plate and zero-order beam. Therefore, the alignment has to be done in a Fourier-domain representation.

For phase plates less susceptible to charging, an acceptable alignment can be attained by exclusively using the defocused-condenser method, i. e. the Fourier-domain alignment step can be completely avoided.

3.5.3 *Electrostatic Zach Phase Plates*

In LM mode, the very coarse position of a Zach phase plate can be determined (cf. figure 3.16), by using a template correlation approach. Subsequently, the phase plate position error can be further minimized by using the defocused-condenser method, similar to the method used for the Zernike phase plates. The feature to detect is of course no longer a concentric ring system, but resembles the appearance depicted in figure 4.12.

For finding the phase plate position in a Fourier-transformed image, the same imaging conditions as for Zernike film phase plates should be used, i. e. minimal lens aberrations and a scattering amorphous sample background. The Zach phase plate offers a wide-open area similar to an objective aperture. Therefore, minimisation of the lens aberrations by focusing with an applied phase plate can be done with the standard focusing algorithm using an induced beam tilt (cf. section 3.1.2).

If the phase plate is close to the zero-order beam after a coarse alignment step, a static voltage to activate the phase-shifting property can be applied, which causes increased transfer of spatial frequencies localized at a position corresponding to the current phase plate position. This can be seen in figure 3.28. Due to the odd symmetry of the Zach phase plate design, the ambiguity of the Friedel-symmetry can be resolved.

The phase plate alignment using the defocused-condenser method yields a similar accuracy as with Zernike film phase plates, since the same positioning system can be used. In the vicinity of the zero-order beam, the alignment accuracy is depending on the local charge present on the phase plate tip.

A further unfavourable factor for an alignment in reciprocal space at target-resolution (i. e. rather high magnification) is the poor resolution of

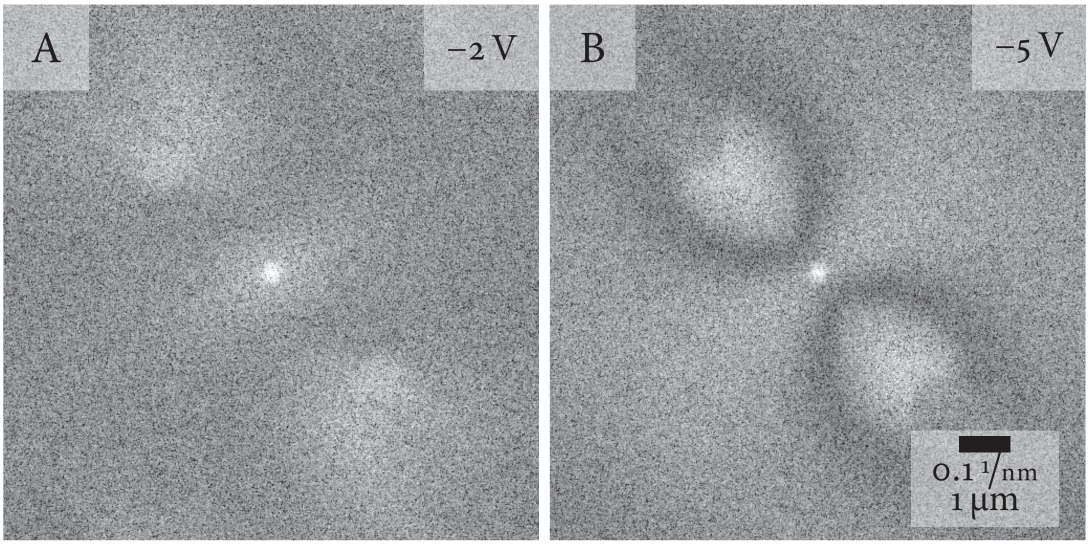

Figure 3.28: Diffractograms of images taken close-to-focus with applied Zach phase plate. In (**A**), a potential of −2 V is applied, which just compensates the trapped charge on the phase plate tip. In (**B**), a potential of −5 V is applied, which highlights the region in front of the phase plate tip.

low spatial frequencies. For achieving a low cut-on frequency, the phase plate tip has to be placed close to the zero-order beam, and monitoring its position becomes difficult. This can be seen in figure 4.3 (**D**). The effect is even more pronounced, if only small detectors are available, since low spatial frequency resolution as well as the attainable signal-to-noise ratio are directly influenced by the detector size. The absolute size of the detector is not important, since the optical system compensates for the physical pixel size. Therefore, cameras featuring 4096 × 4096 or an even higher amount of pixels greatly facilitate a Fourier-domain alignment task.

3.6 AUTOMATED ALIGNMENT

To integrate the routines described in this chapter into Leginon, existing software had to be modified or extended. Leginon's code base is organized into a variety of nodes, each of which responsible for a certain functionality, such as centring a specimen feature on the camera, changing presets or performing an autofocus routine. The software framework provides the necessary infrastructure to facilitate the node communication with each other and the underlying physical instruments like microscope or camera. The modular approach allows to generate so-called applications by defining which of the nodes should be present, and how they are able to communicate with each other.

A crucial part of automated phase plate application is the alignment of the phase plate itself. For that, a specialized node implementing the defocused-condenser as well as the Fourier-domain alignment approach has been developed. The available multi-scale imaging application is used as a base, where the phase plate alignment step is integrated.

Each automated phase plate alignment procedure begins with a very thorough mechanical alignment of the specimen to the object plane. The residual focusing error is then corrected with a small adjustment of the objective lens' current.

3.6.1 *Multi-Scale Phase Plate Alignment*

With the specimen focused, the phase plate is automatically inserted and centred using the methods described throughout this chapter. A multi-scale approach is used, wherein a fixed sequence of microscope settings is used to measure and correct the current phase plate position mismatch. This allows to image the phase plate with varying magnifications. Small magnifications are used in the beginning of the alignment process to be able to deal with large mechanical mismatches. Afterwards, a preset resulting in higher phase plate magnification is used for a precision-alignment step. The position of the respective centre of the optical axis resulting from the changed condenser settings of each preset is calibrated and known to the system. Intermediate images resulting from such an alignment procedure can can be seen in figure 3.29.

Figure 3.30 shows a screen shot of the implemented phase plate alignment node with the current phase plate position and the location of the optical axis defined by the condenser setting used for the final exposure marked.

3.6.2 *Alignment at an Offset Position*

Focusing and phase plate alignment should be done at a specimen position away from the area of interest, since the dose used for achieving focus and alignment is able to destroy all meaningful information of a beam-sensitive specimen. An example is shown in figure 3.31, with the focusing position about 2 µm away from the area of interest, while the high-intensity

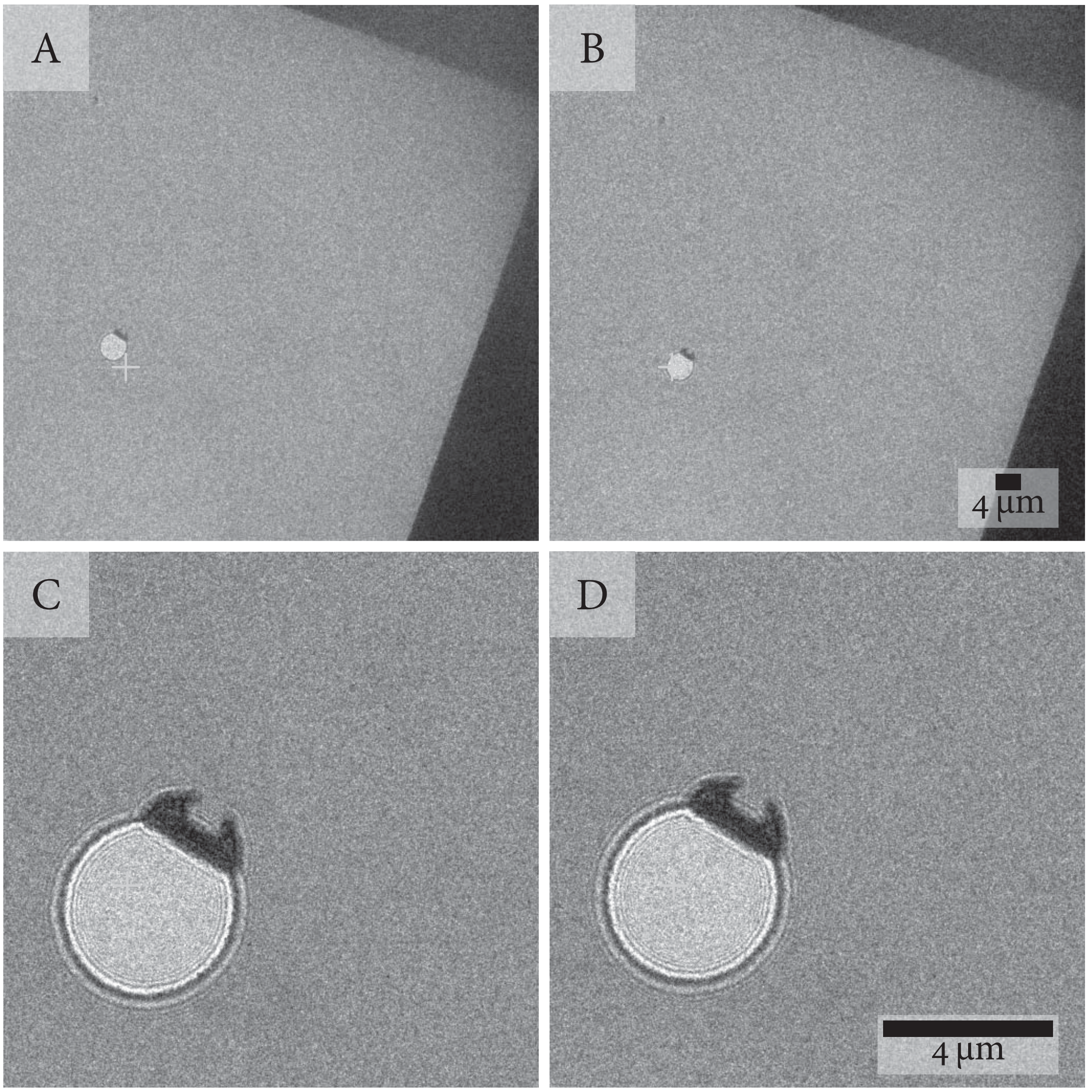

Figure 3.29: Multi-scale alignment of a Zernike film phase plate using the defocused-condenser method. The centre of the optical axis at target magnification is indicated by (+). Imaging parameters:
(**A–B**) illuminated area 28 µm, beam convergence 0.01993, magnification 6500 ×. Solid black features in the right image corners stem from the copper mesh supporting the phase plate film material
(**C–D**) illuminated area 3.953 µm, beam convergence 0.01993, magnification 15 000 ×.
Due to a FIB error, the former content of the hole did not lift off properly and is still attached to the phase plate hole perimeter.

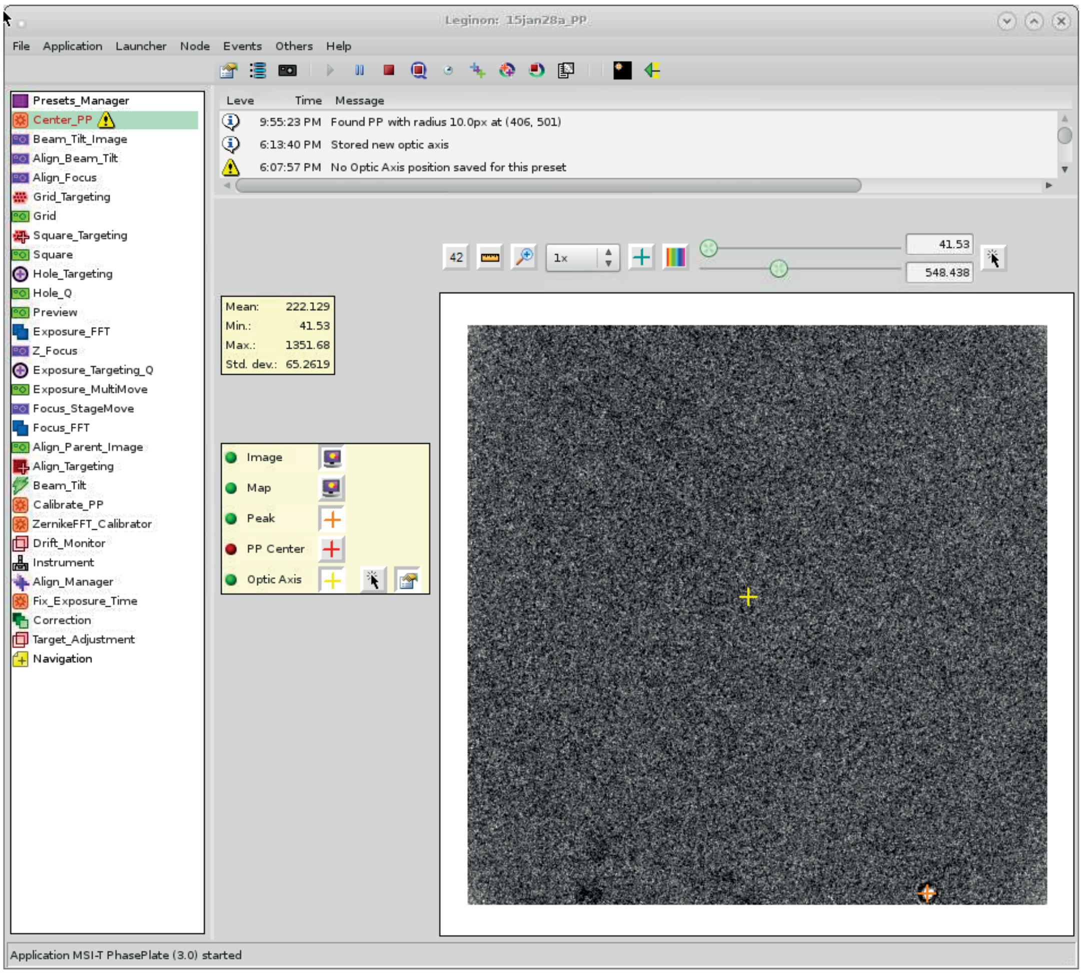

Figure 3.30: Screenshot of Leginon with opened automated alignment node using the defocused-condenser method. The actual phase plate position found by image processing (+) needs to be corrected to coincide with the optical axis position (+).

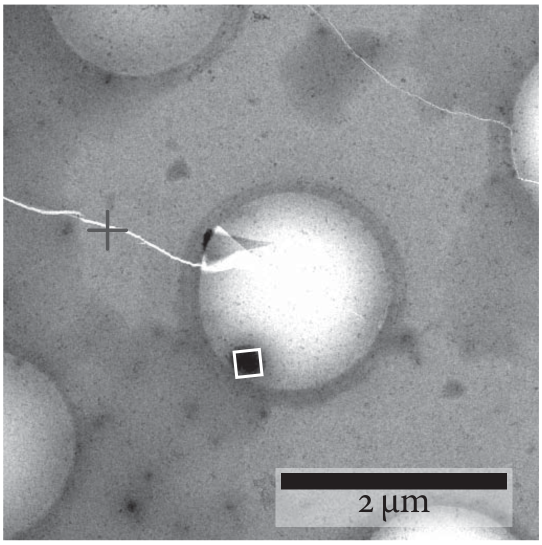

Figure 3.31: Focusing and phase plate alignment for the area of interest (white square) is done at an offset position (+). Images of the area of interest at target resolution can be seen in figures 6.7 and 6.8.

illumination used for focusing is limited to a circular area with i. e. 1.3 µm diameter around the focusing position.

For focusing-purpose, a structure with high contrast qualified to be recognized in a correlation is required. Often, the signal from amorphous-carbon film is sufficient to serve this purpose, but if low-dose and resulting low signal-to-noise ratios are used, it is better to have a distinct feature, such as gold nanoparticles, film edges or contamination spots present at the focusing position.

Phase plate alignment with the defocused condenser method just requires sufficient signal from the phase plate, as described in section 3.5.1. If an alignment in the Fourier-domain is required, the focusing position should be free from artefacts and localized features, as this impedes the performance of the phase-plate-finding algorithm. Figure 3.32 shows an image acquired at the final exposure setting, but still at the offset position, with an amorphous-carbon background. Its main purpose is to check the alignment quality, as the electron-scattering in the vitrified water ice is negligible, which results in low contrast in the corresponding diffractograms [57]. If the phase plate alignment proves to be reliable, this step should be omitted to save time and dose on the phase plate.

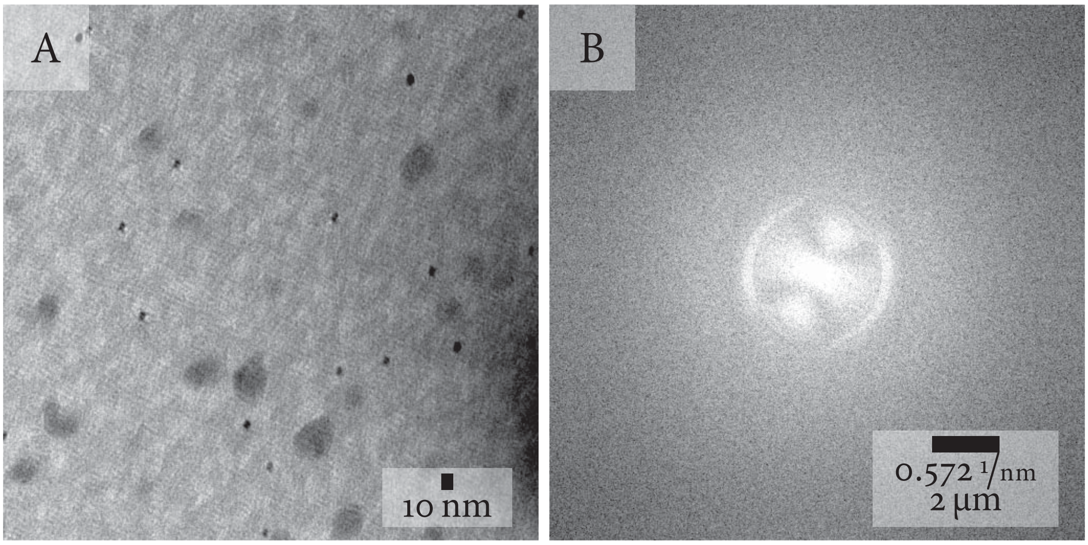

Figure 3.32: Multi-scale phase plate alignment in Fourier-domain. Image at alignment position in (**A**), corresponding Fourier transform in (**B**) shows acceptable alignment. Imaging parameters:
(**A–B**) illuminated area 1.2 µm, beam convergence 0.0104, magnification 64 000 ×.
Note the effects of some parasitic charge on the phase plate, which introduces a modulation within the phase plate hole.

3.6.3 *Timing*

One of the goals of automated electron microscopy is taking as many images as possible in a given time frame, and enabling a better use of an expensive instrument e. g. by permanently running it. The current naive implementation of the alignment procedure takes a lot of additional time, which drastically decreases the throughput compared to standard automated microscopy. It may be possible to omit some of the steps in the multi-scale alignment approach, if the robustness of the phase plate finding algorithm is further increased and some peculiarities of the motors can be cured[4].

Depending on the time needed for mechanically translating the phase plate, bringing the microscope in another preset configuration, obeying wait times to stabilize the lens currents and waiting for the camera to expose an image, the time needed for each multi scale alignment step varies. The timings from one automated phase-contrast imaging session with slightly more than 200 individual alignment procedures have been measured. The results are presented in figure 3.33.

The first data point is the time the machine needs to insert the phase plate after having performed the focusing routine. This usually takes the longest time, as the motors need to travel a rather long distance from the position of the center of the objective aperture to the phase plate position, which is typically about 3 mm. At maximal speed, the KonTEM drive is able to move with a velocity of about 1 mm/s, but upon approaching the target coordinates, the closed-loop positioning algorithm reduces the speed.

The first two alignment steps use a preset resulting in a small phase plate magnification, as shown in figure 3.30 (**A–B**).

In between the second and the third step, the preset is changed to a higher phase plate magnification (cf. figure3.30 (**C–D**)), which takes several seconds. The phase plate is mechanically translated in between the first and the fourth steps. In the final step, the preset used for imaging the specimen is sent to the microscope, and the remaining positioning-error is accounted for by a small adjustment to the illumination tilt, with a magnitude usually smaller than 0.1 mrad. In each iteration, the time spent for automated phase plate alignment sums up to about two minutes.

---

4 The current implementation takes about the same time to travel a distance of 3 mm as to travel a couple of μm. Furthermore, there are some non-linearities in the motions present, which make a check at the same preset necessary.

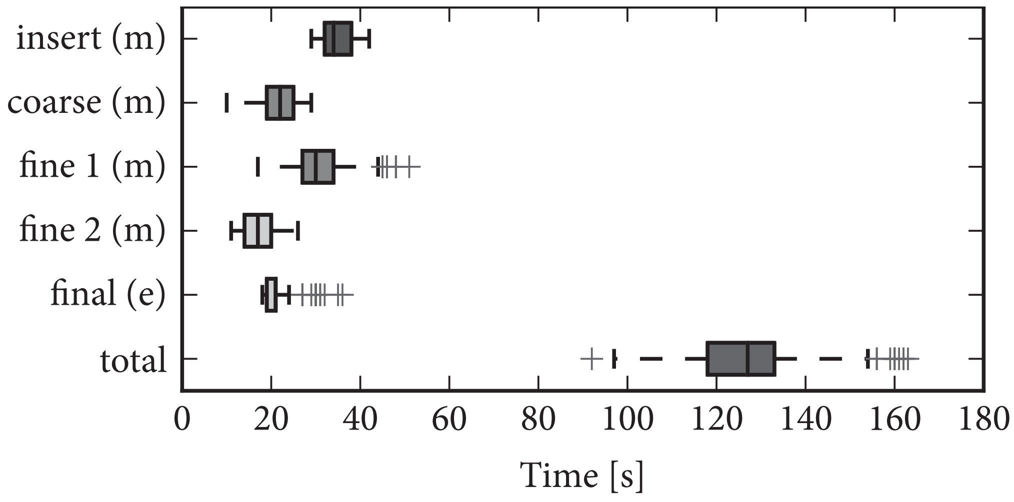

Figure 3.33: Timing of automated phase plate centring, including times for changing the microscope settings, additional wait times to stabilize electron-optical elements and camera exposure times. The first four steps correspond to the images shown in figure 3.30. Mechanical movements are indicated by (m), changes to the optical axis by using the illumination tilt deflectors by (e).

If the second iteration of each preset can be saved, and the final check is omitted, the alignment time could probably be reduced to about 80 s, with a further improvement possible by modifying the closed-loop positioning routine of the KonTEM device.

For generating a self-aligning Volta phase plate (cf. section 2.5.2), a charge of about 50 nC is needed [16], which takes about 30 s at the illumination conditions used for the final exposure of the discussed automated alignment session. Some more time needs to be accounted for translating the aperture drive, which may take another 30 s. Therefore, the self-aligning phase plates may not only have an advantage in attainable image quality, but also in the achievable throughput.

4 RESULTS WITH ELECTROSTATIC PHASE PLATES

In this chapter, the results for application of electrostatic Zach phase plates are presented, which were all manufactured by Simon Hettler/KIT [39]. Using a Zeiss 923 microscope with standard optics, the principal function and applicability of the electrostatic phase plates are verified. The properties of the optical system are found to limit the achievable image quality, most importantly the large obstructions of the electron-obstructing phase plate structure. To remedy this problem, the phase plates are physically inserted in the magnified diffraction plane of a Zeiss Libra 200 MC CRYO DMU, short KRONOS. *The effects of the optical system on the quality of the attainable images are discussed.*

4.1 RESULTS WITH ZEISS 923

The Zeiss 923 features standard electron-optics with a FEG, a three-lens condenser system, a Riecke-Ruska type condenser-objective lens with a focal length of 3.7 mm, a projective and an imaging energy-filter. The phase plates are applied to the first diffraction plane, directly below the objective lens and in the vicinity of an anticontaminator, i. e. a metal surface cooled to liquid-nitrogen temperature for improving the local vacuum conditions. The instrument is used with an acceleration voltage of 200 kV.

4.1.1 *Characterisation of Zach Phase Plates*

For verification of the phase-shifting property of an electrostatic phase plate, an amorphous specimen is inserted in the microscope object plane, and the phase plate electrode is aligned to the zero-order beam using the mechanical translation of the Kleindiek micromanipulator. To monitor the current position of the phase plate, the methods described in section 3.4 can be used.

With coincidence of back focal and phase plate plane verified in diffraction mode, the convergence angle of the illumination is adjusted to be parallel. In diffractograms of an amorphous sample, the obstructions of the electron-opaque phase plate structure are then visible in a sharp Friedel-symmetric pattern (cf. figure 4.1).

For using the phase plate, the electrode-tip needs to be aligned with respect to the zero-order beam. To visualize the phase shifting effect of an applied potential, the objective lens is defocused to introduce Thon rings in the diffractogram, which can be seen in figure 4.1. During acquisition of the voltage-series, the defocus remains fixed.

Application of a potential to the electrode changes the pCTF by introduction of an additional phase shift, as described by equation 2.4. For an applied potential corresponding to an additional phase shift of $\pi/2$ to the zero-order beam, the wave aberration function is no longer modulated by a sine, but by a cosine function. With constant defocus and a phase shift of $\pi/2$, the position of the pCTF zero-crossings are located at the same position as the pCTF maxima for the unshifted case. This can be seen in figure 4.1 (**A**) and (**E**).

For a quantitative evaluation of the phase shifting properties, the pCTF parameters φ_{pp}, Δz and A_1 can be extracted from the individual diffractograms by a suitable software such as *ctffind4* [67]. The respective results are graphically integrated in figure 4.1 and additionally visualized in a separate plot shown in figure 4.2, which reveals a quasi-linear relationship of induced phase shift and applied potential. Additionally, a small influence on the effective defocus can be seen, which has been predicted in [56] for the more localized field-distribution of a Boersch phase plate.

The rather large distance of about 2 μm from electrode-tip to zero-order beam requires a voltage of approximately 5 V to generate the necessary phase shift of $\pi/2$. This results in a large extent of the phase shifting potential distribution with a relatively small field gradient in the vicinity of the zero-order beam. The conditions are therefore unsuitable to influence low spatial frequencies, as a relative phase shift difference of $\pi/2$ between scattered and unscattered electrons is only present at large distances to the zero-order beam (cf. section 2.5.1).

A large distance to the zero-order beam reduces the influence of a localized parasitic charge on the electrode-structure. The effect of such a residual charge is visible in figure 4.1 (**C**), as it produces a small phase shift even though no external potential is applied. Another effect is the introduction of a small astigmatism, which can be seen in the elliptical shape of the pCTF zero-crossings in the diffractograms.

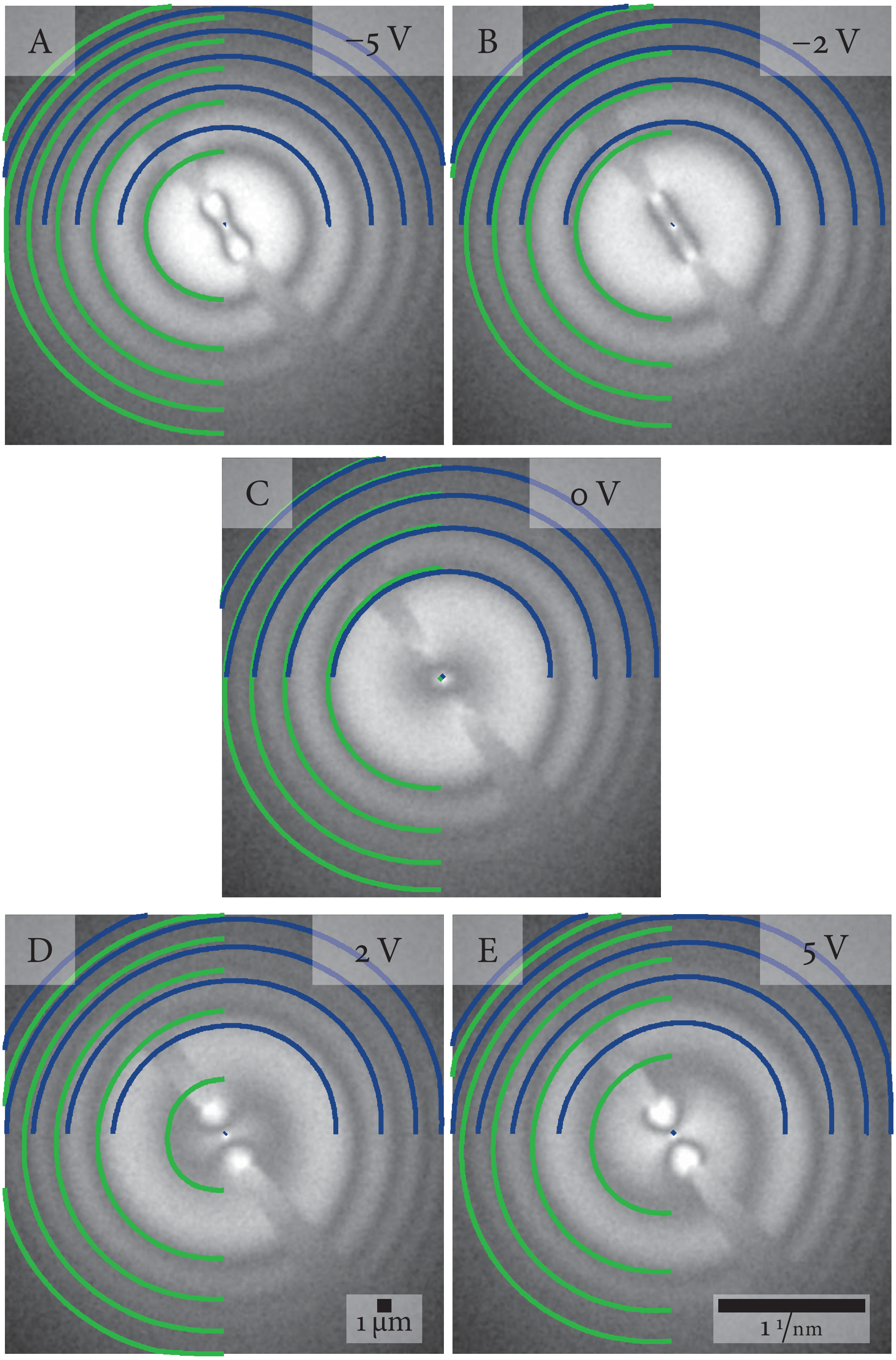

Figure 4.1: Diffractograms with inserted Zach phase plate and varied applied potential. The fitted positions of the pCTF zero-crossings are highlighted in green. The zero-crossings of the corresponding calculated pCTF with the additional phase shift set to 0 is shown in blue. For ±5 V, the phase shift is approximately $\pm\pi/2$.

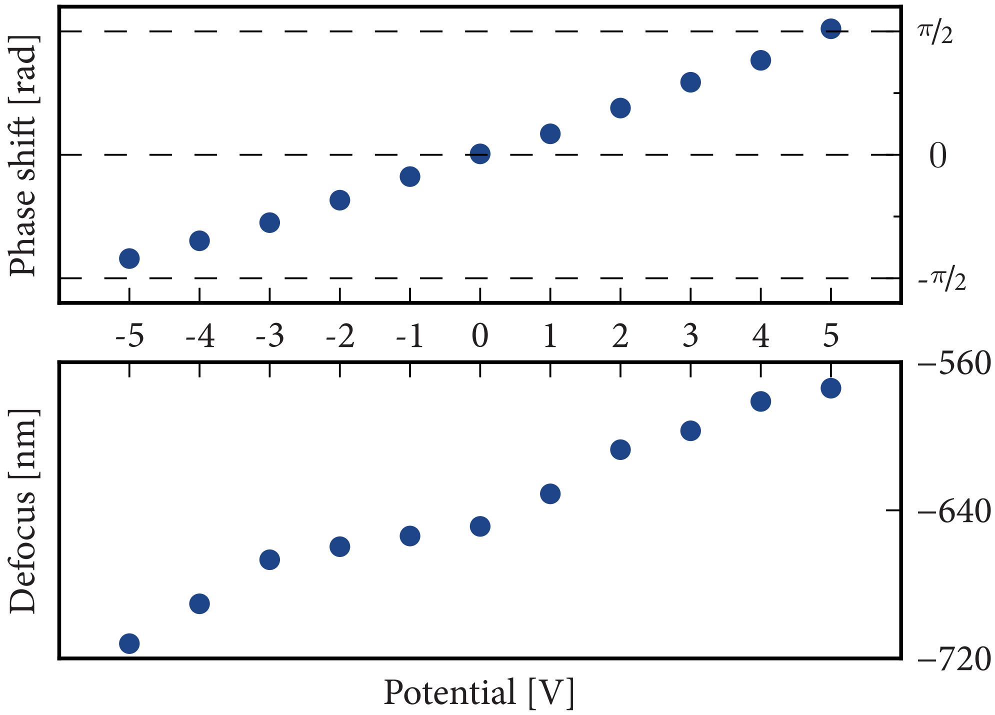

Figure 4.2: Zach phase plate characterisation at a distance of approximately 2 µm from the zero-order beam. The applied potential influences the phase shift linearly and has also a small effect on the defocus.

4.1.2 *Contrast Transfer of Low Spatial Frequencies*

If the phase plate is operated with a lower voltage, the resulting phase shifting field is more confined, and the electrode-tip needs to be positioned closer to the zero-order beam to impose the necessary phase shift of $\pi/2$. At the same time, the effective cut-on is reduced due to the larger gradient of the potential distribution around the zero-order beam.

Successful application to a filamentous biological specimen could be demonstrated, as shown in [32] and figure 4.3. The filaments have a diameter of 10–15 nm, resulting in the presence of the corresponding structure factors with low spatial frequencies in the direction perpendicular to the filament orientation.

By varying the sign of the applied potential, positive and negative phase contrast conditions can be established. The specific distribution of the main structure factors of elongated filaments allows the observation of multiple origins of the generated contrast: Only the filaments oriented

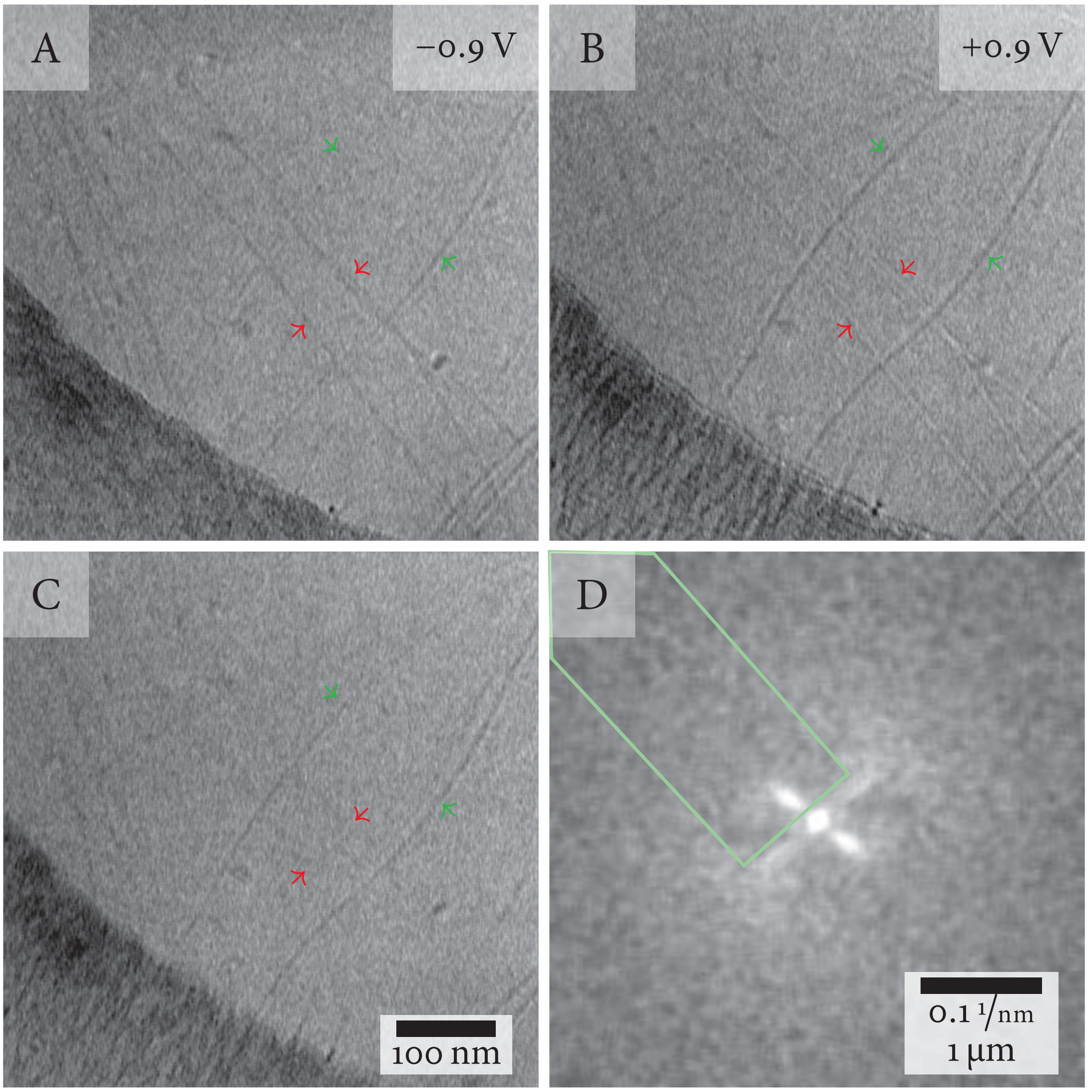

Figure 4.3: Application of a Zach phase plate on a filamentous actin specimen. Depending on the sign of the phase shift, positive (**A**) and negative (**B**) phase contrast can be achieved. The image without applied potential (**C**) still shows phase contrast transfer due to single-sideband contrast, which influences filaments oriented parallel (→) and perpendicular (→) to the phase plate electrode differently. A periodogram in (**D**) shows the Friedel-symmetric phase plate tip very close to the zero-order beam. Images courtesy of Nicole Frindt/CryoEM.

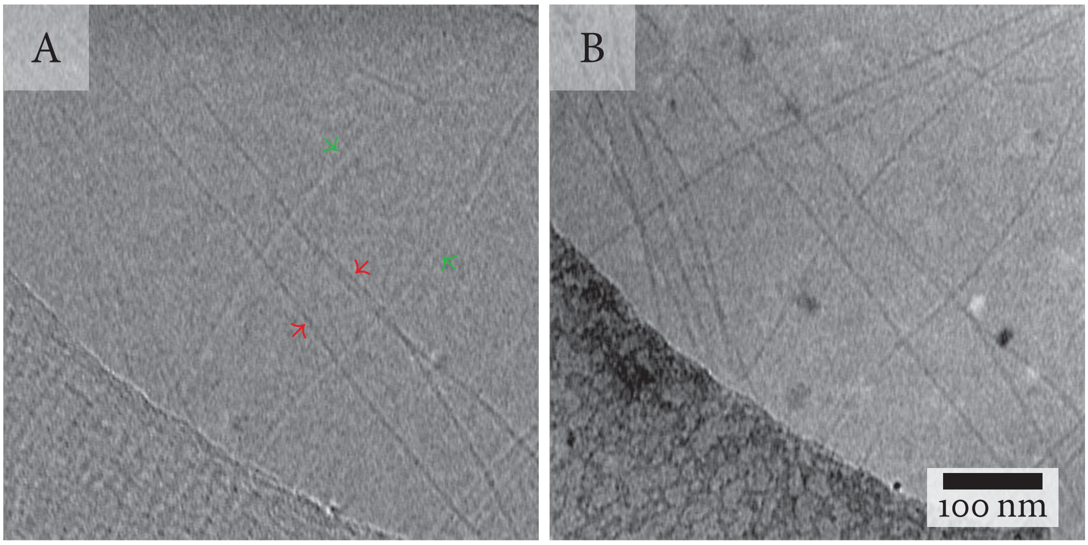

Figure 4.4: The difference image of positive and negative phase contrast images in (**A**) suppresses the parts, which have been transferred regardless of the applied potential. In contrast to the image without applied potential in figure 4.3 (**C**), the signal from the filaments parallel to the electrode orientation is present. A defocused image with retracted phase plate is shown in (**B**). Note the apparent image shift due to a tilted illumination. Images courtesy of Nicole Frindt/CryoEM.

parallel to the phase plate electrode show the corresponding contrast modulation. Without an applied potential, but with the electrode still at the same position, the resulting image shows phase contrast due to the obstruction of one of the Friedel pairs corresponding to the structure factors of the filaments oriented perpendicular to the electrode orientation.

The contribution from positive and negative phase contrast can be highlighted by subtracting the negative phase contrast image from the positive one, which suppresses the contributions equally present in both images, i. e. stemming from single-sideband contrast. The filaments oriented parallel to the electrode orientation show a signal which means the contrast is produced by the potential application. This can be seen in figure 4.4 along with a defocused view of the sample area with removed phase plate, which shows regular positive phase contrast.

4.1.3 *Considerations for Improvement*

To reduce the influence of the electron-obstructing structure on the contrast, the electrode would need to be further miniaturized. The realized size of about 1 µm at the electrode tip is already close to the manufacturable limit. As detailed in section 2.5.1, there are in principle two more possibilities to attain an optical miniaturisation of the phase plate structure: Choosing a longer wavelength by a smaller acceleration voltage or using a longer effective focal length. For the latter, the DMU in the Zeiss Kronos has been designed, which provides a 3.2 × magnified diffraction plane. This results in an effective focal length of about 15 mm, which is about four times larger than the conditions in the Zeiss 923.

4.2 RESULTS WITH ZEISS KRONOS

As member of the model line succeeding the Zeiss 923, the Zeiss Kronos features the same principal electron-optical components with the notable addition of a monochromator in the electron-source, the integration of a C_S-corrector and a DMU. The overall quality of the electron-optical set-up is improved by provisioning for more components enabling a better electron-optical alignment. Furthermore, the design of many elements has been revised, so that the microscope offers a better electrical and mechanical stability. For phase plate experiments, the instrument is used with an acceleration voltage of 200 kV.

Due to the magnified environment, the aperture of the Zach phase plate needs to be scaled as well in order to not obstruct electrons scattered into high angles. The dimensions of the electrode tip should not be scaled to benefit from the relative miniaturisation.

At first, phase plates with scaled structures were not available and preliminary tests using the available phase plates designed for the Zeiss 923 were performed. This can be seen in the diffractograms of figure 4.5, in which a significant proportion of the higher spatial frequencies is obstructed by the aperture. Since phase plates are primarily applied to improve the contrast transfer of low spatial frequencies, the small phase plates can still be used for a performance evaluation.

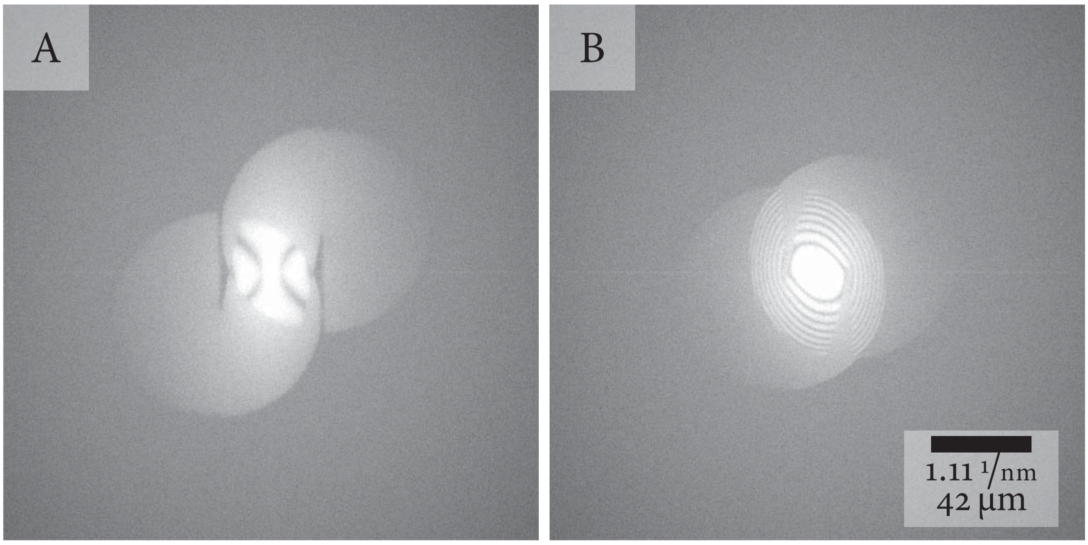

Figure 4.5: Small Zach phase plate designed for the Zeiss 923 in the magnified diffraction plane of the Kronos. Even with the zero-order beam far from the phase plate tip, apparent signs of charging are present in the close-to-focus (**A**) and defocused image (**B**).

4.2.1 *Application of Zach Phase Plates in the DMU*

First experiments immediately revealed much stronger distortions compared to the experience from the Zeiss 923. Phase plates well usable in the Zeiss 923 proved to be unsuitable for the Kronos instrument, as signs of charging were present even at large distances of the electrode to the zero-order beam. This can be seen in figure 4.5.

Several ineffective methods for improving the charging behaviour were tried, such as application of a plasma cleaner prior to installing the phase plate into the microscope and minimizing the phase plate exposure to ambient atmosphere in between the plasma cleaning and the installation step [31].

Two means proved to be effective. First, a heating device was fitted to the phase plate assembly and later directly integrated on the phase plate chip. The phase plate is permanently heated while not in use, which helps the vacuum system remove the contamination [40].

Secondly, an additional coating of the structure with amorphous-carbon and subsequent removal of the resulting short-circuit at the electrode-tip by FIB polishing proved to be beneficial [31, 32, 39]. The much better results can be seen in the left column of figure 4.6, which shows only minor

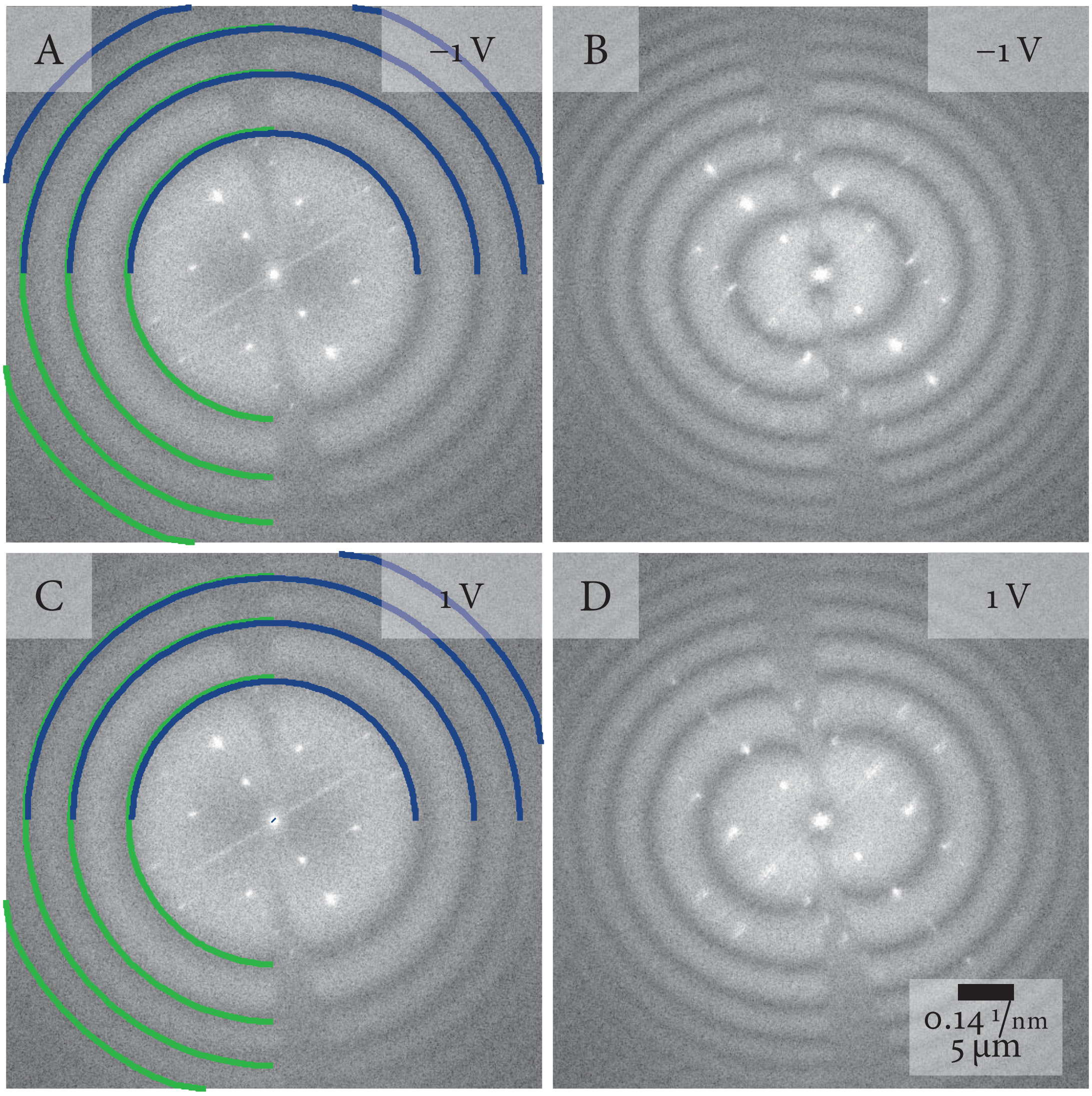

Figure 4.6: Amorphous-carbon coated Zach phase plate in the DMU. The Thon rings have a regular form in (**A**) and (**C**) at a large distance to the zero-order beam of about 4.5 µm, and are compatible with a standard pCTF model. The application of a potential has only marginal effect.
In (**B**) and (**D**), the distance is reduced to about 2.5 µm, where application of a potential has some effect, but results in an irregular distribution of the pCTF minima.

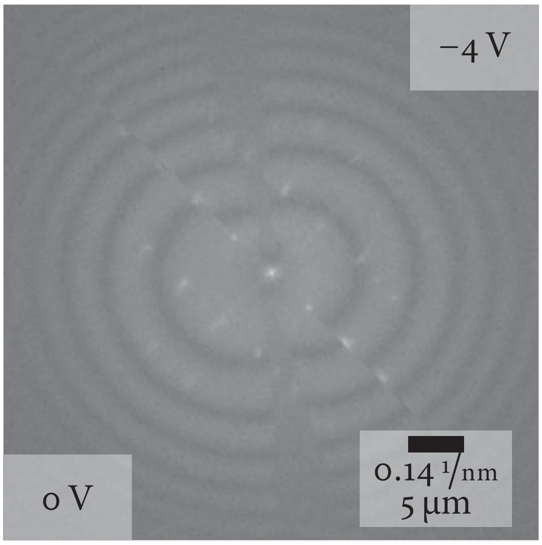

Figure 4.7: Comparing the effect of varied applied potential of 0 and −4 V using a strong defocus in an image montage. The modification from pCTF zeros to maxima and vice versa suggests a phase shift of about $\pi/2$.

distortions for a distance in between electrode and zero-order beam of about 4.5 µm.

Due to the gentle gradient in the static potential distribution, the phase shifting effect on the zero-order beam is negligible at this distance, even for applied potentials of 5 V.

The phase shifting effect can be increased by reducing the distance between electrode-tip and zero-order beam. At a distance of about 2.5 µm, the diffractograms show a significant effect on varying the magnitude of the applied potential, as can be seen in the right column of figure 4.6. Unfortunately, reducing the distance also amplifies the apparent pCTF distortions.

By application of a sufficient voltage adapted to the distance in between zero-order beam and electrode, phase shifts of approximately $\pi/2$ can be achieved. This is shown in the comparing montage of diffractograms with and without applied potential in figure 4.7. At least for a few spatial frequencies, the pCTF zeros of the former coincide with the positions of the pCTF maxima of the latter, similar to the situation in figure 4.1 (**A**) and (**E**).

A possible remedy for the problem has been described in [31], which involves positioning the phase plate at an uncritical distance similar to the one shown in figure 4.6 (**A**) and (**C**), as well as changing the phase plate electrode geometry to apply a more extended field of higher magnitude.

Although this may hide the effects of the charging problem, it broadens the area with soft cut-on (cf. section 2.5.1). This impedes the transfer of low spatial frequencies, which in turn contradicts the design goal of the DMU. Therefore, for full usability of the Zach phase plate in the DMU, a solution to the distortion problem has to be found.

4.2.2 *Analysis of the Problem*

In the DMU, the Zach phase plates are applied in a prototype instrument with complicated optics, which employ not only round lenses, but also hexapoles used in the C_s corrector. As the shadow-image of the opaque phase plate aperture is reproduced with the expected shape in the diffractograms, the general existence of regular imaging capabilities of the optical system can be assumed. However, to rule out the possibility of a distortion in the phase plate plane, which is corrected by another electron-optical element in the system, the properties of the beam in the phase plate plane need to be characterized.

Analysis of intermediate beam conditions in a transmission electron microscope column is challenging, as the image is influenced by all elements present in the beam path from the electron-source to the fluorescent screen or camera. Direct and undistorted probing of a problematic electron-optical element is normally impossible.

Shape and Diameter of the Zero-Order Beam

However, the diffraction plane in the DMU is physically accessible and phase plates or apertures with defined shapes can be inserted. Intense electron-exposure usually alters the optical properties of the film material of a Zernike phase plate, due to introduction of a static charge or the adsorption of contamination particles sourced from the vacuum [27, 20].

Using similar illumination conditions as for evaluating the Zach phase plate in the last section, the astigmatism of the zero-order beam in the phase plate plane can be visualized by the appearance of the round phase plate hole (cf. figure 3.4.2). Then, the beam is stigmated, focused in the phase plate plane and aligned to the Zernike phase plate hole. Subsequent mechanical translation of the phase plate film with flood-beam illumination results in the elongated patterns shown in figure 4.8. The round shapes are generated by resting the zero-order beam on the film surface for a short time.

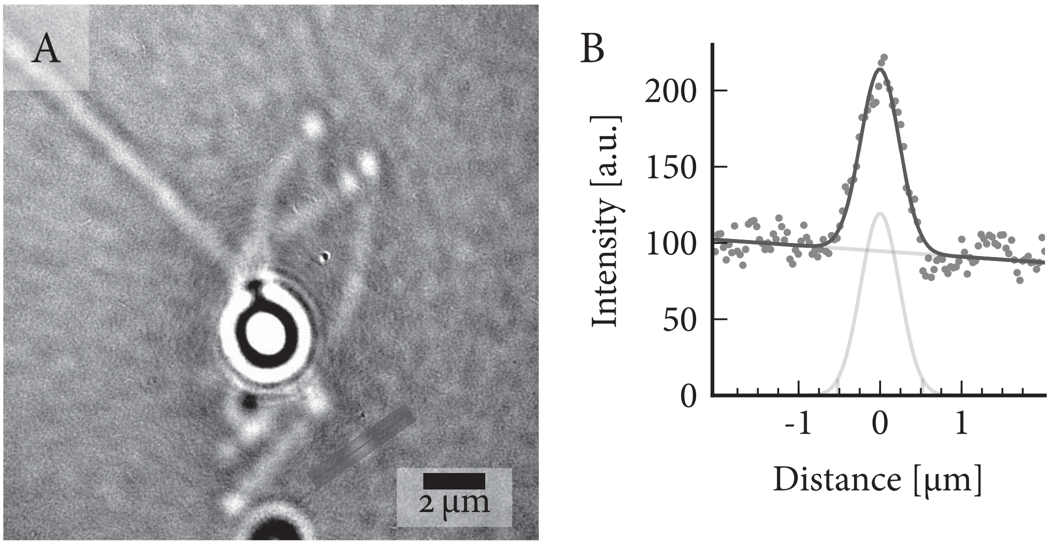

Figure 4.8: Determination of minimal zero-order beam diameter in the magnified diffraction plane. A Zernike phase plate film is used as a surface for imprinting the beam, as well as length calibration and assessment of on-plane condition. Raw image in (**A**), line scan data and fit in (**B**).

Too strong electron-exposure results in a distorted signal, as the phase shift imprinted on the film material exceeds π and reverses the contrast impression. For data collection, a round shape with an undistorted signal is therefore chosen, as highlighted in figure 4.8. The data is extracted in a line scan which is then subjected to a fit procedure with the sum of a Gaussian and a linear term used as the model function.

The Gaussian distribution has a full width at tenth maximum of about 1 µm, which should correspond to the minimal diameter of the zero-order beam in the magnified diffraction plane. Some uncertainty of this rather large value exists, since the length calibration is done using the phase plate hole diameter as a reference, which is hard to determine due to the highly defocused imaging conditions.

A similar value of 0.75 µm for the zero-order beam diameter has been found for the Zeiss 923 [77], where the phase plates do not show such detrimentally distorted figures. Therefore, the size and shape of the zero-order beam does not seem to be the crucial factor for the distortion problem.

Character of the Distortion

All Zach phase plates inserted into the magnified diffraction plane showed a similar characteristic distortion which can be seen in the diffractograms

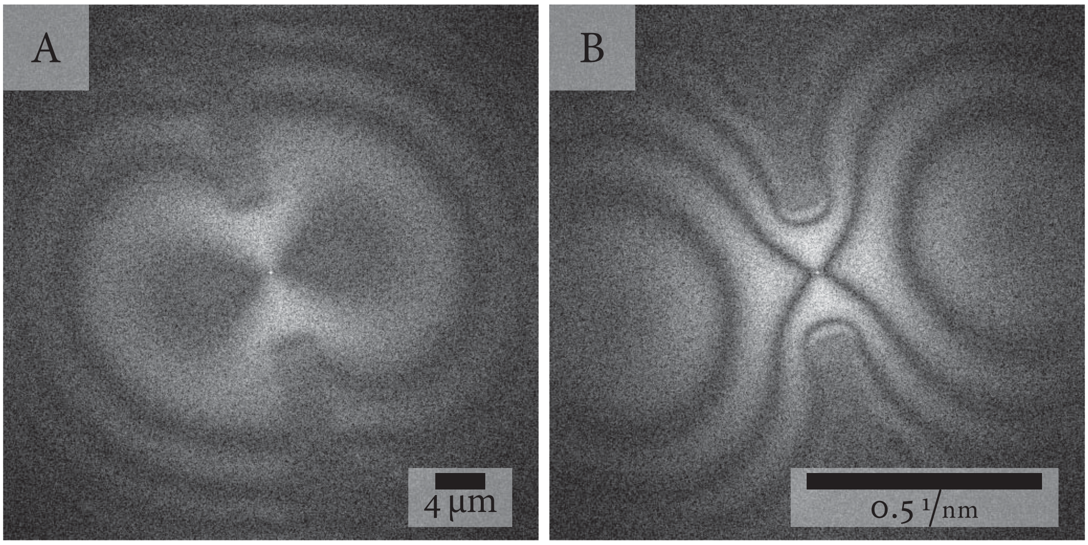

Figure 4.9: Example of typical artifacts due to a charged phase plate in the magnified diffraction plane. Upon changing the focus conditions from defocused (**A**) to close-to-focus (**B**), the pattern of the pCTF zeros changes from a rather round distribution to a distinct symmetric shape.

shown in figure 4.9. The pattern shows a dependence on the tunable lens aberrations, such as defocus and twofold astigmatism. While round shapes of the figure can be attained for large values of Δz, the figure reduces to a distinct symmetric shape for small defocus, shown in figure 4.9 (**B**). As a change to the defocus in either direction results in the same change to the pattern, this value is believed to approximate in-focus conditions.

This particular shape can be approximated in a simulation for vanishing defocus and certain combinations of the lens aberrations C_s and A_1, as shown in figure 4.10.

However, the scale on which the shapes are produced differs from that of the observed shapes with an applied phase plate. For instance, to generate a similar pattern with the same imaging conditions as used for the observed pattern, a huge spherical aberration coefficient of 2 m and a large value for the twofold astigmatism are required. The actual magnitude of C_s is more likely in the range of a few µm. For such values, the shape can only be reproduced using much higher magnifications. Therefore, the source causing the distortions has to be stronger than the influence of C_s on the low spatial frequencies.

During application of Zach phase plates with the Zeiss 923, often small adjustments of the twofold astigmatism are necessary. It is well possi-

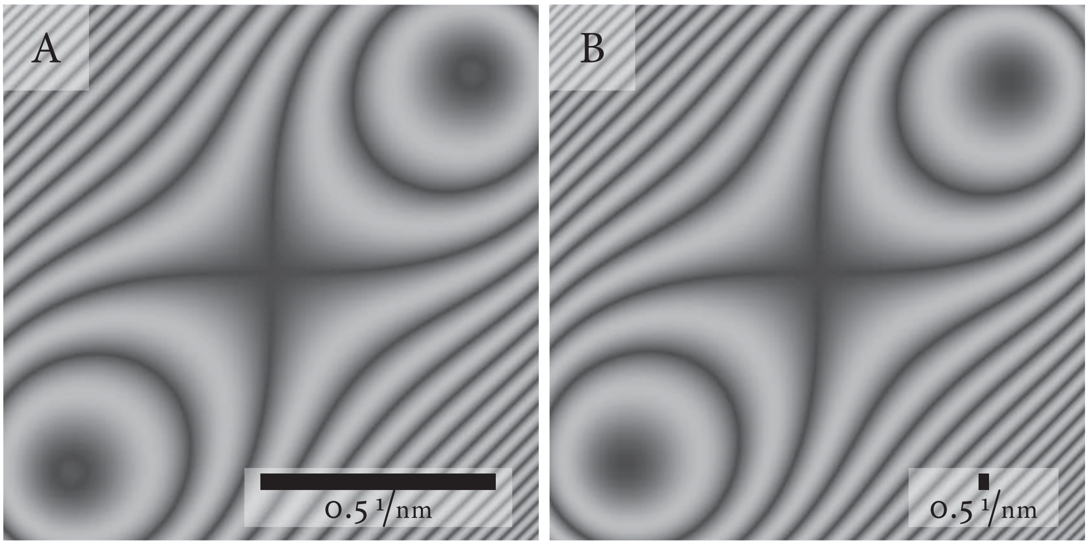

Figure 4.10: Attempt to reproduce the characteristic pattern from figure 4.9 with a calculated pCTF pattern. By keeping $\Delta z = 0$ and varying C_s and twofold astigmatism A_1, shapes similar to the ones in figure 4.9 can be generated. Used parameters for C_s and A_1:
(**A**): 2 m and 4.5 µm, same pixel size, dimensions and electron-wavelength as in figure 4.9.
(**B**): 10 µm and 10 nm.

ble that the scale the distortions work on with the shorter focal length conditions approximately match the effect of the twofold astigmatism aberration, which is correctable with a stigmator. Therefore, correction of the distortion effect might be possible using a shorter focal length.

The KRONOS microscope also features a regular diffraction plane directly after the objective lens, with a standard aperture drive and several objective apertures. Attempts to insert the phase plate motor in the first diffraction plane were hindered by the design of the anticontaminator, which features only two openings for specimen and objective aperture insertion. In principle, the phase plate could be integrated by replacing the standard objective aperture drive. However, the objective apertures are thermally coupled with the anticontaminator. This connection can be disassembled, but hardly reassembled on-site (personal communication Dmitry Kolmykov/Zeiss). For not impeding regular microscope use, this potentially harmful operation was not attempted.

4.2.3 *Attempts at Problem Mitigation*

Alignment Optimisation

During the characterisation of the imaging-properties of the DMU, several flaws in the electron-optical alignment of the microscope were discovered. The most prominent effect was the induced tilt by changing the convergence angle of the illumination. Since the long effective focal length of the microscope amplifies small deviations from perfect alignment, the error margin is reduced compared to standard instruments. At first, it could not be ruled out that a crooked beam path through the DMU lens is the reason for the distortions, e. g. by using the marginal parts of the lens. Therefore, some efforts towards alignment improvement were undertaken.

Fortunately, the laboratory enjoyed good support from the microscope manufacturer, especially by Dmitry Kolmykov, who succeeded in attaining an electron-optical alignment, which allowed changing any lens current in between electron gun and magnified diffraction plane without inducing a severe tilt. This was only possible by manually tuning the deflectors in the C_s-corrector and by adjusting the physical position of the corrector relative to the DMU by several mm.

The efforts to improve the general electron-optical alignment did not show any effect on the distortions. Therefore, it was concluded that a residual trapped charge on the phase plate is mainly responsible for the pronounced distortions, which appear much more severe due to the magnified environment.

In-Situ Plasma Cleaning

Since carbon coating and subsequent polishing of the tip electrode did not result in a sufficient suppression of the charging effects, it was tried to actually remove the contamination from the phase plate. For this purpose, an ibss GV10x downstream asher was fitted to the DMU for in-situ plasma cleaning. The effects of the first tests using an Argon-Oxygen gas mix are shown in figure 4.11.

Due to the lack of a lead shielding for the plasma cleaner, it was removed from the microscope column after the cleaning session to acquire the image in figure 4.11 (**B**). Therein, the phase plate seems to be reduced in size, which is attributed to a removed amorphous-carbon coating. However, the irregularities on the phase plate surface are virtually unchanged. For the acquisition of this image the vacuum had to be broken to remove the plasma cleaning device. This exposes the phase plate to a nitrogen atmosphere at ambient pressure.

To rule out a contamination occurring during removal of the plasma cleaner, the experiment was repeated and image (**C**) could be acquired after an additional plasma cleaning attempt without breaking the vacuum[1]. As this did not show any significant improvement, a much longer plasma cleaning session was attempted. The results of 40 h of plasma cleaning using ambient air are shown in figure 4.12. The imaged phase plate is the sister phase plate located on the same phase plate chip, which showed a less structured surface. Suitable non-parallel illumination conditions are chosen to highlight certain features on the phase plate surface, which are attributed to charge centres.

A noticeable effect after the application of the plasma cleaning device was a persistent change of the terminal pressure attained by the turbo molecular pump improving from about 4.35×10^{-7} mbar to about 3.75×10^{-7} mbar, as measured with the microscope pressure sensors. Although a small cleaning effect on the tip of the phase plate is visible, the apparent charging effects of the phase plate were not improved by the procedure. In fact, the effect of removing the amorphous-carbon coating is not beneficial at all, as the formerly passivated contamination spots on the surface re-emerge.

1 With the permission of the X-ray Safety Officer. Even without a lead shield, the X-ray dose rate did not appear to be different from the background radiation level.

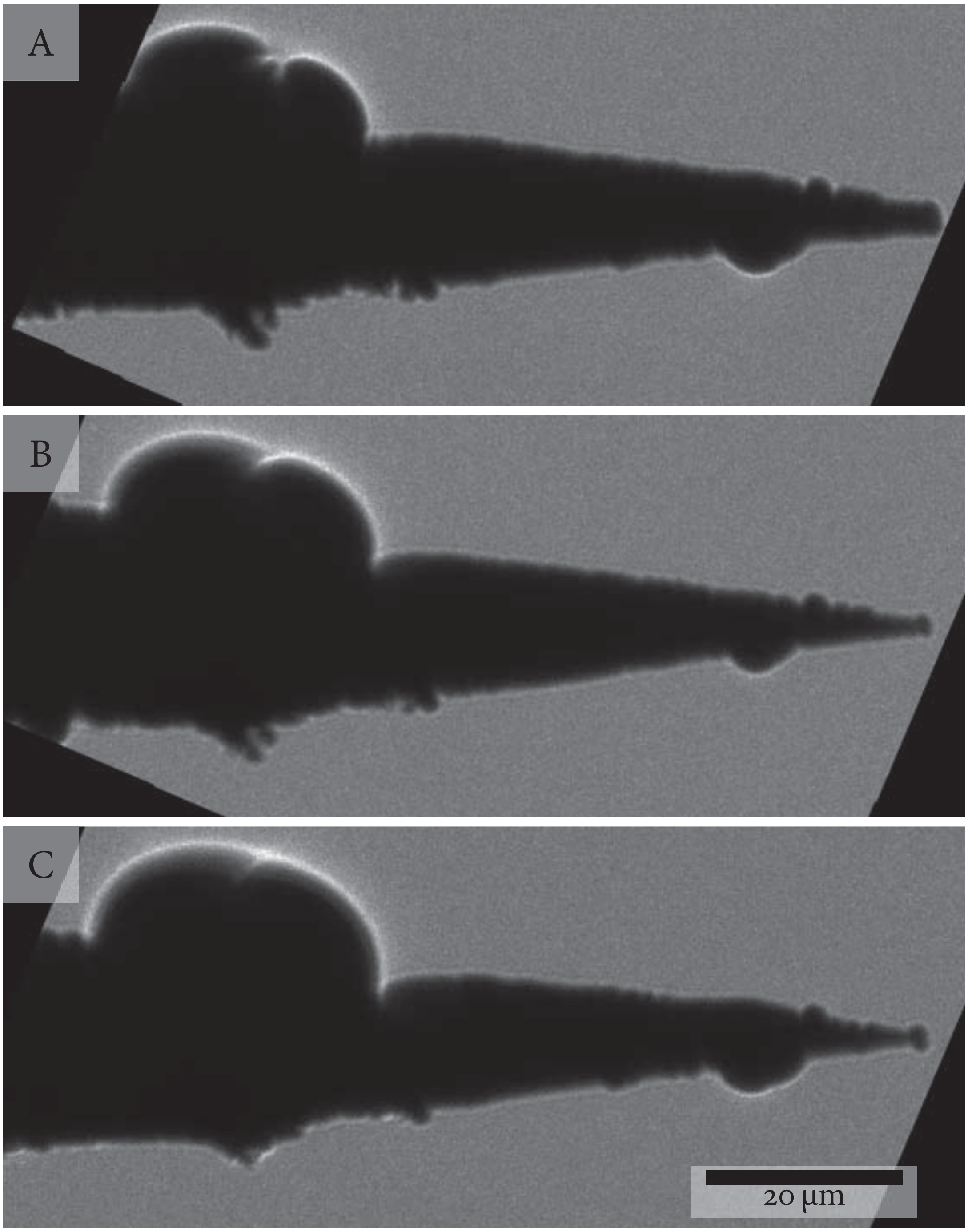

Figure 4.11: First attempt at in-situ plasma cleaning. The state before plasma cleaning (**A**) shows thick amorphous-carbon coating. After application of 1.5 h of plasma cleaning using an RF power of 70 W and an Argon-Oxygen mix as process gas, the carbon coating is virtually removed (**B**). In (**C**), the state after additional 2.5 h of plasma cleaning using a Nitrogen-Oxygen gas mix does not show a significant change.

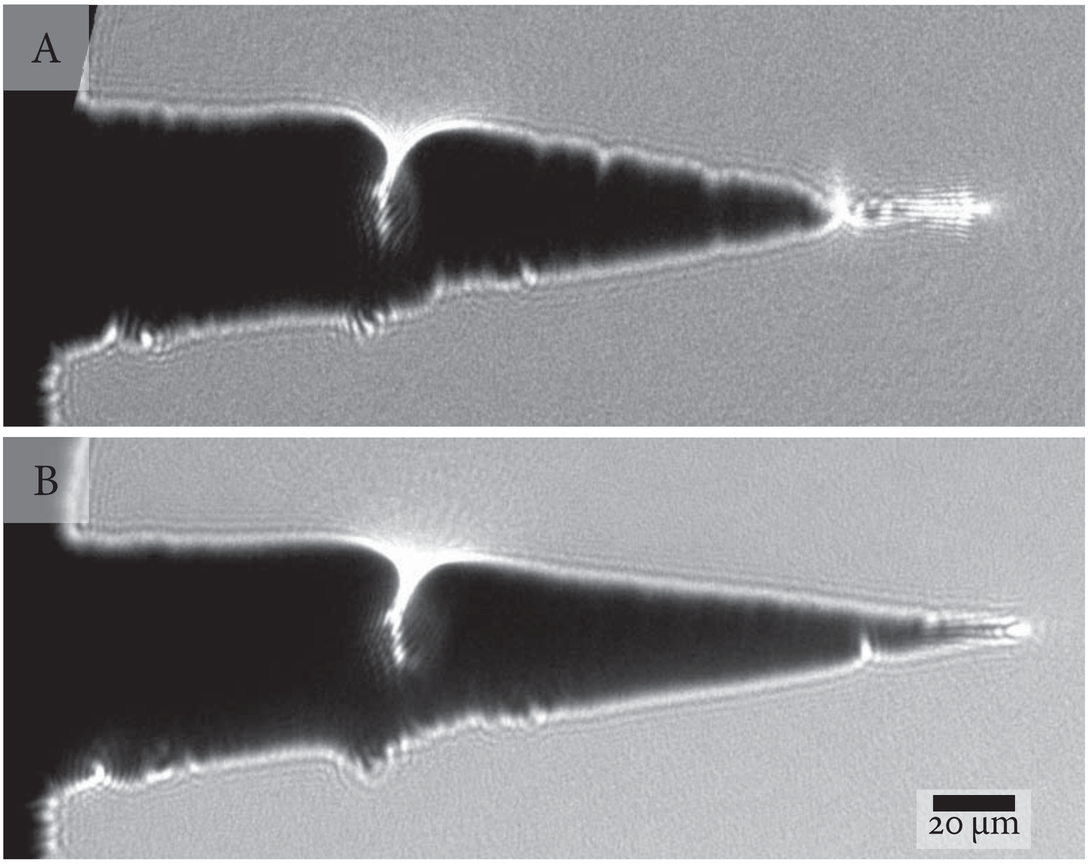

Figure 4.12: Comparison of the appearance of the phase plate electrode in the magnified diffraction plane using non-parallel illumination to highlight the charged parts of the phase plate. The initial image (**A**) shows distortions concentrated at the phase plate tip, which can be reduced by the application of an in-situ plasma cleaning device for 40 h using ambient atmosphere as process gas (**B**). An LM view of this phase plate can be seen in figure 3.16.

The results are in accordance to the findings reported in [82], where a similar approach was attempted with a Boersch phase plate in the PACEM microscope.

4.2.4 *Further Possibilities to Remedy the Charging Problem*

The effects of an exposure of the electrode to accelerated electrons were studied using simulation techniques reported in [82]: The primary 200 keV electrons were found to be energetic enough to penetrate the electrode-material. They are well capable of creating scattering events below the shielding electrode and can therefore produce secondary electrons in the insulating material which cannot be compensated due to the low electron-mobility within the material.

A possible remedy is increasing the distance from the trapped charge to the tip of the electrode by partially removing the insulator. This has been attempted in [82] by employing back-etching techniques which resulted in the removal of the insulator for about 500 nm.

The method did show some beneficial effect, but was ultimately not capable to provide a solution to the charging problem. As the effects of a charge present on the electrode can be observed on a large length scale of at least 2 μm (cf. figure 4.1), it should be investigated, whether a more extreme patterning resulting in a truly free-standing electrode is able to provide a better effect.

As the amorphous-carbon coating proved to be very effective, further attempts should be directed towards optimizing this technique. Polishing of the electrode tip should be performed using a helium FIB to avoid implanting gallium ions in the insulator.

Furthermore, the phase plate manufacturing should be reviewed with regard to the possibility of reducing the surface roughness and presence of pockets (cf. figure 2.9). A possible cure of the contamination problem could be the variation of the surface material from gold to e. g. amorphous-carbon coated titanium, which showed good performance in [34]. Adaptation of this material composition to a Zach phase plate has been attempted in [39] and yielded only small distortions in the diffractograms, but this specific phase plate unfortunately failed to produce any phase shift.

The plasma cleaning device may offer an additional degree of freedom for handling of the phase plates. As in-situ plasma cleaning is able to remove the carbon coating, a thick amorphous carbon protection layer could be applied, which can then be removed in the microscope to avoid any surface contamination by the ambient atmosphere. For this, the final coating has to be applied in an evaporator capable of adding the protective coating afterwards. Additionally, after the final manufacturing steps in a helium FIB, an additional protection layer has to be applied without exposing the phase plate to ambient atmosphere, e. g. by using a vacuum transfer from the FIB to a suitable coating device.

If an oxidised surface is the main source of poor conductivity, the plasma cleaner could be used with hydrogen as process gas, which reduces the oxidations.

Generally, the attainable final pressure in the DMU is at least an order of magnitude worse compared to the conditions found with an anticontaminator. To enhance the lifetime of a Zach phase plate free from parasitic charge, the vacuum system should be upgraded accordingly.

4.3 DISCUSSION

The charging behaviour of electrostatic Zach phase plates imposes a severe limitation on their practical use. For the Kronos microscope, no working phase plate with small enough charging behaviour to be suitable for meaningful imaging could be obtained. To enable (automated) phase plate application, the charging problem has to be solved first.

Analysis of the imaging behaviour of the magnified diffraction plane did not show obvious evidence of the optical set-up to be responsible for the increased distortions. Since the magnetic field in the DMU is different to the conditions found in the vicinity of the objective lens, a contribution to the problem cannot be ruled out, though. The main effect is attributed to stem from the presence of a parasitic and static charge on the phase plate electrode, which is amplified by the magnified environment.

The examination of the behaviour of primary electrons in the insulator from [82] hint at a fundamental limitation of the use of insulating material in the vicinity of the zero-order beam.

To reduce the cut-on effects, the electrode has to be brought close to the zero-order beam. The magnifying optics of the DMU not only affect the electrons scattered by the sample, but also broaden the zero-order beam. Therefore, in order to attain low cut-on frequencies, the extent of the zero-order beam needs to be reduced, which can be done by using smaller convergence angles of the illumination. Using the available technology, this means a further reduction of the illumination intensity, which in turn puts higher demands on the mechanical stability of the system, as exposure times need to be increased accordingly.

Although better working phase plates were available for the Zeiss 923 microscope, automated application was not attempted due to the restrictions of the microscope and the available micromanipulator. As access to a less magnified diffraction plane in the KRONOS instrument was not available, and development of an effective cure for the problems unlikely, the efforts to make the electrostatic phase plates work were reduced and directed towards a new application variant Zernike film phase plates, which is presented in the following chapters.

5 THE CUT-ON PROBLEM

This chapter discusses the influence of a finite cut-on frequency of a Zernike film phase plate on the imaging process. Afterwards, a method to overcome the effects is presented and the properties of the resulting non-linear contrast formation are discussed.

5.1 SIMULATION OF CUT-ON EFFECTS

With the Zernike phase plate aligned to the zero-order beam, the effect of a finite cut-on frequency is equivalent to a high-pass filter. A lens diagram of the corresponding geometry can be seen in figure 2.12. For a discussion, the most important property of the Zernike phase plate is the hole radius and its orientation to the zero-order beam. The effects from varying these parameters can be studied in numerical simulations.

The simulation environment is based on the discrete Fourier transform, which allows to access an image representation corresponding to the conditions in the back focal plane of the objective lens. The phase plate effects are simulated by a multiplying the specimen's structure factors with the modulation by the phase plate. A subsequent inverse Fourier transform produces the modulated image wave, from which the image intensity can be calculated by taking its squared absolute value. At first, a pure phase object in the shape of a Siemens star pattern is used as a synthetic test specimen for the image simulation, as shown in figure 5.1 (**A**).

The change of the original specimen to the filtered image is shown in figure 5.1. The cut-on frequency has been chosen to be 1/8 of the Nyquist frequency, i. e. the lower 1/8 of the representable spatial frequencies are excluded from the image-formation process.

The center of the filtered test pattern appears undistorted, since it consists only of a high-frequency components that are transferred without alterations. Lower spatial frequencies are missing, and the large unmodulated regions relating to a solid and featureless bulk area of a specimen appear distorted.

The standard approach to alter the cut-on frequency for Zernike phase plates is modifying the size of the hole. Its effect can be seen in figure 5.2.

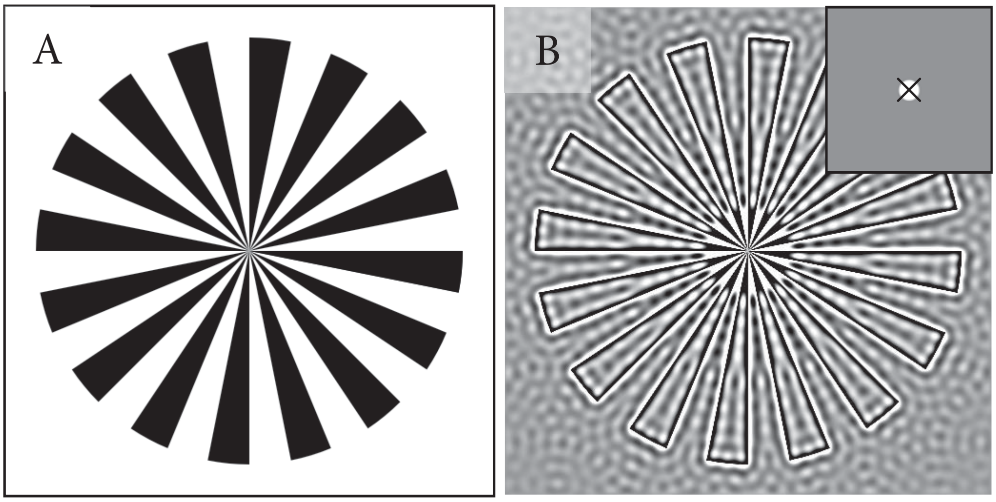

Figure 5.1: The synthetic pure phase object in the shape of a Siemens star test pattern (**A**) features a radially varying spatial frequency content. Application of a Zernike phase plate (**B**) distorts the shape, leaving only the Siemens star centre with high spatial frequency content intact.
The effective filter in Fourier-domain is depicted in the inset, with the position of the zero-order beam marked by (×). Spatial frequencies traversing the film material (gray) gain an additional phase shift of $\pi/2$ and contribute to the image formation process.

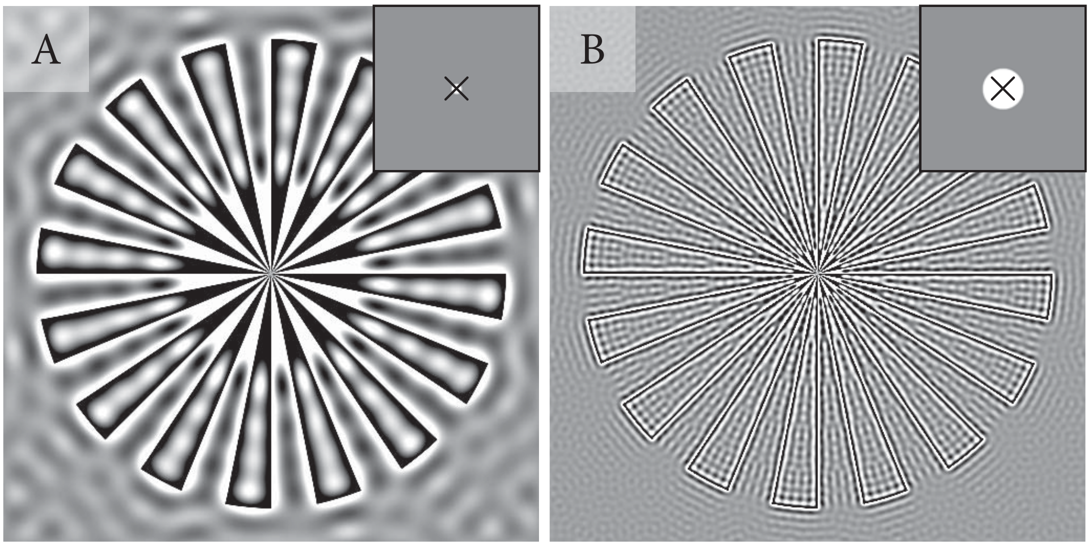

Figure 5.2: Variation of the apparent cut-on frequency from $1/16$ (**A**) to $1/4$ of the Nyquist frequency (**B**). Smaller physical distances in reciprocal space relate to larger object dimensions in direct space.

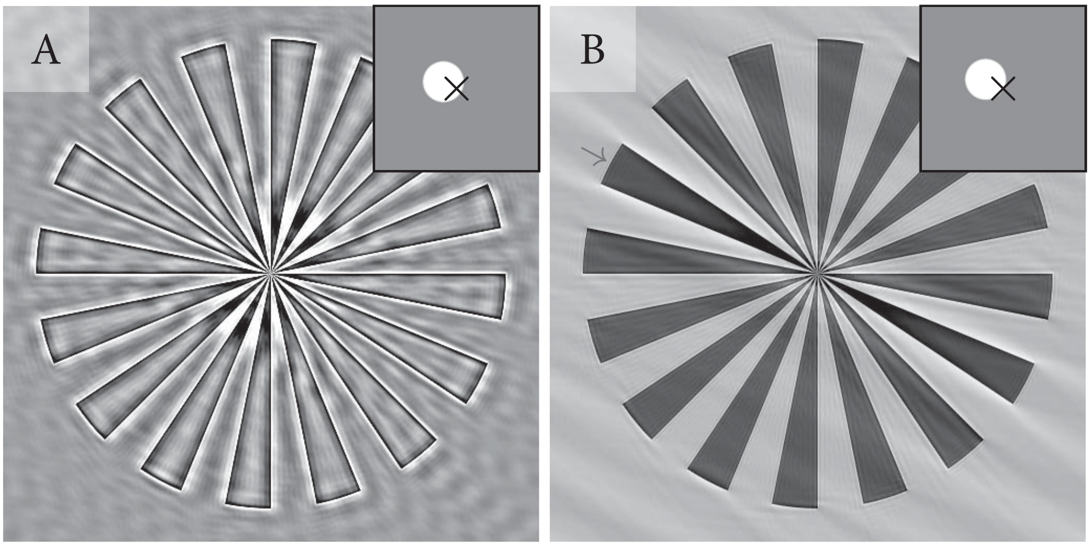

Figure 5.3: Effects of medium (**A**) and strong (**B**) phase plate misalignments of 3/4 q_c and q_c. The cut-on frequency is 1/4 of the Nyquist frequency, identical to figure 5.2 (**B**). The azimuthal orientation of lowest distance to the zero-order beam is marked by ($\rightarrow$).

Smaller holes in the film material result in a reduced cut-on frequency which allows larger structures of the object to be faithfully transferred.

5.1.1 *Misaligned Phase Plates*

With the help of simulations, the effects of a phase plate misalignment on the apparent image contrast can be studied.

Figure 5.3 shows the effects of moderate and strong misalignments of a Zernike phase plate. A strong misalignment corresponding to the radius of the phase plate hole results in phase contrast transfer of low spatial frequencies, but introduces an azimuthally varying contrast modulation. For this misaligned configuration, the corresponding lens diagram in figure 5.4 shows that certain low spatial frequencies traverse the phase plate film material, while their Friedel pairs pass through the phase plate hole. For those spatial frequencies, the situation is similar to an applied Hilbert phase plate (cf. section 2.5.2), only with a smaller film thickness corresponding to a phase shift of $\pi/2$, rather than π for regular Hilbert conditions. This results in a certain modulated phase contrast transfer which is detailed in appendix A.

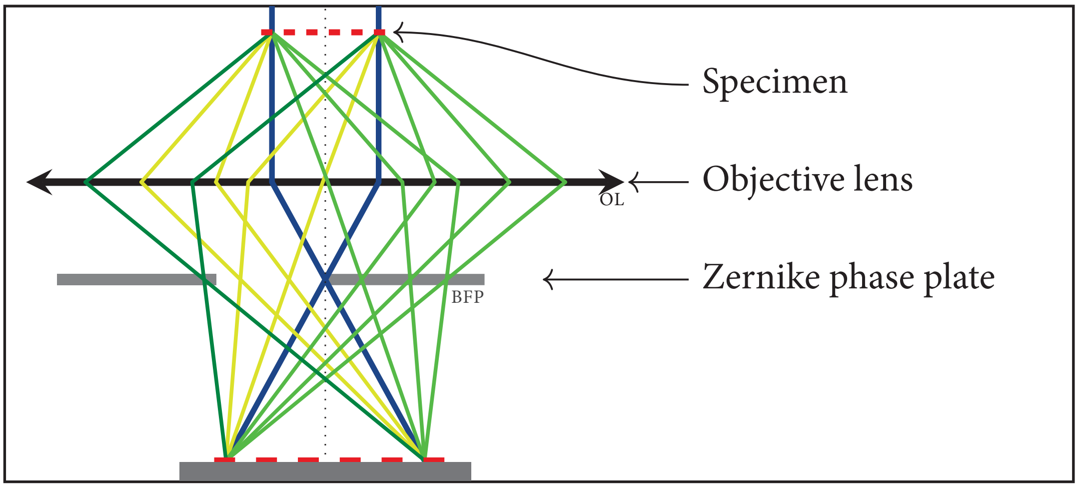

Figure 5.4: Cut-on reduction with misaligned Zernike phase plate in the back focal plane. The phase plate edge is shifted towards the zero-order beam position. Electrons scattered in the opposite direction (green) or to sufficiently high angles (dark green) are now affected by the phase plate. Other angles are not affected (yellow), while their Friedel pairs traverse the film material.

Electrons scattered to even higher angles are transferred with regular Zernike contrast, as both Friedel pairs traverse the phase plate film material.

For a limited set of spatial frequencies corresponding to object features along a certain azimuthal orientation, the cut-on frequency can therefore be adjusted by *deliberate misalignment* of the Zernike phase plate. The effective cut-on frequency is determined by the remaining distance between phase plate edge and zero-order beam.

5.1.2 *Deliberate Misalignment*

The contrast transfer can be extended to cover more azimuthal orientations by integrating the signal contributions for different zero-order beam misalignments on the camera. This can be accomplished by a relative movement of the zero-order beam along the perimeter of the phase plate edge, which results in a precessing motion following the circular shape of the phase plate hole. The idea to utilize a precession movement to change the effective cut-on frequency of the phase plate was communicated by the KonTEM staff, but has been published elsewhere in the meantime [60]. A similar use of a precessing motion of the zero-order beam for phase plate

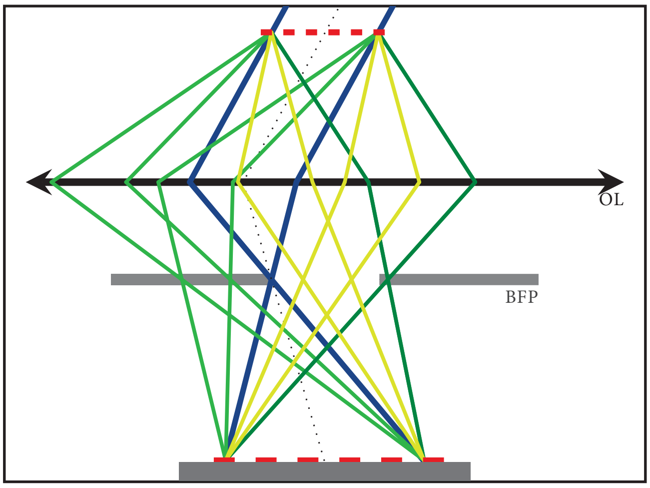

Figure 5.5: Cut-on reduction with tilted illumination. In the back focal plane, the optical axis and the zero-order beam cross-over position are shifted towards the phase plate edge. Electrons scattered in the direction of the illumination tilt (green) or in any direction to sufficiently high angles (dark green) are affected by the phase plate, while others (yellow) are not.

application is described in [6]. The following study is novel and has not been reported yet.

One implementation possibility is to execute the movement by physically translating the Zernike phase plate using its motorized aperture drive, resulting in the conditions shown in figure 5.4. This imposes high demands on the mechanical precision of the manipulator.

A more robust way to implement the precession movement is keeping the phase plate stationary and scanning the zero-order beam with the illumination tilt deflectors during the exposure time of the camera. The static situation is visualized in another lens diagram in figure 5.5. Opposed to the situation with a physical movement of the phase plate, this is no longer side-effect free:

As mentioned in section 3.1.2, changing the illumination tilt can induce an image shift on the camera, if a certain amount of defocus is present. Worst-case conditions for this acquisition scheme can be assumed for small focal lengths (e. g. 2 mm) and large phase plate hole radii (e. g. 2 μm), which results in a necessary illumination tilt magnitude of 1 mrad. Such small angles allow neglecting higher-order effects, that the resulting image shift **s** depends linearly on the defocus, induced tilt angle β and the magnification M of the projective

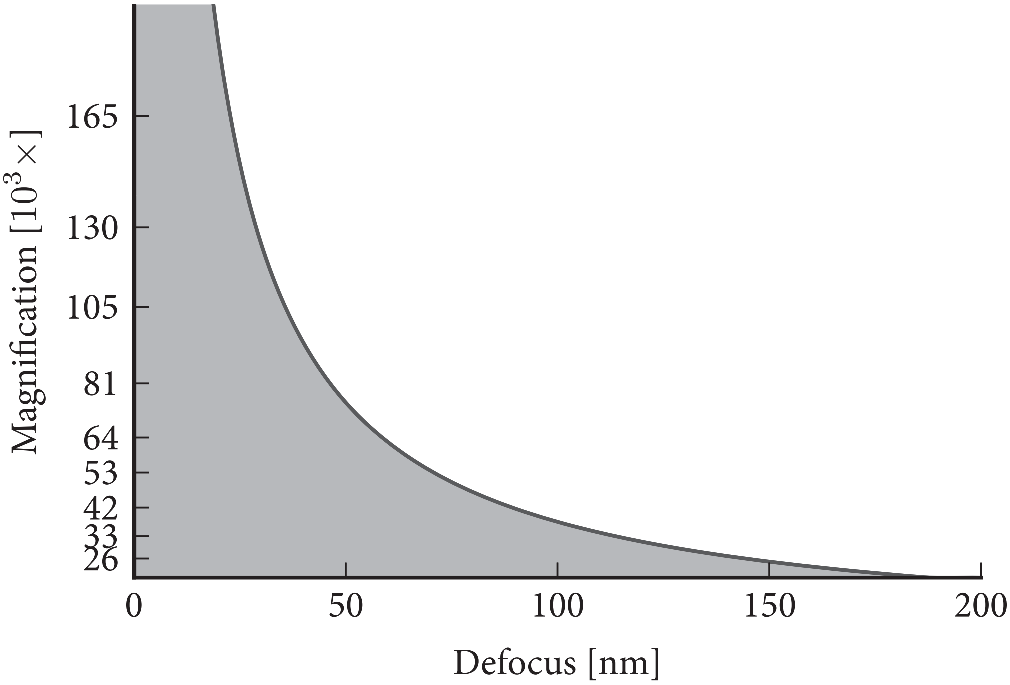

Figure 5.6: Focus-precision needed for sustaining the image resolution with varied illumination tilt during the exposure. The maximal focus error is plotted and the area of tolerable defocus coloured. The calculation is valid for a physical pixel size of 15 µm and a variation of the illumination tilt of 1 mrad.

$$\mathbf{s} \approx 2M \cdot \Delta z \cdot \beta,$$

as detailed in [48]. Any image shift smaller than half a pixel on the camera sensor should not introduce any loss of spatial resolution. Physical camera pixel sizes are typically in the order of 15 µm. The maximal magnification attainable with a certain focus error and a given illumination tilt can be calculated to

$$M \leq \frac{\text{pixel size}}{4\beta \cdot \Delta z}.$$

With the estimated values for pixel size and illumination tilt, the necessary focus precision can be calculated and is in the range of 20–150 nm for an intermediate resolution range. A plot of the distribution is shown in figure 5.6.

Since phase plates need to be applied using close-to-focus conditions, the requirement on the focus precision is usually not restricting. For high-resolutions using an uncorrected instrument with nonvanishing spherical aberration, the limitations may impose a small disadvantage, where the use of an optimal defocus to extend the passband of phase contrast transfer might be prohibited (cf. section 2.5).

Likewise, the double amount of the needed focus precision can be regarded as an upper limit for the maximum specimen thickness, if the image depth-of-field should cover the whole bulk of the sample.

In an uncorrected microscope, a significant phase error is introduced by tilting the illuminating beam to large angles, as discussed in [90]. Therein, the additional phase shift is given by

$$\Delta\varphi(\beta) = -2\pi C_s \lambda^2 q^3 \beta.$$

For $C_s = 2\,\mathrm{mm}$ and an acceleration voltage of 200 kV, this means for a resolution of 3 Å, a maximum tilt angle of about 0.2 mrad is acceptable to limit the additional phase shift to $\pi/4$. For a resolution of 5 Å, the maximum tolerable tilt is about 0.9 mrad. For a focal length of 2.7 mm the values correspond to phase plate hole radii of about 500 nm and 2.5 µm.

The effects of both detrimental properties are therefore controllable by using close-to-focus imaging conditions and using a phase plate with the radius of the hole adapted to the desired resolution range.

5.1.3 *Properties of the Precession Technique*

In practice, the precession movement needs to be approximated by a polygon with a finite number of edges. Using an equivalent scheme, the effects on the resulting image contrast can also be studied by simulation:

For each individual misalignment position, the resulting contrast is simulated. The results are subsequently integrated into a combined image intensity by incoherent summation.

In actual microscopy, such an incoherent summation can be done similarly by acquiring an image for each misaligned position and combining the parts by image-processing. A less controlled, but potentially much quicker approach is to exploit the integrating character of the sensor by *dynamic* application of the relative motion during the acquisition time of the camera.

Simulated results for the Siemens star pattern, where the circular trajectory is approximated by a polygon with different effective radii are shown in figure 5.7. Compared to the equivalent static situation in figure 5.3, the image contrast does not show an angular dependence anymore.

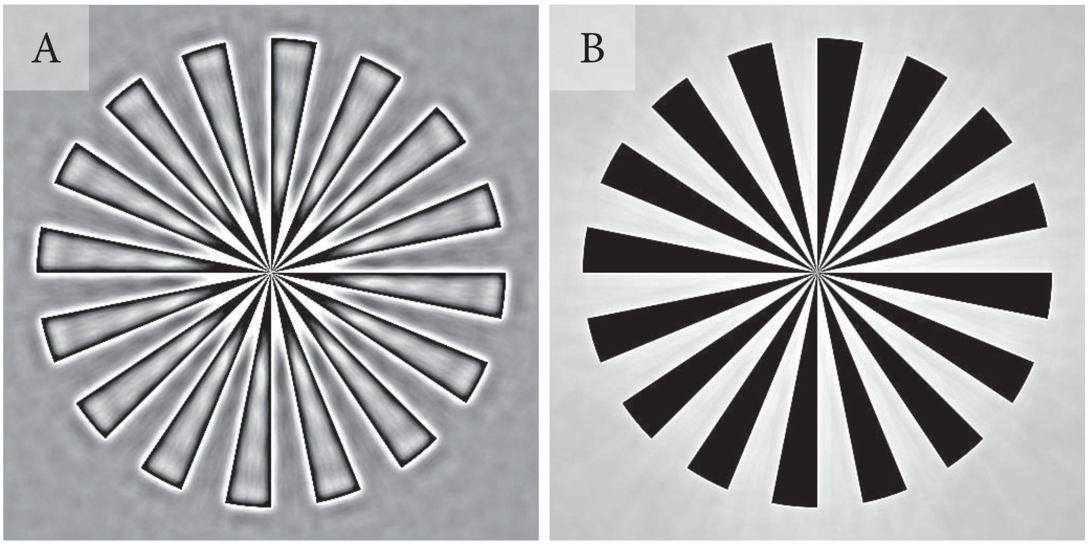

Figure 5.7: Incoherently summed results of 16 simulated images with the Zernike phase plate position varied along a circular trajectory, with the same imaging conditions as in figure 5.3. The approximated precession radii are $3/4\ q_c$ (**A**) and q_c (**B**).

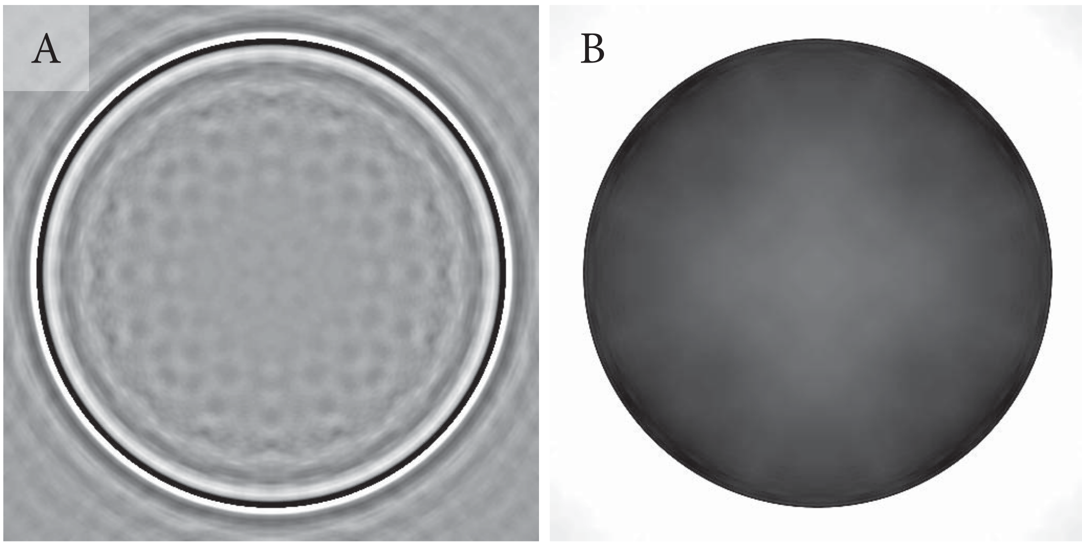

Figure 5.8: Simulation results for a disc-shaped test specimen. Other simulation parameters same as in figure 5.7. While contrast transfer of low spatial frequencies is enabled by using a maximal precession radius, the image intensity is still modulated (**B**).

For another synthetic test specimen with higher amount of low spatial frequencies, application of the same simulation parameters still results in visible image artefacts, as shown in figure 5.8. The low spatial frequency structure factors are present, but transferred with wrong amplitudes.

For an analysis, the static geometry in the diffraction plane with a misaligned Zernike phase plate is shown in figure 5.9. Therein, spatial frequencies of same magnitude but varying angular orientation are highlighted if they traverse the phase plate film material and gain a phase shift. For different spatial frequencies, the ratio of shifted to unshifted spatial frequencies varies.

This is the reason for the contrast modulation in figure 5.8 (**B**). To correct its effect, the modulation needs to be characterized as a function of the spatial frequency: The amount of shifted spatial frequencies of a certain magnitude q_i corresponds to the length of the individual arcs subtending the film material, which in turn corresponds to $1 - \theta/\pi$ (cf. figure 5.9). Using the cosine rule, θ can be calculated to

$$\theta = \arccos\left(\frac{-q_c^2 + q^2 + d^2}{2qd}\right).$$

Using $\arccos(-\theta) = \pi - \arccos(\theta)$, the amount of shifted spatial frequencies f of same magnitude q can be expressed as

$$f(q) = \frac{1}{\pi}\arccos\left(\frac{q_c^2 - d^2 - q^2}{2qd}\right).$$

If the Zernike phase plate is the only means for contrast generation, i. e. no lens-aberrations are present, f also gives the modulation of the contrast transfer for the modified Hilbert conditions (cf. section 5.1.5) using the beam precession method.

By choosing reasonable values corresponding to the values of the extrema of the function's restricted domain, f can be defined for all q to

$$f(q) = \begin{cases} 0 & \text{for } |q| \in [0, q_c - d] \\ \frac{1}{\pi} \cdot \arccos\left(\frac{q_c^2 - d^2 - q^2}{2qd}\right) & \text{for } |q| \in]q_c - d, q_c + d[\\ 1 & \text{otherwise} \end{cases} . \qquad (5.1)$$

Figure 5.10 shows f for the different precession radii d, corresponding to the radii used for the image simulations.

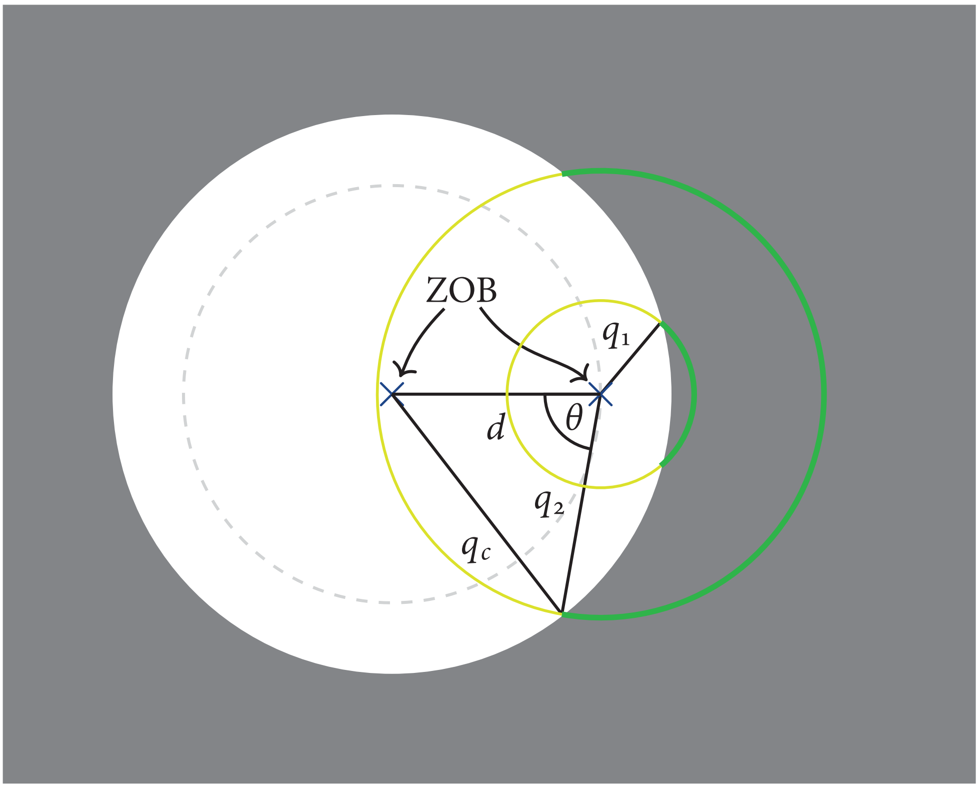

Figure 5.9: Geometry in the back focal plane with Zernike phase plate consisting of phase-shifting film material (grey) and cut-out hole with radius corresponding to a spatial frequency q_c. The zero-order beam positions for aligned conditions and misaligned by a distance d are indicated by (×). The dynamic mode implements the precession motion along the dashed circle with radius d.
With a zero-order beam (ZOB) misalignment of $3/4\, q_c$, certain spatial frequencies of magnitude q_1, q_2 traverse the film material and gain a phase shift of $\pi/2$. Depending on the magnitude of q_i, the ratio of shifted (green) to unshifted (yellow) spatial frequencies varies.
The setting is a top view of the diffraction plane in figures 5.4 and 5.5.

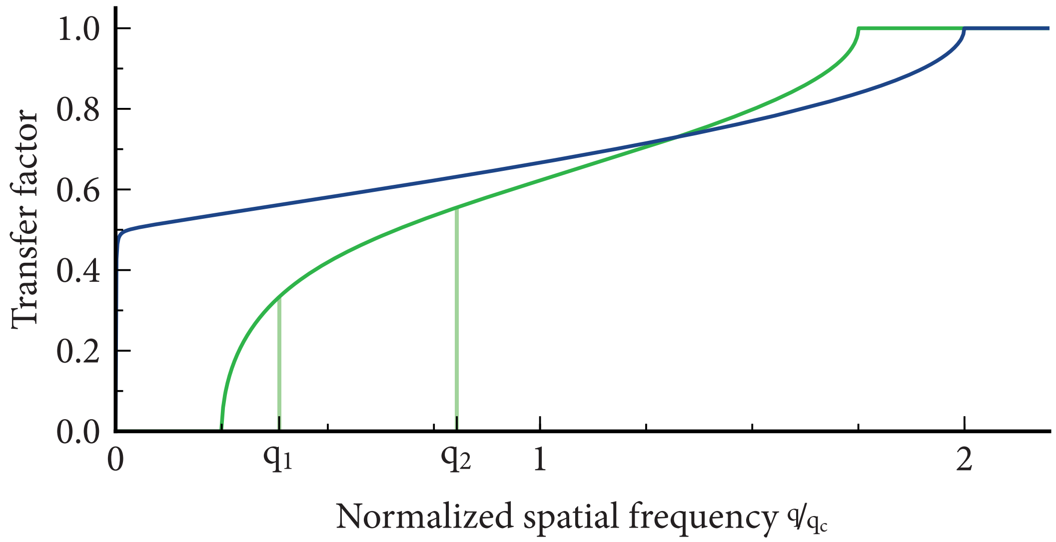

Figure 5.10: Transfer factors for precession radii of 3/4 (green) and q_c (blue). The position of the structure factors q_1 and q_2 from figure 5.9 are highlighted.

5.1.4 *Correction of the Precession Contrast Transfer Modulation*

With the geometrical reason of the non-linear transfer attenuation recognized, its effect can be compensated by multiplying the structure factors with the inverse of f. The corrected simulation results are shown in figure 5.11.

5.1.5 *Contrast Transfer with Hilbert Conditions*

The asymmetric application of the phase plate to the Friedel pairs in the relevant range of spatial frequencies results in a modulated contrast transfer similar to using a regular Hilbert phase plate. As detailed in appendix A, the image contrast transfer for in-focus conditions can be reduced to

$$I(\mathbf{r}) \approx 1 + \varepsilon(\mathbf{r}) - a_0 \varphi(\mathbf{r})$$

with a_0 the transmittance of the phase plate film material and a, φ the amplitude and phase structure factors of the specimen. The image intensity potentially contains a mixture of amplitude and phase contrast. If the amplitude structure factors vanish, e. g. for thin specimen consisting of atoms with low atomic numbers, the image modulation is proportional to the specimen phase modulation.

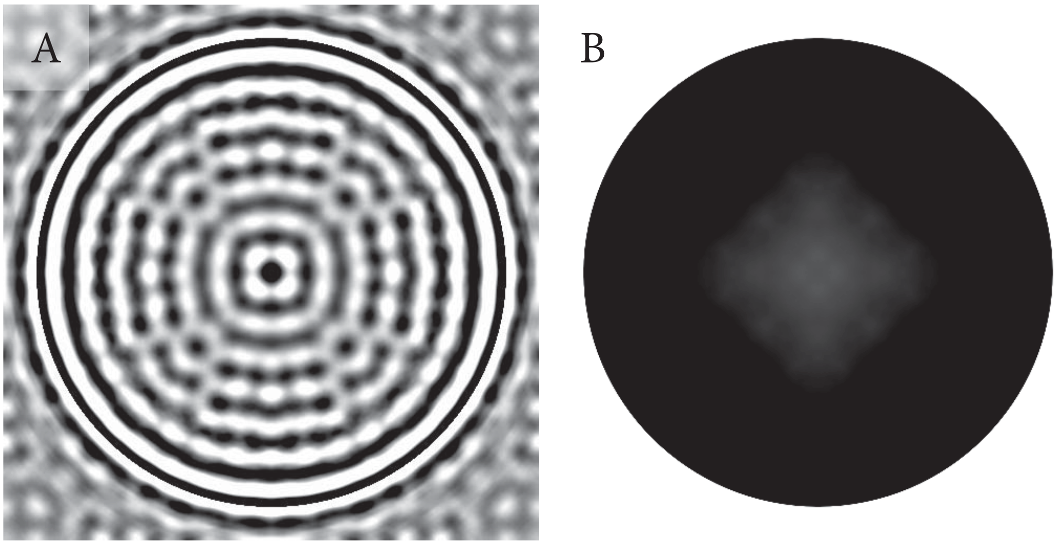

Figure 5.11: Simulation results for the disk test specimen. Simulation parameters same as in figure 5.7, with the structure factors corrected according to equation 5.1. In (**A**), the image still suffers from cut-on, as the precession radius is too small to cover the spatial frequencies responsible to accurately describe the bulk of the sample. With the extreme precession radius in (**B**), only the lowest spatial frequencies are not faithfully transferred due to the discretisation in the simulation.

Sufficiently high spatial frequencies are transferred with regular Zernike contrast, as either of the Friedel pairs is phase shifted. For the smaller spatial frequencies, the dynamic imaging mode's transfer modulation applies and the combined image intensity for in-focus conditions of a pure phase object is then given by

$$\mathcal{F}\left[I\left(\mathbf{r}\right)\right] \quad = \quad \begin{cases} 0 & \text{for } |\mathbf{q}| \in [0, \mathrm{q_c} - \mathrm{d}] \\ \left(\delta\left(\mathbf{q}\right) - a_0 \hat{\varphi}\left(\mathbf{q}\right)\right) \cdot f(\mathbf{q}) & \text{for } |\mathbf{q}| \in \left]\mathrm{q_c} - \mathrm{d}, \mathrm{q_c} + \mathrm{d}\right[\\ \delta(\mathbf{q}) - 2a_0 \hat{\varphi}\left(\mathbf{q}\right) & \text{otherwise} \end{cases} \cdot$$

5.2 DISCUSSION

The proposed dynamic imaging mode is a major improvement to the existing technology, as it allows an adaptation of the cut-on frequency of a Zernike film phase plate with a certain hole size to the requirements of the specimen. By choosing a precession radius equivalent to the radius of the phase plate hole, the cut-on effects are eliminated. The formerly vanishing transfer of the spatial frequencies smaller than q_c is replaced by a non-linear phase contrast modulation.

As the simulations with a pure phase object and a perfectly transparent phase plate show, nearly perfect reconstruction is achieved if the non-linear attenuation of structure factors is accounted for in a subsequent image processing step. Application of the precession technique can be realized using beam deflectors present in any transmission electron microscope, and especially does not rely on additional and complicated electron optics.

The presence of a C_S-corrector in the beam path after the phase plate is beneficial. Due to the vanishing spherical aberration, the necessarily tilted illumination does not result in an additional phase shift for high spatial frequencies, and the contrast transfer is optimized for in-focus conditions.

Depending on the lowest spatial frequency present in the specimen, the cut-on frequency can be tuned accordingly by choosing precession radii smaller than the hole in the film material. This introduces some margin for alignment errors. The precision of the physical alignment of the phase plate hole to the zero-order beam is critical, if extreme precession radii are chosen. Failure to attain perfect alignment and employment of the dynamic imaging mode exposes the delicate edge of the phase plate hole to the intense zero-order beam, which usually alters the phase plate structure.

The dynamic imaging mode also allows the use of irregularly shaped openings in the film material, as only the distance of zero-order beam and edge of the opening is relevant to attain the desired contrast transfer. Using a phase plate of odd symmetry such as the pentagonal structure proposed in section 3.5.2, the zero-order beam can be positioned in the corners of the polygon. If the compensating image processing step is adjusted accordingly, also a phase plate hole of polygonal shape is able to enable full spatial frequency contrast transfer.

6

RESULTS WITH ZERNIKE FILM PHASE PLATES

Two different types of Zernike film phase plates could be obtained. Both were installed in the back focal plane of a FEI Titan Krios with standard electron-optics.

The properties of the dynamic imaging mode are validated and the automated application for single-particle and tomography data acquisition is demonstrated.

6.1 CHARACTERISATION OF ZERNIKE PHASE PLATES

Zernike film phase plates were installed in a FEI Titan Krios featuring a standard electron-optical set-up and operated at 200 kV. To apply the phase plates, the objective aperture drive was replaced by a KonTEM high-precision micromanipulator.

The microscope features an automatic cooling system allowing to sustain the sample at cryogenic temperatures for extended periods of time. The quasi-permanent use of an anticontaminator results in very clean vacuum conditions in the vicinity of the sample and the phase plate. The relevant terminal pressure is estimated to be better than 5×10^{-8} mbar, which results in reduced sample and phase plate contamination.

In Zernike phase plates, the actual phase shift is determined by the thickness and composition of the film material (cf. section 2.2). In principle, the attained phase shift can be verified by using defocused imaging conditions and taking two exposures one with an applied and another with retracted phase plate. The effect from the phase plate can then be seen as a shift of the Thon ring system in the diffractograms.

As charged phase plates may introduce a defocus change, this technique usually fails. Therefore, the phase-shifting behaviour has to be determined in a single exposure.

To provide an overdetermined equation system, many zero-crossings should be present in the diffractograms. This can be realized by either attaining a high magnification and a smaller defocus aberration or a medium magnification and a higher defocus. Phase plate alignment in the Fourier-domain is facilitated by using large hole radii, therefore the largest available

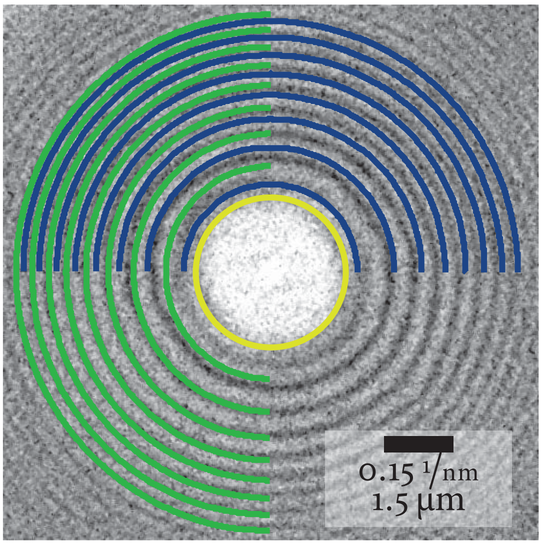

Figure 6.1: Diffractogram of an amorphous-carbon film imaged with an aligned KonTEM Zernike phase plate and high defocus. With 200 keV electrons and C_s of 2.7 mm, the fitted pCTF parameters are: Δz: −11.0 µm, A_1: 250 nm, φ_{pp}: -0.45π rad. The resulting pCTF zeros with the phase shift by the phase plate (green) and with the additional phase shift set to 0 (blue) are highlighted. The phase plate hole size is indicated by a yellow circle.

holes are chosen for phase plate film characterisation. It is further facilitated using low magnifications, since the Friedel-symmetric figure appears larger. Therefore, an intermediate magnification of 64 000 × resulting in an equivalent pixel size of 2.1 Å on the detector is chosen.

An amorphous sample is positioned in the object plane and the phase plate hole is centred to the optical axis. Many CTF zero-crossings are produced by using a high defocus of e. g. −11.5 µm. The convergence angle of the illumination is adjusted such that the focus of the zero-order beam coincides with the phase plate plane. To attain a sufficient signal-to-noise ratio, an exposure time of 30 s with a dose rate of 14 e^{-} $Å^{-2}$ s^{-1} is used.

For KonTEM's crystalline metal film phase plates based on chromium (personal communication Jörg Wamser/KonTEM), an annotated diffractogram shown in figure 6.1 features a sufficient number of Thon rings to allow determination of the CTF parameters. A regression using *ctffind4* [67] reveals a phase shifting property of −0.45 π.

In the annotated diffractogram, some of the zero-crossings found using the regression do not coincide with the actual location of the individual Thon rings. The effect is most pronounced in the vicinity of the edge of the phase plate hole and extends for about one µm into the film material.

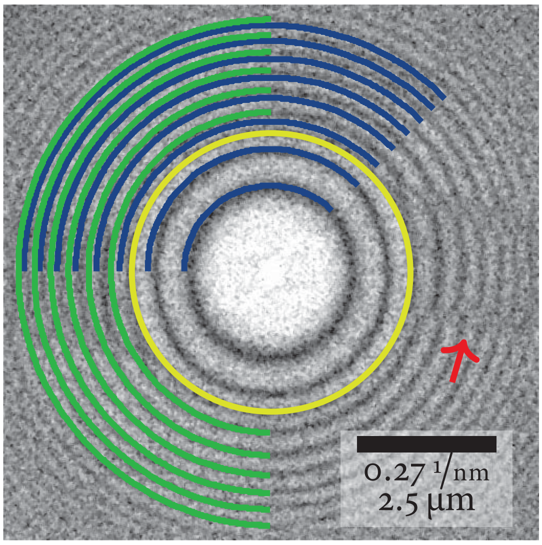

Figure 6.2: Diffractogram of an amorphous-carbon film imaged with an aligned amorphous-metal film Zernike phase plate and high defocus. The fitted pCTF parameters are: Δz: −11.6 µm, A_1: 100 nm, φ_{pp}: -0.36π rad. Colour meanings same as in figure 6.1. Note the irregular Thon rings due to a double film layer (→).

Higher spatial frequencies well match the resulting pattern of the pCTF parameters found by the regression. The irregular phase-shifting behaviour next to the phase plate hole points to a static charge present at the hole perimeter.

The image was acquired with an intended defocus of −11.5 µm. In the regression, the actual Δz is determined to be about −11 µm, which is a significant deviation pointing to a focus-changing effect of the phase plate.

In addition, two amorphous-metal Zernike film phase plate assemblies with the film material made of the alloy $Pd_{77.5}Cu_6Si_{16.5}$ and an amorphous-carbon coating could be obtained from Manuel Dries and Tina Schulze/LEM [21] . On request, large holes of up to 4.5 µm diameter have been cut into the film surface of one of the phase plate assemblies.

Their performance is characterized in a similar set-up as for the KonTEM phase plate. The regression based on the image shown in figure 6.2 suggests a phase shifting property of −0.36 π.

Due to the larger size of the hole in the film material compared to the KonTEM phase plate, pCTF zero-crossings are present in the unshifted area inside the hole. This allows observation of unshifted and shifted pCTF signal in a single exposure. The actual positions of the zero-crossings well match the expectation, suggesting a reduced charging problem.

In every hole cut into the film material of this specific assembly, the former content of the hole is not removed, but placed at a random position next to the edge of the hole (cf. figure 3.29). At the specific regions covered by a double film layer, the phase contrast transfer is modulated accordingly:

With the phase plate centred to the optical axis, the individual Friedel pairs for spatial frequencies passing through the film in this area receive a phase shift of $\pi/2$ and π respectively. This results in a changed contrast transfer, similar to the irregular Hilbert contrast for a misaligned phase plate (cf. section 5.1.5).

For the dynamic imaging mode, the contrast transfer is similar to the regular Hilbert contrast conditions, as a total phase shift difference of π is introduced between the Friedel pairs. The contrast transfer is expected to be modulated accordingly for a certain azimuthal range of low spatial frequencies. Furthermore, a small charge seems to be present at the double film region, as the pCTF zeros inside the hole show a small kink at the same location. This can also be seen as an intensity modulation in diffractogram of images acquired close-to-focus (cf. figure 6.9). Apart from that, fitted and intended defocus values show no significant difference.

6.2 DYNAMIC IMAGING MODE

To demonstrate the enhanced transfer of low spatial frequencies by the dynamic imaging mode, a beam-sensitive biological sample of phospholipids in an aqueous solution is used. They feature a hydrophilic, phosphor-containing headgroup and a lipophilic tail consisting of long fatty acid chains. In an aqueous environment, they self-assemble into structures which minimize the exposure of the lipophilic part to water molecules. This results in the formation of characteristic shapes, such as micelles, bilayer sheets and bilayer vesicles, which can also be nested. A schematic view of possible geometries is shown in figure 6.3.

Depending on the length of the fatty acid chains, a characteristic lipid bilayer with a defined distance of the hydrophilic head parts is formed [50]. Typical characteristic distances of the lipid bilayers vary around 42–52 Å [62].

Since the hydrophilic head part contains phosphor, which has a higher phase shifting potential than atoms with a lower atomic number (e. g. carbon), a lipid bilayer oriented perpendicular to the electron-beam generates two elongated areas of dark contrast with a brighter area inside, as long as positive phase contrast conditions are chosen.

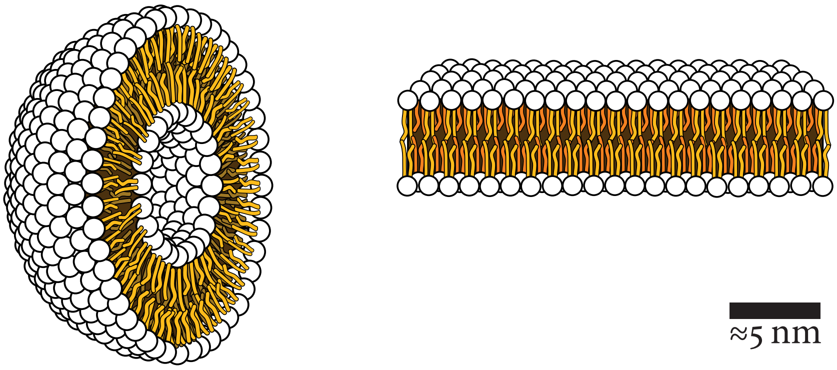

Figure 6.3: Phosphorous lipid bilayer. In aqueous solutions, the structure self-assembles due to the phosphor-containing hydrophilic outer part (white circles) and the hydrophobic inner part, forming a characteristic bilayer with specific distances. Typical shapes contain micelles, liposomes (left) and sheets (right). Image adapted from [80].

For conventional imaging of lipid bilayer structures, large defocus values in the order of about −1.5 to −2.0 µm need to be chosen. Zernike phase plates used with dynamic imaging mode enable contrast transfer of the relevant spatial frequencies without the strong modulation, which are inevitable using such large defocus values. This can be seen in an annotated plot of the resulting pCTF shown in figure 6.4, where the structure factors of the phospholipids are highlighted.

Application

Since the delicate bilayer structure is quickly destroyed by electron-exposure, low-dose imaging techniques need to be employed. The sample-area containing a vesicle is chosen at a low magnification of 4800 ×, while focusing and exposure is done using a magnification of 64 000 ×. To avoid exposing the area of interest to the electron-beam during focusing and phase plate alignment, the image and illumination shift deflectors are used to shift the optical axis in order to focus a nearby area of the sample. A similar situation has been shown in figure 3.31.

To demonstrate the effects of the different imaging conditions, two images with applied phase plate (dynamic imaging mode and static) and two more without (defocused and focused) are taken at the same specimen location, in the same order as listed here. From first to last exposure, a degradation of the specimen is to be expected. The images with applied phase plate and the focused images are acquired using the same intended objective lens excitation. However, since acquisition of the defocused

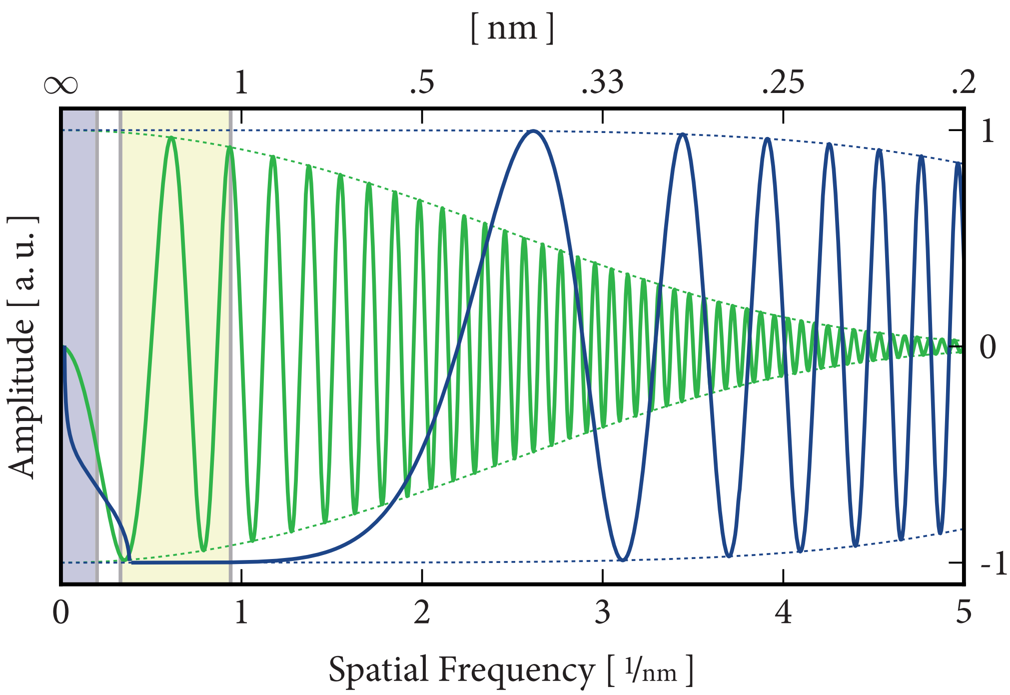

Figure 6.4: Phase contrast transfer with a high Δz of -1.6 µm (green) compared to the transfer modulation of an applied Zernike film phase plate using the dynamic imaging mode (blue). The relevant range of structure factors for a lipid bilayer are highlighted (light yellow area). The size of the phase plate hole is indicated (light blue area). For the envelopes, an energy width of 0.1 eV is assumed.

image requires a change of the objective lens current, which is reset for acquiring the close-to-focus image, the effective focus might be slightly changed due to hysteresis effects. The specific order optimizes the signal in the defocused image, as the specimen suffers from only two rather than three previous exposures.

CHROMIUM FILM PHASE PLATE For a pristine KonTEM phase plate of 2 μm diameter, the focusing routine has to be performed with the applied phase plate, as insertion of the phase plate introduces a focus change. The following image series is acquired using a rather high dose of about $25\,e^{-}\,\text{Å}^{-2}$, which can be seen in figures 6.5 and 6.6.

The change from static to dynamic imaging mode with a precession radius corresponding to the phase plate hole radius results in an apparent reduction of the cut-on frequency. The most striking effect is the elimination of the typical fringing artefacts present in the image taken with statically applied phase plate (cf. figure 6.5). However, the bilayer structure is not faithfully reproduced, as it shows an inverted contrast compared to expectation and the positive phase contrast in the defocused image.

The inverted contrast requires a particular phase shift for the low spatial frequencies corresponding to the lipid bilayer structure. The most probable source for such a phase shift are overfocus conditions or an irregular phase shift of the phase plate.

It is not clear, whether the focusing step with applied phase plate was successful, as the close-to-focus image shows a significant amount of phase contrast transfer. However, the particular amount of defocus does not result in recognizable Thon rings in a diffractogram, and no apparent artefacts of strong defocus can be seen in the image. Therefore, the magnitude of defocus mismatch should be rather small and not sufficient to affect the low spatial frequencies of the lipid bilayer structure.

As can be seen in figure 6.1, the phase-shifting potential of the phase plate deviates from the intended $-\pi/2$ in an area of the phase plate film close to the hole perimeter, probably due to charging. This phase shift is probably sufficient to result in an inverted image contrast and most likely the reason for the observed effect.

Interestingly, there is also an apparent shift of images acquired with and without applied phase plate, which cannot be attributed to a tilted illumination, since both close-to-focus and defocused images have a constant image shift compared to the ones with applied phase plate. This is another symptom of a less-than-ideal phase plate.

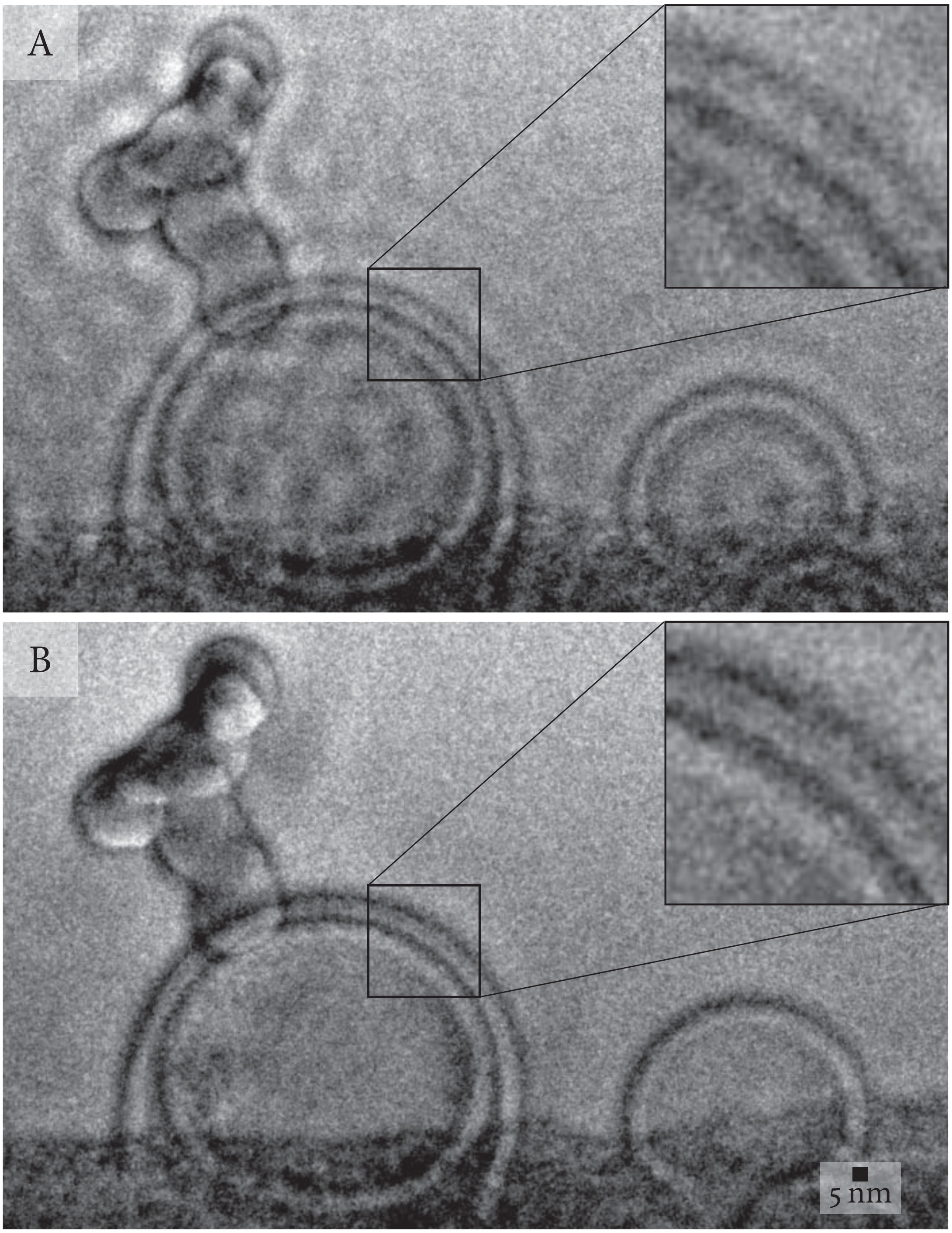

Figure 6.5: Semi-automated application of a Zernike phase plate on a beam-sensitive specimen. Centred phase plate in (**A**) with heavy fringe artefacts, which are reduced using the dynamic imaging mode in (**B**). Note the inverted contrast of the lipid bilayer.

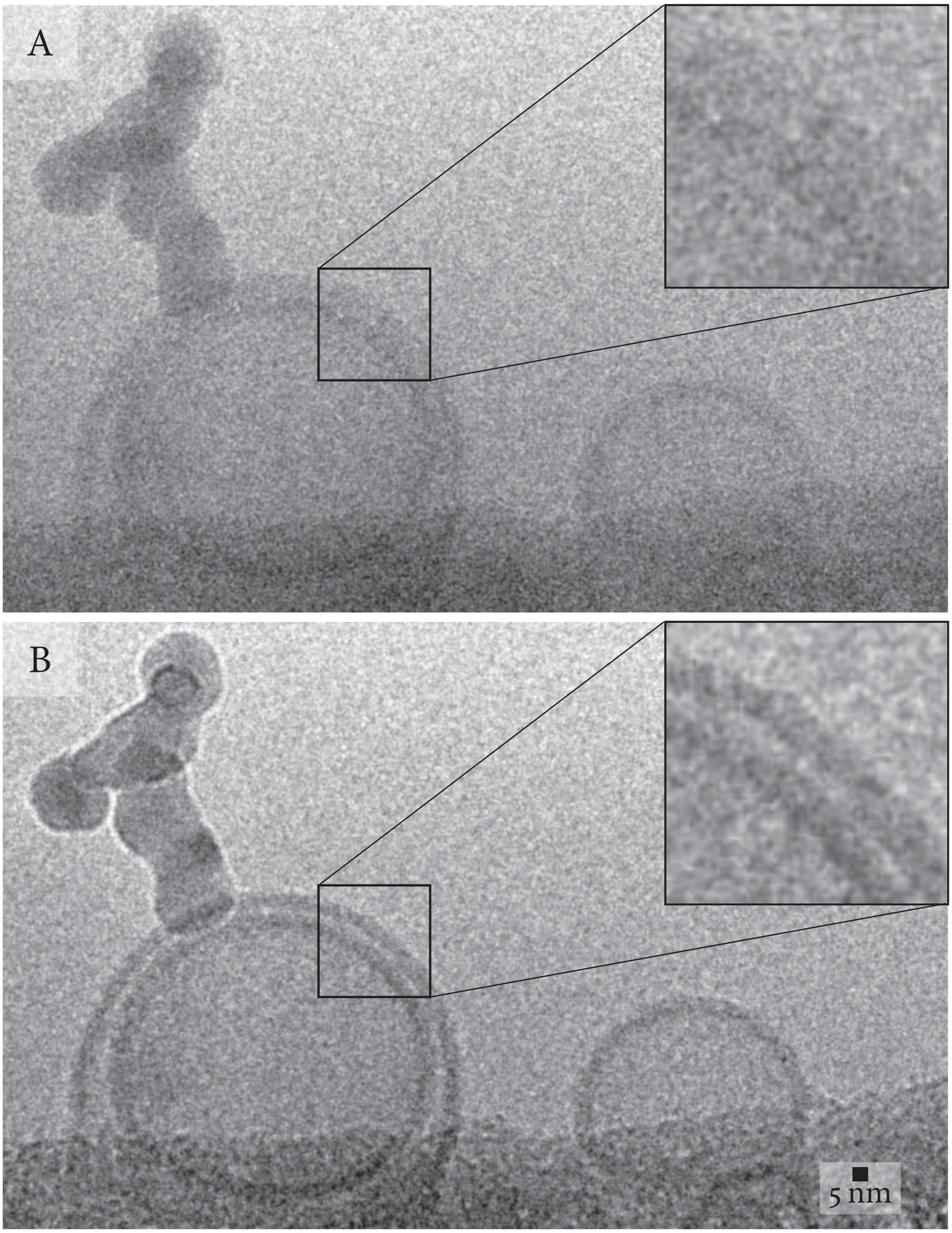

Figure 6.6: Same area and imaging conditions as in figure 6.5, but with removed phase plate. What should be focus conditions in (**A**) show significant amount of phase contrast, as the formerly found conditions have been influenced by the phase plate. In (**B**), an additional defocus of −1.6 µm is applied. Note the apparent image shift compared to the images acquired with the phase plate shown in figure 6.5, even for similar focusing conditions (**A**).

CARBON-COATED AMORPHOUS-METAL PHASE PLATE The experiment is repeated with a fresh preparation of a liposome specimen and another Zernike phase plate obtained from Manuel Dries and Tina Schulze/KIT. With the new phase plates, the effective focus is hardly altered by inserting the phase plate. Therefore, the focusing can be done without applied phase plate, which reduces both complexity of the preparatory steps and the electron-exposure of the phase plate. Apart from that, the image acquisition process is comparable to the one described above, save for the necessary adjustments to the precession radius and a small increase of the acquisition time for a higher dose of about 30 e^{-} Å^{-2} per image.

This time, application of the phase plate qualitatively results in the expected positive phase contrast transfer. Static and focused conditions are shown in figure 6.8.

Low spatial frequencies in the bulk of the nested multilamellar vesicles are transferred with highest contrast using the dynamical imaging mode. However, they also show some imperfections, manifesting itself in a loss of phase contrast transfer in a specific azimuthal orientation, and a strange contrast of the gold nanoparticles. Both shortcomings are a sign of a phase plate degradation. The underlying mechanism is discussed in the following section.

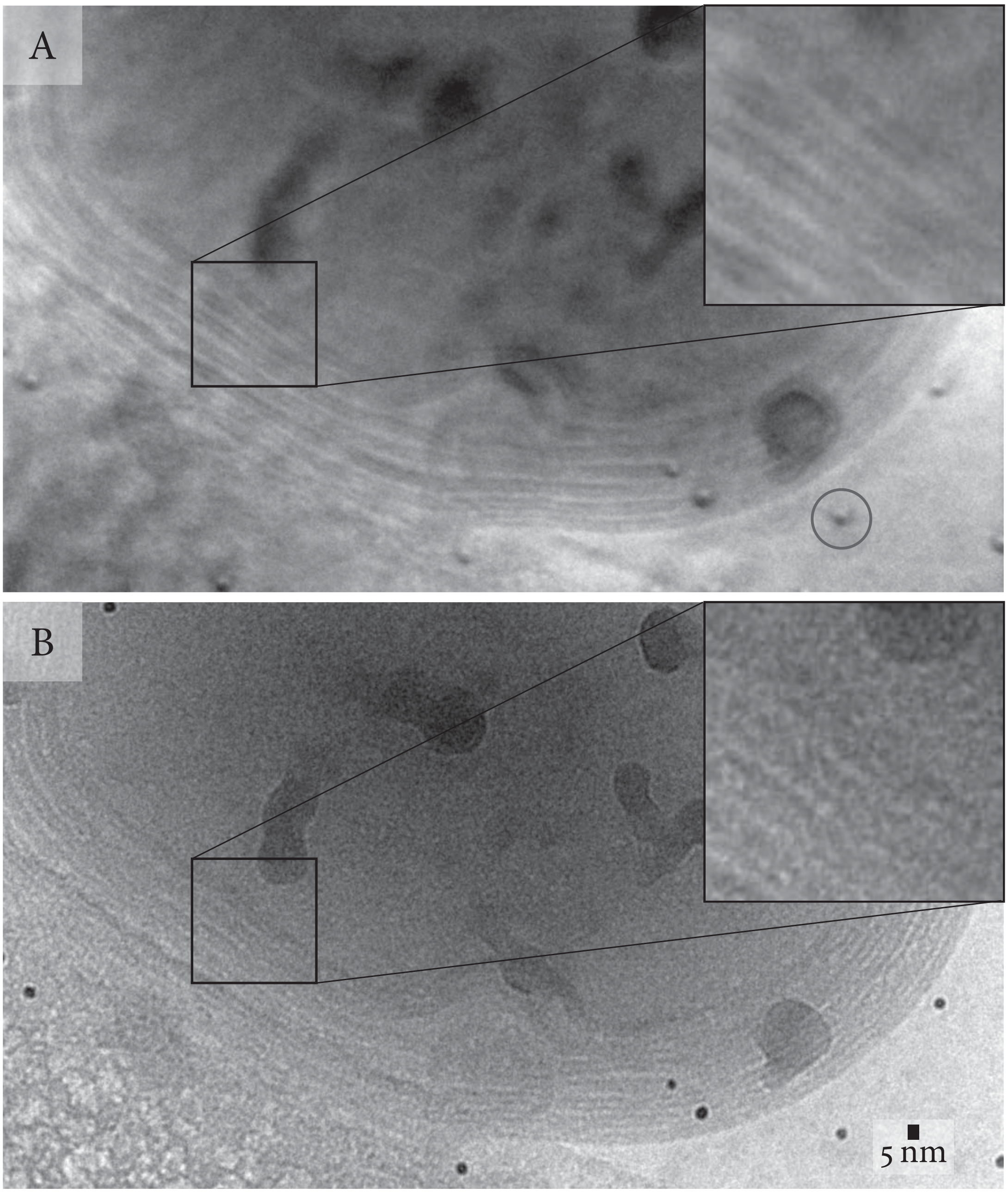

Figure 6.7: Dynamic phase plate imaging mode (**A**). The non-linear low spatial frequency contrast has been corrected in an image processing step. Note the particular contrast of the gold nanoparticles, e. g. the marked one (○).
The same area is imaged with removed phase plate and applied defocus of −1.6 µm (**B**), where the specimen is degraded by two additional exposures compared to (**A**).

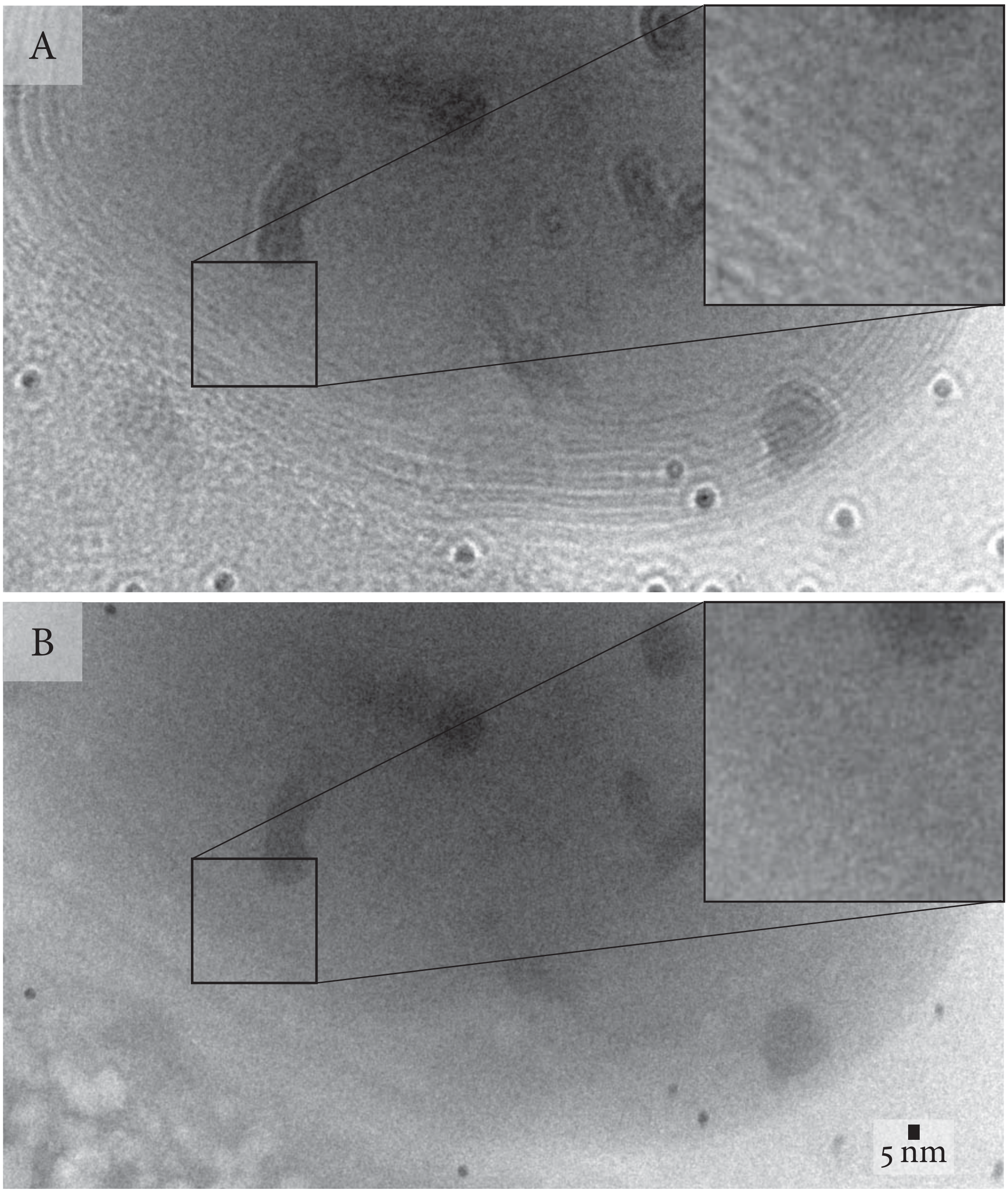

Figure 6.8: Static phase plate (**A**) and focus conditions (**B**) for the same area of interest as shown in figure 6.7.

6.3 FAILURE MECHANISM

For an analysis of the phase plate degradation mechanism, the diffractogram images acquired on a specimen region with amorphous-carbon background directly after the automated phase plate alignment sequence are evaluated. The used method follows to the procedure described in section 3.6, i. e. specimen focusing without applied phase plate on amorphous-carbon background and subsequent phase plate alignment in four steps using presets with low and intermediate magnifications and the corresponding defocused condenser settings. The individual microscope settings used for alignment and imaging are executed in a defined sequence, which minimises lens hysteresis effects.

In figure 6.9, an image-series acquired using a large phase plate with a hole diameter of approximately 2.5 µm is shown. Initially, the phase plate shows only minor signs of charging, as can be seen in the modulated intensity next to the phase plate hole. In the resulting images, no suspicious charging artefacts are visible, and insertion of the phase plate results in an unnoticeable focus change and negligible image shift.

The mechanical alignment is repeated for each new specimen position and the resulting diffractograms of the post-alignment images are shown in the subsequent images in figure 6.9. They show a progressive charging effect, as the intensity modulation in the vicinity of the phase plate hole becomes more pronounced.

Apart from that, the initial repeatability of the automated alignment process is very good, as the apparent phase plate positions are virtually identical. Therefore, the source of the constant mismatch of about 200 nm is most likely a failure to accurately account for the shift of the optical axis in between the preset used for alignment and the preset used for imaging. The corresponding preset alignment accounted for lens hysteresis effects by using the exact sequence of condenser excitations that were also occurring during the alignment sequence, but used a different reference phase plate. Probably, the slightly different charging characteristics give rise to the resulting position mismatch.

Within the shown sequence, the phase plate is not used in dynamic imaging mode, i. e. the zero-order beam is kept stationary at the aligned position, and the misalignment does not result in a direct contact of the phase plate film material with the focused zero-order beam. Therefore, the source of the accumulated charge of the film material is either the diffracted electrons from the sample or the defocused zero-order beam used during alignment. The former is probably of negligible intensity

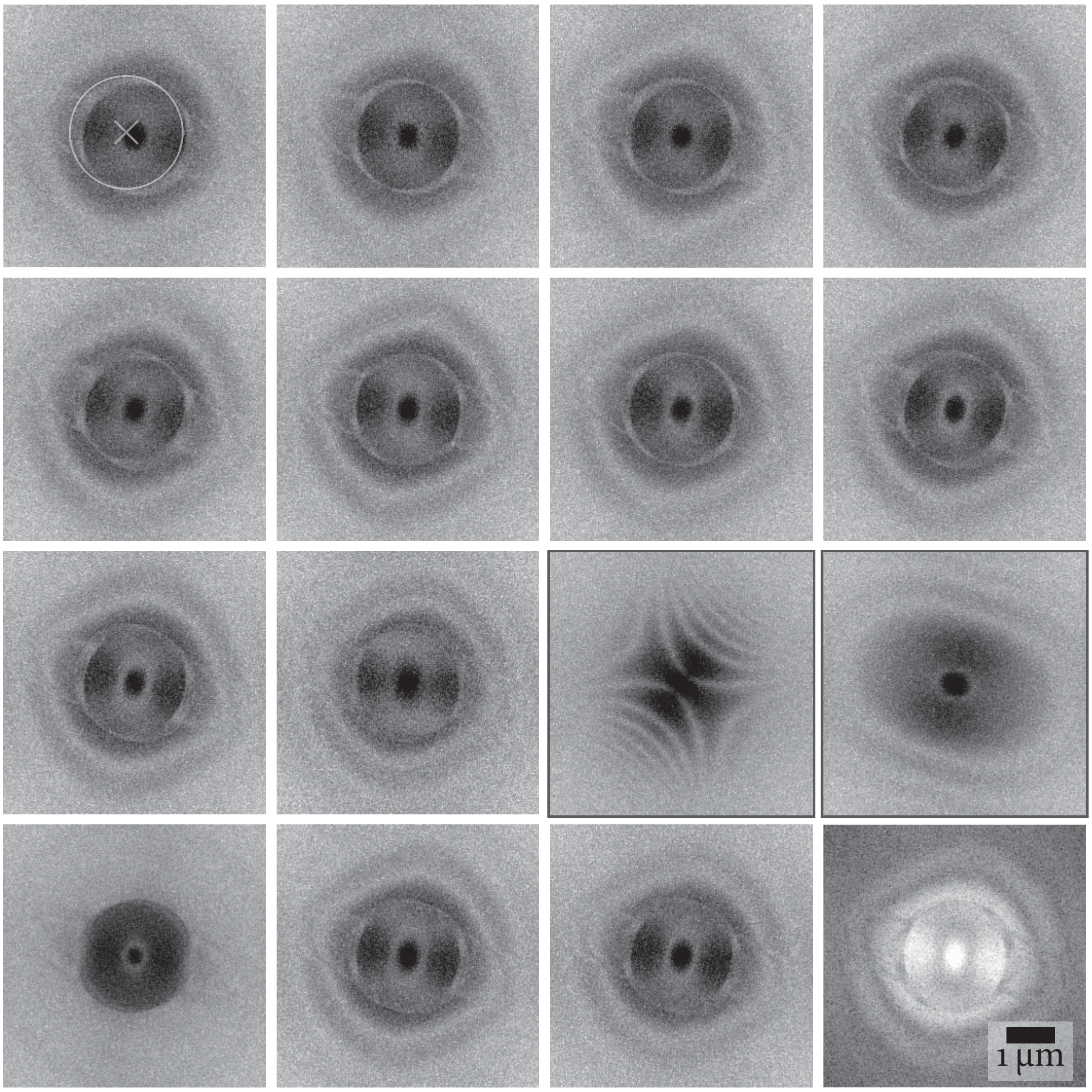

Figure 6.9: Evolution of phase plate charging with static imaging mode. From left-to-right and top-to-bottom, the diffractogram images show the condition of the phase plate directly after consecutive automated alignment sequences. The charging effects can be seen in a circular intensity modulation in the film material following the phase plate hole and hole remainder outline. With each alignment sequence, the charging becomes worse. The repeatability of the attained phase plate position (marked in the first diffractogram) is satisfactory.
The highlighted diffractograms (□) show the situation after an unsuccessful phase plate alignment attempt, where the zero-order beam is focused on the film material far away from the location of the phase plate hole.

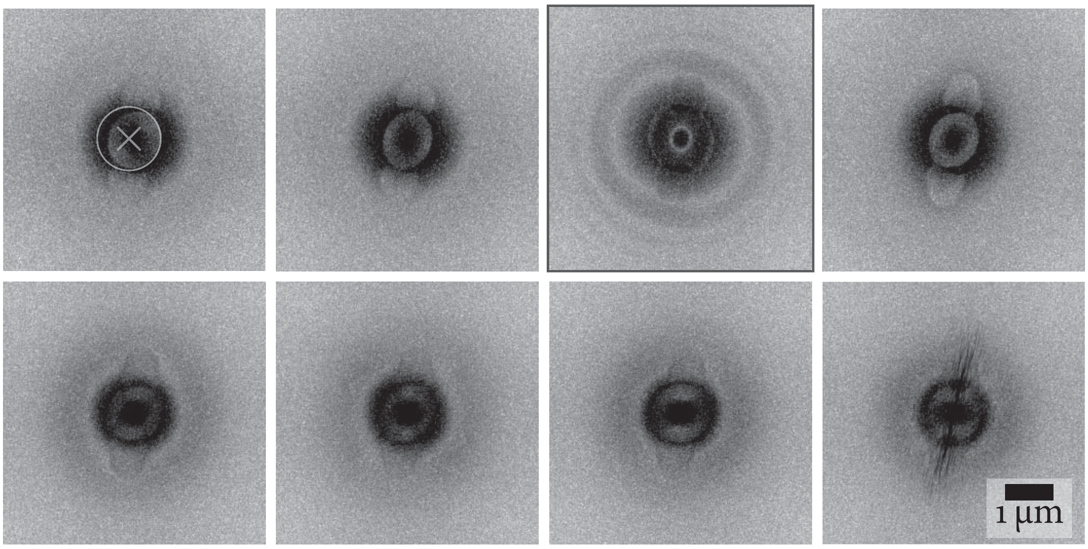

Figure 6.10: Evolution of phase plate charging with applied dynamic imaging mode. From left-to-right and top-to-bottom, the diffractograms show the phase plate condition directly after consecutive automated alignment sequences. Phase plate charging influences the focus of the zero-order beam, such that its focus is no longer in the same plane as the phase plate. This can be seen in a blurred edge of the phase plate hole. The Thon rings in the highlighted (□) diffractogram stem from a focusing error, with a defocus mismatch of about 4 µm.

compared to the latter and pointing to the alignment process as the culprit of phase plate charging.

However, as discussed in section 3.5.1, a certain signal-to-noise ratio has to be attained while probing the phase plate for a reliable position determination. Therein, presence of thicker parts of the sample, which reduces the signal by about a factor of two result in a significantly higher probability of a failed position determination. Hence, there is not much margin for further reduction of the probing intensity.

The phase plate degradation becomes worse, if the margin for alignment errors is reduced by application of smaller phase plates and use of the dynamic imaging mode. Similarly to the circumstances described above, images documenting the phase plate position directly after the alignment sequence are acquired. In figure 6.10, the alignment history of the specific phase plate used in section 6.2 is recorded from first insertion to acquisition of the images shown in figures 6.7 and 6.8.

There is an initial misalignment of about 100 nm, most likely for the same reasons as discussed above. This time, the dynamic imaging mode is used after the phase plate alignment, and the zero-order beam is scanned along the hole perimeter with a precession radius of 0.177 mrad, while the phase plate hole has a radius corresponding to 0.18 mrad. The corresponding real-space distance is only about 15 nm, which is smaller than the initial misalignment and hence the focused zero-order beam is scanned over the film material.

Surprisingly, no immediate effect can be seen in the second diffractogram. In the third image, a pronounced ring system is visible. An analysis of the recorded data from the automated image acquisition software shows that the preceding focusing sequence failed, as a minor focus mismatch was corrected with a defocus change of 4.1 μm. Therefore, the observed rings are not caused by the phase plate charging, but are regular Thon rings. This is confirmed in the following exposure, which shows an unsuspicious modulation of the diffractogram.

Starting with the fifth exposure, the edge of the phase plate hole appears blurred. This is due to the charged phase plate affecting the location of the zero-order beam focus in z-direction, i. e. the plane of zero-order beam focus and phase plate is no longer coincident.

By this, the phase plate is effectively no longer applied in a diffraction plane and especially not in a plane with a clear spatial separation of scattered and unscattered electrons. During the precessing motion, the phase plate edge intersects the cone of the zero-order beam and modulates it with the film material. Since the remainder of the cut-out hole is still present at a specific orientation, the structure factors corresponding to that azimuthal range of spatial frequencies are subjected to an irregular contrast transfer. This results in the particular contrast modulation of the gold nanoparticles.

In figure 6.11, representative nanoparticles from each exposure corresponding to the respective phase plate conditions (cf. figure 6.10) are shown. In the upper row, no specific signs of irregular contrast can be seen, while the lower row shows a progressing deterioration.

6.4 VERIFICATION OF HIGH-RESOLUTION COMPATIBILITY

To demonstrate the compatibility of high-resolution imaging and dynamic imaging mode, an inverted, thermally annealed bulk heterojunction consisting of an 1:1 blend of F_4ZnPc/C_{60} with a thickness of about 45 nm is used [63]. Compared to the sample used for demonstrating the enhanced low spatial frequency contrast transfer (cf. section 6.2), which quickly

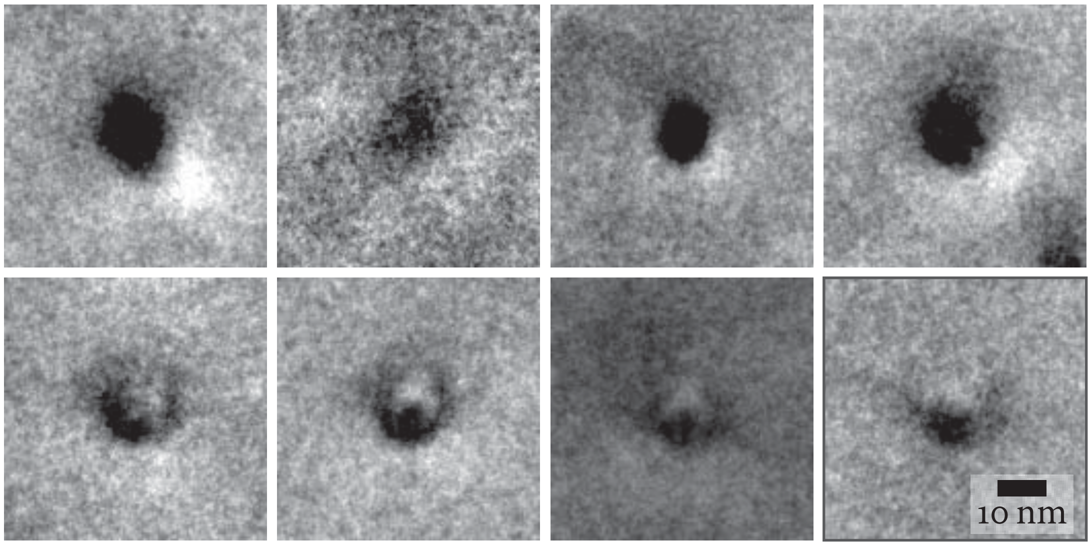

Figure 6.11: Nanoparticle contrast evolution using dynamic imaging mode. From left-to-right and top-to-bottom, the phase plate accumulates charge, which changes the zero-order beam focus in z-direction, i. e. the zero-order beam is no longer focused in the phase plate plane. Because of this, the structure factors corresponding to the same azimuthal orientation as the phase plate hole remainder are partially influenced differently, which results in an inverted contrast. The highlighted image (□) shows the nanoparticle marked in figure 6.7 (**A**).

shows degeneration upon multiple exposures, the present sample allows acquisition of at least three images with a doubled dose of 60 e^{-} Å^{-2}, before the high spatial frequency information present in the sample starts to vanish. This allows performing the focusing sequence at the area of interest.

Figure 6.12 shows the sample imaged with an applied amorphous-metal Zernike film phase plate with a larger hole size of approximately 2.25 µm radius in static and dynamic imaging mode. For the latter, the precession radius has been chosen not to intimately follow the phase plate hole perimeter. On the one hand, this reduces the electron-exposure of the delicate phase plate edge. On the other hand, this gives a higher probability of a successful high spatial frequency information transfer. As detailed in section 5.1.2, the illumination tilt applied during the dynamic imaging mode blurs high resolution image information, if the focus mismatch is too large. There is a small uncertainty of the attained focus due to the sample topology.

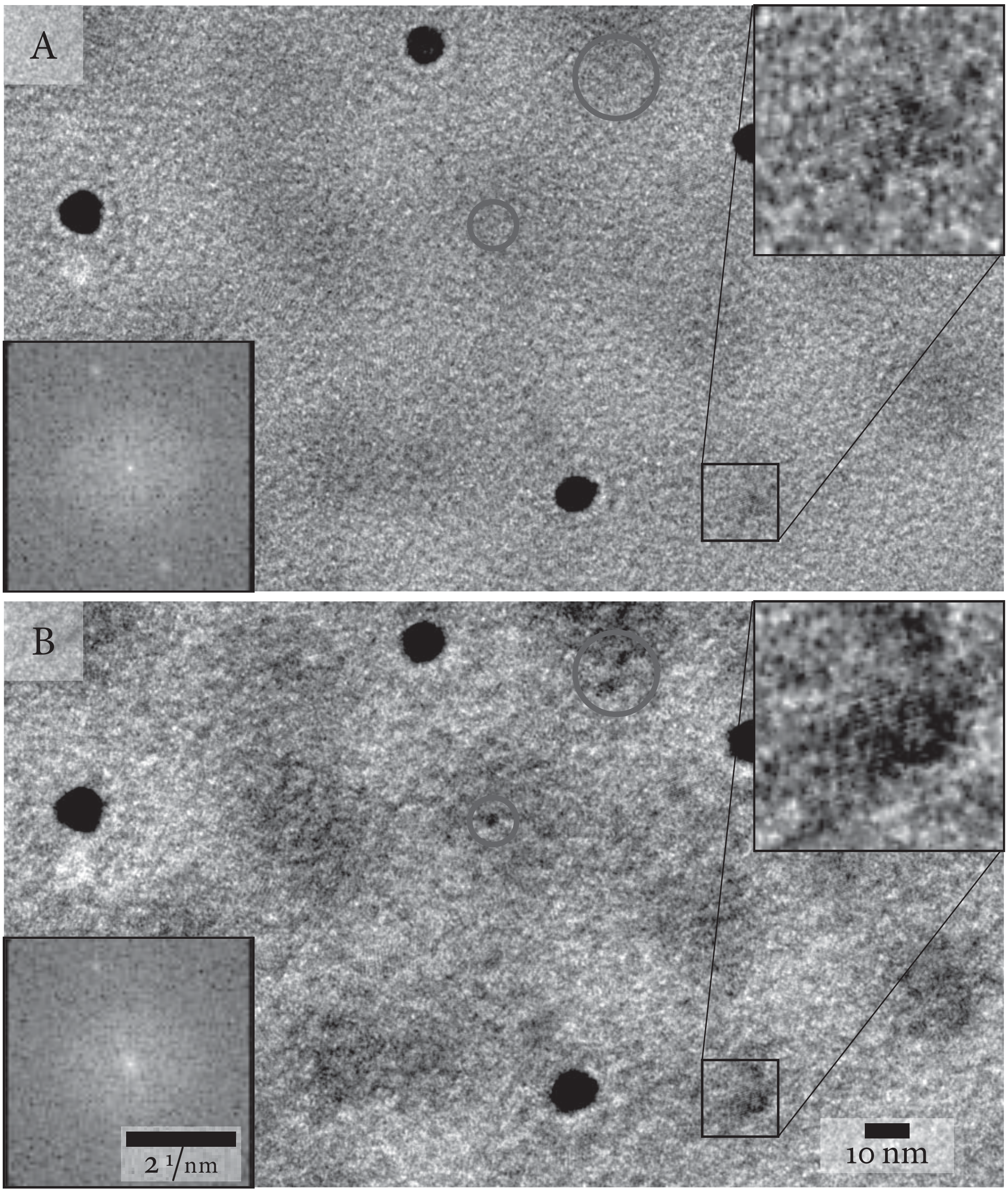

Figure 6.12: Close-to-focus images of an inverted organic photovoltaic cell imaged with an applied Zernike phase plate in static (**A**) and dynamic imaging mode (**B**). The non-linear contrast contribution of the dynamic imaging mode has been corrected by image processing. In the highlighted areas (○), a clear contrast improvement is visible. The lowest spatial frequencies are not affected, as the precession radius is not sufficient. Top right insets show a region with high-resolution image information. The corresponding diffractograms are shown in the lower left.

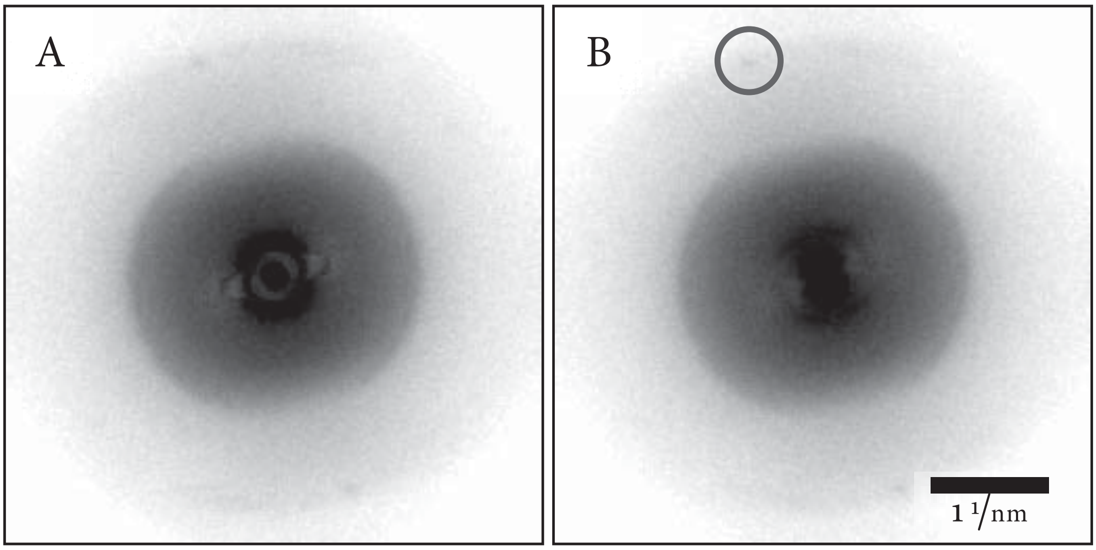

Figure 6.13: Periodograms of images depicted in figure 6.12. Static phase plate (**A**) shows intensity around the phase plate hole perimeter, suggesting a small charge. Using dynamic imaging mode (**B**), this edge is relocated to about 1.5 × the phase plate radius. This results in information transfer from about 50 to 5 Å (○).

Nevertheless, with 0.35 mrad the precession radius is chosen larger than in the experiment to demonstrate the influence on the low spatial frequencies (cf. section 6.2). With the much larger phase plate, this results in an effective cut-on frequency of about $0.2\,\mathrm{nm}^{-1}$.

The sample is highly crystalline and offers structures with periodicities in excess of $2\,\mathrm{nm}^{-1}$. In figure 6.12, the insets show successful transfer of an exemplary feature with a periodicity of 5.3 Å. The corresponding periodograms shown in figure 6.13 assess the presence of that resolution in both static and dynamic phase plate application modes.

At the same time, the dynamic imaging mode enables a better contrast of features with a size of up to 5 nm, corresponding to the chosen precession radius. Enhanced contrast transfer of such features can be seen in the highlighted regions of figure 6.12.

High spatial frequency contrast transfer is impeded by the additional attenuation of the phase plate film material, the modulation of the pCTF due to non-vanishing wave aberrations (cf. figure 6.4 for a plot of the approximate wave aberration conditions), the dampening envelopes and a further attenuation by the detector's MTF and DQE.

6.5 PHASE PLATE TOMOGRAPHY

The literature knows a few reports of successful acquisition and reconstruction of tomograms with applied Zernike film phase plates [15, 14], mostly to address low-resolution problems in the range of 5–10 nm. Compared to a standard approach using high defocus and a large field of view of $1.8 \times 1.8\,\mu m^2$, three- to fivefold contrast increase of the low spatial frequencies at an identical dose is reported [14]. The use of a phase plate is described as an enabling technology to identify the interesting parts of the sample. Similarly, a low spatial frequency contrast transfer enhancement is reported in [41].

In [15, 14], a fully manual approach is described, which takes about 2 to 3 h for the acquisition of a single tilt series from −60 to 60° in 3° increments. A semi-automated approach with manual specimen and phase plate hole tracking is reported in [41].

In principle, the algorithm described in section 3.1.4, can be trivially extended to support automated tilt-series acquisition with an applied phase plate, as the geometry model accounts for the 3D sample movement, i. e. specimen shift in x, y and z. However, for the available microscope, several instrumental shortcomings need to be addressed for a successful application.

6.5.1 *Adaptation to the Titan Krios*

In trial runs without an applied phase plate, the mismatch of optical axis and mechanical tilt axis was measured and corrected for, and the required model of the geometry set up. The standard acquisition scheme begins with a stage tilt of 0°, and uses negative tilt increments up to the maximum tilt value, then returns to 0°, accounts for a possible mismatch compared to the first untilted image, and begins with acquisition of another tilt series using positive tilt increments. Unfortunately, the exact location of the mechanical tilt axis seems to be dependent on the tilting direction, which introduces a large mismatch of tilt axis and optical axis of about 600 nm.

Inability of the system to align specimen-plane, mechanical tilt axis and optical axis inevitably results in a 3D specimen shift as a function of the mechanical stage tilt, which need to be compensated using the image shift deflectors and the focus of the objective lens.

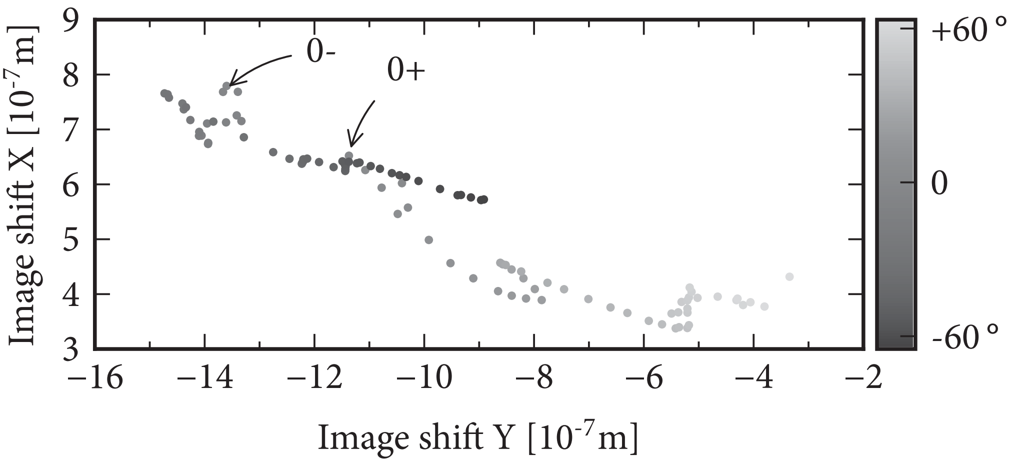

Figure 6.14: Compensatory image shifts as applied during a typical tilt series. The magnitude of applied image shifts is minimal in the negative tilting direction, as the electron-optical alignment is optimized for it. The values for the start of both tilt series at 0° is not coincident, since the stage fails to mechanically reproduce the original specimen position, which is compensated by an image shift.

Shift Compensation

A typical distribution of the image shifts to compensate for the specimen movement during a tilt-series acquisition is shown in figure 6.14.

The graph shows a complicated movement pattern with necessary image shifts of up to about 1 μm. For phase plate application, use of the image shift deflectors has to be side-effect free, i. e. must not change the inclination of the optical axis. Using the alignment protocol detailed in appendix B, this requirement can be met for the needed distances.

Defocus Compensation

To provide an advantage, phase plates need to be applied with vanishing or very small wave-aberrations. Therefore, tight control of the attained focus is of high importance, which demands a precise determination of the parameters of the model geometry. In principle, very accurate predictions in x, y and z are attainable, as reported in [91].

However, for the present instrument, the algorithm fails in a reproducible way. For one tilting direction, the position of the optical axis can be chosen to be coincident with the tilt axis. This results in minor focus deviations. For the tilt axis position for the other tilting direction, the focus predictions from the model are not accurate and result in a large mismatch

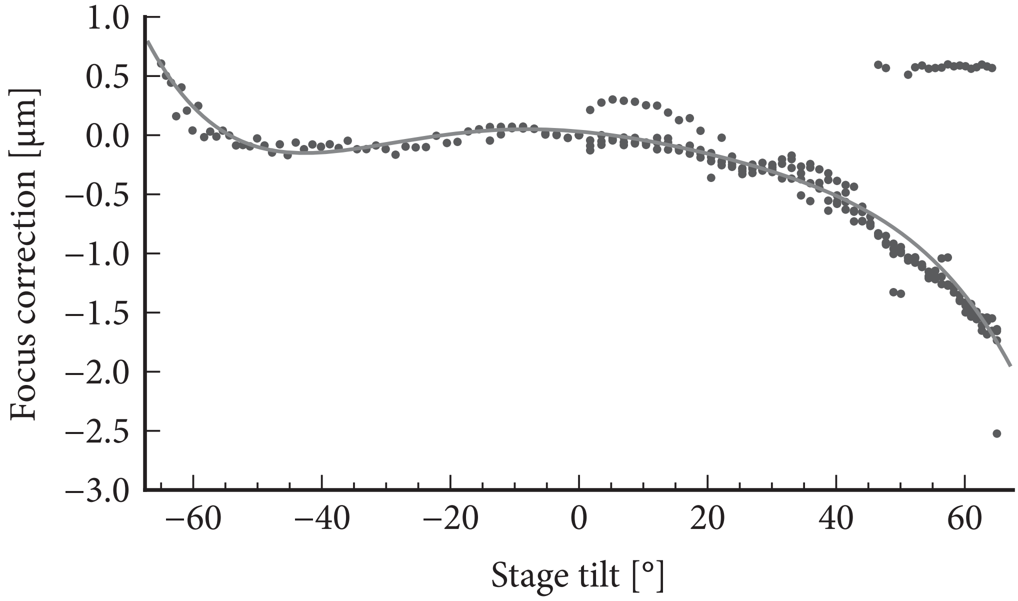

Figure 6.15: Defocus compensation during tilt series acquisition. Probably due to mechanical imperfections of the stage, the algorithms fails to predict correct values for focus compensation. Smoothed values are found by application of a regression using a sixth order polynomial on the defocus variation of several tilt series.

of desired and attained focus. The exact reasons for this behaviour could not be determined with certainty, but can most likely be attributed to the mechanical properties of the stage, which is not reproduced by the model geometry.

Fortunately, the focus mismatch was found to be well reproducible and can therefore be corrected. For the necessary characterisation, several tilt series with large initial defocus were acquired and evaluated using *ctffind4* [67]. The resulting data are shown in figure 6.15.

From the data, a behavioural model of the defocus mismatch was generated: By using the random sample consensus algorithm [30] to exclude outliers from the regression, a sixth order polynomial was fitted to the normalized defocus values for expressing the necessary focus correction as a function of the mechanical stage tilt.

The model was tested by acquisition of several tilt series with large intended initial defocus. A subsequent analysis of the attained focus using *ctffind4* confirmed its suitability.

An alternative way of optimizing the focusing behaviour could be an accurate calibration of the mechanical tilt axis location and a mechanical relocation of the specimen to this point upon changing the tilting direction.

6.5.2 *Application*

With the aforementioned adaptations, integration of a phase plate is trivial. After having chosen the area of interest in a lower magnification image, focus area and area of interest were selected, similarly to the procedure described in section 3.1.3. After precise focusing with the stage using an untilted view, the phase plate was aligned at the same offset position as the focusing was done (cf. section 3.6.2). Then, the first half of the tilt series was acquired. Since the alignment of the condenser system allows to apply large image shifts without introducing any tilt (cf. section 3.3), the phase plate position remained stable throughout the tilt-series acquisition.

After the first half of the tilt-series has been acquired, the phase plate is removed and the preset switched to the lower magnification setting to account for any mechanical shift of specimen and stage. The necessary image shift offset is calculated, and the phase plate recentred at the former focusing position. Then, the other half of the tilt-series was acquired.

Upon visual inspection, the phase plate appeared to remain centred for every member of the tilt series. Average diffractograms from all tilted views and all slices of the reconstructed tomogram can be seen in figure 6.16. The averages show the characteristic features of a well-aligned phase plate.

The acquisition of the whole tilt series using a field of view of $435 \times 435\,\mathrm{nm}^2$ in 98 individual views ranging from -65 to $65°$ could be successfully demonstrated. Including the time for focusing and aligning the phase plate two times, the procedure takes about 0.5 h.

No additional degradation of the phase plate could be discovered after acquisition of the last member of the tilt series. This may be due to the increased stability of metal film phase plates compared to amorphous-carbon film phase plates, the greater distance from the zero-order beam as a result of using a larger phase plate or the well controlled acquisition scheme, which avoids contact of the focused zero-order beam with the phase plate film material.

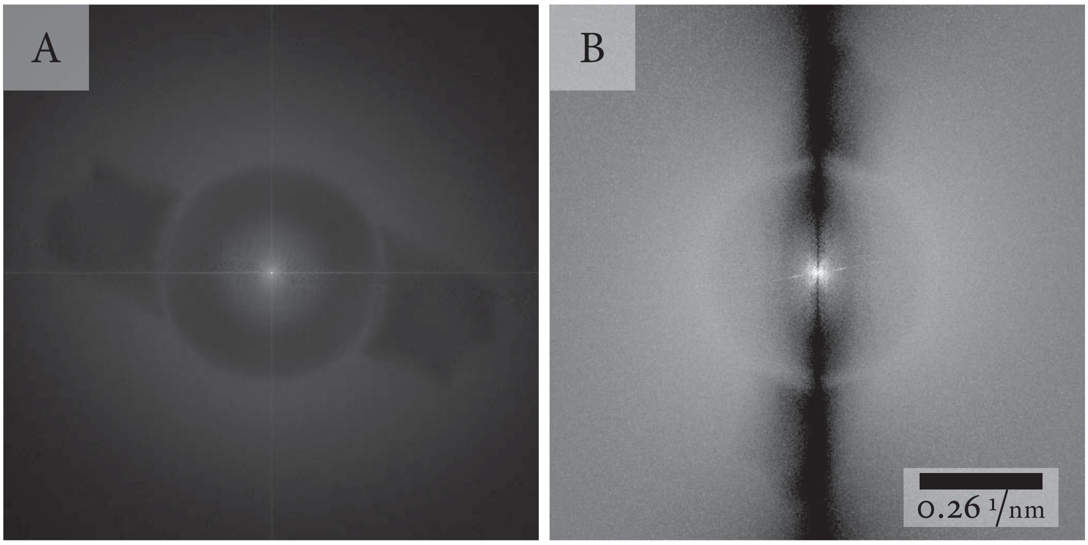

Figure 6.16: Diffractogram averages of tomogram data. Average of all members of the tilt series (**A**) and of all z slices of the tomogram reconstruction (**B**).

6.6 DISCUSSION

From the two tested phase plate types, only the amorphous-carbon coated metal film phase plates were able to generate the expected contrast for low spatial frequencies. Moreover, they produced only negligible image and focus shifts upon insertion and they could be aligned without having to use identical illumination conditions as for the final exposure. All of this hints at a smaller charging susceptibility. Therefore, an amorphous-carbon coating seems to be key to reduce the charging behaviour of metal film phase plates, just as it was the case for the electrostatic phase plates.

The dynamic imaging mode proves to be compatible with high-resolution imaging. Preconditions for the successful application are a very precise focusing and a reasonable size of the round phase plate. If a C_s-corrected instrument is available, the latter restriction is less striking, as discussed in section 5.1.3. Also, a clear improvement of the low spatial frequency contrast transfer can be seen, as the prominent fringing artefacts are completely eliminated, and the attained contrast is higher than in images with appropriate defocus.

Application to beam-sensitive specimen can be done easily, if the electron-optical alignment allows to change the field of view without altering the relative position of the phase plate with respect to the zero-order beam.

With very careful calibration of the movements of the microscope stage, this even enables the unattended acquisition of tomographic tilt-series. The dynamic imaging mode was not tested with tomogram acquisition, as the defocus gradient present in the tilted views combined with a precessing illumination would result in a blurring of the image on the detector. If the precessing motion was implemented with a mechanical phase plate translation, this restriction would not apply.

Future attempts to improve the situation could possibly make use of the image tilt/diffraction shift deflectors located below the phase plate plane to generate a compensating tilt, which could enable the use of the dynamic imaging mode also for out-of-focus conditions. The feasibility depends on the distance of specimen-plane and the image tilt deflectors, which introduces a non-linear dependence of defocus and tilt on the image shift. For small phase plate holes, small field of views and low resolution requirements, the approach might be realizable but needs a careful evaluation beforehand.

The lifetime of a Zernike film phase plate depends on the way it is used. Contact of the zero-order beam with the delicate hole perimeter has to be avoided by all means. This complicates the applicability of the dynamic imaging mode.

Using the defocused condenser method for alignment, a degradation is visible even for the small doses used. If the phase plate is aligned on a thin part of the sample, the dose can be reduced without penalising the attained precision. Also, the number of images taken during the multi-scale alignment procedure can be reduced, if the accuracy of the mechanical translation is improved. Alternatively, this can be realized with the present hardware by employing the beam tilt deflectors for phase plate alignment. This might require using a C_s-corrected system to avoid a negative influence on the image quality.

However, reduction of the dose only prolongs the usable time of the phase plate and does not solve the fundamental charging problem. For that, development of film materials less susceptible to charging is necessary.

An alternative alignment approach using parallel illumination and large phase plate holes might be feasible and offer a superior performance in terms of charging behaviour: The mechanical precision of the translation device is good enough to bring the phase plate to a lateral position, where the zero-order beam is threaded through the hole, if a non-charging phase plate is used. Absence of a charge also ensures a focused zero-order beam in the phase plate plane, which in turn produces a recognizable signal for an image processing algorithm to determine the position-mismatch with a suitable specimen-background. The ambiguity imposed by the Friedel-symmetry can be resolved by an asymmetric phase plate structure, such as the proposed pentagonal hole. This Fourier-domain based approach is most likely less robust compared to the defocused-condenser method, as presence of a small charge or unsuitable specimen background increases the probability of an unsuccessful position determination.

7 SUMMARY AND OUTLOOK

There is a growing interest to understand the structure-function relationships of low atomic-number samples in material-science and structural-biology. TEM is a key technology to visualize such samples on a broad scale, as its imaging regime ranges from Ångstrom resolution to the micrometer scale. Furthermore, it has the ability to extract information not only from the surface of the sample, but also from the bulk, unlike many other microscopy technologies.

Unfortunately, as the main contrast mechanism of low-Z materials is a modulation of the phase of the electron wave, contrast transfer in conventional TEM is severely impeded by the unfavourable properties of the pCTF. Especially when interested in faithful representation of the low spatial frequencies present in the sample, conventional TEM demands use of excessive defocus values to apply the necessary phase shift of $\pi/2$, which in turn causes contrast inversions and image aberrations, rendering the image contrast subject to interpretation.

Phase plate technology for TEM is a potential cure to this problem, but the practicability of its application is severely impeded by the additional and delicate steps required to bring them to use, as well as the limited lifetime of the available phase plates.

7.1 AUTOMATION

Several methods and procedures to enable automated phase plate alignment have been integrated into the Leginon framework. Necessary modifications were the augmentation of the internal data structures, e. g. to enable tight control of the beam conditions in the diffraction plane, as well as addition of the necessary infrastructure to manipulate the position of a phase plate. Furthermore, several image processing algorithms to determine the current phase plate position have been developed, integrated and evaluated. Due to the modular approach, the extensions are compatible with Leginon's standard automation workflows, which has been demonstrated in single-particle and tomography contexts.

During application, several aspects of automated image acquisition were found essential for reliable phase plate alignment:

- Dedicated presets with a known relationship of the relative optical axis position allow phase plate centring across different scales. This is very helpful, as it allows compensation of large positioning errors with very low dose.
- The defined sequence of presets controls the hysteresis effects of the optical system.
- Automated focusing routines proved to be suitable to precisely attain the desired focus for controlling the residual wave aberrations.
- Focusing and phase plate alignment can routinely be carried out at an offset position, which enables application to beam-sensitive specimen.

The controlled imaging conditions allow a reliable phase plate detection and a very precise phase plate alignment with respect to the zero-order beam. This is a key capability to enable deterministic application and advanced acquisition schemes, such as the dynamic imaging mode with Zernike film phase plates.

7.2 PHASE PLATES

All phase plates used in this work suffered from strong charging effects, which eventually dominate the phase shifting property. By cautious use during phase plate alignment, where the amount of electrons interacting with the phase plate structure is limited, the lifetime of the phase plates could be increased.

First and foremost, the exposure of the phase plate structure to the focused zero-order beam has to be avoided. Also a defocused zero-order beam should be avoided, as it was shown that it also results in a progressively increasing static charge on the phase plate. But since a certain probing of the phase plate structure is inevitably necessary for position-determination, optimised conditions should be chosen, which minimise the used dose. To enable a successful phase plate alignment in fewer attempts, the accuracy of the mechanical translation should to be improved.

Phase plate technology would greatly benefit from the availability of highly conductive materials immune to charging-effects. This is a current research interest, e. g. the investigations of Manuel Dries and Simon Hettler/LEM.

7.2.1 *Zernike Film Phase Plates*

Two different implementations of Zernike hole film phase plates could be evaluated, one plain-metal phase plate by KonTEM, and another made of an amorphous metal foil with amorphous-carbon coating by Manuel Dries and Tina Schulze/LEM. The latter showed a reduced charging behaviour, which allowed phase contrast imaging with the expected qualitative contrast for low spatial frequencies at least for a couple of exposures.

For both phase plate types, the cut-on effects can be effectively reduced by using the dynamic imaging mode, which renders the effective cut-on frequency a tunable parameter. Since the hole diameter is no longer decisive for the attained cut-on frequency, large phase plate holes can be used, which offer better detectability in a Fourier-domain based alignment scheme.

Depending on the chosen precession radius, the phase plate hole perimeter needs to sustain an elevated electron dose due to the finite size of the zero-order beam and potentially a high amount of low spatial frequencies present in the sample. Large phase plate holes offer a much greater hole perimeter area, which helps distribute the charge on a larger surface. This in turn increases the effective lifetime of the phase plate.

With the dynamic imaging mode, the low spatial frequency contrast transfer is modulated according to the chosen precession radius and the physical size of the phase plate hole. For quantitative image contrast, this modulation can be accounted for in an image processing step. Since both phase and amplitude contrast are similarly transferred, the dynamic imaging mode is only applicable to certain specimen which offer mainly phase contrast information and only negligible amplitude contrast.

7.2.2 *Electrostatic Zach Phase Plate*

Electrostatic phase plates provide superior properties, such as a tunable phase shift and avoiding an additional scattering process for the electrons already diffracted by the sample. However, the available Zach phase plates installed in the magnified diffraction plane of the Zeiss KRONOS microscope were unfit to leverage their theoretical advantage and failed to produce usable images. The problems can be attributed to the presence of an insulating material, which traps implanted charges. Eventually, those charges dominate the phase-shifting effect of the phase plate.

To avoid the charging effects, the insulator needs to be removed in the area close to the phase plate tip to a sufficient distance. To manufacture such a free-standing electrode, back-etching techniques can be used.

Even noble metals (gold) used as the material for the electrode surface were found to exhibit a charging behaviour in the electron-beam. To improve the applicability of electrostatic phase plates, the electrode material needs to be optimized, e. g. by using a coating with titanium and amorphous carbon.

If the charging problem can be solved, the amount of obstructed spatial frequencies can be minimized by physical miniaturisation of the electrode assembly. For that, the methods developed for the semiconductor-industry could be leveraged. Alternatively, the installation of the phase plate in a magnified diffraction plane was shown to be feasible.

7.3 INSTRUMENTATION

The magnified diffraction plane in the prototype phase contrast instrument Zeiss KRONOS failed to provide an advantageous environment for the phase plates. This is not caused by insufficient electron-optical properties of the diffraction plane but rather the amplification of the detrimental charging effects of the available phase plates due to the magnified conditions.

Also due to the magnified conditions, the requirements on the quality of the electron-optical alignment of the instrument are elevated compared to a standard configuration. The situation is further complicated by the presence of a C_S-corrector located in front of the magnified diffraction plane.

Generally, phase plate application benefits from a very small focus of the zero-order beam in the diffraction plane, which corresponds to a high spatial coherence of the electron source. This is especially true when the phase plates are installed in a magnified diffraction plane. The standard approach uses small condenser apertures and a suitable electron-optical demagnification of the electron source, which decreases the luminosity. This in turn requires longer exposure times and a corresponding higher electrical and mechanical stability of the microscope column. An alternative approach may be the use of better electron sources with cold rather than thermally-assisted Schottky emitters.

For Zernike film phase plates, the conditions presented in a microscope with standard electron optics and an intermediate focal length, such as the Titan Krios proved to be sufficient. The clean vacuum conditions established by a quasi-permanently applied anticontaminator effectively prevent adsorption of contamination particles on the phase plate structure. With the dynamic imaging mode, the effective cut-on frequency is a tunable parameter. Its applicability could be further increased by integration of a C_s-corrector and a better electron source.

7.4 SAMPLES

This work focused on the development of the necessary methods and approaches to enable automated phase contrast imaging and not on actual application with the primary intent to gain further insight on the imaged specimen. The developed automated approach allows using the dynamic imaging mode in a dose-limited environment, as shown at the example of a beam-sensitive biological specimen. With a material science sample, an active layer of an organic photovoltaic cell featuring highly crystalline regions, the compatibility of the dynamic imaging mode with high-resolution image information was shown. On both samples, the tunability of the effective cut-on frequency could be demonstrated and a better low spatial frequency contrast transfer free from the typical cut-on artefact could be achieved.

With the methods developed in this work, the phase plate imaging should be applied to suitable samples with the intent to exploit the superior imaging conditions. This should be done on both biological and material-science specimen.

7.5 OUTLOOK

Such experiments should also compare the performance of Zernike phase plates used with dynamic imaging mode, electrostatic Zach phase plates and Volta phase plates. To ensure deterministic and repeatable imaging conditions, this comparison should be implemented using an automation software supporting tight control of the diffraction plane, such as the extensions to Leginon developed in this work. The proposed improvement of the Zernike phase plate hole in form of a symmetry-breaking pentagonal shape should be evaluated, just as the possibilities to make the dynamic imaging mode compatible with tomography applications by application of a matching tilt below the phase plate.

If a constant phase shift of $\pi/2$ is the only required property, the Volta phase plate might provide sufficient results for the majority of the specimen. Advanced imaging techniques, such as gathering the necessary information for an exit-wave reconstruction in only three images requires a tunable phase shift, which could be provided by electrostatic and laser phase plates.

Since the magnified diffraction plane in the KRONOS instrument amplifies the detrimental charging effects, the performance of a Zach phase plate should be evaluated in a modern conventional electron-optical set-up. With minor modifications, the phase plate could be installed in the first diffraction plane of the TITAN KRIOS with the KonTEM micromanipulator, and the performance evaluated. The developed routines integrated into the Leginon software can be used for automated phase plate application. For that, only minor modifications are necessary, such as the adjustment of the template used for identifying the current phase plate position.

If the proposed improvements to the Zach phase plate are not sufficient to reduce the charging behaviour to an acceptable level, the matter-free design of the proposed anamorphic phase plate should be evaluated. This design requires a specialised electron-optical set-up with two successive, elongated and orthogonally oriented diffraction planes. For the design of such a microscope element, the experience gained from the prototype instrument Zeiss KRONOS can be adapted:

The proposed column element should be placed directly below the objective lens to avoid unnecessary complication of the electron-optical alignment. This probably requires an additional transfer lens to relay the first diffraction plane of the objective lens to the plane where the first phase plate is located. If the transfer lens is carried out using a zoom system consisting of two lenses, the effective focal length of the system becomes adjustable. In the beam path between the electron-source and the phase plate planes, every round lens should be provided with a full set of deflectors to enable the possibility of a perfect electron-optical alignment. Special attention should be given to the design of the vacuum system, which should be capable of attaining at least the same terminal pressure as reached in the specimen plane with an applied anticontaminator.

While C_s-correction is not strictly required for demonstrating the applicability of the set-up, it is highly desired for actual imaging. Therefore, provisions to integrate such a system should be made. To avoid alignment problems, it should be located in the beam path below the diffraction planes.

Apart from the improvements to the optical system, the instrument should be equipped with a detector providing a large field of view as well as high MTF and DQE to improve the signal available for Fourier-domain-based phase plate alignment.

Part I

APPENDIX

A HILBERT CONDITIONS WITH SEMI-TRANSPARENT $\pi/2$ FILM

Similarly to the conditions found when using a Hilbert phase plate, for a misaligned Zernike hole phase plate, the phase-shifting film material is only effective on one Friedel pair. The difference to Hilbert conditions is the phase-shifting capability of the film material, as it is only half of that of an ideal Hilbert phase plate. This results in different contrast transfer to the image intensity, as shown below.

Following the argumentation in [19] for weak phase weak amplitude objects, the modulated diffraction wave can be written as

$$\begin{aligned} G(\mathbf{q}) &= B(\mathbf{q}) \exp(iP(\mathbf{q})) \\ \Phi(\mathbf{q}) &= [\delta(\mathbf{q}) + \hat{\varepsilon}(\mathbf{q}) - i\hat{\varphi}(\mathbf{q})]\, G(\mathbf{q}) \end{aligned}$$

with $\hat{\varepsilon}$ and $\hat{\varphi}$ the amplitude and phase structure factor contributions at spatial frequency q, which are modulated by a complex modulation function G, which can account for various amplitude and phase modulations B and P of the object wave. Splitting the latter in symmetric and asymmetric contributions, designated by indices $_S$ and $_A$, neglecting second order effects and exploiting symmetry relationships of Fourier transforms for a real valued intensity representation in direct space, the image intensity can be expressed by

$$\begin{aligned} I(\mathbf{r}) = \; & B^2(0) + 2B(0)\mathcal{F}^{-1}\Big\{\hat{\varepsilon}(\mathbf{q})\big[B_S(\mathbf{q})\cos(P_S(\mathbf{q})) \\ & + iB_A(\mathbf{q})\sin(P_S(\mathbf{q}))\big]\exp(iP_A(\mathbf{q})) \\ & - \hat{\varphi}(\mathbf{q})\big[-B_S(\mathbf{q})\sin(P_S(\mathbf{q})) \\ & + iB_A(\mathbf{q})\cos(P_S(\mathbf{q}))\big]\exp(iP_A(\mathbf{q}))\Big\} \end{aligned} \tag{A.1}$$

as shown in [19].

Here, the modulation function G consists of the wave aberration function $\gamma(\mathbf{q})$ and contributions from the phase plate on one half of the diffraction plane. The zero-order beam or illumination term is described by $B(0)$. The spatial frequency at which the edge of the phase plate is located is designated by q_0, similar to the cut-on frequency, but only effective in one spatial frequency unit vector q_x perpendicular to the phase plate edge.

As a side effect of the phase-shifting capability, any matter film phase plate will exert some attenuation $a_0 \in [0,1]$ on the passing electrons, due to scattering and absorption. Contrary to standard Hilbert phase plates, the phase shift is not $-\pi$, but $-\pi/2$. The complex object wave modulation G is then

$$G(\mathbf{q}) = \begin{cases} \exp(i\gamma(\mathbf{q})) & q_x \geq q_0 \\ a_0 \exp\left(i\left(\gamma(\mathbf{q}) - \frac{\pi}{2}\right)\right) & q_x < q_0 \end{cases}, \quad q_0 \leq 0.$$

In the following, it is assumed that $q_0 = 0$, i. e. the phase plate edge is in contact with the zero-order beam.

The object wave modulation is split into symmetric and asymmetric parts of amplitude and phase modulation factors:

$$\begin{aligned} P_S &= \gamma(\mathbf{q}) - \tfrac{\pi}{4} & P_A &= \tfrac{\pi}{4} \cdot \operatorname{sign}(q_x) \\ B_S &= \tfrac{1+a_0}{2} & B_A &= \tfrac{1-a_0}{2} \cdot \operatorname{sign}(q_x) \end{aligned}$$

and inserted into equation A.1. To increase clarity, phase and amplitude contributions are expanded separately. For the amplitude contrast modulation $\alpha(\mathbf{q})$, using equation A.1:

$$\begin{aligned} \alpha(\mathbf{q}) &= \left[B_S(\mathbf{q}) \cos(P_S(\mathbf{q})) \right. \\ &\quad \left. + iB_A(\mathbf{q}) \sin(P_S(\mathbf{q}))\right] \exp(iP_A(\mathbf{q})) \\ &= \left[\frac{1+a_0}{2} \cos\left(\frac{\pi}{4} - \gamma(\mathbf{q})\right)\right. \\ &\quad \left. + i\frac{1-a_0}{2} \cdot \operatorname{sign}(q_x) \sin\left(\gamma(\mathbf{q}) - \frac{\pi}{4}\right)\right] \exp\left(i\frac{\pi}{4} \cdot \operatorname{sign}(q_x)\right) \end{aligned}$$

which is hard to simplify any further. However, if the wave aberration function vanishes (i. e. for focus conditions and small q), further simplifications are possible, since $\sin\frac{\pi}{4} = \cos\frac{\pi}{4} = \frac{\sqrt{2}}{2}$. It follows

$$\begin{aligned}
\alpha(\mathbf{q}) &\approx \frac{\sqrt{2}}{2}\left(\frac{1+a_0}{2} - i\operatorname{sign}(q_x)\frac{1-a_0}{2}\right)\frac{\sqrt{2}}{2}\left(1 + i\operatorname{sign}(q_x)\right)\\
&\approx \frac{1}{4}\left(1 + a_0 + i\operatorname{sign}(q_x)(1+a_0) - i\operatorname{sign}(q_x)(1-a_0) + (1-a_0)\right)\\
&\approx \frac{1}{2}\left(1 + a_0 i\operatorname{sign}(q_x)\right).
\end{aligned}$$

Similarly, for the phase contrast modulation $\varphi(\mathbf{q})$:

$$\begin{aligned}
\psi(\mathbf{q}) &= \left[-B_S(\mathbf{q})\sin(P_S(\mathbf{q}))\right.\\
&\quad \left.+iB_A(\mathbf{q})\cos(P_S(\mathbf{q}))\right]\exp(iP_A(\mathbf{q}))\\
&= \left[-\frac{1+a_0}{2}\sin\left(\gamma(\mathbf{q}) - \frac{\pi}{4}\right)\right.\\
&\quad \left.+i\frac{1-a_0}{2}\cdot\operatorname{sign}(q_x)\cos\left(\gamma(\mathbf{q}) - \frac{\pi}{4}\right)\right]\exp\left(i\frac{\pi}{4}\cdot\operatorname{sign}(q_x)\right),
\end{aligned}$$

which again is not easily simplified. With vanishing wave aberrations, this becomes

$$\begin{aligned}
\psi(\mathbf{q}) &\approx \frac{\sqrt{2}}{2}\left[\frac{1+a_0}{2} + i\operatorname{sign}(q_x)\frac{1-a_0}{2}\right]\frac{\sqrt{2}}{2}\left(1 + i\operatorname{sign}(q_x)\right)\\
&\approx \frac{1}{4}\left((1+a_0) + i\operatorname{sign}(q_x)(1-a_0)\right)\left(1 + i\operatorname{sign}(q_x)\right)\\
&\approx \frac{1}{2}\left(a_0 + i\operatorname{sign}(q_x)\right).
\end{aligned}$$

The image intensity then becomes

$$\begin{aligned}
I(\mathbf{r}) &\approx B^2(0) + 2B(0)\mathcal{F}^{-1}\left\{\hat{\varepsilon}(\mathbf{q})\,\alpha(\mathbf{q}) - \hat{\varphi}(\mathbf{q})\,\psi(\mathbf{q})\right\}\\
&\approx B^2(0) + B(0)\mathcal{F}^{-1}\left\{\hat{\varepsilon}(\mathbf{q})\left(1 + a_0 i\operatorname{sign}(q_x)\right)\right.\\
&\qquad\qquad \left.- \hat{\varphi}(\mathbf{q})\left(a_0 + i\operatorname{sign}(q_x)\right)\right\}
\end{aligned}$$

Considering the alternative case with the phase plate edge placed at the other side of the zero-order beam, the only difference is the sign of q. If the resulting image intensities are incoherently summed, the sign terms with negative and positive contributions compensate each other due to the linearity of the Fourier transform. Therefore, the combined intensity of two images with a $\pi/2$ Hilbert phase plate on either side of the zero-order beam becomes

$$I(\mathbf{r}) \approx B^2(0) + B(0)\mathcal{F}^{-1}\left\{\hat{\varepsilon}(\mathbf{q}) - a_0\hat{\varphi}(\mathbf{q})\right\},$$

or with plane-wave illumination identified with unity and the structure factors transformed into direct space

$$I(\mathbf{r}) \approx 1 + \varepsilon(\mathbf{r}) - a_0\varphi(\mathbf{r}).$$

In the context of the dynamic imaging mode with the zero-order beam precessing along the perimeter of a Zernike phase plate hole, the contrast of the recorded in-focus image for the low spatial frequencies corresponding up to twice the radius of the phase plate hole is therefore proportional to a mixture of the object's amplitude and phase contrast information. Using a suitable specimen with vanishing amplitude contrast, this allows in-focus recording of the object's phase information. The recorded contrast is only half of what is attainable using a $\pi/2$ phase plate on both Friedel pairs concurrently, even for high phase plate film transmittances $a_0 \rightarrow 1$.

With the dynamic image acquisition mode described in chapter 5, an additional deterministic frequency-dependent modulation occurs, as detailed in section 5.1.3. With known parameters of the imaging process, this additional modulation is correctable.

B

CONDENSER ALIGNMENT OPTIMISATION

1. Normalize the objective lens and choose illumination conditions suitable for phase-contrast imaging. Select values for varying the illuminated area. Make sure the condenser system can attain parallel illumination for both values.

2. Use diffraction mode with a long camera length (e. g. 2 m) to visualize any tilt induced by the condenser

3. Toggle between the two illuminated areas, normalize the condenser lenses after each toggle

   a) For high excitations of the second condenser lens, adjust the *shift* in between second and third condenser lens

   b) For low excitations of the second condenser lens, adjust the *tilt*

   c) The goal is to find a setting where the centres of both caustic figures are coincident. Ideally, this is then also the case for the intermediate values of illuminated area.

4. Align the condenser tilt to the optical axis defined by the objective lens normal using *illumination tilt*

5. Repeat at 3 until satisfied

B.1 ILLUMINATION TILT AND SHIFT

The standard tilt calibration routines used by the microscope manufacturer usually apply rapidly alternating tilt values for each deflector system axis and ask the user to optimize the ratio of the deflector excitations in such a way that a spot or the image of the luminous field aperture remains stationary in image mode. Likewise, for calibrating the ratios for image shift, alternating values are applied, and the values modified such that the spot formed by the zero-order beam in the diffraction plane remains stationary. Within the scope of machines manufactured by FEI, this alignment is called *pivot-point alignment*.

For phase plate usage, the alignments for illumination shift and tilt are *very* important, as they enable changing the area of interest on the specimen without affecting the beam path below the objective lens. For both manufacturers, FEI and Zeiss, the necessary alignment routines are only enabled by using elevated user rights, such as so-called *supervisor* accounts or require *service* or *factory* logins to the control software. In case of FEI, the tilt pivot-point alignment is also accessible to an ordinary user.

If highest demands on precision are needed for a single lens configuration which e. g. brings the phase plate close to the diffraction plane, another technique can be used as follows:

1. Using image mode, the illumination is adjusted in such a way, that a feature (e. g. contamination spot for film phase plates) in the phase plate plane (i. e. on the film of a Zernike phase plate) is visible. The closer the conditions to the on-plane configuration the better.

2. For both deflector system axes, a certain offset to the image shift parameter (starting from a few nm up to about 10 μm) needs to be applied. Then, the corresponding pivot point calibration parameters need to be adjusted until the feature remains stationary regardless of the chosen image shift.

PUBLICATIONS

PUBLICATIONS

- Nicole Frindt, Marco Oster, Simon Hettler, Björn Gamm, Levin Dieterle, Wolfgang Kowalsky, Dagmar Gerthsen and Rasmus R. Schröder: In-Focus Electrostatic Zach Phase Plate Imaging for Transmission Electron Microscopy with Tunable Phase Contrast of Frozen Hydrated Biological Samples. Microscopy and Microanalysis, 2014.
- Simon Hettler, Jochen Wagner, Manuel Dries, Marco Oster, Christian Wacker, Rasmus R. Schröder, Dagmar Gerthsen: On the role of inelastic scattering in phase-plate transmission electron microscopy. Ultramicroscopy, 2015.
- S. Hettler, M. Dries, J. Zeelen, M. Oster, R. R. Schröder and D. Gerthsen: High-resolution transmission electron microscopy with an electrostatic Zach phase plate, submitted to New Journal of Physics, 2016.
- Sarah F. Wulf, Virginie Ropars, Setsuko Fujita-Becker, Marco Oster, Goetz Hofhaus, Leonardo G. Trabuco, Olena Pylypenko, H. Lee Sweeney, Anne M. Houdusse and Rasmus R. Schröder: Force-producing ADP state of myosin bound to actin, PNAS 2016.

CONFERENCES

- Marco Oster, Nicole Frindt and Rasmus Schröder, Simulations of Phase Plate Mediated Phase Contrast. MC Kiel, 2011.
- Nicole Frindt, Björn Gamm, Simon Hettler, Marco Oster, Irene Wacker, Dagmar Gerthsen and Rasmus R. Schröder: Zach phase plate imaging for transmission electron microscopy of macromolecular complexes. MC Kiel, 2011.
- Marco Oster, Nicole Frindt, Simon Hettler, Rasmus R. Schröder: Automating Phase Contrast Microscopy. EMC Manchester, 2012.

- Nicole Frindt, Simon Hettler, Marco Oster, Björn Gamm, Manuel Dries, Katrin Schultheiß, Dagmar Gerthsen and Rasmus R. Schröder: Tunable Phase Contrast of Vitrified Macromolecular Complexes by an Obstruction minimized Electrostatic Phase Plate. Microscopy and Microanalysis Phoenix, 18(Suppl 2):468, 2012.

- Nicole Frindt, Simon Hettler, Marco Oster, Björn Gamm, Manuel Dries, Katrin Schultheiß, Dagmar Gerthsen and Rasmus R. Schröder: Electrostatic Zach phase plate imaging with invertible phase contrast of frozen-hydrated biological samples. EMC Manchester, 2012.

- Simon Hettler, Jochen Wagner, Manuel Dries, Marco Oster, Rasmus R. Schröder and Dagmar Gerthsen: Application of Zach Phase Plates for Phase-Contrast Transmission Electron Microscopy: Status and Future Experiments. Microscopy and Microanalysis Hartford, 20 (Suppl 3):214, 2014.

- S. Hettler, M. Dries, T. Schulze, M. Oster, C. Wacker, R. R. Schröder, D. Gerthsen: High-resolution transmission electron microscopy with Zach phase plate, MC Göttingen, 2015.

- A. K. Kast, M. Oster, M. Pfannmöller, L. Veith, I. Wacker, G. Benner, W. Kowalsky, R. R. Schröder: Laterally resolved EELS of organic solar cells – optimizing spatial and energy resolution to localize charge transfer states with TEM, MC Göttingen, 2015.

- Marco Oster, Christian Wacker and Rasmus R. Schröder: Automatic Zernike phase plate alignment and its use to eliminate cut-on artifacts[1], MC Göttingen, 2015.

1 Won a best-poster award.

DANKSAGUNGEN

Ich bedanke mich bei meinen Betreuern und Gutachtern Prof. Dr. Wolfgang Kowalsky und Prof. Dr. Rasmus Schröder für das entgegengebrachte Vertrauen, die Unterstützung meines Promotionsverfahrens an der Universität Braunschweig, sowie der Bereitstellung der zum Anfertigen der Arbeit notwendigen Mikroskope.

Ich danke Rasmus Schröder für das Ermöglichen des interessanten Projekts, die fachliche Begleitung mit guten Ratschlägen, Organisation von interessantem Probenmaterial, konstruktiven Diskussionen zur Interpretation von Messergebnissen, die herausfordernden Visionen zur experimentellen Anwendung der Phasenplattentechnologie, sowie die Ermöglichung diverser Konferenzteilnahmen.

An meine Kollegen aus der CryoEM Arbeitsgruppe an der Universität Heidelberg ein herzliches Dankeschön für die Unterstützung mit Rat und Tat, der an dieser Stelle nur unzulänglich Rechnung getragen werden kann. Exemplarisch seien herausgestellt der Einsatz meines Zimmernachbarn Götz Hofhaus für sein Kümmern um den guten Zustand des Titans, die Unterstützung und Duldung der nicht immer seiteneffektfreien Phasenplattenexperimente, Hilfe bei der Präparation sowie Überlassen von Probenmaterial und der Erweiterung meines Horizonts in zahlreichen Diskussionen.

Johan Zeelen sei gedankt für sein Kümmern um das Zeiss 923, der röntgenschutztechnischen Begleitung der Experimente, das Überlassen von Probenmaterial und die vielen guten Hinweise auf ungenutztes Verbesserungspotential.

Christian Wacker danke ich für sein bereitwilliges und verständnisgerechtes Erklären der physikalischen und mathematischen Zusammenhänge, die unterhaltsamen und oft erkenntnisbringenden Gespräche und die guten Denkanstöße.

Ira Mang danke ich für die guten Ratschläge in allen Lebenslagen und die Überlassung diverser mehr oder weniger schwachen Phasenobjekte.

Auch den ehemaligen Mitarbeitern in der Arbeitsgruppe CryoEM, Nicole Frindt und Levin Dieterle ein herzliches Dankeschön für die gute Zusammenarbeit bei den Experimenten mit elektrostatischen Phasenplatten.

Ein besonderer Dank an die Kollaborationspartnern des Labors für Elektronenmikroskopie am KIT für die nichtselbstverständliche, gute Zusammenarbeit, ohne die die Ergebnisse der Arbeit nicht möglich gewesen wären. Tina Schulze und Manuel Dries seien für die Überlassung von funktionierenden, aufladungsarmen Zernike Filmphasenplatten gedankt. Danke an Simon Hettler für die Herstellung der elektrostatischen Zach Phasenplatten, seinen unerschütterlichen Optimismus, dass die Probleme sicher schon bei der nächsten Phasenplatte behoben sein werden, die hilfreichen Diskussionen zur Einordnung der beobachteten Effekte sowie die Motivation zu sportlichen Höchstleistungen.

Michael Scherer vom InnovationLab sei gedankt für die Überlassung der schönen organischen Solarzellenproben.

Danke auch an die ehemaligen Mitarbeiter der Firma KonTEM, vor allem Patrick Kurth und Steffen Pattai für ihren Einsatz beim Optimieren ihrer Positioniereinheit, der Erweiterung der Steuerung um eine Softwareschnittstelle und nicht zuletzt für die Kommunikation der Idee des dynamischen Bildaufnahmemodus.

Nichtselbstverständliche Hilfestellung zur Optimierung des elektronenoptischen Alignments kamen von Gerd Benner und Dmitry Kolmykov/Zeiss, Jörg Ranwez/FEI sowie Thomas Riedel/CEOS, dafür vielen Dank.

Großen Dank gebührt auch meinen Korrekturlesern, meiner Schwester Mariella und meinen Kollegen Anne Kast, Johan Zeelen und Christian Wacker, mit deren Hinweisen und Vorschlägen ich die Qualität der Arbeit deutlich verbessern konnte.

Der Deutschen Forschungsgemeinschaft danke ich für die Finanzierung des Projektes. Meiner Familie danke ich für die unbegrenzte Unterstützung und den verlässlichen Rückhalt. Danke an Sophie für die gute Zeit.

BIBLIOGRAPHY

[1] Abbe, E. Über die Grenzen der geometrischen Optik. *Jenaische Zeitschrift für Naturwissenschaft* 8(1):71–109, 1879 (Cited on page 3.)

[2] Badde, H. G. and Reimer, L. Der Einfluß einer streuenden Phasenplatte auf das elektronenmikroskopische Bild. *Zeitschrift für Naturforschung A* 25(5):760–765, 1970. doi:10.1515/zna-1970-0532 (Cited on page 37.)

[3] Bartesaghi, A., Merk, A., Banerjee, S., Matthies, D., Wu, X., Milne, J. L. S. and Subramaniam, S. 2.2 Å resolution cryo-EM structure of β-galactosidase in complex with a cell-permeant inhibitor. *Science* 348(6239):1147–1151, 2015. doi:10.1126/science.aab1576 (Cited on page 7.)

[4] Barthel, J. and Thust, A. Aberration measurement in HRTEM: Implementation and diagnostic use of numerical procedures for the highly precise recognition of diffractogram patterns. *Ultramicroscopy* 111(1):27–46, 2010. doi:10.1016/j.ultramic.2010.09.007 (Cited on pages 26 and 82.)

[5] Beleggia, M. A formula for the image intensity of phase objects in Zernike mode. *Ultramicroscopy* 108(9):953–958, 2008. doi:10.1016/j.ultramic.2008.03.003 (Cited on page 29.)

[6] Benner, G. Phasenkontrast-Elektronenmikroskop mit ringförmiger Beleuchtungsapertur, 2003. `http://www.google.com/patents/EP1329936A1?cl=de`. EP Patent App. EP20,020,023,322 (Cited on page 125.)

[7] Benner, G. and Matijevic, M. Phasenkontrast-Elektronenmikroskop, 2007. `https://www.google.com/patents/DE102006011615A1?cl=de`. DE Patent App. DE200,610,011,615 (Cited on page 32.)

[8] Boersch, H. Über die Kontraste von Atomen im Elektronenmikroskop. *Z. Naturforschg.* 2a:615–633, 1947 (Cited on pages 4, 6, and 29.)

[9] Brink, Gross, Tittmann, Sherman and Chiu. Reduction of charging in protein electron cryomicroscopy. *Journal of Microscopy* 191(1):67–73, 1998. doi:10.1046/j.1365-2818.1998.00342.x (Cited on page 59.)

[10] Brink, J., Sherman, M. B., Berriman, J. and Chiu, W. Evaluation of charging on macromolecules in electron cryomicroscopy. *Ultramicroscopy* 72(1-2):41–52, 1998. doi:10.1016/s0304-3991(97)00126-5 (Cited on pages 38 and 59.)

[11] Buijsse, B., van Laarhoven, F. M., Schmid, A. K., Cambie, R., Cabrini, S., Jin, J. and Glaeser, R. M. Design of a hybrid double-sideband/single-sideband (schlieren) objective aperture suitable for electron microscopy. *Ultramicroscopy* 111(12):1688–1695, 2011. doi:10.1016/j.ultramic.2011.09.015 (Cited on pages 31, 32, and 41.)

[12] Campbell, M. G., Veesler, D., Cheng, A., Potter, C. S. and Carragher, B. 2.8 Å resolution reconstruction of the Thermoplasma acidophilum 20S proteasome using cryo-electron microscopy. *eLife* 4, 2015. doi:10.7554/elife.06380 (Cited on page 7.)

[13] Carl Zeiss AG - Nano Technology Systems Division. KRONOS Cryo Energy Filter Transmission Electron Microscope User's Manual. Carl Zeiss AG - Nano Technology Systems Division, 2011 (Cited on page 72.)

[14] Dai, W., Fu, C., Khant, H. A., Ludtke, S. J., Schmid, M. F. and Chiu, W. Zernike phase-contrast electron cryotomography applied to marine cyanobacteria infected with cyanophages. *Nature Protocols* 9(11):2630–2642, 2014. doi:10.1038/nprot.2014.176 (Cited on page 154.)

[15] Dai, W., Fu, C., Raytcheva, D., Flanagan, J., Khant, H. A., Liu, X., Rochat, R. H., Haase-Pettingell, C., Piret, J., Ludtke, S. J., Nagayama, K., Schmid, M. F., King, J. A. and Chiu, W. Visualizing virus assembly intermediates inside marine cyanobacteria. *Nature* 502(7473):707–710, 2013. doi:10.1038/nature12604 (Cited on page 154.)

[16] Danev, R., Buijsse, B., Khoshouei, M., Plitzko, J. M. and Baumeister, W. Volta potential phase plate for in-focus phase contrast transmission electron microscopy. *Proceedings of the National Academy of Sciences* 111(44):15635–15640, 2014. doi:10.1073/pnas.1418377111 (Cited on pages 40 and 97.)

[17] Danev, R., Glaeser, R. M. and Nagayama, K. Practical factors affecting the performance of a thin-film phase plate for transmission electron microscopy. *Ultramicroscopy* 109(4):312–325, 2009. doi:10.1016/j.ultramic.2008.12.006 (Cited on pages 19 and 38.)

[18] Danev, R. and Nagayama, K. Transmission electron microscopy with Zernike phase plate. *Ultramicroscopy* 88(4):243–252, 2001. doi:10.1016/s0304-3991(01)00088-2 (Cited on pages 29 and 38.)

[19] Danev, R. and Nagayama, K. Complex Observation in Electron Microscopy: IV. Reconstruction of Complex Object Wave from Conventional and Half Plane Phase Plate Image Pair. *J. Phys. Soc. Jpn.* 73(10):2718–2724, 2004. doi:10.1143/jpsj.73.2718 (Cited on pages 40 and 171.)

[20] Danov, K., Danev, R. and Nagayama, K. Electric charging of thin films measured using the contrast transfer function. *Ultramicroscopy* 87(1-2):45–54, 2001. doi:10.1016/s0304-3991(00)00061-9 (Cited on pages 38 and 109.)

[21] Dries, M. Experimentelle und theoretische Untersuchungen zum Hilbert-Phasenkontrast in der Transmissionselektronenmikroskopie. Ph.D. thesis, Karlsruher Institut für Technologie, 2015 (Cited on page 137.)

[22] Dries, M., Hettler, S., Gamm, B., Müller, E., Send, W., Müller, K., Rosenauer, A. and Gerthsen, D. A nanocrystalline Hilbert phase-plate for phase-contrast transmission electron microscopy. *Ultramicroscopy* 139:29–37, 2014. doi:10.1016/j.ultramic.2014.01.002 (Cited on pages 37 and 38.)

[23] Dries, M., Schultheiß, K., Gamm, B., Rosenauer, A., Schröder, R. and Gerthsen, D. Object-wave reconstruction by carbon film-based Zernike- and Hilbert-phase plate microscopy: A theoretical study not restricted to weak-phase objects. *Ultramicroscopy* 111(2):159–168, 2011. doi:10.1016/j.ultramic.2010.10.009 (Cited on page 26.)

[24] Duda, R. O. and Hart, P. E. Use of the Hough transformation to detect lines and curves in pictures. *Commun. ACM* 15(1):11–15, 1972. doi:10.1145/361237.361242 (Cited on page 80.)

[25] Edgcombe, C., Ionescu, A., Loudon, J., Blackburn, A., Kurebayashi, H. and Barnes, C. Characterisation of ferromagnetic rings for Zernike

phase plates using the Aharonov-Bohm effect. *Ultramicroscopy* 120:78–85, 2012. doi:10.1016/j.ultramic.2012.06.011 (Cited on page 41.)

[26] Egerton, R., Li, P. and Malac, M. Radiation damage in the TEM and SEM. *Micron* 35(6):399–409, 2004. doi:10.1016/j.micron.2004.02.003 (Cited on page 9.)

[27] Ennos, A. E. The origin of specimen contamination in the electron microscope. *British Journal of Applied Physics* 4(4):101–106, 1953. doi:10.1088/0508-3443/4/4/302 (Cited on pages 9 and 109.)

[28] Erni, R. Aberration-Corrected Imaging in Transmission Electron Microscopy. World Scientific Pub Co Pte Lt, 2010. doi:10.1142/9781848165373_0002 (Cited on pages 15 and 18.)

[29] Fernandez, J.-J., Sorzano, C., Marabini, R. and Carazo, J.-M. Image processing and 3-D reconstruction in electron microscopy. *IEEE Signal Processing Magazine* 23(3):84–94, 2006. doi:10.1109/msp.2006.1628881 (Cited on page 7.)

[30] Fischler, M. A. and Bolles, R. C. Random sample consensus: a paradigm for model fitting with applications to image analysis and automated cartography. *Communications of the ACM* 24(6):381–395, 1981 (Cited on page 156.)

[31] Frindt, N. Development and implementation of electrostatic Zach phase plates for phase contrast transmission electron microscopy. Ph.D. thesis, Universität Heidelberg, 2013 (Cited on pages 106 and 108.)

[32] Frindt, N., Oster, M., Hettler, S., Gamm, B., Dieterle, L., Kowalsky, W., Gerthsen, D. and Schröder, R. R. In-Focus Electrostatic Zach Phase Plate Imaging for Transmission Electron Microscopy with Tunable Phase Contrast of Frozen Hydrated Biological Samples. *Microsc Microanal* 20(01):175–183, 2014. doi:10.1017/s1431927613013901 (Cited on pages 102 and 106.)

[33] Gamm, B., Dries, M., Schultheiß, K., Blank, H., Rosenauer, A., Schröder, R. and Gerthsen, D. Object wave reconstruction by phase-plate transmission electron microscopy. *Ultramicroscopy* 110(7):807–814, 2010. doi:10.1016/j.ultramic.2010.02.006 (Cited on pages 7 and 26.)

[34] Glaeser, R. M., Sassolini, S., Cambie, R., Jin, J., Cabrini, S., Schmid, A. K., Danev, R., Buijsse, B., Csencsits, R., Downing, K. H., Larson, D. M., Typke, D. and Han, B. Minimizing electrostatic charging of an aperture used to produce in-focus phase contrast in the TEM. *Ultramicroscopy* 135:6–15, 2013. doi:10.1016/j.ultramic.2013.05.023 (Cited on pages 38 and 117.)

[35] Glaeser, R. M. and Taylor, K. A. Radiation damage relative to transmission electron microscopy of biological specimens at low temperature: a review. *Journal of Microscopy* 112(1):127–138, 1978. doi:10.1111/j.1365-2818.1978.tb01160.x (Cited on page 7.)

[36] Haider, M., Hartel, P., Müller, H., Uhlemann, S. and Zach, J. Information Transfer in a TEM Corrected for Spherical and Chromatic Aberration. *Microsc Microanal* 16(04):393–408, 2010. doi:10.1017/s1431927610013498 (Cited on page 17.)

[37] Haider, M., Uhlemann, S., Schwan, E., Rose, H., Kabius, B. and Urban, K. Electron microscopy image enhanced. *Nature* 392(6678):768–769, 1998. doi:10.1038/33823 (Cited on pages 17 and 26.)

[38] Henderson, R. The potential and limitations of neutrons, electrons and X-rays for atomic resolution microscopy of unstained biological molecules. *Quart. Rev. Biophys.* 28(02):171–193, 1995. doi:10.1017/s003358350000305x (Cited on page 7.)

[39] Hettler, S. Transmissionselektronenmikroskopie mit elektrostatischen Zach-Phasenplatten. Ph.D. thesis, Karlsruher Institut für Technologie, 2015 (Cited on pages 99, 106, and 117.)

[40] Hettler, S., Gamm, B., Dries, M., Frindt, N., Schröder, R. R. and Gerthsen, D. Improving Fabrication and Application of Zach Phase Plates for Phase-Contrast Transmission Electron Microscopy. *Microsc Microanal* 18(05):1010–1015, 2012. doi:10.1017/s1431927612001560 (Cited on page 106.)

[41] Kishchenko, G. P., Danev, R., Fisher, R., He, J., Hsieh, C., Marko, M. and Sui, H. Effect of fringe-artifact correction on sub-tomogram averaging from Zernike phase-plate cryo-TEM. *Journal of Structural Biology* 191(3):299–305, 2015. doi:10.1016/j.jsb.2015.07.009 (Cited on page 154.)

[42] Kleindiek, S. Elektromechanische Positioniereinheit, 1996. `https://www.google.de/patents/DE4440758A1?cl=de`. DE Patent App. DE19,944,440,758 (Cited on page 56.)

[43] Kleindiek Nanotechnik. MM3A-EM Micromanipulator Datasheet. Kleindiek Nanotechnik, Kleindiek Nanotechnik GmbH Aspenhaustrasse 25 72770 Reutlingen Germany (Cited on page 56.)

[44] Koeck, P. Improved Zernike-type phase contrast for transmission electron microscopy. *Journal of Microscopy* 259(1):74–78, 2015. doi:10.1111/jmi.12250 (Cited on page 29.)

[45] Kohl, H. and Reimer, L. Transmission Electron Microscopy. Springer, 2008. doi:10.1007/978-0-387-40093-8 (Cited on pages 13, 15, 18, 19, 20, 21, 22, and 45.)

[46] Koster, A., Chen, H., Sedat, J. and Agard, D. Automated microscopy for electron tomography. *Ultramicroscopy* 46(1-4):207–227, 1992. doi:10.1016/0304-3991(92)90016-d (Cited on page 53.)

[47] Koster, A., de Ruijter, W., Van Den Bos, A. and Van Der Mast, K. Autotuning of a TEM using minimum electron dose. *Ultramicroscopy* 27(3):251–272, 1989. doi:10.1016/0304-3991(89)90018-1 (Cited on page 48.)

[48] Koster, A., Van den Bos, A. and van der Mast, K. An autofocus method for a TEM. *Ultramicroscopy* 21(3):209–222, 1987. doi:10.1016/0304-3991(87)90146-x (Cited on page 126.)

[49] Lentzen, M., Jahnen, B., Jia, C., Thust, A., Tillmann, K. and Urban, K. High-resolution imaging with an aberration-corrected transmission electron microscope. *Ultramicroscopy* 92(3-4):233–242, 2002. doi:10.1016/s0304-3991(02)00139-0 (Cited on pages 24 and 28.)

[50] Lewis, B. A. and Engelman, D. M. Lipid bilayer thickness varies linearly with acyl chain length in fluid phosphatidylcholine vesicles. *Journal of Molecular Biology* 166(2):211–217, 1983. doi:10.1016/s0022-2836(83)80007-2 (Cited on page 138.)

[51] Majorovits, E., Barton, B., Benner, G., Dietl, C., Kühlbrandt, W., Lengweiler, S., Mandler, T., Matijevic, M., Niebel, H. and Schröder, R. Phase Contrast Aberration Corrected Electron Microscope for Phase Plate Imaging. *Microsc Microanal* 16(S2):534–535, 2010. doi:10.1017/s1431927610057740 (Cited on page 32.)

[52] Majorovits, E., Barton, B., Schultheiß, K., Pérez-Willard, F., Gerthsen, D. and Schröder, R. Optimizing phase contrast in transmission electron microscopy with an electrostatic (Boersch) phase plate. *Ultramicroscopy* 107(2-3):213–226, 2007. doi:10.1016/j.ultramic.2006.07.006 (Cited on page 31.)

[53] Malac, M., Beleggia, M., Egerton, R. and Zhu, Y. Imaging of radiation-sensitive samples in transmission electron microscopes equipped with Zernike phase plates. *Ultramicroscopy* 108(2):126–140, 2008. doi:10.1016/j.ultramic.2007.03.008 (Cited on page 29.)

[54] Malac, M., Beleggia, M., Kawasaki, M., Li, P. and Egerton, R. F. Convenient contrast enhancement by a hole-free phase plate. *Ultramicroscopy* 118:77–89, 2012. doi:10.1016/j.ultramic.2012.02.004 (Cited on page 32.)

[55] Marko, M., Meng, X., Hsieh, C., Roussie, J. and Striemer, C. Methods for testing Zernike phase plates and a report on silicon-based phase plates with reduced charging and improved ageing characteristics. *Journal of Structural Biology* 184(2):237–244, 2013. doi:10.1016/j.jsb.2013.08.008 (Cited on page 38.)

[56] Matsumoto, T. and Tonomura, A. The phase constancy of electron waves traveling through Boersch's electrostatic phase plate. *Ultramicroscopy* 63(1):5–10, 1996. doi:10.1016/0304-3991(96)00033-2 (Cited on pages 29 and 100.)

[57] McMullan, G., Vinothkumar, K. and Henderson, R. Thon rings from amorphous ice and implications of beam-induced Brownian motion in single particle electron cryo-microscopy. *Ultramicroscopy* 158:26–32, 2015. doi:10.1016/j.ultramic.2015.05.017 (Cited on pages 26 and 94.)

[58] Meyer, R., Kirkland, A. and Saxton, W. A new method for the determination of the wave aberration function for high resolution TEM. *Ultramicroscopy* 92(2):89–109, 2002. doi:10.1016/s0304-3991(02)00071-2 (Cited on pages 6, 21, 26, and 46.)

[59] Mindell, J. A. and Grigorieff, N. Accurate determination of local defocus and specimen tilt in electron microscopy. *Journal of Structural Biology* 142(3):334–347, 2003. doi:10.1016/s1047-8477(03)00069-8 (Cited on page 82.)

[60] Moers, M. and Danev, R. Abbildung einer Probe in einem TEM, das mit einer Phasenplatte ausgerüstet ist, 2014. https://encrypted.google.com/patents/EP2704178B1?cl=de. EP Patent 2,704,178 (Cited on page 124.)

[61] Müller, H., Jin, J., Danev, R., Spence, J., Padmore, H. and Glaeser, R. M. Design of an electron microscope phase plate using a focused continuous-wave laser. *New J. Phys.* 12(7):073011, 2010. doi:10.1088/1367-2630/12/7/073011 (Cited on page 41.)

[62] Nagle, J. F. and Tristram-Nagle, S. Structure of lipid bilayers. *Biochimica et Biophysica Acta (BBA) - Reviews on Biomembranes* 1469(3):159–195, 2000. doi:10.1016/s0304-4157(00)00016-2 (Cited on page 138.)

[63] Nanova, D., Scherer, M., Schell, F., Zimmermann, J., Glaser, T., Kast, A. K., Krekeler, C., Pucci, A., Kowalsky, W., Schröder, R. R. and Lovrinčić, R. Why Inverted Small Molecule Solar Cells Outperform Their Noninverted Counterparts. *Advanced Functional Materials* 25(41):6511–6518, 2015. doi:10.1002/adfm.201502943 (Cited on page 150.)

[64] Penczek, P. A. Image Restoration in Cryo-Electron Microscopy. *Cryo-EM, Part B: 3-D Reconstruction* 35–72, 2010. doi:10.1016/s0076-6879(10)82002-6 (Cited on pages 6 and 26.)

[65] PiezoMotor. Piezo LEGS® Linear Twin 20N Datasheet. PiezoMotor Uppsala AB, Stålgatan 14 SE-754 50 Uppsala, Sweden (Cited on page 56.)

[66] Rhinow, D. Towards an optimum design for thin film phase plates. *Ultramicroscopy* 160:1–6, 2016. doi:10.1016/j.ultramic.2015.09.003 (Cited on page 42.)

[67] Rohou, A. and Grigorieff, N. CTffind4: Fast and accurate defocus estimation from electron micrographs. *Journal of Structural Biology* 192(2):216–221, 2015. doi:10.1016/j.jsb.2015.08.008 (Cited on pages 26, 100, 136, and 156.)

[68] Ruska, E. The development of the electron microscope and of electron microscopy. *Rev. Mod. Phys.* 59(3):627–638, 1987. doi:10.1103/revmodphys.59.627 (Cited on page 4.)

[69] Ruskin, R. S., Yu, Z. and Grigorieff, N. Quantitative characterization of electron detectors for transmission electron microscopy. *Journal of Structural Biology* 184(3):385–393, 2013. doi:10.1016/j.jsb.2013.10.016 (Cited on page 22.)

[70] Russo, C. J. and Passmore, L. A. Ultrastable gold substrates for electron cryomicroscopy. *Science* 346(6215):1377–1380, 2014. doi:10.1126/science.1259530 (Cited on page 60.)

[71] Scharber, M. and Sariciftci, N. Efficiency of bulk-heterojunction organic solar cells. *Progress in Polymer Science* 38(12):1929–1940, 2013. doi:10.1016/j.progpolymsci.2013.05.001 (Cited on pages 1 and 2.)

[72] Scherzer, O. Über einige Fehler von Elektronenlinsen. *Z. Physik* 101(9-10):593–603, 1936. doi:10.1007/bf01349606 (Cited on page 17.)

[73] Scherzer, O. The Theoretical Resolution Limit of the Electron Microscope. *Journal of Applied Physics* 20(1):20–29, 1949. doi:10.1063/1.1698233 (Cited on pages 6 and 24.)

[74] Schröder, R. R., Barton, B., Rose, H. H. and Benner, G. Contrast Enhancement by Anamorphotic Phase Plates in an Aberration-corrected TEM. *MAM* 13(S02), 2007. doi:10.1017/s1431927607074867 (Cited on page 41.)

[75] Schultheiß, K. Entwicklung und Anwendung elektrostatischer Phasenplatten in der Transmissionselektronenmikroskopie. Ph.D. thesis, Karlsruher Institut für Technologie, 2010 (Cited on page 30.)

[76] Schultheiß, K., Pérez-Willard, F., Barton, B., Gerthsen, D. and Schröder, R. R. Fabrication of a Boersch phase plate for phase contrast imaging in a transmission electron microscope. *Review of Scientific Instruments* 77(3):033701, 2006. doi:10.1063/1.2179411 (Cited on page 29.)

[77] Schultheiß, K., Zach, J., Gamm, B., Dries, M., Frindt, N., Schröder, R. R. and Gerthsen, D. New Electrostatic Phase Plate for Phase-Contrast Transmission Electron Microscopy and Its Application for Wave-Function Reconstruction. *Microsc Microanal* 16(06):785–794, 2010. doi:10.1017/s1431927610093803 (Cited on page 110.)

[78] Suloway, C., Pulokas, J., Fellmann, D., Cheng, A., Guerra, F., Quispe, J., Stagg, S., Potter, C. S. and Carragher, B. Automated molecular

microscopy: The new Leginon system. *Journal of Structural Biology* 151(1):41–60, 2005. doi:10.1016/j.jsb.2005.03.010 (Cited on page 44.)

[79] Suloway, C., Shi, J., Cheng, A., Pulokas, J., Carragher, B., Potter, C. S., Zheng, S. Q., Agard, D. A. and Jensen, G. J. Fully automated, sequential tilt-series acquisition with Leginon. *Journal of Structural Biology* 167(1):11–18, 2009. doi:10.1016/j.jsb.2009.03.019 (Cited on page 54.)

[80] Villarreal, M. R. Phospholipids in aqueous solution structures, 2007. `https://en.wikipedia.org/wiki/File:Phospholipids_aqueous_solution_structures.svg` (Cited on page 139.)

[81] Vulović, M., Franken, E., Ravelli, R. B., van Vliet, L. J. and Rieger, B. Precise and unbiased estimation of astigmatism and defocus in transmission electron microscopy. *Ultramicroscopy* 116:115–134, 2012. doi:10.1016/j.ultramic.2012.03.004 (Cited on pages 26 and 82.)

[82] Walter, A., Steltenkamp, S., Schmitz, S., Holik, P., Pakanavicius, E., Sachser, R., Huth, M., Rhinow, D. and Kühlbrandt, W. Towards an optimum design for electrostatic phase plates. *Ultramicroscopy* 153:22–31, 2015. doi:10.1016/j.ultramic.2015.01.005 (Cited on pages 9, 31, 117, and 118.)

[83] Williams, D. B. and Carter, C. B. Transmission Electron Microscopy. Springer, 2009. doi:10.1007/978-0-387-76501-3 (Cited on page 18.)

[84] Yang, F., Shtein, M. and Forrest, S. R. Controlled growth of a molecular bulk heterojunction photovoltaic cell. *Nat Mater* 4(1):37–41, 2004. doi:10.1038/nmat1285 (Cited on page 1.)

[85] Yu, G., Gao, J., Hummelen, J. C., Wudl, F. and Heeger, A. J. Polymer Photovoltaic Cells: Enhanced Efficiencies via a Network of Internal Donor-Acceptor Heterojunctions. *Science* 270(5243):1789–1791, 1995. doi:10.1126/science.270.5243.1789 (Cited on page 2.)

[86] Zach, J. Phasenplatte, Bilderzeugungsverfahren und Elektronenmikroskop, 2008. `https://www.google.de/patents/DE102006055510A1?cl=de`. DE Patent App. DE200,610,055,510 (Cited on page 32.)

[87] Zemlin, F., Weiss, K., Schiske, P., Kunath, W. and Herrmann, K.-H. Coma-free alignment of high resolution electron microscopes with the aid of optical diffractograms. *Ultramicroscopy* 3:49–60, 1978. doi:10.1016/s0304-3991(78)80006-0 (Cited on page 61.)

[88] Zernike, F. Das Phasenkontrastverfahren bei der mikroskopischen Beobachtung. *Z. Tech. Phys* 16:454–457, 1935 (Cited on page 4.)

[89] Zernike, F. Phase contrast, a new method for the microscopic observation of transparent objects. *Physica* 9(7):686–698, 1942. doi:10.1016/s0031-8914(42)80035-x (Cited on pages 20 and 31.)

[90] Zhang, X. and Hong Zhou, Z. Limiting factors in atomic resolution cryo electron microscopy: No simple tricks. *Journal of Structural Biology* 175(3):253–263, 2011. doi:10.1016/j.jsb.2011.05.004 (Cited on page 127.)

[91] Zheng, Q. S., Braunfeld, M. B., Sedat, J. W. and Agard, D. A. An improved strategy for automated electron microscopic tomography. *Journal of Structural Biology* 147(2):91–101, 2004. doi:10.1016/j.jsb.2004.02.005 (Cited on pages 54 and 155.)

[92] Zheng, S. Q., Keszthelyi, B., Branlund, E., Lyle, J. M., Braunfeld, M. B., Sedat, J. W. and Agard, D. A. UCSF tomography: An integrated software suite for real-time electron microscopic tomographic data collection, alignment, and reconstruction. *Journal of Structural Biology* 157(1):138–147, 2007. doi:10.1016/j.jsb.2006.06.005 (Cited on page 54.)

[93] Ziese, U., Janssen, A. H., Murk, J.-L., Geerts, W. J. C., Van der Krift, T., Verkleij, A. and Koster, A. Automated high-throughput electron tomography by pre-calibration of image shifts. *J Microsc* 205(2):187–200, 2002. doi:10.1046/j.0022-2720.2001.00987.x (Cited on page 53.)